

Monday Morning, November 10, 2014

2D Materials Focus Topic

Room: 310 - Session 2D+EM+NS+PS+SS+TF-MoM

2D Materials Growth and Processing

Moderator: Thomas Greber, University of Zurich

8:20am **2D+EM+NS+PS+SS+TF-MoM1 Exploring the Flatlands: Synthesis, Characterization and Engineering of Two-Dimensional Materials, Jun Lou**, Rice University **INVITED**

In this talk, we report the controlled vapor phase synthesis of MoS₂ atomic layers and elucidate a fundamental mechanism for the nucleation, growth, and grain boundary formation in its crystalline monolayers. The atomic structure and morphology of the grains and their boundaries in the polycrystalline molybdenum disulfide atomic layers are examined and first-principles calculations are applied to investigate their energy landscape. The electrical properties of the atomic layers are examined and the role of grain boundaries is evaluated. More importantly, if precise two-dimensional domains of graphene, h-BN and MoS₂ atomic layers can be seamlessly stitched together, in-plane heterostructures with interesting electronic applications could potentially be created. Here, we show that planar graphene/h-BN heterostructures can be formed by growing graphene in lithographically-patterned h-BN atomic layers. Our approach can create periodic arrangements of domains with size that ranging from tens of nanometers to millimeters. The resulting graphene/h-BN atomic layers can be peeled off from their growth substrate and transferred to various platforms including flexible substrate. Finally, we demonstrate how self-assembled monolayers with a variety of end termination chemistries can be utilized to tailor the physical properties of single-crystalline MoS₂ atomic-layers. Our data suggests that combined interface-related effects of charge transfer, built-in molecular polarities, varied densities of defects, and remote interfacial phonons strongly modify the electrical and optical properties of MoS₂, illustrating an engineering approach for local and universal property modulations in two-dimensional atomic-layers.

9:00am **2D+EM+NS+PS+SS+TF-MoM3 Influence of Substrate Orientation on the Growth of Graphene on Cu Single Crystals, Tyler Mowll**, University at Albany-SUNY, Z.R. Robinson, U.S. Naval Research Laboratory, P. Tyagi, E.W. Ong, C.A. Ventrice, Jr., University at Albany-SUNY

A systematic study of graphene growth on on-axis Cu(100) and Cu(111) single crystals oriented within 0.1° from the surface normal and a vicinal Cu(111) crystal oriented 5° off-axis has been performed. Initial attempts to grow graphene by heating each crystal to 900°C in UHV, followed by backfilling the chamber with C₂H₄ at pressures up to 5x10⁻³ Torr did not result in graphene formation on either the on-axis Cu(100) or on-axis Cu(111) surfaces. For the vicinal Cu(111) surface, epitaxial graphene was formed under the same growth conditions. By backfilling the chamber with C₂H₄ before heating to the growth temperature, epitaxial graphene was formed on both the on-axis Cu(100) and off-axis Cu(111) surfaces, but not the on-axis Cu(111) surface. By using an argon overpressure, epitaxial overlayers could be achieved on all three Cu substrates. These results indicate that the most catalytically active sites for the dissociation of ethylene are the step edges, followed by the Cu(100) terraces sites and the Cu(111) terrace sites. The need for an argon overpressure to form graphene the on-axis Cu(111) surface indicates that the Cu sublimation rate is higher than the graphene growth rate for this surface. This research was supported in part by the NSF (DMR-1006411).

9:20am **2D+EM+NS+PS+SS+TF-MoM4 Synthesis of Large Scale MoS₂-Graphene Heterostructures, Kathleen McCreary, A.T. Hanbicki, J. Robinson, B.T. Jonker**, Naval Research Laboratory

A rapidly progressing field involves the stacking of multiple two-dimensional materials to form heterostructures. These heterostructures have exhibited unique and interesting properties. For the most part, heterostructure devices are produced via mechanical exfoliation requiring the careful aligning and stacking of the individual 2D layered components. This tedious and time consuming process typically limits lateral dimensions to micron-scale devices. Chemical vapor deposition (CVD) has proven to be a useful tool in the production of graphene and has very recently been investigated as a means for the growth of other 2D materials such as MoS₂, MoSe₂, WS₂, WSe₂, and hexagonal boron nitride. Using a two-step CVD process we are able to synthesize MoS₂ on CVD grown graphene. AFM, Raman spectroscopy, and Photoluminescence spectroscopy of the MoS₂-graphene heterostructure show a uniform and continuous film on the cm scale.

9:40am **2D+EM+NS+PS+SS+TF-MoM5 Growth of 2D MoS₂ Films by Magnetron Sputtering, Andrey Voevodin**, Air Force Research Laboratory, C. Muratore, University of Dayton, J.J. Hu, Air Force Research Laboratory/UDRI, B. Wang, M.A. Haque, Pennsylvania State University, J.E. Bultman, M.L. Jespersion, Air Force Research Laboratory/UDRI, P.J. Shamberger, Texas A&M University, R. Stevenson, Air Force Research Laboratory, A. Waite, Air Force Research Laboratory/UTC, M.E. McConney, R. Smith, Air Force Research Laboratory

Growth of two dimensional (2D) MoS₂ and similar materials over large areas is a critical pre-requisite for seamless integration of next-generation van der Waals heterostructures into novel devices. Typical preparation approaches with chemical or mechanical exfoliation lack scalability and uniformity over appreciable areas (>1 mm) and chemical vapor deposition processes require high substrate temperatures. We developed few-layer MoS₂ growth under non-equilibrium magnetron sputtering conditions selected to minimize the MoS₂ nucleation density and maximize 2D growth of individual crystals [1]. In this process, the thermodynamically driven tendency to form islands is accomplished by maximizing atomic mobility through the control of incident flux kinetic energies, densities, and arriving angle to the substrate while avoiding defect formation (i.e., vacancy creation by sputtering of S atoms). Amorphous SiO₂, crystalline (0001) oriented Al₂O₃, and (002) oriented graphite substrates were used to grow few monolayer thick MoS₂ films. Continuous 2D MoS₂ films were produced over 4 cm² areas. They were composed of nano-scale domains with strong chemical binding between domain boundaries, allowing lift-off from the substrate and electronic transport measurements with contact separation on the order of centimeters. Their characteristics were similar to few-layer MoS₂ films produced by exfoliation with a direct band gap in thin samples of approximately 1.9 eV from photoluminescence spectra. The electron mobility measured for as-grown MoS₂ films was very strongly dependent on film thickness and substrate choice.

[1] "Continuous ultra-thin MoS₂ films grown by low-temperature physical vapor deposition", C. Muratore, J.J. Hu, B. Wang, M.A. Haque, J.E. Bultman, M. L. Jespersion, P.J. Shamberger, A.A. Voevodin, Applied Physics Letters (2014) in press.

10:00am **2D+EM+NS+PS+SS+TF-MoM6 Formation of Graphene on the C-face of SiC{0001}: Experiment and Theory, Jun Li, G. He, M. Widom, R.M. Feenstra**, Carnegie Mellon University

There are two {0001} surfaces of SiC, the (0001) surface known as the "Si-face", and the (000-1) surface or "C-face". The formation of graphene (by heating the SiC to 1100 – 1600 °C in various gaseous environments) has been studied for both surfaces, although it is much better understood on the Si-face. In that case, an intermediate C-rich layer, or "buffer layer" forms between the graphene and the SiC crystal. This buffer layer has 6√3x6√3-R30° symmetry; its structure is well established,¹ and it acts as a template for the formation of subsequent graphene layers. In contrast, graphene formation on the C-face is much less well understood. More than one interface structure between the graphene and the SiC has been observed,^{2,3} and, with one notable exception,⁴ the quality of the graphene formed on the C-face is generally lower than that for the Si-face.

In this work we provide new experimental and theoretical results that allow us to understand graphene formation on the C-face of SiC. Experimentally, by heating the SiC in a disilane environment, we map out the phase diagram of different surface and interface structures that form on the SiC as a function of disilane pressure and sample temperature. New surface structures that develop just prior to the graphene formation are observed. With additional heating, graphene forms on the surface, but some remnant of the surface structure prior to the graphene formation is believed to persist at the graphene/SiC interface. From first-principles theory, we find that the hydrogen in the disilane environment plays a critical role in the surface/interface structures that form. Experimentally, for disilane pressures below 5x10⁻⁵ Torr, we find a 2x2 surface structure forming prior to graphene formation. From theory we identify this structure as consisting of a silicon adatom together with a carbon restatom on the surface, with H-termination of those atoms being possible but not necessary. At higher disilane pressures we observe a 4x4 structure, and we identify that as consisting of a lower density of Si adatoms than the 2x2, now with at least some of the adatoms and restatoms being H-terminated. With graphene formation, this structure converts to the observed √43x√43-R± 7.6° interface structure. At higher disilane pressures we theoretically predict the formation of a surface consisting simply of H-terminated carbon restatoms. Experiments are underway to observe that surface, along with subsequent graphene formation on the surface.

(1) Y. Qi et al., PRL **105**, 085502 (2010).

- (2) F. Hiebel et al., PRB **78**, 153412 (2008).
 (3) N. Srivastava et al., PRB **85**, 041404 (2012).
 (4) W. A. de Heer et al., PNAS **108**, 16900 (2011).

10:40am **2D+EM+NS+PS+SS+TF-MoM8 Graphene on Hexagonal Boron Nitride Heterostacks Grown by UHV-CVD on Metal Surfaces**, *Juerg Osterwalder, S. Roth, A. Hemmi*, University of Zurich, Switzerland, *F. Matsui, Nara Institute of Science and Technology, Japan, T. Greber*, University of Zurich, Switzerland **INVITED**

Chemical vapor deposition (CVD) performed under ultra-high vacuum conditions on single-crystal metal surfaces enables the growth of large-area and high-quality graphene and hexagonal boron nitride (h-BN) single layers. We explore the CVD parameter space of precursor pressure and temperature in order to go beyond the self-saturating single-layer growth, or to grow heterostacks of the two materials. Formed layers are characterized structurally by LEED, STM and x-ray photoelectron diffraction. On Cu(111) a graphene layer could be grown on a pre-deposited single layer of h-BN when using 3-pentanone as a precursor at a pressure of 2.2 mbar and a substrate temperature of 1100 K [1]. On Rh(111) the same procedure leads to incorporation of carbon into the metal surface layers, while a graphene layer is formed only upon a second high-pressure dose [2]. In both cases the heterostructures show clearly the stacking sequence and structural and ARPES signatures of graphene on h-BN but are far from defect-free.

- [1] S. Roth et al., Nano Lett. **13**, 2668 (2013).
 [2] S. Roth, PhD Thesis, Department of Physics, University of Zurich (2013).

11:20am **2D+EM+NS+PS+SS+TF-MoM10 Kinetics of Monolayer Graphene Growth by Carbon Segregation on Pd(111)**, *Abbas Ebnonnasir, H.S. Mok, Y. Murata*, University of California at Los Angeles, *S. Nie, K.F. McCarty*, Sandia National Laboratories, *C.V. Ciobanu*, Colorado School of Mines, *S. Kodambaka*, University of California at Los Angeles

In this research, using in situ low-energy electron microscopy and density functional theory calculations, we elucidate the growth kinetics of monolayer graphene on single-crystalline Pd(111). In our experiments, carbon saturated Pd(111) samples were cooled down from 900 °C to segregate carbon on the surface in the form of graphene. Upon cooling the substrate, graphene nucleation begins on bare Pd surface and continues to occur during graphene growth. Measurements of graphene growth rates and Pd surface work functions along with DFT calculations establish that this continued nucleation is due to increasing C adatom concentration on the Pd surface with time. We attribute this anomalous phenomenon to a large barrier for attachment of C adatoms to graphene coupled with a strong binding of the non-graphitic C to the Pd surface.

Electronic Materials and Processing Room: 314 - Session EM+MI+NS-MoM

Complex Oxides and Their Interfaces

Moderator: Jessica Hilton, Mantis Deposition, Lisa M. Porter, Carnegie Mellon University

8:20am **EM+MI+NS-MoM1 Emergent Phenomena at Complex Oxide Interfaces**, *Susanne Stemmer*, University of California at Santa Barbara **INVITED**

Two-dimensional electron gases (2DEGs) at interfaces between two insulating oxides have attracted significant attention because they can exhibit unique properties, such as strong electron correlations, superconductivity, and magnetism. In this presentation, we will discuss properties arising from strong electron correlations in narrow quantum wells of the band insulator SrTiO₃, sandwiched between Mott insulating rare earth titanates, SmTiO₃ and GdTiO₃, respectively. These quantum wells exhibit very high sheet electron high-densities, of approximately 1 electron per planar unit cell of the quantum well. We demonstrate electron correlation effects due to short-range Coulomb interactions, including mass enhancement, interface-induced magnetism in the electron gas, and a transition to a correlated insulator at the lowest thickness in quantum wells bound by ferrimagnetic GdTiO₃. We show that the metal-insulator transition is coupled with the sudden onset of structural distortions in the quantum well. In contrast, quantum wells bound by antiferromagnetic SmTiO₃ exhibit almost no structural distortions, incipient antiferromagnetism, no metal-insulator transition, and non-Fermi liquid behavior. We will discuss the implications of the results in the context of two-dimensional electron correlation physics.

This work was performed in collaboration with Clayton Jackson, Pouya Moetakef, Jack Zhang, Jinwoo Hwang, Leon Balents, and Jim Allen.

9:00am **EM+MI+NS-MoM3 Atomic and Electronic Structure of the Ferroelectric BaTiO₃-Ge (001) Interface**, *Kurt Fredrickson*, The University of Texas at Austin, *P. Ponath, A.B. Posadas*, University of Texas at Austin, *M.R. McCartney, T. Aoki, D.J. Smith*, Arizona State University, *A.A. Demkov*, University of Texas at Austin

In this study, we demonstrate the epitaxial growth of BaTiO₃ on Ge(001) by molecular beam epitaxy using a thin Zintl template buffer layer. A combination of density functional theory, atomic-resolution electron microscopy and *in situ* photoemission spectroscopy is used to investigate the electronic properties and atomic structure of the BaTiO₃/Ge interface. Aberration-corrected scanning transmission electron micrographs reveal that the Ge(001) 2x1 surface reconstruction remains intact during the subsequent BaTiO₃ growth, thereby enabling a choice to be made between several theoretically predicted interface structures. The measured valence band offset of 2.7 eV matches well with the theoretical value of 2.5 eV based on the model structure for an in-plane-polarized interface. The agreement between the calculated and measured band offsets, which is highly sensitive to the detailed atomic arrangement, indicates that the most likely BaTiO₃/Ge(001) interface structure has been identified.

9:20am **EM+MI+NS-MoM4 Strain-Controlled Stoichiometry Variations in CaMnO₃ Epitaxial Thin Films**, *Rajeswari Kolagani, G. Yong, Z. Warecki, C. Stumpf, D. Schaefer, P. Sharma, C. Hart, A. Burger*, Towson University

CaMnO₃ is a material of interest for application in novel energy technologies such as thermoelectric power generation, and as a photo catalyst for hydrogen energy storage. We are currently investigating the properties of epitaxial thin films of CaMnO₃ (CMO) and its electron doped derivatives towards tuning material properties that enable these applications. Oxygen stoichiometry and its effect on structural and electronic properties are key variables in optimizing thin films of these materials. We will present our studies of CMO thin films grown epitaxially by Pulsed Laser Deposition on several compatible oxide substrates with varying degrees of tensile and compressive lattice mismatch. Lattice mismatch results in the distortion of the unit cell symmetry from cubic to tetragonal. In hole-doped rare earth manganites such as La_{0.7}CaMnO₃, tensile as well as compressive lattice mismatch strain is known to cause a suppression of the insulator-metal transition, leading to an increase in electrical resistivity. In contrast, our studies of the structural and electrical properties of CMO thin films indicate that tensile strain causes a pronounced decrease in the electrical resistivity. The strained films have an expanded out of plane lattice parameter which is consistent with reduced oxygen stoichiometry. These results indicate that the tensile strain causes CMO thin films to be more susceptible to the formation of oxygen vacancies, thus reducing electrical resistivity. This is in agreement with recent theoretical predictions correlating strain and oxygen vacancies, where tensile strain induced in-plane expansion of the unit cell is shown to favor oxygen deficiency. The potential for employing lattice mismatch strain for tuning film composition has important implications for technological applications. We will present our detailed investigations of the correlation of strain and oxygen stoichiometry in CaMnO_{3-d} and related manganite compositions, employing high resolution X-ray diffraction, temperature dependent resistivity measurements, and characterization of the film surface morphology using atomic force microscopy.

9:40am **EM+MI+NS-MoM5 Controlling Complex Oxide Chemistry to Enable Advanced Dielectric, Ferroelectric, and Electronic Applications**, *Lane Martin*, University of California, Berkeley **INVITED**

Current and next-generation advanced functional materials are testing our ability to produce high-quality, complex materials with ever increasing precision. Particular interest has been given to candidate complex oxide materials which present a diverse range of material properties and functionality not easily produced in other classes of materials. The ultimate integration and utilization of these materials, however, will require that we can carefully and deterministically balance the intrinsic phenomena of interest in these materials with a knowledge of the potential extrinsic effects that can arise from defects which result from our inability to produce these complex materials with the precision we desire. This is made more challenging by the fact that these complex oxide systems are prone to and can accommodate large densities of point defects through a range of internal compensation mechanisms. In this presentation, we will explore the interrelationship between the complex oxide growth process, the chemical nature of these complex materials, the resulting structure and strain evolution, and the ultimate effect on properties in a range of prototypical complex oxide materials. We will explore these interrelationships in model systems including the classic dielectric materials SrTiO₃ and LaAlO₃, highly-controlled heterointerfaces that exhibit exotic physics including the

LaAlO₃/SrTiO₃ system, and ferroic systems such as BaTiO₃ and others. In this context, we will demonstrate routes by which we can deterministically utilize the tendency for these materials to form point defects to enhance epitaxial thin film strain, developing new modalities of strain control of thin-film materials that go beyond traditional lattice mismatch effects, and how the combination of epitaxial strain and defects in materials can be used to enhance performance, independently tune susceptibilities, and provide new insights into the nature of these complex materials. For instance, in BaTiO₃ we will illustrate how one can couple epitaxial strain to defect structures to provide an additional out-of-plane strain component that can dramatically enhance ordering temperatures and will explore the use of compositionally-graded heterostructures to further extend what can be done with epitaxial strain to manipulate dielectric, ferroelectric, and electronic properties of materials.

10:40am **EM+MI+NS-MoM8 Monolithic Integration of Epitaxial BaTiO₃ on Si and SiGe for Ferroelectric Devices**, *L. Mazet, R. Bachelet, G. Saint-Girons*, Institut des Nanotechnologies de Lyon (INL) - CNRS - ECL, France, *D. Albertini, B. Gautier*, Institut des Nanotechnologies de Lyon (INL) - CNRS - INSA de Lyon, France, *M.M. Frank, J. Jordan-Sweet, I. Lauer, V. Narayanan*, IBM T.J. Watson Research Center, *M. Hych, S. Schamm-Chardon*, CEMES - CNRS - Université de Toulouse, France, *Catherine Dubourdieu*, Institut des Nanotechnologies de Lyon (INL) - CNRS - ECL, France

INVITED

Ferroelectric oxides integrated on a semiconductor substrate are of particular interest for various applications such as memory or logic devices, electro-optic devices or as piezoelectric materials for sensors and actuators. Among the ferroelectric compounds, BaTiO₃ is an attractive candidate for large-scale applications compared to Pb- or Bi-based oxides. It is a well-known perovskite largely studied for its dielectric, piezoelectric and ferroelectric properties.

In this talk, I will briefly review the challenges associated with the monolithic integration of crystalline complex oxides on a semiconductor and more particularly with the integration of ferroelectrics. Molecular Beam Epitaxy (MBE) provides unique advantages to precisely construct, almost atom by atom, the oxide/semiconductor interface.

I will then present an experimental work on the epitaxy of BaTiO₃ thin films (1.2 - 20 nm) on silicon and Si_{1-x}Ge_x substrates. Films are grown by MBE, in the thickness range of 1.2-20 nm. Different growth conditions such as temperature and oxygen pressure are explored to optimize the BaTiO₃ film quality and to minimize the SiO₂ interfacial layer regrowth between Si and the SrTiO₃ buffer layer. The surface quality is monitored *in-situ* by reflection high-energy electron diffraction (RHEED) and *ex-situ* by X-ray reflectometry (XRR) and atomic force microscopy (AFM). The crystalline structure is studied by conventional and synchrotron X-ray diffraction. It is also investigated at the nanoscale using advanced transmission electron microscopy techniques. Strain maps determined with high precision (0.05%), 5 nm spatial resolution and with a large field of view (1 μm) using dark field electron holography will be discussed for selected samples. The crystalline domain orientations (*c*- versus *a*-domains) will be discussed with respect to the growth conditions and thickness. The ferroelectric properties are investigated by piezoresponse force microscopy (PFM). Ferroelectric films are obtained in optimized conditions that will be discussed. Ultrathin films of few monolayers are investigated to determine the onset of ferroelectricity.

I will conclude with ongoing perspectives on the integration of such heterostructures in new field-effect devices for low power logic applications.

11:20am **EM+MI+NS-MoM10 The Surface Study of Hexagonal LuFeO₃ Multiferroic Thin Films**, *Shi Cao, X.S. Xu, T. Paudel, E.Y. Tsymbal, P.A. Dowben*, University of Nebraska-Lincoln

The surface properties of hexagonal LuFeO₃ thin film have been studied by ultra-high vacuum based characterization technologies such as X-ray/ultraviolet photoemission spectroscopy (XPS/UPS), inverse photoemission spectroscopy (IPES) and XMCD-PEEM. Hexagonal LuFeO₃ is a stable multiferroic at room temperature with potential magneto-electric properties. The application of this material in voltage controlled magnetic devices depends very significantly on the interface composition and interface magnetism. The angle resolved XPS shows the possible iron-rich termination and the oxygen deficiency due to the sensitivity of the surface to the of sample preparation methods. The combined UPS and IPES allow us to infer that this multiferroic oxide, LuFeO₃, has a band gap about 2.35eV. All these characterizations are consistent with the density function theory calculations of the surface and bulk band structure.

11:40am **EM+MI+NS-MoM11 Integration of Ferroelectric Perovskites on Ge(001) by ALD: A Case Study of BaTiO₃**, *Thong Ngo, M.D. McDaniel, S.N. Chopra, J.G. Ekerdt, A.B. Posadas, A.A. Demkov*, The University of Texas at Austin

Germanium, which exhibits higher hole and electron mobilities than silicon, might become a candidate to replace silicon as a channel material in a field effect transistor (FET) beyond the 3D FET generation. Unlike Si, when the high-κ dielectrics are integrated on Ge, the chemical instability of GeO₂ is an advantage. Moreover, the instability of GeO₂ also enables epitaxial functional oxides on Ge. Crystalline perovskites can be high-κ insulating, with many also being ferromagnetic, ferroelectric, multiferroic, or superconducting. This wide range of properties, combined with possibilities for lattice match to Ge(001), allows for multi-functional oxides to be engineered on Ge(001).

Epitaxial integration of ferroelectric barium titanate, BaTiO₃ (BTO), on Ge has attracted much attention due to the low lattice mismatch between Ge(001) and BTO (0.25% above Curie temperature, T_c = 120 °C). The efforts to epitaxially integrate ferroelectric BTO on Ge(001) have been demonstrated using molecular beam epitaxy (MBE) by several groups. However, for device manufacturing applications, atomic layer deposition (ALD) has advantages over MBE due to its high step coverage, significantly low thermal budget, scalability, and low cost.

We demonstrate an all-chemical route to epitaxially integrate BTO directly on Ge(001). Amorphous BTO films were grown on the 2×1 reconstructed, clean Ge(001) surface at 225 °C using ALD. Barium bis(triisopropylcyclopentadienyl), titanium tetrakisopropoxide, and water were employed as co-reactants. The films become highly crystalline after a vacuum anneal at 600–700 °C. In-situ x-ray photoelectron spectroscopy confirms the stoichiometry of the BTO films with no detectable GeOx formation or carbon incorporation. In-situ reflection high energy electron diffraction (RHEED) shows high order of BTO film crystallinity after vacuum annealing. X-ray diffraction (XRD) is used to determine the crystallinity and the orientation of BTO films. Electrical characterization, including capacitance-voltage, leakage current, interface trap density, and piezoresponse force microscopy measurements will also be performed to explore the high-κ insulating and ferroelectric properties of BTO films on Ge(001). The integration of BTO films on Ge(001) by ALD is a promising method for fabricating a ferroelectric FET at production scale.

Magnetic Interfaces and Nanostructures

Room: 311 - Session MI+EM-MoM

Interfacial Effects in Oxide Heterostructures

Moderator: Greg Szulczewski, The University of Alabama

8:40am **MI+EM-MoM2 Linear Dichroism of La_{0.7}Sr_{0.3}MnO₃ Magnetic Dead Layers**, *Robbyn Trappen, M.B. Holcomb, J. Zhou, C.-Y. Huang*, West Virginia University, *Y.-H. Chu, V. Tra*, National Chiao Tung University, Taiwan, Republic of China

Magnetic dead layers are a phenomenon in which a normally ferromagnetic material loses its magnetization below a critical thickness, which poses a problem for thin film applications. Density functional calculations predict the behavior of the dead layer in complex oxide films to be antiferromagnetic, which is attributed to interdiffusion of the magnetic film into the neighboring layers. Here, we investigate the transition from ferromagnetic to antiferromagnetic behavior in the complex oxide La_{0.7}Sr_{0.3}MnO₃ using x ray magnetic linear and circular dichroism on the Mn L-edge (2p to 3d transition). These measurements were taken at the Advanced Light Source at Lawrence Berkeley National Labs. If the mechanism of the formation of the dead layers is understood, it can potentially be reversed and the same physics may be able to even enhance the magnetization beyond its bulk parameter.

9:00am **MI+EM-MoM3 Magnetotransport at the Superconducting LaAlO₃/SrTiO₃ Interface**, *Stefano Gariglio, D. Li, A. Fête, W. Liu, J.-M. Triscone*, University of Geneva, Switzerland

INVITED

The conducting interface between the two band insulators LaAlO₃ and SrTiO₃ has drawn a large share of attention, as it presents a variety of exciting electronic properties that are tunable by an electric field [1].

At low temperatures, magnetotransport analysis has revealed a strong Rashba spin-orbit interaction originating from the breaking of inversion symmetry [2] and, in field effect devices, the ground state has been tuned from an insulating to a superconducting state. I will discuss these results in light of recent magnetotransport experiments in field-effect devices to probe the evolution across the phase diagram of the weak localization /weak anti-

localization transport regime, its relation to the strength and anisotropy of the superconducting state.

Moreover, this interface naturally provides a versatile system to artificially build stacks of multiple 2D superconductors that would allow coupled 2D superconducting layers to be studied. I will show that we can prepare metallic and superconducting interfaces with LaAlO₃ layers grown on an artificial SrTiO₃ film [3].

[1] A. D. Caviglia *et al.*, Nature **456**, 624 (2008). [2] A. D. Caviglia *et al.*, Phys. Rev. Lett. **104**, 126803 (2010); A. Fête *et al.*, Phys. Rev. B **86**, 201105 (2012). [3] D. Li *et al.* Appl. Phys. Lett. Mat. **2**, 012102 (2014).

9:40am **MI+EM-MoM5 Symmetry Breaking in Strained Vanadium Dioxide Films, Mengkun Liu**, UC San Diego **INVITED**

We report on nanoscopic aspects of the insulator-to-metal transition (IMT) in a canonical correlated electron material, vanadium dioxide (VO₂). Using scattering-type scanning near-field optical microscopy (s-SNOM) and spectroscopy (nano-FTIR), we revealed unique phase separation in strained VO₂ films at sub-micrometer scale over a wide temperature range (320K-380K). Investigating the three dimensional formation of this microscopic stripe state, we resolved the enigma of the macroscopic electronic anisotropy and disentangled distinct stages of the VO₂ phase transition with spontaneous symmetry breaking [Phys. Rev. Lett. **111** (9), 096602 (2013), Appl. Phys. Lett. **104** (12), 121905 (2014) and follow-up studies]. With these results we demonstrated that the novel spectroscopic techniques of near-field optics provide powerful and universal methodologies for studying mesoscopic and interfacial physics for many classes of transition metal oxides and phase transition materials.

10:40am **MI+EM-MoM8 Interface Assisted Molecular Spintronics, Karthik Raman**, Indian Institute of Science, India **INVITED**

The adsorption of molecules on magnetic surfaces offers a new directionality to the study of molecular spintronics. The creation of new interface states formed by the hybridization of molecular orbitals with the spin-polarized bands of the surface leads to the development of a unique electronic and magnetic character. Such a richness of the interface spin-chemistry allows developing new handles to functionalize the properties of the adsorbed molecules, opening up a molecular-genome initiative to develop spin-functional tailor-made devices. Along with the exploration of single molecular magnets, the use of carbon based aromatic molecules, both non-magnetic and open shell magnetic systems, have presented many interesting interface phenomena. In addition to the experimental demonstrations, these studies share a strong theoretical support from computational *ab initio* interface modeling. The mechanism of inducing molecular magnetism with stability up to room temperature, inducing interface magnetic exchange coupling with strengthens of the order of thermal energy at and above room temperature, enhancement in the magnetic anisotropy of the surface and the spin-filtering property demonstrating interfacial magnetoresistance opens up a new channel to develop molecular designs for applications in sensor, memory and computing applications. This talk shall drive interest in the emergent subfield of interface assisted molecular spintronics, by presenting a strong foundation of the interface spin-physics and spin-chemistry and propose novel schemes promoting the use of advanced spectroscopy tools for the investigation of molecular spin responses. Efforts to template molecules on surfaces offer a way forward towards molecular scaling-up, providing a future outlook to the field.

References:

1. N. Atodiresi & K. V. Raman, "Interface assisted spintronics: tailoring at the molecular scale", MRS Bulletin (**July** 2014).
2. K. V. Raman, 'Focusing on the molecular scale', Nature Nanotechnology **8**, 886 (2013).
3. K. V. Raman *et al.*, 'Interface engineered templates for molecular spin memory devices', Nature **493**, 509 (2013).
4. K. V. Raman, J. Chang, J. S. Moodera, 'New method of spin injection into organic semiconductors using spin filtering tunnel barriers', *Org. Electronics* **12**, 1275 (2011).
5. K. V. Raman, S. M. Watson, J. H. Shim, J. A. Borchers, J. Chang, J. S. Moodera, "Effect of molecular ordering on spin and charge injection in rubrene", *Phy. Rev. B* **80**, 195212 (2009).

11:20am **MI+EM-MoM10 Coverage-Dependent Surface Magnetism of Iron Phthalocyanine on an O-Fe(110) Surface, Jack Rowe, D.B. Dougherty**, North Carolina State University, E. Vescovo, National Synchrotron Light Source

Iron phthalocyanine adsorbed on an oxygen covered Fe(110) surface shows a complex coverage-dependent spin polarization during growth of the first molecular monolayer. Spin polarization is modified at low submonolayer

coverages, absent at intermediate submonolayer coverages, and re-appears in modified form for a complete monolayer. This is attributed to coverage-dependent adsorption configurations from a random adsorption system to a packed monolayer with a well-defined interfacial spin polarization. In addition, we report on the observation of a rotation of the spin direction of photoelectrons in the presence of molecules, which is attributed to molecular modifications of surface magnetic anisotropy.

11:40am **MI+EM-MoM11 Time Resolved Imaging At 10Ghz And Beyond Using The Ssrl Scanning Transmission X-Ray Microscope, Hendrik Ohldag**, SLAC National Accelerator Laboratory, S. Bonetti, R. Kukreja, Stanford University, J. Frisch, H. Duerr, J. Stoehr, SLAC National Accelerator Laboratory

Understanding magnetic properties at ultrafast timescales is crucial for the development of new generations of magnetic devices. Such devices will employ the spin torque or spin Hall effect, whose manifestation at the nanoscale is not yet sufficiently understood, which is why studies addressing these effects are of great fundamental significance as well. The samples of interest are often thin film magnetic multilayers with thicknesses in the range of a atomic layers. This fact alone presents a sensitivity challenge in STXM microscopy, which is more suited toward studying thicker samples. In addition the relevant time scale is of the order of 10 ps, which is well below the typical x-ray pulse length of 50 – 100 ps. Altogether this means that pushing the time resolution of a synchrotron x-ray microscopy experiment is synonymous with improving the signal to noise ratio on the detector and providing stable, low jitter excitation to not further dilute the already small magnetic signals.

The SSRL STXM is equipped with a single photon counting electronics that effectively allows us to use a double lock-in detection at 476MHz (the x-ray pulse frequency) and 1.28MHz (the synchrotron revelation frequency). The pulsed or continuous sample excitation source is synchronized with the synchrotron source with a few picosecond drift over 24 hours. This setup currently allows us to achieve a signal to noise ratio of better than 10000, enabling us to detect miniscule variations of the x-ray absorption cross section.

In this talk I will describe the time resolved STXM setup developed at SSRL and present firsts results that have been obtained using the instrument in collaboration with an outstanding group of external users. The instrument operates in ultra high vacuum (~10⁻⁸ torr) and allows us to apply electrical pulses to our samples that can be placed in out of plane magnetic fields up to 0.8 Tesla or in plane magnetic fields up to 0.3 Tesla. We have used the instrument to successfully image spin waves excited in spin-torque and spin Hall oscillators with nano contacts of the size of ~100nm. We also succeeded in imaging different excitation modes of magnetic samples in ferromagnetic resonance at 9.6GHz excitation frequency, where the opening angle of the precession cone is of the order of 10mrad.

The facility that is dedicated to ultrafast studies of materials under electric and magnetic fields is open to general users who are interested in this field.

Advanced Surface Engineering

Room: 302 - Session SE+EM+EN+PS+TF-MoM

New Developments in Atmospheric Pressure Plasma Deposition and Thin Films for Energy Applications

Moderator: Hana Barankova, Uppsala University, Sweden, Michael Stueber, Karlsruhe Institute of Technology

8:40am **SE+EM+EN+PS+TF-MoM2 Real Time Characterization of Polymer Surface Modification by an Atmospheric Pressure Plasma Jet, Andrew Knoll, P. Luan, E.A.J. Bartis, C. Hart**, University of Maryland, College Park, Y. Raitses, Princeton Plasma Physics Laboratory, G.S. Oehrlein, University of Maryland, College Park

Atmospheric pressure plasma jets (APPJ) have been shown to modify surfaces, leading to a variety of potential industrial and medical applications. APPJ treated surfaces are typically evaluated post treatment, but few studies exist showing surface changes in real time. In this study, we characterized both closely-coupled and remote APPJ treatments of a PMMA-based 193 nm photoresist polymer (PR193) using *in situ* ellipsometry to monitor film thickness and refractive index in real time. The kilohertz-driven, two-ring electrode APPJ was fed with low admixtures of O₂ and N₂ to Ar. Voltage and current waveforms were collected to electrically characterize the APPJ and measure power dissipation. In addition, high speed photography of the APPJ was conducted in order to characterize plasma interaction with various controlled environments and with PR193. Ellipsometry shows that PR193 etch rates depend on the feed gas chemistry and treatment time. Etch rates are reduced for Ar/O₂

compared with pure Ar and Ar/N₂. This reduction is correlated to a decrease in plasma density with O₂ addition. It is also shown that the etch rate changes over time initially during APPJ heating and reaches steady state as the temperature stabilizes. When the plasma is brought close enough to the sample, the discharge couples with the surface and arcing to the film occurs. This interaction greatly increases the etch rate and introduces major damage to the polymer, which can be observed by the naked eye. From electrical data and high speed photography we see that the pure Ar discharge exhibits filamentary behavior that is enhanced by O₂ addition and rendered more diffuse by N₂ addition. High speed photography shows that the coupling of the plasma and the environment increases when the environment matches the feed gas chemistry, which causes the plume to extend farther than in open air. While the Ar plume is confined to a single plasma channel, N₂ admixture to Ar branches out into many smaller discharges, similar to a Lichtenberg figure. We also correlate damage seen on the polymer surface with observed arcing. The authors gratefully acknowledge financial support by US Department of Energy (DE-SC0001939).

9:00am **SE+EM+EN+PS+TF-MoM3 Gas-Liquid Mixed Phase Plasma at Atmospheric Pressure, Akira Ando, G. Tang, R. Ohno, A. Komuro, K. Takahashi, Tohoku University, Japan** **INVITED**

A gas-liquid mixed phase plasma discharge is investigated using nanosecond high-voltage pulse generator. Non-thermal atmospheric pressure plasmas have recently attracted significant attention due to their good energy efficiency in production of reactive species. Plasma in water can generate many reactive species, such as ozone, hydroxyl radicals and oxygen radicals. These products have strong oxidizing power and is applicable for many applications without any thermal stress.

We have utilized a nanosecond high-voltage pulse to produce a discharge within bubbles introduced into water, where semiconductor opening switching (SOS) diodes are used in the pulse generator.

The reactor for the gas-liquid hybrid plasma consists of two regions, gas and liquid regions, separated by a thin plate with a small holes (1mm in diameter). Several working gases are fed into the reactor from the gas region and bubbles are formed via the separator holes in the water. High-voltage pulse with 10-15kV are applied to a wire electrode situated in the gas phase. A grounded electrode is set into the water. When the high voltage pulse with the duration of 40ns is applied, a streamer-like discharge occurs within the bubbles and the streamer extends along the surface of gas-liquid interface.

The formation process of discharge bubbles were observed with a high-speed CCD images of the discharge. The area of discharge extension depends on the gas species and conductivity. Production rate of reactive species, ozone and hydroxyl radicals in a discharge reactor was also depends on the parameters. As the life time of hydroxyl radicals is very short, the amount is estimated from concentration of hydrogen peroxide produced in treated water, which is produced by the recombination process of hydroxyl radicals.

In order to evaluate the oxidation power in the gas-liquid mixed plasma, we applied it to water purification, such as decolorization, sterilization and decomposition of persistent organic pollutants (POPs). The sterilization effect in the water is estimated from the survival ratio of bacillus subtilis and it reaches more than 99.5% after 15min treatment. The survival ratio is large in air discharge and the value of pH in water as well as ultraviolet (UV) ray generated by plasma discharge affects the sterilization. SEM images shows the surface of the bacteria were damaged by the treatment.

9:40am **SE+EM+EN+PS+TF-MoM5 Atmospheric Pressure High Power Impulse Plasma Source (AP-HiPIPS) for Plasma Enhanced Chemical Vapor Deposition of Thin Films, Vasiliki Poenitzsch, R. Wei, M.A. Miller, K. Coulter, Southwest Research Institute**

Southwest Research Institute is currently developing a High Power Impulse Plasma Source (HiPIPS) that supplies a high flux of energetic reactants to a surface while maintaining a low processing temperature. HiPIPS is a new plasma enhanced chemical vapor deposition technology that combines variable pressure plasma jets with advanced pulsed power technology. Several complementary techniques, including mass spectroscopy, optical emission spectroscopy (OES) and electrical and thermal probes were employed, for measuring and calculating the plasma characteristics in a wide range of the HiPIPS process parameters and conditions. The preliminary HiPIPS experiments have revealed that high peak power (~40 kW) in the pulses can be achieved resulting in a high peak current (~200 A) and increased plasma density (i.e. $n = \text{Ar}: 10^{20} \text{ cm}^{-2} \text{ s}^{-1}$) while maintaining a low average power (35W) and a low substrate processing temperature (50-150 °C). A prototype atmospheric-pressure HiPIPS (AP-HiPIPS) was successfully developed and proof-of-concept AP-HiPIPS diamond-like carbon (DLC) film deposition was demonstrated. Beyond DLC films, HiPIPS plasmas could be applicable to deposition of many classes of films and many types of surface treatments. In contrast to conventional state-of-

the-art non-thermal atmospheric pressure plasma jets, typically driven by RF or AC, the power densities and currents during pulse on-time are 2-3 orders of magnitude higher in HiPIPS. Since plasma is created through inelastic electron collision with precursor gas molecules, the increased power and current directly equates to significantly improved ionization and dissociation of precursor gases in HiPIPS. Thus, distinguishing features of HiPIPS as compared to RF or AC APPJs are increased ionization, enhanced molecular gas dissociation, and higher flux of reactive species while maintaining the same low deposition temperatures. In this presentation, an overview of HiPIPS and AP-HiPIPS will be given with a specific focus on plasma characteristics and areas for further development.

10:00am **SE+EM+EN+PS+TF-MoM6 Importance of Argon's Spectral Emission for Plasma Diagnostics at an Atmospheric Open Air Plasma Discharge, Vladimir Milosavljevic, J. Lalor, P. Bourke, P.J. Cullen, Dublin Institute of Technology, Ireland**

In recent years, plasma on atmospheric pressure attracts a lot of attention due to their numerous applications in plasma biology, health care, and medicine, as well as surface and materials processing and nanotechnology. Among several atmospheric pressure plasma devices, a dielectric barrier discharge plasma jet (DBDPJ) is the most used, because of its simplicity and a fact that the generated plasma is in surrounding air and not in a confined space. The dynamics of DBDPJ in noble gases reveal that the plasma plumes propagate at a speed several orders of magnitude higher than the gas flow velocity. This is why it is generally accepted that the propagation of the plasma plumes is driven electrically rather than by the gas flow, which imposes in the first place the importance of the plasma diagnostics. Because of the frequent collisions between electrons and neutrals at high pressure, the electrical probe methods are generally less useful for plasmas produced at atmospheric pressure. Therefore, other diagnostic methods are needed and optical emission spectroscopy (OES) has been used as one of the alternative diagnostics because of its simplicity and non-intrusive nature.

Nitrogen dominates the ionic composition of atmospheric discharge and has an impact on the breakdown voltage. Nitrogen acts as a 'sensor gas' and OES diagnostics are applied in assumption that most nitrogen molecular emissions are excited during electron impact of ground state N₂(X). When nitrogen is added/mixed with argon plasma discharges, the argon emission lines are significantly quenched and the resulting plasma spectral emission is changed. Measurements and analysis of neutral argon spectral emission lines give very important information about the plasma properties. In this work the absolute spectral emissions of the atomic and molecular lines associated with argon, oxygen, nitrogen and hydrogen are presented. Wavelength resolved optical emission profiles of argon's spectral lines shows that the change in electron energy distribution functions (EEDF) has taken place for a low gas flow rate only. After the gas flow rate goes above a certain limit, the EEDF remains constant. At the same time the density of argon metastable atoms are changed with the gas flow rate. Overall, analysis of the spectral intensities assist in the development of optimised plasma processing parameters for treatments such as surface activation or removal of contaminants.

The research leading to these results has received funding from the European Union's Seventh Framework Programme managed by REA Research Executive Agency (FP7/2007-2013) under Grant Agreement number 605125

10:40am **SE+EM+EN+PS+TF-MoM8 Hot 'n Flaky: Thermal Properties of Layered Atomic Structures, Christopher Muratore, University of Dayton, V. Varshney, Air Force Research Laboratory/UTC, J.J. Hu, Air Force Research Laboratory/UDRI, A.A. Voevodin, Air Force Research Laboratory** **INVITED**

Synthesis capability for uniform growth of 2D materials over large areas at lower temperatures without sacrificing their unique properties is a critical pre-requisite for seamless integration of next-generation van der Waals heterostructures into novel devices. We have demonstrated, for the first time, vapor phase growth techniques for precisely controlled synthesis of continuous, uniform molecular layers of all MoX₂ and WX₂ transition metal dichalcogenide (TMD) compounds on diverse substrates, including graphene, hexagonal boron nitride, highly oriented pyrolytic graphite (HOPG), SiO₂, and metal substrates over several square centimeters. Preliminary results show MoX₂ and WX₂ transition metal dichalcogenide materials grown in a novel ultra-high vacuum (UHV) physical vapor deposition (PVD) process demonstrate properties identical or even superior (e.g., electron mobilities >500 cm² V⁻¹ s⁻¹) to exfoliated layers. Growth of bi-layer MoS₂ on few-layer graphene with a 30% lattice mismatch and TMD/TMD heterostructures are shown to demonstrate how natural accommodation of stresses at 2D van der Waals interfaces has the remarkable potential to transform the way materials selection is considered for synthetic heterostructures, as concerns regarding lattice constant matching can be abandoned with preference given to desired properties and

performance. Investigations relating to application of these materials in thermoelectric device applications are presented. Thermal conductivity values of TMD thin films were compared to bulk crystals, revealing expected trends with mass, but a >10 fold reduction in thin film thermal conductivity. Phonon scattering lengths at domain boundaries based on computationally derived group velocities were consistent with the observed film microstructure, accounting for the reduction. We also explore thermal anisotropy in MoS₂ films. Measurement results are correlated with MD simulations of thermal transport for perfect and defective MoS₂ crystals, demonstrating the importance of thermal boundary scattering.

Monday Afternoon, November 10, 2014

2D Materials Focus Topic

Room: 310 - Session 2D+AS+EM+NS+SS-MoA

Dopants, Defects, and Interfaces in 2D Materials

Moderator: Jun Lou, Rice University

2:00pm **2D+AS+EM+NS+SS-MoA1 Cutting and Assembling 2 Nanometer Voids in Single Layer Hexagonal Boron Nitride**, *Thomas Greber, H.Y. Cun, M. Iannuzzi, A. Hemmi, J. Osterwalder*, University of Zurich, Switzerland **INVITED**

Argon implantation beneath hexagonal boron nitride nanomesh on Rh(111) [1] leads to the formation of vacancy and interstitial defects [2]. The nanomesh is a single layer of hexagonal boron nitride on Rh(111), where 13x13 h-BN units accommodate on 12x12 Rh unit cells. The resulting super-honeycomb has a lattice constant of 3.2 nm and consists in regions where the h-BN “wets” the Rh substrate (pores), and regions where h-BN is quasi freestanding (wires) [3].

The interstitial defects are called “nanotents”, where atoms are trapped beneath the ultimately thin “rainfly” made of a single layer of h-BN [2,4]. They are stable at room temperature and survive exposure to air.

The vacancy defects are sites where a boron or a nitrogen atom was kicked out by the Ar ion impact. If the implanted structures are annealed to 900 K the can-opener effect occurs: 2 nm h-BN-flakes or “lids” are cut out of the h-BN nanomesh and 2 nm voids form [2]. At higher temperatures the resulting voids may diffuse and assemble, due to their repulsive interaction, in a super-structure with some order, i.e., a nearest neighbor distance of about 15 nm. Near the disintegration temperature of the h-BN nanomesh we finally observe self-healing of the voids in the nanomesh, which we assign to their annihilation in larger holes in the structure.

The report bases on scanning tunneling microscopy, x-ray photoelectron spectroscopy, molecular dynamics and density functional theory calculations.

Financial support by the Swiss National Science Foundation and support by the EC under the Graphene Flagship (contract no. CNECT-ICT-604391) is gratefully acknowledged. We thank the Swiss National Supercomputer Centre (CSCS) for allocation of computer time.

[1] M. Corso et al. *Science*, 303 (2004) 217.

[2] H. Y. Cun et al. *Nano Letters* 13 (2013) 2098.

[3] S. Berner et al. *Angew. Chem. Int. Ed.* 46 (2007) 5115.

[4] H.Y. Cun et al. *ACS Nano* 8 (2014) 1014.

2:40pm **2D+AS+EM+NS+SS-MoA3 Engineering Structural Defects in Graphene Materials**, *Jeremy Robinson, M. Zhaludinov, J. Culbertson, C. Junkermer, P.E. Sheehan, T. Reinecke, A. Friedman*, Naval Research Laboratory

Graphene's atomic thinness makes it highly sensitive to surface adsorbates or defects within its carbon backbone. Aside from the known effects and impact on electronic properties, here we demonstrate the impact of defects on the mechanical properties and the response of mechanical resonators. In particular, once defects are formed in atomically-thin materials they can be quite mobile and form more complicated defect structures such as bi- or tetra-vacancy clusters. We execute experiments using mechanical drum resonators made from single- to multi- to many-layer graphene systems. We use both CVD grown graphene and reduced graphene oxide (rGO) films to capture a wide range of defect structures. By measuring the fundamental frequency response of the resonators (in the MHz range) we extract properties such as tension, quality factor, and modulus as a function of external manipulation [1]. For highly defective rGO films measuring 10-40nm thick, we can tune the frequency response by 500% and quality factor by 20x through laser annealing, which effectively rearranges defects throughout the film [1]. Alternatively, using graphene 1-4 layers thick, we find the resonator response is significantly more sensitive to the formation and annihilation of meta-stable defects, such as the tetra-vacancy structure. We will show how the defect mobility and resonator response changes with different energy photons and come to understand these differences based on calculated defect migration energies of different defects types in graphene.

[1] *Nano Letters* 12, 4212 (2012)

3:00pm **2D+AS+EM+NS+SS-MoA4 Graphene Cleaning using a Low Energy Ar Ion Beam**, *KiSeok Kim, G. Yeom*, Sungkyunkwan University, Republic of Korea

Recently, graphene has been widely investigated due to the superior electrical, mechanical, thermal, and chemical properties. Especially, CVD graphene which was grown on Cu foil and transferred to various substrates using PMMA has been used most widely due to the possible large area applications such as electronic devices for displays, semiconductors, etc. However, in order to apply the transferred CVD graphene to the various electronic device fabrication, PMMA residue on the graphene surface formed during the transfer process and lithography process needs to be completely removed without damage. Various methods have been investigated to remove the residue on the graphene surface such as current cleaning, heat treatment, chemical cleaning, etc. However, it is reported that these methods are not effective in removing the residue on graphene or not applicable to industry.

In this study, a controlled Ar ion beam has been used to effectively remove the PMMA residue on graphene surface. By controlling the Ar ion beam condition, the residue on graphene surface could be removed while minimizing the damage on the graphene surface. Especially, by lowering the Ar beam energy less than 10 eV, it was possible to effectively remove the PMMA residue without damaging the graphene. The removal of PMMA residue on the graphene surface could be identified using Raman Spectroscopy showing the red shift of 2D peak (2670 cm^{-1}) and blue shift of G peak (1580 cm^{-1}) in addition to the decrease of RMS roughness from 1.3nm to 0.3 nm using an AFM (Atomic Force Microscopy). The effectiveness of graphene cleaning was also confirmed by XPS (X-ray Photoelectron Spectroscopy), by the uniform deposition of ALD HfO_2 layer on the cleaned graphene surface, by measuring the electrical properties of deposited ALD HfO_2 , etc.

3:40pm **2D+AS+EM+NS+SS-MoA6 Electronic Structure Modification in van der Waals Heterostructures: Interlayer Hybridization in the Case of Graphene/MoS₂**, *Matthias Batzill, H. Coy-Diaz*, University of South Florida, *M.C. Asensio*, Synchrotron Soleil, France, *J. Avila*, Synchrotron Soleil

Artificial van der Waals heterostructures promise to combine materials with diverse properties. Simple mechanical stacking or conventional growth of molecular hetero-layers would enable fabrication of novel materials or device-structures with atomically precise interfaces. Because covalent bonding in these layered materials is limited to molecular-planes, interface interactions between dissimilar materials are expected to modify the properties of the individual layers only weakly. Here we prepare graphene/MoS₂ heterostructures by transferring CVD-grown graphene onto a MoS₂ substrate. It is shown that high quality interfaces between graphene and MoS₂ can be obtained by UHV annealing. The quality of the graphene is demonstrated by atomic resolution scanning tunneling microscopy of ultraflat graphene. The electronic structure of the interface between the polycrystalline graphene and a MoS₂ substrate is measured by angle resolved photoemission spectroscopy (ARPES) and nano-ARPES utilizing a focused photon beam at the SOLEIL synchrotron. We show that at the Fermi-level graphene exhibits a perfect, gapless and undoped Dirac-cone. However, in regions where the π -band of graphene overlaps with states of the MoS₂ substrate, opening of several band-gaps are observed. This demonstrates that the electronic properties in van der Waals heterostructures can be significantly modified by interlayer interaction and thus exemplifying opportunities for tuning materials properties of graphene and other 2D-materials by interfacing them with dissimilar van-der Waals materials.

4:00pm **2D+AS+EM+NS+SS-MoA7 Edge States and Exposure to Hydrogen of Silicon at the 2D Limit on Ag(111)**, *A.J. Mannix, B.T. Kiraly*, Argonne National Laboratory, *M.C. Hersam*, Northwestern University, *Nathan Guisinger*, Argonne National Laboratory

Chemical functionalization of atomically thin materials results in significant modifications to their electronic properties, which can be exploited in device applications. Compared to the chemical inertness of graphene, 2D silicon is expected to exhibit greater reactivity, and thus a greater amenability to chemical functionalization. Among potential functionalization chemistries, hydrogen termination is favored for its relative simplicity and proven efficacy with graphene and bulk Si surfaces. Using ultra-high vacuum (UHV) scanning tunneling microscopy (STM), we have studied the temperature-dependent effects of exposing 2D silicon platelets grown on Ag(111) to molecular and atomic hydrogen. At low doses, atomic hydrogen results in limited adsorption and temperature dependent etching. In the bulk, the formation of vacancies and extended

etch pits is observed. In addition, edge states can play a critical role in the electronic properties of 2D materials. We have also examined at the atomic-scale the edges of 2D silicon platelets.

4:20pm 2D+AS+EM+NS+SS-MoA8 Chlorine Trap-Doping for Transparent, Conductive, Thermally Stable and Damage-Free Graphene. *Pham Viet Phuong, K.N. Kim, M.H. Jeon, K.S. Kim, G. Yeom*, Sungkyunkwan University, Republic of Korea

We propose a novel doping method of graphene by cyclic trap-doping with low energy chlorine adsorption. Low energy chlorine adsorption for graphene chlorination avoided defect (D-band) formation during doping by maintaining the π -bonding of the graphene, which affects conductivity. In addition, by trapping chlorine dopants between the graphene layers, the proposed doping method dramatically decreased the sheet resistance by ~88% at an optimized condition. Among the reported doping methods including chemical, plasma, photochemical methods etc., the proposed doping method is believed to be the most promising for producing graphene of extremely high transmittance, low sheet resistance, high thermal stability, and high flexibility for use in various flexible electronic devices. Results of angle resolved X-ray photoelectron spectroscopy (XPS), high-resolution transmission electron spectroscopy (HR-TEM), Raman spectroscopy, ultraviolet-Visible spectroscopy (UV-Vis) and sheet resistance, showed that this method is also non-destructive and controllable. The sheet resistance of the doped tri-layer graphene was $70 \Omega/\text{sq}$ at 94% transmittance, which was maintained for more than 6.5 h at 230°C. Moreover, the defect intensity of graphene was not increased during the cyclic trap-doping.

4:40pm 2D+AS+EM+NS+SS-MoA9 Modification of Graphene by Neutral Beam Irradiation and Edge Structure Analysis. *Takeru Okada, S. Samukawa*, Tohoku University, Japan

Since the discovery of single layer of Graphite, Graphene, a single layer of hexagonal carbon atoms, has attracted much attention and shown exciting specific properties. Graphene is a zero band gap semiconductor. Therefore band gap control is one of most important issue to apply for electronic device applications. In order to construct electronic devices with logic operation, both p- and n-type conduction and the control of the carrier density in an active channel are required. Doping with foreign atoms, such as N and B, has proven to be an effective way to modify the electronic properties of carbon related materials and extend their applications. In particular, nitrogen doping brings a carrier which could turn carbon nanotube into n-type semiconductors. It is also feasible to modify the electronic properties of Graphene. Although several doping methods have reported so far, process damages (defect generation) cause degradation of electronic properties.

In this paper, we introduce ultra-low damage neutral beam system which consists of a plasma and process chambers that are separated by a carbon aperture. Charged species and ultra-violet photon from the plasma can be effectively eliminated by the aperture. As a result, only the neutral beam arrives the surface of the sample at the substrate in the process chamber.

We used nitrogen gas for plasma generation and adopted multi-layer Graphene to investigate nitridation mechanism. Graphene multi-layer was irradiated by nitrogen neutral beam with controlled energy of 10 eV at room temperature. The surface modification was analyzed by x-ray photoelectron spectroscopy (XPS). XPS analysis indicated that the carbon atoms were substituted to nitrogen atom and atomic concentration of nitrogen reaches 15 %. Additionally, bonding state of C and N was found to depend on neutral beam irradiation time. Thus beam energy controlled neutral beam can selective nitridation of Graphene. Furthermore the doping density is estimated by Raman spectroscopy and result in $10^{12} [\text{cm}^{-2}]$, which is enough to n-type doping of Graphene.

5:00pm 2D+AS+EM+NS+SS-MoA10 Growth Mechanism of Metal Clusters on a Graphene/Ru(0001) Template. *Shixuan Du, L.Z. Zhang*, Chinese Academy of Sciences, *W. Hofer*, University of Liverpool, UK, *H.-J. Gao*, Chinese Academy of Sciences

Metal nano-clusters have attracted considerable interest because of the potential applications in catalysis and information storage. Due to the soft nature of epitaxial graphene and the lattice mismatch between graphene and metal substrates periodic moiré patterns can be formed. A graphene/metal template, moiré template, can be used to grow dispersed metal nano-clusters with controllable size and shape, or metal clusters with large size and metal layers. However, how intrinsic properties of metal atoms and the moiré template influence the selective adsorption and the growth mode of metal clusters is still open to debate. A general rule, predicting the morphology of metal nano-clusters on a G/metal surface, important to guide experimenters, is still missing. Using first-principles calculations combined with scanning tunneling microscopy experiments, we investigated the adsorption configurations, electronic structures and the corresponding growth mechanism of several transition metal (TM) atoms (Pt, Ru, Ir, Ti, Pd, Au,

Ag, and Cu) on a graphene/Ru(0001) moiré template (G/Ru(0001)) at low coverage. We find that Pt, Ru, Ir, and Ti selectively adsorb on the fcc region of G/Ru(0001) and form ordered dispersed metal nano-clusters. This behavior is due to the unoccupied d orbital of the TM atoms and the strong sp^3 hybridization of carbon atoms in the fcc region of G/Ru(0001). Pd, Au, Ag, and Cu form nonselective structures because of the fully occupied d orbital. This mechanism can be extended to metals on a graphene/Rh(111) template. By using Pt as an example, we provide a layer by layer growth path for Pt nano-clusters in the fcc region of the G/Ru(0001). The simulations agree well with the experimental observations. Moreover, they also provide guidance for the selection of suitable metal atoms to form ordered dispersed metal nano-clusters on similar templates.

References:

1. L.Z. Zhang *et al.* Advanced Materials Interfaces, accepted.
2. Y. Pan *et al.* Applied Physics Letter, 95, 093106 (2009)

Electronic Materials and Processing Room: 314 - Session EM-MoA

Nanoparticles for Electronic Materials

Moderator: Jessica Hilton, Mantis Deposition, Joseph G. Tischler, Naval Research Laboratory

2:00pm EM-MoA1 Synthesis of Nanoparticles Via Gas-Aggregated Sputtering. *Cathal Cassidy*, Okinawa Institute of Science and Technology, Japan **INVITED**

Synthesis of nanoparticles via gas-aggregated sputtering allows direct integration with electronic devices and their manufacturing processes. In this talk, I will discuss the fundamentals of gas-aggregated sputtering, and the diverse capabilities it offers for synthesis of novel nanoparticle materials. Analytical models will be introduced, as well as molecular dynamics modeling insights into growth and substrate landing of nanoparticles. Example results, with a focus on transmission electron microscopy studies, will be presented. Finally, the strengths and weaknesses of sputtered nanoparticles for various device applications, such as sensor layers, data storage and backend interconnects, will be discussed.

2:40pm EM-MoA3 Soft Landing of Size-Selected Nanoparticles: Novel Materials for Electrocatalysis. *Grant Johnson, R.J. Colby, M.H. Engelhard, D. Du, Y. Lin, J. Laskin*, Pacific Northwest National Laboratory

Soft landing of mass-selected ions onto surfaces is a powerful approach for the highly controlled preparation of materials that are often unobtainable using conventional synthesis techniques. A non-thermal physical synthesis method, DC magnetron sputtering combined with inert gas-aggregation, has been employed to produce anionic metal nanoparticles in the gas-phase across a range of sizes, shapes and elemental compositions for controlled deposition onto conductive electrode surfaces. Simultaneous sputtering of multiple metal targets employing up to three independent DC magnetrons in the same gas aggregation region is demonstrated to produce complex binary alloy nanoparticles with well-defined elemental composition and morphology. Size-selection of the anionic nanoparticles employing a quadrupole mass-filter prior to soft landing is shown to provide effective control over the size of nanoparticles delivered to surfaces. A suite of cutting edge analytical techniques including atomic force microscopy, scanning and transmission electron microscopy, x-ray photoelectron spectroscopy and medium energy ion scattering is utilized to demonstrate how the size, shape, elemental composition and surface density of soft landed nanoparticles may be tuned to promote the efficient electrocatalytic reduction of oxygen.

3:00pm EM-MoA4 Aerosol Spray Pyrolysis Synthesis and Characterization of CZTS Nanoparticles. *Stephen Exarhos, L. Mangolini*, University of California - Riverside

A novel synthesis technique for the production of copper zinc tin sulfide (CZTS) nanocrystals has been developed using aerosol spray pyrolysis. CZTS is a quaternary semiconducting material that shows promise as a replacement to common semiconductors such as CdTe and CIGS for use in photovoltaic devices. CIGS is currently being commercialized in the photovoltaic industry, but rare and expensive indium and gallium components threaten its long term viability. CZTS looks to be one of the best alternatives to CIGS with all earth abundant and non-toxic materials and a band gap of 1.5 eV [1]. A number of synthesis techniques have been thoroughly studied and detailed previously. In our novel approach, we synthesize single-phase 15 nm nanocrystals starting with zinc, copper, and tin diethyldithiocarbamate precursors in a toluene solvent. The precursor solution is aerosolized using a Collison type nebulizer wherein the droplets

are pushed through a tube furnace and nucleation occurs at atmospheric pressure. The powder is then collected in a series of methanol-filled bubblers. We reproducibly synthesize kesterite, $\text{Cu}_2\text{ZnSnS}_4$, nanocrystals. This technique continuously converts the chemical precursor into high-purity nano powder with a production rate of $\sim 50\text{mg}/\text{hour}$ from $\sim 100\text{mL}$ of precursor solution with $\sim 500\text{mg}$ total of the three diethyldithiocarbamate precursors for an un-optimized lab-scale reactor. The motivation to use this synthesis process as an inexpensive, quick, and simple method of nanocrystal formation will be outlined. Further, a discussion of process parameters on the stoichiometry of the nanoparticles will be presented as well as results from extensive material characterization via Raman spectroscopy, EDS, XRD, and TEM. We are currently in the process of producing a printable ink technique with which to coat CZTS as the absorbing layer for use in photovoltaic devices.

[1] H. Wang. "Progress in Thin Film Solar Cells Based on $\text{Cu}_2\text{ZnSnS}_4$," International Journal of Photoenergy, 2011.

3:40pm **EM-MoA6 Peter Mark Memorial Award Lecture - Novel Semiconductor and Epitaxial Nanocomposite Materials for Electronic and Photonic Applications, Joshua Zide***, University of Delaware
INVITED

Advances in electronic materials (specifically, semiconductors and nanocomposites) enable new device technologies and improve the properties of existing technologies. In this talk, I will present efforts within my group on the growth of new materials by molecular beam epitaxy and the resulting advances in solar cells, thermoelectrics, and optoelectronics.

Specifically, I will discuss two material systems: (1) nanocomposites consisting of metallic nanoparticles (such as ErAs and TbAs) within III-V semiconductors (such as InGaAs and GaAs), and (2) dilute bismuthide semiconductors in which bismuth is incorporated into III-V materials to reduce the bandgap significantly, with unique band alignments that cannot be easily achieved in other materials. In the former, the nanoparticles serve as buried Schottky junctions, pinning the Fermi level and significantly altering carrier dynamics. In the latter, we focus on In(Ga/Al)BiAs, where compositional variations permits independent tuning of valence and conduction bands.

Although these materials are built upon relatively-mature III-V systems, electronic, thermal, and optical properties can be quite different from those of conventional materials, with significant promise for applications in a variety of technologies. Understanding the properties of these materials enables the creation of designer semiconductors for particular applications of interest.

4:20pm **EM-MoA8 Assembly of Functional Nanocrystal Films at Fluid Interfaces, Kevin Whitham, T. Hanrath**, Cornell University

Opportunities to create materials with properties by design continue to emerge from our ability to control the structure and composition of nanomaterials through wet-chemistry synthesis methodologies. Access to these materials has provided critical insights into basic structure-property relationships. Concurrent advances in prototype nanomaterial-based devices underscored their immense technological potential in a broad range of energy applications including photovoltaics, catalysis, energy storage, and thermoelectrics. Along with rising expectations, there is growing recognition that sustained progress towards the acclaimed promise of nanomaterial-enabled energy technologies depends critically on solving outstanding processing challenges - in particular the directed assembly of nanoparticles (NPs) into functional superstructures. We embrace this challenge as an opportunity to establish the scientific and engineering foundation for the processing of ordered and multifunctional NP thin films via advanced liquid coating methods.

Our group recently demonstrated a significant advance to resolve this challenge by creating NP assemblies that combine high spatial coherence and strong interparticle electronic coupling. In brief, we discovered that spreading a NP suspension across the surface of a non-polar antisolvent subphase results in the formation of two-dimensional (2D) superlattice of epitaxially connected NPs. Our approach to 'connect the dots' was inspired by analogies to polymerize or crosslink NPs as monomers into highly connected superstructures. The ability to form 'confined-but-connected' 2D NP assemblies with predefined symmetries introduces exciting opportunities to create materials with properties by design. By analogy to atomic 2D systems (e.g. graphene), we see 2D NP assemblies as a fertile ground for scientific discovery with a clear path towards practical applications.

* Peter Mark Memorial Award Winner

4:40pm **EM-MoA9 Characterization of Cu_{2-x}S Nanoparticles in Organic Matrices, Michael Majeski, I. Bolotin, L. Hanley**, University of Illinois at Chicago

Transition-metal chalcogenide nanomaterials show promise for applications in photovoltaics and plasmonic devices. Of these class of materials, Cu_2S encompasses the environmentally friendly and earth abundant qualities not afforded to many other heavy metal semiconductors. Copper sulfide nanoparticles are prepared by physical vapor deposition without the surface ligand capping effects known to inhibit and otherwise complicate charge transfer. Another obstacle to the use of copper sulfide for photovoltaics is the self-doping that occurs upon oxidation, which is compensated for here by all-gaseous preparation of Cu_{2-x}S nanoparticles into organic matrices. These films are characterized by X-ray photoelectron spectroscopy, transmission electron microscopy, high-angle annular dark-field scanning transmission electron microscopy, X-ray absorption experiments, and other methods. $2.3 \pm 0.4 \text{ nm}$ Cu_{2-x}S nanoparticles with copper in the +1 oxidation state were deposited into pentacene films and additional structural information will be presented.

5:00pm **EM-MoA10 Optical Properties of PbSe Nanorods with Controlled Diameter and Length, Diogenes Placencia, J.E. Boercker, E.E. Foos, J.G. Tischler**, Naval Research Laboratory

PbSe nanorods are attractive for use in next-generation optoelectronic devices due to their exceptional physical properties such as larger Stokes shifts and more efficient multiple exciton generation (MEG), relative to spherical nanocrystals.¹⁻³ However, further development of PbSe nanorods for viable technological components requires precise control of the nanorod diameter and length as well as an understanding of how the nanorod dimensions affect their optoelectronic properties. We have investigated the nature of the PbSe nanorod synthesis, yielding an understanding of how to independently control the nanorod diameter and length. Additionally we have developed an elementary comprehension of how the nanorod dimensions affect their optical properties.

Recently, single-crystal, homogeneous, PbSe nanorods were synthesized using a solution synthesis.⁴ In our work, we show that water present in this synthesis has a dramatic effect on the nanorod aspect ratio and yield. By varying the water concentration from 0 to 204 mM, the nanorod aspect ratio and yield can be controlled from 1.1 to 10 and 1 to 14%, respectively. Water indirectly affects the nanorod morphology and yield by reacting with the tris(diethylamino)phosphine used in the reaction to form bis(diethylamido)phosphorus acid. The latter is responsible for both the nanorod aspect ratio and yield variations. Furthermore, the excess oleic acid in the reaction can also create bis(diethylamido)phosphorus acid from tris(diethylamino)phosphine. When both excess oleic acid and water are removed, the reaction slows and highly uniform, non-branching, nanorods are formed.⁵

Exploration of various synthetic parameters (e.g., temperature, reaction time) within the nanorod reaction free of water and excess oleic acid resulted in our ability to independently control the nanorod diameter and length. Aspect ratios ranging from 1 to 14 have been synthesized, showing no branching, varying levels of quantum yields, and a wide absorption energy range ($\sim 1200 \text{ nm} - 2000 \text{ nm}$).

References

- [1] Tischler J G, Kennedy T A, Glaser E R, Efros A L, Foos E E, Boercker J E, Zega T J, Stroud R M and Erwin S C 2010 *Phys. Rev. B* **82** 245303
- [2] Cunningham P D, Boercker J E, Foos E E, Lumb M P, Smith A R, Tischler J G and Melinger J S 2011 *Nano Lett.* **11** 3476
- [3] Sandberg R L, Padilha L A, Qazilbash M M, Bae W K, Schaller R D, Pietryga J M, Stevens M J, Baek B, Nam S W and Klimov V I 2012 *ACS Nano* **6** 9532
- [4] Koh W-K, Bartnik A C, Wise F W and Murray C B 2010 *JACS* **132** 3909
- [5] Boercker J E, Foos E E, Placencia D and Tischler J G 2013 *JACS* **135** 15071

5:20pm **EM-MoA11 Plasmonic Behavior of Copper Iron Sulfide Nanoparticles, Katherine Plass, N.J. Freymeyer, C. Kim, C.J. Wisdo**, Franklin & Marshall College

Copper vacancies in copper chalcogenide result in sufficiently high levels of p-type doping to generate plasmon resonances. The natural tendency towards increased copper vacancies with time and air exposure is exacerbated in nanoparticles.¹ We present here investigations into the stabilization of plasmonic copper sulfide-based semiconductors. Incorporation of iron slows the transition to copper deficiency² Here we will discuss the affect of iron incorporation into copper sulfide nanoparticles on the plasmonic behavior. Various phases were produced, ranging from different polymorphs of Cu_2S to CuFeS_2 , including solid solutions. The

solid-state structure, band gaps and edges, and plasmon band absorption of these copper iron sulfide nanoparticles were responsive to the extent of iron incorporation, as investigated by powder X-ray diffraction, cyclic voltammetry, and visible/near-IR light absorption spectroscopy. The surface chemistry influences the plasmonic behavior of these copper iron sulfide nanoparticles and will be examined.³

(1) Lotfipour, M.; Machani, T.; Rossi, D. P.; Plass, K. E. *Chem. Mater.* **2011**, *23*, 3032–3038.

(2) Machani, T.; Rossi, D. P.; Golden, B. J.; Jones, E. C.; Lotfipour, M.; Plass, K. E. *Chem. Mater.* **2011**, *23*, 5491–5495.

(3) Freymeyer, N. J.; Cunningham, P. D.; Jones, E. C.; Golden, B. J.; Wiltrout, A. M.; Plass, K. E. *Cryst. Growth Des.* **2013**, *13*, 4059–4065.

Energy Frontiers Focus Topic

Room: 315 - Session EN+EM+MN+NS+TR-MoA

Energy Harvesting with Nanostructures

Moderator: Phillip Christopher, University of California - Riverside

2:00pm EN+EM+MN+NS+TR-MoA1 **Optical Engineering for Colloidal Quantum Dot Photovoltaics**, *Susanna Thon*, Johns Hopkins University **INVITED**

The next generation of photovoltaics seeks to improve both efficiency and cost through the use of flexible platforms and new materials. Colloidal quantum dots (CQDs), semiconductor nanoparticles synthesized from solution, are a particularly attractive material for solar energy. The bandgap of films composed of arrays of CQDs can be tuned via the quantum confinement effect for tailored spectral utilization. The performance of CQD solar cells is currently limited by an absorption-extraction compromise, whereby photon absorption lengths in the near infrared regime exceed minority carrier diffusion lengths. I will review several photonic and optical engineering schemes aimed at overcoming this compromise. These include nanophotonic and geometric light trapping techniques, as well as jointly-tuned plasmonic-excitonic photovoltaics. Additionally, I will discuss how nanoscale engineering of CQDs and related materials can lead to emergent optical properties for building color-tuned optoelectronic films.

2:40pm EN+EM+MN+NS+TR-MoA3 **Energy Transfer from Nanocrystal Quantum Dots to Si Nanomembranes Monitored via Wavelength Dependent Photocurrent Response**, *Weina Peng, S. Sampat, S. Rupich, B. Anand, H. Nguyen, D. Taylor, Y. Gartstein, Y.J. Chabal, A. Malko*, University of Texas at Dallas

We report the observation of wavelength dependent photocurrent in thin silicon nanomembranes (75 nm) coupled to colloidal CdSe/ZnS nanocrystal quantum dots (NQDs). The measurement was performed on back-gated, FET-type thin Si structures, which are functionalized with self-assembled monolayer (SAM) of ester termination groups to prevent surface oxidation and the formation of surface defect states. A thin film of nanocrystals is drop casted on the surface and an increase of photocurrent, up to several hundred nA, are recorded as a function of excitation wavelength on NQD/SAM/Si devices vs. plain SAM/Si structures. Quantitative analysis of photocurrent vs. NQD absorption spectrum allows us to ascribe the observed photocurrents to the photoexcited NQD excitons transferred to the underlying Si substrate via non-radiative and radiative energy-transfer mechanisms¹.

¹H. M. Nguyen, O. Seitz, W. N. Peng, Y. N. Gartstein, Y. J. Chabal, and A. V. Malko, *ACS Nano* **6**, 5574 (2012).

3:40pm EN+EM+MN+NS+TR-MoA6 **Triboelectric Nanogenerator - A New Energy Technology**, *ZhongLin Wang*, Georgia Institute of Technology **INVITED**

Triboelectrification is an effect that is known to each and every one probably ever since the ancient Greek time, but it is usually taken as a negative effect and is avoided in many technologies. We have recently invented a triboelectric nanogenerator (TENG) that is used to convert mechanical energy into electricity by a conjunction of triboelectrification and electrostatic induction. As for this power generation unit, in the inner circuit, a potential is created by the triboelectric effect due to the charge transfer between two thin organic/inorganic films that exhibit opposite tribo-polarity; in the outer circuit, electrons are driven to flow between two electrodes attached on the back sides of the films in order to balance the potential. Ever since the first report of the TENG in January 2012, the output power density of TENG has been improved for five orders of magnitude within 12 months. The area power density reaches 500 W/m²,

and a conversion efficiency of ~50% has been demonstrated. The TENG can be applied to harvest all kind mechanical energy that is available but wasted in our daily life, such as human motion, walking, vibration, mechanical triggering, rotating tire, wind, flowing water and more. Alternatively, TENG can also be used as a self-powered sensor for actively detecting the static and dynamic processes arising from mechanical agitation using the voltage and current output signals of the TENG, respectively, with potential applications for touch pad and smart skin technologies. The TENG is possible not only for self-powered portable electronics, but also as a new energy technology with a potential of contributing to the world energy in the near future.

[1] Z.L. Wang “Triboelectric Nanogenerators as New Energy Technology for Self-Powered Systems and as Active Mechanical and Chemical Sensors”, *ACS Nano* **7** (2013) 9533-9557.

[2] G. Zhu, J. Chen, T. Zhang, Q. Jing, Z. L. Wang* “Radial-arrayed rotary electrification for high-performance triboelectric generator”, *Nature Communication*, **5** (2014) 3456.

4:20pm EN+EM+MN+NS+TR-MoA8 **Conflicting Roles of Charge Traps in ETA Solar Cells: The CREM Point of View**, *Hagai Cohen*, Weizmann Institute of Science, Israel

The characterization of multi-interfacial devices commonly encounters critical difficulties due to the limited access of standard electrical probes to selected inner domains. In this respect, the XPS (x-ray photoelectron spectroscopy) based CREM (chemically resolved electrical measurements) [1] is a technique proposing particularly useful capabilities. Demonstration of internal junction fields evaluation has already been provided, as well as the direct measurement of layer-specific photovoltages in ETA (extremely thin absorber) solar cells.[2] However, the complex dynamics realized during charge separation in such cells has not yet been investigated thoroughly by CREM.

The present work focuses on this issue, showing conflicting roles of charge trap states and, specifically, their different expression under controllably varied conditions. Comparison with complementary characterization techniques is further discussed, demonstrating the unique insight provided by CREM for their interpretation.

References

1. H. Cohen, *Appl. Phys. Lett.* **85**, 1271 (2004).

2. Y. Itzhaik, G. Hodes, H. Cohen, *J. Phys. Chem. Lett.* **2**, 2872 (2011).

4:40pm EN+EM+MN+NS+TR-MoA9 **Understanding Morphological and Structural Effect on Organic Photovoltaic Devices from Plasmonic Particles using Advanced Characterization Techniques**, *Nuradhika Herath, V. Lauter, J. Browning*, Oak Ridge National Laboratory

Organic electronics have been under intense scientific interest in recent years because of their attractive properties such as low cost fabrication processes, ability to performance under low light, and flexibility. Major achievements are based on use of new conjugated polymer and small molecules in bulk heterojunction (BHJ) devices to increase the inner donor acceptor interfaces of fully functional devices such as organic photovoltaics (OPVs) and organic light emitting devices (OLEDs). Many strategies have been introduced to enhance the power conversion efficiency (PCE) of organic electronics. Among them, one of the most promising solutions to enhance the absorption and device efficiencies of OPVs is incorporation of various metal nanoparticles (NPs). Metallic NPs enhanced the efficiency of the devices through local surface plasmonic responses (LSPR). This phenomenon reduced the recombination level of geminate excitons and increases the exciton dissociations, which enhanced the photocurrent and fill factors of devices. However, metallic NPs blended within the active layer can act as polaron traps detracting the device performances. In this study, we investigate layer and interfacial structure of small molecule (SM), *p*-DTS(FBTTh₂) and fullerene, PC₇₀BM system incorporated with silver (Ag) NPs, using neutron reflectometry (NR), X-ray reflectometry and Atomic Force Microscopy (AFM). We present detailed composition changes with Ag NPs concentrations along the film depth to understand morphological and dynamical effects of BHJ devices incorporated with plasmonic particles. To complement and enhance the findings from NR, we report optical properties of the samples using UV-Visible absorption and Photoluminescence spectroscopy. Our findings provide unique information and clear insights into dynamics of plasmonic organic solar cells and their future applications for further enhancement of PCE.

This research was conducted at Spallation Neutron Source and at the Center for Nanophase Materials Sciences, which is sponsored at ORNL by the Scientific User Facilities Division, Office of Basic Energy Sciences, U.S. Department of Energy.

5:00pm **EN+EM+MN+NS+TR-MoA10 Doped TiO₂ Based Core-Shell Structures for High Efficiency Hybrid Solar Cells**, *Jonas Weickert, J. Dorman, M. Noebels, M. Putnik, T. Pfadler*, University of Konstanz, Germany, *A. Wisnet, C. Scheu*, LMU Munich, Germany, *L. Schmidt-Mende*, University of Konstanz, Germany

Hybrid solar cells, with an inorganic/organic interface for charge separation, have been extensively investigated in the past decade in order to replace the expensive Si based technology with an inexpensive alternative. Typically, these devices incorporate a mesoporous TiO₂ film which is decorated with dye molecules and filled with a hole transport polymer, for example P3HT, to conduct the electrons and holes, respectively. Recently, we have shown that the efficiency of nanowire based hybrid solar cells can be increased from ~1.8 % to 2.5 % through the formation of a Sn-doped TiO₂|TiO₂ core-shell device created via a hydrothermal growth and subsequent TiCl₄ treatment. However, this surface treatment presents difficulties in creating a crystalline conformal coating, limiting the control over the extent of coating and the crystallinity, directly affecting the charge injection from the polymer into the TiO₂ array. In this work, we directly deposit a controllable TiO₂ film through atomic layer deposition to conformally coat the nanowire arrays with various thicknesses. By changing the thickness and TiO₂ crystallinity, we are able to engineer the energy levels at the TiO₂-dye-P3HT interface due to the magnitude and position of the Fermi levels of the core and shell material, influencing the rate of charge injection and recombination. Furthermore, the crystallinity of the shell layer directly affects the amount of dye that can be absorbed on the surface of the nanostructures with a reduction in light absorption by roughly 30% from anatase to rutile TiO₂. Finally, a detailed mechanism will be proposed for the device performances based on the energy level alignment between the pinned Fermi-level TiO₂ structure and the HOMO of the P3HT resulting in a shifting open circuit voltage based on the crystal phases. Additionally, the core-shell structures are characterized with photovoltage decay and impedance spectroscopy measurements to study the charge transport and recombination across these various interfaces.

5:20pm **EN+EM+MN+NS+TR-MoA11 Stack Numbers Dependence of the Activation Energies for Carrier Escape from and Recombination in Strain-Balanced InGaAs/GaAsP MQW**, *Atsuhiko Fukuyama, T. Ikari, K. Nishioka, T. Aihara, H. Suzuki*, University of Miyazaki, Japan, *H. Fujii, M. Sugiyama, Y. Nakano*, The University of Tokyo, Japan

Fabrication of multiple quantum well (MQWs) in an absorption layer can extend the absorption region toward a longer wavelength and enhance the short-circuit current in the solar cells. However, MQWs function as recombination centers, leading to degradation in both open-circuit voltage and fill factor. We have already reported that the increase in stack number of QW causes the degradation of carrier collection efficiency [1]. In this study, we investigate the effects of stacks number on temperature dependences of the photoluminescence (PL), photothermal (PPT) and the surface photovoltage (SPV) signals. Although the photoexcited carriers in the barrier should relax by the radiative recombination (PL), carriers can thermally escape (SPV) or non-radiatively recombine (PPT) at the same time. Therefore, the latter two methodologies give us new insights for the carrier recombination and drift through the QW.

The present strain-balanced InGaAs/GaAsP MQWs absorption layer was composed of a 7.0-nm-thick In_{0.25}Ga_{0.75}As well and a 10.8-nm-thick GaAs_{0.66}P_{0.34} barrier. All layers were grown on an *n*-type GaAs substrate using metal-organic vapor phase epitaxy. We prepared different samples with MQW stack numbers of 10, 20, 30, and 40 in the *i*-region.

All PPT and SPV spectra showed three distinctive peaks followed by a step like function. They were decomposed into inter-subband transitions expressed by the two dimensional density of states for the QW and exciton peaks [2]. Although the PL intensity decreases with increasing the temperature, signals for PPT and SPV increases. We suppose two activation energies for the process: one is that for the carrier escape from the QW and another is for the non-radiative recombination in the QW. The three rate equations were built for PL, PPT and SPV and the temperature dependences are numerically fitted to estimate the two activation energies. As a result, we have estimated the activation energy for carrier escaping from the QW is constant as 70 meV for all samples with different stacks number. This is the same as the calculated barrier height. However, the activation energy for the non-radiative recombination increases from 6 to 49 meV for the sample with 10 and 40 stacks. This means that radiative recombination increases with increasing the stack number. The carriers thermally escape from the QW again relax into next well and may contribute to increase the radiative recombination.

[1] H. Fujii et al., *Jpn. J. Appl. Phys.* **51**, 10ND04 (2012).

[2] M. Kondow, A. Fukuyama, and T. Ikari et al., *Appl. Phys. Express* **2**, 041003 (2009).

Tuesday Morning, November 11, 2014

Electronic Materials and Processing

Room: 314 - Session EM-TuM

Advanced Interconnects and Materials

Moderator: Sean King, Intel Corporation, Andrew Antonelli, Lam Research

8:00am EM-TuM1 Cu/ULK ULSI On-Chip Wiring Technologies, and Related Devices, *Daniel Edelstein*, IBM INVITED

We are familiar with microelectronics "scaling" (reducing dimensions) of integrated circuits, so they get denser and cheaper (Moore's Law), and faster (Dennard's Law), in turn increasing the computational power of IC chips. Perhaps less appreciated is that scaling has always gone against the performance and reliability of the multilevel on-chip wiring, commonly termed "Back End of the (Manufacturing) Line", or BEOL, needed to connect these circuits. This invited talk focuses on forefront efforts in materials and nano-scale engineering to combat BEOL scaling and extendibility problems.

Our work has begun on the 7 nm CMOS node, with our 11th generation Cu BEOL. The smallest wires are ~17 nm wide, ($< 1/10^{\text{th}}$ the lithographic wavelength!), and represent ~1/25x scaling from the 1st Cu generation. As we migrate to these dimensions, significant innovations in patterning and metallization have been required to preserve defect-free fabrication and electromigration reliability. In order to reduce parasitic wiring capacitance, with its signal delay and power loading, our insulator dielectric constants have migrated from 4.1 to 2.4. But in turn, these materials get more fragile, both electrically and mechanically, requiring significant learning in interface and material mechanics, plus dielectric reliability physics.

Concurrently, system-level performance and cost scaling push more diverse functions onto the chip, and into the wiring levels. Recent innovations add new devices to the finer wiring levels, as well as "reverse-scaled" (larger) wiring levels allow us to collapse more diverse packaging functions onto the chip. Examples of what we fabricate will be presented, with some of their integration-specific issues and solutions. These include ultrathick Cu for data bandwidths, high-Q and magnetic inductors for RF and voltage converters, MEMs switches for antenna diversity, through-Si vias for 3D integration, and magnetic and phase-change non-volatile memory devices (MRAM and PCM).

8:40am EM-TuM3 Selectivity Characterization and Enhancement of Metal-Organic Chemical Vapor Deposited (MOCVD) Selective Cobalt Cap for Advanced Back End of Line, *Jeff Shu, Z. Sun, Y.B. Lee, J. Palazzo, Z. Bayindir, M. Hossain, S. Choi, J. Rullan, H. Liu*, GLOBALFOUNDRIES U.S. Inc.

The continuous shrink of Cu interconnect feature size leads to higher current densities, which lower electromigration lifetimes. The interface between post chemical mechanical polishing (CMP) Cu and dielectric cap has been identified as a key diffusion path for copper atoms, and the adhesion of the interface is critical to electromigration performance [1]. Alternate metallization schemes for copper interconnect using selective CVD Co capping are considered for 22nm technology and below from integration point of view, metal-organic deposition selectivity is the key for leakage and reliability. During the selective CVD Co deposition, both Cu and porous ultra low k dielectric surface are exposed to the metal-organic precursor, insufficient selectivity will increase metal line to line leakage, degrade metal shorts and time-dependent dielectric breakdown (TDDB) performance. In this paper, we focus on selectivity characterization and enhancement of MOCVD selective Co cap process. Selectivity of different precursors are thoroughly evaluated and compared. Lower reaction rate of the carbon based organic group of the Co precursor and the reducing agent was demonstrated to benefit selectivity. Different ultra low k films with various porosity also play a big role in selectivity. Key tuning knobs for the process window have been defined as process pressure and temperature. The quantity of final Co deposition on porous ultra low k surface has been measured by both X-ray fluorescence (XRF) and Total Reflection X-ray Fluorescence (TXRF), which will subsequently be applied to the definition of selectivity, with comparison to the amount on polished Cu surface. XRF measurement shows some disadvantage due to weak signal to noise ratio while TXRF measurement results are more reliable. X-ray photoelectron spectroscopy (XPS) is used to profile the oxygen penetration into pristine film and the self-limited cobalt oxide thickness has been measured at 15A to 25A, which can be modulated by vacuum break between Co cap and dielectric cap, and by surface pre-clean process before dielectric cap deposition.

[1] J. R. Lloyd, M.W. Lane, E. G. Liniger, "Relationship between interfacial adhesion and electromigration in Cu metallization" 2002 IEEE International Integrated Reliability Workshop Final Report, p.32 - 35 (2002)

9:00am EM-TuM4 Precise Control of the Residual Stress Levels in Polycrystalline Thin Films for Advanced Interconnects and N/MEMS Applications, *Hang Yu, C.V. Thompson*, Massachusetts Institute of Technology

Precise control of residual stress in polycrystalline thin films, which remains a central but difficult task in advanced interconnects and N/MEMS applications, requires synergistic manipulation of multiple processing parameters. Our recent work has demonstrated that stress evolution during film growth is controlled by a series of kinetic processes that include adatom-edge interactions on the surfaces of individual grains, adatom interactions with grain boundaries, and grain growth during film thickening. By synergistically controlling the growth conditions and therefore controlling these kinetic processes, residual stress levels in polycrystalline films can be tailored for optimal performance for specific given applications. In particular, we find that the composition and partial pressure of residual gases in the deposition chamber have a profound effect on the stress evolution behavior. As a consequence, understanding and control of these effects allow tuning of the residual stress of a film. As an example, we demonstrate the use of low levels of oxygen impurities to produce zero stress Ni films.

9:20am EM-TuM5 CVD Mn-based Barrier for Advanced Copper Interconnect Technology: Integration Study, *Nicolas Jourdan*, IMEC, Belgium

To prevent copper diffusion in a circuit, commonly a PVD-TaN/Ta liner is formed on the dielectric surface as a diffusion barrier prior to Cu metallization. The integrity of the PVD-TaN/Ta barrier is expected to reach its limit at a trench dimension below 20nm width. As a result, alternatives must be found for further technology scaling. In recent years, Mn-based barriers have received great consideration as a thin self-formed MnSixOy diffusion barrier can be formed at the surface of the insulator without significant impact on the dielectric constant whilst preserving the total trench volume for Cu filling. Initially, such a "zero-thickness barrier" has been made using a PVD-CuMn seed layer, from which Mn atoms diffuse after a thermal anneal towards the surface of the insulator to form the diffusion barrier. However, because of the use of PVD, limited scalability of this option is expected. Therefore, CVD of Mn-based chemistries has been developed to enable the formation of a thin and conformal barrier [1, 2]. Such a layer has already been integrated in 2ML test vehicles (half pitch ranging from 40nm to 100nm) using a conventional scheme consisting of a PVD-Cu seed followed by Cu electroplating (ECD) and CMP. The authors reported significant RC reduction and comparable Time Dependent Dielectric Breakdown (TDDB) performance with respect to conventional PVD-TaN/Ta barrier [3]. However, integration of a thin Mn-based barrier faces a big challenge due to Mn dissolution taking place in the chemistries used in ECD and CMP operations. The impact of such a phenomenon is even more dramatic in narrow trenches used for advanced technology nodes due to the scaled PVD-Cu seed, which is no longer able to sufficiently protect Mn from dissolution.

In this work, we focus on the optimization of CVD Mn-based barrier in order to make it integration friendly. Furthermore, we will report on physical properties of such a barrier.

[1] N. Jourdan et al.: Electrochemical and Solid-State Letters 15 (5) (2012) H176-H178.

[2] Roy G. Gordon et al.: Proc. Advanced Metallization Conference, p. 1 (2008).

[3] Y. K. Siew et al., Proc. IEEE IITC 2013, p. 1.

9:40am EM-TuM6 Cryogenic Etching vs P4 Approaches: Paths towards Ultra-low Damage Integration of Mesoporous Oxide Dielectric Materials, *Jean-Francois de Marneffe*, IMEC, Belgium, *L. Zhang, M.H. Heyne, M. Krishnab*, IMEC, KU Leuven, Belgium, *A. Goodyear, M. Cooke*, Oxford Instruments Plasma Technologies, *N. Heylen, I. Ciofi, L.G. Wen, C.J. Wilson*, IMEC, Belgium, *V. Rutigliani*, University Bari, Italy, *S. Decoster*, IMEC, Belgium, *T. Savage*, SBA Materials, Inc., *K. Matsunaga, K. Nafus*, Tokyo Electron Kyushu Limited, Japan, *J. Boemmels, Z. Tokci, M. Baklanov*, IMEC, Belgium

In recent year, two innovative strategies have been proposed to decrease plasma-induced low-k damage: the P4 approach [Frot et al., 2011] and the cryogenic etch approach [Zhang et al., 2013]. The P4 or "pore stuffing" uses an extrinsic sacrificial pore filler, allowing protection during plasma

etching and metallization steps. The cryogenic etch is based on in-situ pore filling by etch byproducts and/or SiO_x sidewall passivation.

In this work, a PMO spin-on material with pristine $k = 2.31$ from SBA has been integrated on 300mm wafers. The integration vehicle uses narrow-spacing structures, i.e. 30nm low-k lines at 180nm pitch.

For the cryogenic etch approach, after lithography, the SiC/SOC/SOG hardmask is trimmed and opened using standard etch. Low-k etching is performed by means of a SF₆-based plasma chemistry in an ICP chamber equipped with a liquid-N₂ cooled substrate holder set at a base temperature of -120°C. Careful optimization of etch conditions allows to considerably decrease the loss of Si-CH₃ bonds, keeping an acceptable etch rate, good hardmask selectivity, and reduced bottom roughness. After patterning and subsequent byproduct removal by annealing, a conventional Cu metallization is performed using TaNTa barrier, Cu seed and electroplating. After chemical-mechanical polishing (CMP) and SiC passivation, functional circuits gave integrated dielectric constant of $k_{int} = 2.38$, i.e. showing a $\Delta k = 0.07$ relative to pristine.

For the pore stuffing approach, PMMA was used as filling material and driven in after low-k deposition. Due to thermal instability of PMMA, a low-temperature Si₃N₄ hardmask was used, as well as low-temperature TaNTa barrier. PMMA was removed after CMP, by means of He-H₂ downstream plasma ashing or thermal decomposition. Functional circuits gave integrated dielectric constants $k_{int} = 2.73$ (thermal unstuffing) and $k_{int} = 3.14$ (He-H₂ ashing).

By comparison of both approaches, it is observed that pore stuffing increases interconnect flow complexity, by the addition of stuffing and unstuffing steps which can also damage the low-k material; however post-etch surfaces are smooth and barrier metal penetration is suppressed. The pore stuffing approach could be improved by using more thermally stable polymers and the search for damage-free unstuffing methods. The current cryogenic etch process requires only minor changes into the process flow, however currently it requires a base temperature of -120°C. The cryogenic etch process could be improved by the use of plasma additives enhancing by-products condensation and/or pre-condensation steps. We acknowledge support from the European Union under grant agreement No. 318804 (SNM).

11:00am **EM-TuM10 Reliability of Advanced Interconnects**, *Carl V. Thompson*, Massachusetts Institute of Technology **INVITED**

As interconnect dimensions have continued to shrink with each new CMOS generation, increased electrical resistivity has had a growing impact on overall circuit performance. This has driven the search for radical changes in interconnect technologies based, for example, on nanomaterials such as carbon nanotubes and graphene. However, with kilometers of interconnect per integrated circuit subject to stringent yield and reliability requirements, viable alternatives to metal-based interconnects have not yet been found. Therefore, for the foreseeable future, further improvements in IC performance and functionality will require evolutionary advances in interconnect materials systems. Recent work on performance enhancement has focused on reduced surface and grain boundary scattering in Cu, and the use of dielectric environments with low dielectric constants. These developments are constrained by the need to maintain high reliability, and sometimes come at the expense of reliability. Also, performance improvements can sometimes be enabled by reliability improvements and changes in design constraints imposed by reliability concerns. Design and layout strategies that lead to improved interconnect reliability and allow relaxation of constraints imposed by reliability concerns will be reviewed. The impact on evolving technologies on electromigration-limited reliability will also be discussed, as will needed changes in reliability assessment methodologies.

11:40am **EM-TuM12 Metal Resistivity Below 10 nm**, *Daniel Gall, P. Zheng, D. Guan*, Rensselaer Polytechnic Institute, *J.S. Chawla*, Intel Corporation, *T. Zhou*, Rensselaer Polytechnic Institute

Electron scattering at surfaces and grain boundaries causes the resistivity of metals to increase with decreasing wire width or film thickness. This effect is quantified using (i) *in situ* transport measurements on single-crystal, atomically smooth Cu(001) layers, (ii) textured Cu(111) layers and patterned Cu wires with independently varying grain size, thickness and line width, (iii) *in situ* grown interfaces including Cu-Ni, Cu-Ta, Cu-MgO, Cu-Ti, Cu-SiO₂ and Cu-oxygen, and (iv) epitaxial layers of various other metals including Ag(001), W(001), Ta(001), Ni(001), and TiN(001). The layers are grown by ultra-high vacuum magnetron sputter deposition on MgO(001) substrates and are found to be atomically smooth single crystals by a combination of x-ray diffraction θ - 2θ scans, ω -rocking curves, pole figures, reciprocal space mapping, Rutherford backscattering, x-ray reflection, transmission electron microscopy, and *in-situ* scanning tunneling microscopy.

The measured resistivity is interpreted within the classical models by Fuchs and Sondheimer for surface scattering and Mayadas-Shatzkes for grain boundary scattering. The data is well described by these models. However, fitting of the resistivity vs thickness for metal layers with non-spherical Fermi surfaces provides values for the bulk electron mean free paths that deviates from the expected free-electron values by factors of 5-10, indicating the breakdown of these semiclassical models. In addition, the F-S model also does not correctly predict the temperature dependence, as the measured scattering specularly as well as the product of bulk resistivity times mean free path are temperature dependent.

First-principles density functional (DFT) calculations are employed to develop an understanding of electron transport in metals at reduced length scales: (i) The Fermi surface of the bulk metal is determined and the electronic-structure contribution to the conductivity calculated by integration over the Brillouin zone. This provides, in combination with the known bulk resistivity, values for the bulk electron mean free path of 40, 3.3, and 16 nm for Cu, Ta, and W, respectively. (ii) Application of the Boltzmann transport equation and simultaneous integration over real and reciprocal space of the thin film and Brillouin zone, shows considerable anisotropy effects. For example, electron scattering at a W(100) surface has a two times larger effect on the resistivity than scattering on W(110). (iii) Simulation of transport using the 2D Fermi surfaces of thin films, and (iv) non-equilibrium DFT simulations are used quantitatively determine electron scattering which will be directly mapped on a phenomenological model.

Energy Frontiers Focus Topic

Room: 315 - Session EN+AS+EM+SE-TuM

Fuel Formation and Thermal Transport

Moderator: Michael Filler, Georgia Institute of Technology

8:00am **EN+AS+EM+SE-TuM1 Unraveling Thermodynamic and Kinetic Factors in Solar-Thermochemical Fuel Production**, *Sossina Haile*, California Institute of Technology **INVITED**

Perhaps the greatest challenge facing our planet is sustainable energy. Given the vast solar energy resource base available to modern society, key to addressing this challenge is the conversion of solar energy into a storable form suitable for on-demand utilization. So emerges the concept of 'Solar Fuels.' Amongst many approaches currently pursued to generate solar fuels, thermochemical dissociation of water splitting is particularly attractive. It provides the benefits of full utilization of the solar spectrum and inherent temporal separation of hydrogen and oxygen gases. In recognition of these advantages, numerous multi-step cycles have been considered over the past several decades. Recently, two-step cycles making use of *non-stoichiometric* oxides have received attention because of the simplicity of their implementation. The approach relies on the large oxygen nonstoichiometry change that the material undergoes in response to variations in oxygen partial pressure (pO_2) and temperature (T). Specifically, upon exposure to high temperatures ceria undergoes reduction without change in crystalline phase to release oxygen. On cooling in the presence of H₂O (or CO₂), the oxide is reoxidized, releasing H₂ (or CO). The success of the method relies not only on favorable thermodynamics but also on facile kinetics, both in terms of surface reaction rates and bulk diffusion coefficient. Accordingly, we have undertaken a comprehensive study of ceria and its doped derivatives to assess both the equilibrium redox behavior by thermogravimetric methods and the kinetic response by conductivity relaxation methods. We find, for example, that introduction of Zr strongly increases the absolute non-stoichiometry of ceria, but at a penalty in terms of the sensitivity of the nonstoichiometry to changes in environmental conditions and in terms of bulk diffusivity. In another example, we find that the relaxation behavior of Sm-doped ceria is substantially more rapid than that of both undoped and Zr-doped ceria, a result that is tentatively assigned to differences in species mobilities. The implications of these fundamental differences in material properties for thermochemical fuel production are discussed.

8:40am **EN+AS+EM+SE-TuM3 Controlling Catalysis on Metal Nanoparticles by Direct Photoexcitation of Adsorbate-Metal Bonds**, *M.J. Kale, T. Avanesian*, University of California, Riverside, *H. Xin, J. Yan*, SLAC National Accelerator Laboratory, *Phillip Christopher*, University of California, Riverside **INVITED**

Heterogeneous photocatalysis is typically assumed to occur via photon absorption by a solid-state photocatalyst (only the photocatalyst electronic states are involved in photon absorption) followed by charge carrier diffusion through the photocatalyst bulk and subsequent transfer to adsorbates. This process of energetic charge carrier generation and transfer results in wavelength dependent quantum efficiencies that strictly follow the

absorption spectrum of the solid-state photocatalysts, regardless of the chemical transformation. The substrate (photocatalyst) mediated photo-absorption process inhibits approaches to control reaction selectivity by matching photon excitation wavelengths to bond specific electronic transitions, as typically done in molecular systems.

Here, we show that strong chemisorption bonds formed between CO and Pt metal surfaces can be activated with visible photons to drive catalysis through direct, resonant photoexcitation of hybridized Pt-CO states. This is enabled as the dominant photoexcitation mechanism (over substrate mediated photoexcitation) driving catalysis by using sub-5-nanometer Pt nanoparticle catalysts, where high surface area to volume ratios force photon absorption onto surface metal atoms. The direct photoexcitation process is observed to be significantly more efficient for driving photocatalysis than the indirect photoexcitation process when the energy of exciting photons is resonant with adsorbate specific electronic transitions involving hybridized metal-adsorbate states. It is also demonstrated that resonant photoexcitation of Pt-CO bonds on sub-5-nanometer Pt nanoparticles by visible light significantly enhances selectivity towards CO₂, over H₂O production, in the selective oxidation of CO by O₂ in an H₂ rich stream (also known as preferential CO oxidation). These results open new avenues to control catalytic reaction selectivity on sub 5-nm catalytic particles by resonant photoexcitation of adsorbate-specific electronic transitions involving hybridized metal and adsorbate states. It is expected that the development of insights into resonant electronic transitions between hybridized metal-adsorbate states should allow rational control of catalytic selectivity that cannot be achieved exclusively with thermal energy input.

9:20am **EN+AS+EM+SE-TuM5 Atomistic Insights as the the pH Dependence of Onset Potential of the Oxygen Evolution Reaction on Hematite, Anders Hellman**, Chalmers University, Sweden

Hematite (α -Fe₂O₃) is an extensively investigated semiconductor for photochemical water oxidation, and recent research has shed light on many of the atomic processes involved. However, a controversy about the nature and role of surface states in the water oxidation reaction remains. Here first-principles calculations are used to investigate surface states present in hematite under photoelectrochemical conditions. Most specifically a model describing how the onset potential for oxygen evolution reaction on hematite depend on the pH of the electrolyte is put-forth. The predictions of this model are confirmed to a high extent by measurements of the onset potential on hematite based model photoanodes. In particular, a linear dependence of the onset potential on the pH was observed, with a 49 mV / pH slope. Detailed photoelectrochemical characterization confirmed that the oxygen evolution reaction takes place via the same surface states irrespective of the pH. Moreover, the photovoltage and flat band potential of the hematite were also found to be pH independent. These results provide a framework for a deeper understanding of the OER when taking place on semiconductors (like hematite) via surface states

9:40am **EN+AS+EM+SE-TuM6 Rational Design of Pt₃Ni Alloy Surface Structures for Oxygen Reduction, Liang Cao, T. Mueller**, Johns Hopkins University

A cluster expansion approach based on ab-initio calculations has been used to investigate the relationship between surface structures of Pt₃Ni(111) alloy catalysts and their catalytic activity. With this approach, we build a direct bridge between the atomic structure and catalytic properties of Pt-Ni alloy system at a variety of compositions and chemical environments. The equilibrium near-surface structures are presented as a function of O₂ partial pressure and the chemical potential difference between Ni and Pt. We discuss the relative importance of strain, ligand, and ensemble effects in determining catalytic activity, and demonstrate how ensemble effects can be leveraged to rationally design alloy surfaces with optimal ORR activity by searching for surfaces with targeted oxygen binding energy.

11:00am **EN+AS+EM+SE-TuM10 Molecular and Mesoscale Design for Organic and Hybrid Thermoelectrics, Rachel Segalman**, University of California, Santa Barbara

INVITED

Thermoelectric materials for energy generation have several advantages over conventional power cycles including lack of moving parts, silent operation, miniaturizability, and CO₂ free conversion of heat to electricity. Excellent thermoelectric efficiency requires a combination of high thermopower (S , V/K), high electrical conductivity (σ , S/cm), and low thermal conductivity (κ , W/mK). To date the best materials available have been inorganic compounds with relatively low earth abundance and highly complex, vacuum processing routes (and hence greater expense), such as Bi₂Te₃. Molecular materials and hybrid organic-inorganics bring the promise of solution processible, mechanically durable devices. While highly conductive polymers are now common place, they generally demonstrate low thermopower. Our work on molecular scale junctions that

nanostructuring of organics allows them to act as thermionic filters between inorganic junctions which can lead to enhanced thermoelectric properties. We have taken inspiration from this fundamental understanding to design material systems in which we combine a high electrical conductivity, low thermal conductivity polymer with a nanoparticle that contributes high thermopower. Additionally, the work functions of the two materials are well-aligned which introduces the possibility of thermionic filtering at the interface and an additional boost to the power factor. The combination of these effects results in a new hybrid, solution processible material with a thermoelectric figure of merit within an order of magnitude of the Bi₂Te₃. In this talk, I will discuss both the use of thermoelectric measurements to gain insight to molecular junctions and how this insight translates to design principles for polymer and hybrid thermoelectrics.

11:40am **EN+AS+EM+SE-TuM12 Advances in Solid-State Energy Harvesting from Asymmetric Thermoelectric Devices, B. Cook, Jay Lewis**, RTI International

The amount of thermal energy rejected as waste heat from industrial processes in the United States has been estimated at 32 quadrillion BTU per year, with an associated emission of 1,680 million metric tons of carbon dioxide. The ability to cost-effectively convert a portion of this thermal energy into useful electrical energy could improve energy efficiency, reduce operating costs, and decrease CO₂ emissions. Waste heat is typically categorized by temperature as high-grade (650°C and above), medium-grade (232°C to 650°C, and low-grade (232°C and below). In order to improve the thermal-to-electrical conversion efficiency of medium-grade waste heat, RTI has combined two different materials to form a high figure-of-merit, hybrid thermoelectric (TE) device. Recently-developed enhanced "TAGS-85", or e-TAGS, was employed as the p-leg, while the n leg was comprised of improved half-Heusler (HH) material. This hybrid material pair provides a high ZT, lead-free TE material solution for waste heat recovery for use in vehicle or industrial platforms. The improved HH material employs two novel techniques to reduce thermal conductivity: (1) high-energy milling, and (2) addition of coherent inclusions. Single n-p-couples were produced that achieved a 9.2% thermal to electric power conversion efficiency for $T_{hot} = 559^\circ\text{C}$ and $\Delta T = 523\text{K}$. This is a significant efficiency improvement at a lower hot side temperature with the hybrid e-TAGS/HH single couple over the performance of a conventional, all HH couple. By optimizing the cross sectional areas of the pellets for equal heat flow, the resulting asymmetric couple achieved a conversion efficiency of 10.5% at $T_{hot} = 537^\circ\text{C}$ and $\Delta T = 497^\circ\text{C}$. A 49-couple hybrid module using HH materials paired with e-TAGS and operated with T_{hot} up to 600°C reached a maximum efficiency of 10%. The improved module efficiency is believed to be due to both improved materials and optimized cross-sectional area ratios between the n- and p- elements. We will also discuss additional advances in thermal to electric power conversion using multi-stage modules.

12:00pm **EN+AS+EM+SE-TuM13 The Effect of Particle Size and Surface Termination of n-Si on Thermal and Electrical Conductivity, Thomas Lopez, L. Mangolini**, University of California - Riverside, S. Bux, J.P. Fleurial, California Institute of Technology

A discussion of synthesis and characterization of bulk nanocrystalline silicon with grain sizes of around 20 nm and thermal conductivities as small as 100 mW/cmK at room temperature, will be presented. Nanostructured materials have great potential for thermoelectric applications because of the reduction in thermal conductivity due to phonon scattering at grain boundaries [1] and silicon is a well-understood, cheap, earth-abundant material. Other silicon nanostructures, such as nanowires [2], are being investigated as viable thermoelectric materials. We have used, for the first time, the combination of a non-thermal plasma process for the synthesis of silicon nanocrystals with hot pressing to produce bulk nanostructured silicon samples. The non-thermal plasma synthetic route has been proposed for the production of photo-luminescent silicon quantum dots with narrow size distribution (3 +/- 0.5 nm) [3]. The same reactor has been scaled up to produce silicon nanocrystals at a rate of hundreds of milligrams per hour. Silicon powder with sizes between 5 nm and 15 nm has been produced using either silane (SiH₄) or silicon tetrachloride (SiCl₄), which are low-cost silicon precursors. Results have shown surface termination of the non-thermal plasma synthesized particle, i.e. H or Cl, play a role in densification kinetics. Hot pressing is a high pressure, high temperature process that allows for the production of samples with bulk like densities while limiting grain growth. In this study we have produced bulk (12 mm diameter, 2-4 mm in thickness) samples of nanocrystalline silicon with relative densities exceeding 95%. Characterization by XRD and TEM confirms that grain sizes are around 30 nm. The effects of surface termination of nano-silicon on grain growth and grain boundary conditions will be extensively discussed.

1. Dresselhaus, M.S., et al., *Advanced Materials*, 2007. 19(8): p. 1043-1053.
2. Hochbaum, A.I., et al., *Nature*, 2008. 451(7175): p. 163-U5.

Tuesday Afternoon, November 11, 2014

Electronic Materials and Processing

Room: 314 - Session EM+2D-TuA

High-k Dielectrics for Advance Semiconductor

Moderator: Andrew C. Kummel, University of California at San Diego

2:20pm EM+2D-TuA1 Time-resolved XPS of ALD, **Rainer Timm**, Lund University, Sweden **INVITED**

Atomic layer deposition (ALD) has been established as the main technique for creating MOS structures based on III-V semiconductors, but still device performance is limited by the quality of the interface towards the high-k oxide layer. X-ray photoemission spectroscopy (XPS) is a well-suited tool for analyzing the structure and chemical composition of such interfaces. However, conventional XPS studies under ultrahigh vacuum conditions can only compare the situation before and after individual half-cycles of the ALD process. Here I will show how ambient-pressure XPS can be used to study surface structure and chemistry live and *in-situ* during the ALD reaction. As an example, we have investigated the deposition of HfO_2 on InAs using TDMA-Hf and water as precursors, revealing several steps within the chemical reaction of InAs exposed to the Hf precursor material, which we interpret as a temperature-dependent adsorption of unreacted precursor molecules preceding the ligand exchange reaction.

3:00pm EM+2D-TuA3 GaSb Oxide Thermal Stability Studied by Dynamic-XPS, **Stephen McDonnell**, **B. Brennan**, **E. Bursa**, University of Texas at Dallas, **K. Winkler**, **P. Baumann**, Omicron NanoTechnology, Germany, **R.M. Wallace**, University of Texas at Dallas

GaSb is a III-V material with applications as a potential channel material for p-type metal-oxide-semiconductor field effect transistors,¹ optoelectronics in the infrared region,² quantum devices,³ and tunnel field effect transistors.⁴ Prior to application specific processing it is often necessary to remove the GaSb native oxide, which can be quite thick. Such oxides can inhibit subsequent epitaxy and also be a source of traps for devices as a result of defect levels in the energy gap.⁵ The thermal desorption of these oxides in ultra high vacuum has been examined in previous works, but is revisited in this study with dynamic-x-ray photoelectron spectroscopy (dynamic-XPS). Dynamic-XPS allows for the collection of core-level spectra in real time (i.e. data acquisition times are < 1 second). Combined with controlled heating, this allows for detailed chemical temperature-dependent chemical analysis to be carried out with temperature resolutions better than 1 Kelvin. The thermal decomposition of the native GaSb oxides is studied using dynamic-XPS. The expected transfer of oxygen from Sb-O to Ga-O before the eventual desorption of all oxides is observed. However an initial reaction resulting in the reduction of Sb_2O_3 along with the concurrent increase in both Ga_2O_3 and Sb_2O_4 is detected in the temperature range of 450-525 K. Using the relative changes in atomic concentrations of the chemical species observed, the initial reaction pathway is proposed.

A. Nainani, T. Irisawa, Z. Yuan, Y. Sun, T. Krishnamohan, M. Reason, B. R. Bennett, J. B. Boos, M. G. Ancona and Y. Nishi, presented at the Electron Devices Meeting (IEDM), 2010 IEEE International, 2010 (unpublished).

F. Chen, G. Liu, Z. Wei, R. Deng, X. Fang, S. Tian, Y. Zou, M. Li and X. Ma, presented at the Optoelectronics and Microelectronics (ICOM), 2012 International Conference on, 2012 (unpublished).

M. V. Lebedev, E. V. Kunitsyna, W. Calvet, T. Mayer and W. Jaegermann, The Journal of Physical Chemistry C **117**, 15996-16004 (2013).

A. W. Dey, B. M. Borg, B. Ganjipour, M. Ek, K. A. Dick, E. Lind, C. Thelander and L.-E. Wernersson, Electron Device Letters, IEEE **34**, 211-213 (2013).

A. Ali, H. Madan, A. Kirk, D. Zhao, D. Mourey, M. Hudait, R. Wallace, T. Jackson, B. Bennett and J. Boos, Appl Phys Lett **97**, 143502-143502-143503 (2010).

3:20pm EM+2D-TuA4 Combined Wet HF and Dry Atomic H Cleaning of SiGe followed by Passivation of the Clean Surface via $\text{H}_2\text{O}_2(\text{g})$ Dosing, **Sang Wook Park**, **T. Kaufman-Osborn**, **E.A. Chagarov**, **A.C. Kummel**, University of California at San Diego

Silicon Germanium (SiGe) is a well-known material for its high mobility and useful applications in strain engineering. Its advantages can be utilized to overcome the challenges when scaling down silicon-based devices. As the interest in introducing new kinds of materials increases, the cleaning

and passivation methods also become more significant in order to provide uniform and clean surfaces, which would result in improved electrical properties such as high mobility and low interface trap density (D_{it}). In this study, combined wet and dry cleaning and passivation of SiGe(100) surface is discussed, using scanning tunneling microscopy (STM), scanning tunneling spectroscopy (STS), and x-ray photoelectron spectroscopy (XPS).

Wet cleaning using 2% hydrofluoric acid (HF) was implemented to strip the native oxide off the SiGe sample but left residual carbon contamination on the surface. Although the oxide layer was removed, additional oxygen adsorbed to the surface during transfer from the HF solution to vacuum chamber. This residual oxygen can be eliminated by keeping the SiGe sample covered in the HF cleaning solution until the sample is introduced to the vacuum chamber or by transferring the sample in an inert environment. Dry in-situ atomic hydrogen cleaning was then implemented to remove the carbon contamination on the surface. A post deposition anneal at 550°C was used to obtain an atomically clean, flat, and ordered SiGe surface and this was verified using STM. The oxygen and carbon contaminant levels were monitored after each cleaning procedure using a monochromatic XPS. The clean SiGe sample was dosed at room temperature with a saturation dose of $\text{H}_2\text{O}_2(\text{g})$. STM and XPS measurements indicate that $\text{H}_2\text{O}_2(\text{g})$ dosing leaves the SiGe surface, which is mostly Ge atoms due to surface segregation, terminated with an ordered monolayer of Ge-OH sites. STS measurements of the Ge-OH sites show the conduction band edge dangling bond states are eliminated due to the passivating Ge-OH bonds, but the Fermi level is pinned near the valence band edge due to the large surface dipole. When the surface is annealed to 310°C, XPS measurements indicate that the -OH species on the surface break bonds with the Ge atom and bond instead to the Si atoms, raising Si atoms towards the surface. XPS also verifies that no oxygen leaves the surface due to the 310°C anneal. Instead, the oxygen remains on the surface in the form on Si-OH or SiO_x species. TMA is subsequently dosed on the surface forming and ordered monolayer of Al-O-Si bonds. STS indicates this unpins the Fermi level, leaving an electrically passive ordered layer which serves as an ideal template for further high-k ALD.

4:20pm EM+2D-TuA7 Interfacial and Electrical Study of Crystalline Oxidation Passivation for AlGaIn/GaN HEMTs, **Xiaoye Qin**, **H. Dong**, **J.Y. Kim**, **R.M. Wallace**, University of Texas at Dallas

AlGaIn/GaN high electron mobility transistors (HEMTs) are of significant interest for high power, high frequency and high temperature devices. However, these are known to experience significant surface related effects, such as large leakage currents and frequency dependent current collapse. Oxidation has been found to have a variety of effects on the atomic and electronic structure of nitride surfaces. Therefore, the oxidation layer and the device performance are closely related. Typically, GaN and AlN are found to form a disordered oxide layer related to high density of states when exposure to with O_2 . Miao *et al.*¹ reported that oxidation of AlN and GaN surface change the density of surface states based on density functional theory (DFT). In their work, a 2 ML crystalline oxide can cause the lowest density of surface states within the band gap. However, experimental evidence of a 2 ML crystalline oxide remains to be established.

In this study, we investigate O_2 plasma- exposed AlGaIn surfaces at 300 °C and 550 °C by *in situ* X-ray photoelectron spectroscopy (XPS), low energy electron diffraction (LEED). The results indicate that a 500°C O_2 remote plasma exposure is able to generate a thin 2 ML ordered oxide on AlGaIn surface and the oxide is stable during subsequent ALD processing, in contrast to arsenide surfaces.² The capacitance- voltage (C- V) results indicates that the 2 ML crystalline oxide reduces the D_{it} and shifts the threshold voltage to positive voltages. The I-V and gate leakage current characteristics for crystalline oxide MOSHEMTs will also be presented. This work is supported by the AFOSR Asian Office of Aerospace Research and Development (AOARD) under Grand No. FA2386- 11- 1- 4077.

References

¹ M.S. Miao, J.R. Weber, and C.G. Van de Walle, J. Appl. Phys. **107**, 123713 (2010).

² D. M. Zherokletov, P. Laukkanen, H. Dong, R. V. Galatage, B. Brennan, M. Yakimov, V. Tokranov, J. Kim, S. Oktyabrsky, and R. M. Wallace, Appl. Phys. Lett., **102**, 211601 (2013)

4:40pm **EM+2D-TuA8 Investigating Electrically Active Defects in High-*k*/InGaAs MOS System using MOS Capacitors and MOSFETs**, Paul Hurley, Tyndall National Institute, Ireland, V. Djara, IBM Research - Zurich, Switzerland, E. O'Connor, S. Monaghan, I.M. Povey, J. Lin, Tyndall National Institute, Ireland, M.A. Negara, Stanford University, B. Sheehan, K. Cherkaoui, Tyndall National Institute, Ireland **INVITED**

As silicon devices reach the limit of dimensional scaling there is a growing interest in the use of high electron mobility channels, such as In_xGa_{1-x}As, in conjunction high dielectric constant (high-*k*) gate oxides for *n*-channel Metal-Oxide-Semiconductor Field Effect Transistors (MOSFETs) and tunnel FET (TFETs) based devices. The understanding and control of electrically active defect states at the high-*k*/In_xGa_{1-x}As interface and of charges within the atomic layer deposited (ALD) high-*k* films will be essential for the successful implementation of high mobility channel materials. The objective of this presentation will be to provide an overview of the current understanding of the density and distribution of electrically active defects at the high-*k*/InGaAs interface both within the InGaAs energy gap and extending into the InGaAs conduction band. The presentation will focus on InGaAs with a 53% Indium concentration. The electrically active interface state density distribution is determined from fully fabricated InGaAs MOSFET structures based on the full gate capacitance in conjunction with the Maserjian Y-function and Poisson-Schrodinger simulations. Very significant progress has been made in recent years in the passivation and intrinsic elimination of high-*k*/In_{0.53}Ga_{0.47}As interface defects to the point where genuine surface inversion for *n* and *p* type InGaAs MOS structures can be achieved and this research will be reviewed. The characteristic signatures of capacitance and conductance for an InGaAs MOS structure in inversion will also be discussed.

Electrically active defects with energies aligned with the InGaAs conduction band are significant for surface inversion mode MOSFETs and can result in a partitioning of charge between free carriers and trapped charge for devices biased above the threshold voltage. The presence of such defect also complicates the extraction of free charge and carrier mobility from device analysis. In this presentation we will also review a new approach where the technique of inversion charge pumping (initially developed for silicon MOSFETs) is applied to InGaAs MOSFETs to determine the free carrier concentration. Results will also be presented which indicate that the duty cycle of the inversion charge pumping technique can be used to discriminate between fast interface states and traps within the oxide for InGaAs MOSFETs biased beyond the threshold voltage.

5:20pm **EM+2D-TuA10 XPS Study of High-*k* Gate Stack and Interaction with Different Channel Materials and Metal Gate**, Malcolm Bevan, Applied Materials Inc. **INVITED**

Deposited high-*k* dielectrics with metal gates have replaced SiON gate with poly electrodes for several Logic nodes and rapidly followed with integration changes from planar to 3D FINFET structures. Performance is no longer through just scaling, and next generation devices have gaps that are being addressed with channel engineering using high mobility materials such as SiGe, Ge and III-V compound semiconductors. Gate stacks now involve several thin films of dissimilar material whose interfaces need to be precisely controlled as well as being conformal around the fin and between the spacers. The stack usually involves the channel material followed by a thin interface layer (iL), high-*k* dielectric and metal gate cap (MG cap) and each layer range from 0.5 to 2nm. In addition several layers may need plasma or thermal treatment to improve reliability and BTI of the gate stack. To understand performance of these stacks, XPS has been applied to compliment device results. In Fab XPS is a powerful tool to provide in short time information on stack thickness, composition and changes in bonding. Examples will be given to show how XPS has been used to optimize and compare high-*k* stack on Si, SiGe and Ge. In addition iL/high-*k*/TiN cap has been studied and further examples given and related to electrical device results.

6:00pm **EM+2D-TuA12 Reliability of nc-CdSe Embedded ZrHfO High-*k* Dielectric Nonvolatile Memory – Temperature Effects**, Shumao Zhang, Y. Kuo, Texas A&M University

Previously, it was reported that by adding the third element into the high-*k* film, the bulk and interface material and electrical properties can be improved [1]. For example, the Zr-doped HfO₂ film (ZrHfO) shows the higher crystallization temperature, a lower interface state density, and a larger effective *k* value than those of the un-doped HfO₂ film [1,2]. Furthermore, nanocrystals have been embedded into this kind of high-*k* film for the nonvolatile memory (NVM) application to replace the conventional floating-gate flash memory due to the improved device characteristics and reliability [3]. The nanocrystalline cadmium selenide (nc-CdSe) embedded ZrHfO MOS capacitor has shown excellent charge trapping and retention capabilities [4]. However, most studies on the nanocrystals embedded high-*k* memory devices are done at the room temperature. Since the temperature

in the high density integrated circuit can be much higher than room temperature, it is imperative to study the reliability at a raised temperature [5]. In this paper, the temperature effects on memory functions were investigated on the nc-CdSe embedded sample in the range of 2 °C to 120°C. Compared with the fresh *C-V* curve, the flat band voltage (*V_{FB}*) of *C-V* curve shifts to the negative or positive gate voltage (*V_g*) direction after being stressed at -6 V or +6 V for 10 s, respectively. With the increase of the temperature, the magnitude of the *V_{FB}* shift increases at -6 V stress but decreases at +6 V stress. With the increase of the temperature, the hole-trapping is enhanced due to the increase of injection and retention of holes to the trapping sites. However, at the high temperature, electrons are possibly transferred through the whole high-*k* stack with minimum trapping to the high-*k* stack. In addition, at the high temperature, the nc-CdSe embedded sample has the large relax current with the high discharge rate due to the increasing release of the trapped charges with large thermal energy. The charge retention capability of the device decreases with the increase of the temperature. For example, the device stressed at -6 V for 20 s will retain 30% of the original trapped holes at 20°C, 23% at 70°C, and 15% at 120°C, respectively, after 10 years. This is because the stored charges gain the high thermal energy and the bulk high-*k* film is more conductive at the high temperature.

Energy Frontiers Focus Topic

Room: 315 - Session EN+EM+NS-TuA

Charge Storage Materials and Devices

Moderator: Susanna Thon, Johns Hopkins University

2:20pm **EN+EM+NS-TuA1 Spatiotemporal Investigation of Li-Air Battery under Operating Condition: Understanding the Cathodic and Anodic Electrochemical Processes and their Interdependence**, Di-Jia Liu, Argonne National Laboratory **INVITED**

Li-O₂ battery has generated a great deal of interests due to its high theoretical energy storage capacity for vehicular application. Many studies were carried out in attempt to understand the fundamental chemical processes inside of Li-O₂ battery. The reports so far have been segmented into the investigation on the individual regions of the battery, cathode, anode and separator, mostly at the post mortem state due to the limitation of the characterization methods used.

We adopted a holistic approach in studying electrochemical processes and mechanism of the Li-O₂ battery using operando methods. Particularly, we introduced the microfocused synchrotron X-ray diffraction (μ -XRD) and tomographic (μ -CT) techniques for the spatiotemporal study on the phase and structural changes in Li-O₂ battery. These tools offered some unique capabilities to probe battery properties under the actual discharge-charging condition. For example, the μ -XRD has a spatial resolution at the micron scale of with a complete side penetration to the battery, rendering it feasible to study battery's composition layer-by-layer without the interruption of battery operation. In this presentation, we will discuss our recent investigation of the Li-O₂ batteries under cycling condition in real time using the cells fabricated with the most representative design and materials. We were able not only to reveal individually the changes at anode, cathode and separator, but also to provide a comprehensive view between the regional chemical processes and their interdependence to the overall battery performance during the multiple discharge-charge cycles. More importantly, the finding of this study provides new insights on the catalytic process inside of Li-O₂ cell and calls for new design and materials which could lead to high capacity and longer battery life.

The work performed at Argonne is supported by DOE under Contract No. DE-AC02-06CH11357 by UChicago Argonne, LLC.

3:00pm **EN+EM+NS-TuA3 Insights into Ionic vs. Electronic Transport in Nanostructured Battery Electrodes Enabled by Microfabrication and Spatially Resolved XPS**, Alexander Pearse, E. Gillette, S.B. Lee, G.W. Rubloff, University of Maryland, College Park

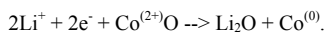
Nanostructured battery electrodes provide a design opportunity to achieve high power at high energy density, using thin active storage layers whose short ion diffusion pathways assure fast transport throughout the layers. However, this must be coupled with fast electron transport through current collectors to all regions of the ion storage layers, posing a design challenge in balancing and optimizing both charge transport components. Spatial inhomogeneity in the utilization of active material due to electronic or ionic transport limitations may lead to decreases in performance, but characterizing this effect with bulk electrochemical measurements is difficult. We address this challenge with a new state-of-charge (SOC) measurement scheme utilizing a patterned ultra-thin film battery electrode and spatially resolved XPS, and focus on the case of limited electronic

transport by examining SOC as a function of distance from the current collector.

We fabricate electrode test structures by evaporating metallic strips as current collectors on an electrically insulating substrate. A patterned thin film of active material (V_2O_5) is then deposited using atomic layer deposition (ALD) and mechanical masking so that only a small fraction of the active material is in contact with the current collector. The use of ALD allows for an ultrathin ($\leq 30\text{nm}$) pinhole-free film. We discharge these electrodes in a liquid electrolyte under different rates and conditions and directly measure the state of charge as a function of distance from the current collector using small spot XPS, achieving a lateral resolution of better than $20\mu\text{m}$. We find that a rate-dependent SOC gradient develops in the electrodes, with the SOC decreasing with distance from the current collector. Unlike microspot Raman or XRD, XPS provides a direct quantitative measurement of the SOC through the concentration of inserted ions and/or reduced vanadium ions. Additionally, in the ultrathin films relevant to nanostructured storage, XPS becomes a “quasi-bulk” measurement, because the escape depth of photoelectrons becomes a significant fraction of the film thickness. We also explore the depth dependence of the SOC using angle resolved XPS and ion beam depth profiling. We compare our observations with simulations using COMSOL Multiphysics, and attempt to resolve discrepancies between the two. We believe this approach can provide design guidance for heterogeneous nanostructures applied to electrical energy storage, and we anticipate it to be broadly applicable to other electrode materials and active ions.

3:20pm **EN+EM+NS-TuA4 The Lithium-Induced Conversion Reaction of CoO Thin Film Battery Materials in Ultra-High Vacuum as Studied by ARXPS and STM, Ryan Thorpe, S. Rangan, A. Howansky, R.A. Bartynski**, Rutgers, the State University of New Jersey

Li-ion conversion batteries can store 2-3 times more charge than intercalation batteries by utilizing the full range of oxidation states of their constituent divalent or trivalent transition metal compounds during discharge. A prototypical conversion compound is CoO, which follows the reaction



Cobalt oxide and other transition metal oxides are attractive for use as Li-ion anodes in portable electronics due to their high charge storage capacity and moderate voltage versus Li^+/Li^0 . However, the cycling stability of conversion electrodes is poor, and capacity losses have thus far prevented their implementation.

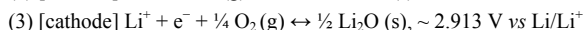
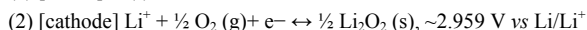
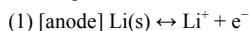
In order to understand phase progression during the conversion reaction of CoO, high-purity CoO thin films grown in UHV were sequentially exposed to atomic lithium. The electronic structure of the pristine films and of the products of lithiation was studied using x-ray photoemission spectroscopy (XPS), UV photoemission spectroscopy, and inverse photoemission spectroscopy. The crystal structure and film reorganization were probed in parallel with transmission electron microscopy (TEM) and scanning tunneling microscopy.

The amount of CoO reduction for a given Li dose was observed to be highly dependent upon the temperature at which lithiation was performed. At 150°C , Li mobility in the active material was sufficient to allow full reduction of the CoO film as confirmed by XPS. Consistent with electrochemically lithiated CoO electrodes, precipitation of Co nanoparticles in a Li_2O matrix was observed in TEM images. However, at room temperature, the Li-rich overlayers that formed on the CoO film after initial lithiations inhibited further Li diffusion. This could be due to the intrinsically poor kinetic properties of Li_2O or to the formation of Li_2O and/or LiOH passivating films.

The reactivity of CoO films was also found to depend on the orientation of the film. CoO(100) films exhibited a higher degree of conversion for a given Li exposure than polycrystalline films. STM and angle-resolved XPS of these films have been used to investigate the differences between these two film morphologies upon exposure to Li.

4:20pm **EN+EM+NS-TuA7 Controlled Cathode/Catalyst Architectures for Li-O₂ Batteries, Malakhi Noked, M.A. Schroeder, A.J. Pearse, C. Liu, A.C. Kozen, S.B. Lee, G.W. Rubloff**, University of Maryland, College Park

Electrochemical power sources based on metal anodes have specific energy density much higher than conventional Li ion batteries, due to the high energy density of the metal anode (3842mAh/g^1 for Li). Rechargeable Li-O₂ batteries consume oxygen from the surrounding environment during discharge to form Li oxides on the cathode scaffold, using reactions



The cathode reaction requires large over-potentials for charging due to the mass transfer resistance of reagents to the active sites on its surface, decreasing the round trip efficiency, making recharge of the Li-O₂ cell difficult. To overcome these problems, the cathode needs good electrical conductivity and a porous structure that enables facile diffusion of oxygen and can accommodate the reduced oxygen species in the pores.

Two significant challenges exist in the use of the traditional activated carbon material as the cathode of the Li-O₂ system. First, in the presence of Li_2O_2 the carbon electrode becomes relatively unstable even at low voltages ($\sim 3\text{V}$). Second, cathode structures must be porous to accommodate a substantial amount of Li-peroxide (Li_2O_2) without blocking ion transport channels in the cathode. While a few studies have been reported on the effect of catalyst on the onset potentials for the oxygen evolution reaction (OER) and oxygen reduction reaction (ORR) in the Li-O₂ cell, the results were inconclusive due to the lack of systematic study in a single system and conditions.

We report here results from a model cathode system which enable determination of the effects of various catalysts on the OER/ORR reactions in the non-aqueous Li-O₂ cell. Mesoporous CNT sponge is used as the model cathode material, decorated with catalyst nanoparticles by nucleation-controlled atomic layer deposition (ALD) of Ru, RuO₂, MnO₂, and Pt catalyst components whose loading and composition are controlled by manipulating the ALD conditions. Using a custom Li-O₂ battery cell, we have studied the effect of different catalysts on the voltage of the OER and ORR, and on the cycling performances of the cell. We demonstrate a Li-O₂ cell that sustains $>3000 \text{ mAhg}^{-1}$ over more than 15 cycles at current density of $200 \text{ mA} \cdot \text{g}^{-1}$. To our knowledge, this is the first comparison of a variety of catalysts with a well-defined morphology (controlled by ALD and monitored by TEM), and under the same electrochemical conditions.

4:40pm **EN+EM+NS-TuA8 Vertically Aligned Carbon Nanotubes on Ni Foam as a 3D Li-O₂ Battery Cathode, Marshall Schroeder, M. Noked, A.J. Pearse, A.C. Kozen, S.B. Lee, G.W. Rubloff**, University of Maryland, College Park

The Li-O₂ battery system is one of the prime candidates for next generation energy storage. Like other metal-O₂ systems, this technology is known for its impressive theoretical specific energy due to use of metallic anodes and because the cathode active material (oxygen) is not stored in the battery, but is available in the cell environment. A typical cell consists of a pure lithium metal anode, an organic electrolyte (in this study), and a porous positive electrode (usually made of carbon or oxides) which acts as a reaction scaffold for oxygen reduction to Li_2O_2 or Li_2O during discharge. Despite remarkable scientific challenges within every component of the cell, the positive electrode is particularly complicated by its role in the oxygen evolution (OER) and reduction (ORR) reactions, leading to strict requirements for electrode architecture and physicochemical stability for optimal performance. We present herein one of the first experimental realizations of a controlled macroscale 3D carbon nanotube architecture with a practical carbon loading of $1\text{mg}/\text{cm}^2$ in an attempt to satisfy these requirements.

The O₂ cathode highlighted in this work features a macroporous nickel foam current collector coated with dense forests of vertically aligned carbon nanotubes (VACNT). This freestanding, hierarchically porous system is the first to feature VACNT robustly and electrically connected to a 3D current collector without a binder, and without requiring delamination of the CNT from the growth substrate. Grown via LPCVD with an Fe catalyst on a thin ALD interlayer, the micron-length VACNT provide a very promising electrode material due to their high electrical conductivity, physicochemical stability, and a high surface area architecture that is conducive to ionic mobility and storage of the reduced oxygen discharge product. As a result, this structure exhibits significant capacity ($>2\text{Ah}/\text{g-carbon}$) at high ORR voltages ($>2.76\text{V}$) without requiring a catalyst.

Electrochemical performance results as a scaffold for oxygen reduction in various non-aqueous electrolytes will be presented with SEM/TEM/XPS of pristine/discharged electrodes.

5:00pm **EN+EM+NS-TuA9 Solid Micro-supercapacitor using Directed Self-Assembly of Tobacco Mosaic Virus and RuO₂, Markus Gnerlich, E.I. Tolstaya, J. Culver, D. Ketchum, R. Ghodssi**, University of Maryland, College Park

The 3D micro-supercapacitor reported here utilizes a novel bottom-up assembly method that combines genetically modified Tobacco mosaic virus (TMV-1Cys) with deposition of RuO₂ on multi-metallic microelectrodes. The nanostructured RuO₂ coating is selectively deposited on the electrodes due their unique composition, which is a significant advantage for microfabrication process integration. Test results show electrode capacitance as high as $18 \text{ mF}/\text{cm}^2$ in $1.0\text{M H}_2\text{SO}_4$ electrolyte and $7.2 \text{ mF}/\text{cm}^2$ in solid Nafion electrolyte.

The device fabrication involves the photolithographic patterning of titanium nitride (TiN) microelectrodes with Au cap on top of polyimide micropillars supported by a silicon wafer. A schematic cross section of the device is shown in Figure 1 and a photograph of the fabricated chip in Figure 2. The complexity of the self-assembly process in multiple chemically reactive solutions required the development of a special kind of micro-electrode. The TiN functions as a chemically resistant current collector, the Au cap as an adhesion layer for the TMV-1cys, and the Ni pad as a sacrificial material during the RuO₂ deposition process. After microfabrication, each chip is submerged in TMV-1Cys solution for 24 hours and then transferred to a 0.5% solution of RuO₄. A nanostructured coating of RuO₂ forms on all exposed electrode areas as the Ni is sacrificed in a galvanic displacement reaction. EDX spectral imaging of the constituent elements on the electrode demonstrates selective RuO₂ coating (Figure 3), and SEM images of the electrodes before and after TMV/RuO₂ coating shows the TMV-1Cys/RuO₂ nanostructures (Figure 4).

Cyclic voltammetry (CV) was performed from 0-800mV versus Ag/AgCl at 10 mV/s in 1.0M H₂SO₄ electrolyte. Figure 5 shows the CV curves, and Figure 6 shows the associated capacity fading, which was insignificant after 100 cycles for electrodes annealed at 150°C. Separately prepared chips were coated with Nafion dispersion and tested in a controlled humidity environment. The measured capacitance drops from 18 to 7.2 mF/cm² per electrode due to ionic conductivity limitations, but 80% capacity is retained after 12,000 cycles (Figure 7). Associated rate capability (Figures 8-9) shows 60% capacity is retained when comparing 3 uA/cm² to 3000 uA/cm², and the low leakage current of only 5 nA (Figure 10) enables use in a wide variety of energy storage applications.

The primary challenge of nanomaterials is often integration into microfabrication processes. The RuO₂ electrode developed here is optimized for compatibility with standard microfabrication steps by using a novel bottom-up assembly approach for manufacturing micro-supercapacitors.

5:20pm **EN+EM+NS-TuA10 Characterization of Tobacco Mosaic Virus-templated Ni/NiO Electrodes for Solid Flexible Supercapacitors**, Sangwook Chu, K.D. Gerasopoulos, M. Gnerlich, J. Culver, R. Ghodssi, University of Maryland, College Park

Characterization of nickel oxide supercapacitor electrodes utilizing *Tobacco mosaic virus* (TMV) nanotemplates is presented. NiO was formed on Ni coated TMV nanotemplates by annealing at high temperatures (Figure 1). The resulting electrode showed excellent electrochemical performance with remarkable cycle stability. The TMV/Ni/NiO nanostructured electrodes were also integrated with a solid electrolyte to demonstrate their potential application as solid flexible supercapacitors.

NiO supercapacitor electrodes have been prepared in literature using various methods, and it has been found that the crystallinity of the NiO is critical for its electrochemical charge capacity [1]. The NiO electrode presented in this work was thermally grown on Ni coated TMVs. Gold electrodes (0.5cm²) were immersed in TMV solution for virus self-assembly followed by electroless deposition of Ni uniformly coating the TMV nanostructure [2]. TMV/Ni electrodes were annealed in a furnace at three different temperatures (200°C, 300°C, and 400°C) and the NiO formation on TMV/Ni surface was characterized by XPS (Figure 2). The results indicate that thermal growth of NiO layer on TMV/Ni electrodes starts at temperatures higher than 300°C, in good agreement with previously reported results.

Electrochemical testing was performed in aqueous 2M KOH electrolyte in a three-electrode configuration. The electrodes annealed at 300°C showed the highest areal capacitance (148mF/cm²) measured by a galvanostatic (2mA/cm²) charge/discharge test shown in Figure 3a. The redox charge storage mechanism was confirmed by cyclic voltammetry (CV) with good rate capability up to 100mV/s (Figure 3b). Excellent cycle stability was measured with little degradation over 500 cycles as shown in Figure 4. This is attributed to the conformal layers of Ni/NiO over the TMV nanostructure, and the stabilizing effect of KOH on NiO. The continuous electrical contact between the Ni and NiO layers ensures an optimized current collector configuration.

A PVA-KOH-H₂O polymer was prepared to study the performance of the nanostructured electrodes with a solid electrolyte. Polymer electrolyte solution was poured onto the nanostructured NiO electrodes and the Pt foil was assembled on top as an anode. The polymer electrolyte film formed after 24hours was flexible and strong enough to support both electrodes. Figure 5 shows CV curves measured with the assembled cell, verifying proper operation of the nanostructures in both liquid and solid electrolytes. The successful integration of TMV/Ni/NiO electrodes with polymer electrolytes highlights the potential of this approach to develop flexible solid-state supercapacitor devices.

5:40pm **EN+EM+NS-TuA11 Charged Particles Micro-Penning-Malmberg Trap: An Approach to Store High Densities with Substantially Lower End Barrier Potentials**, Alireza Narimannezhad, J. Jennings, C. Minnal, M.H. Weber, K.G. Lynn, Washington State University
Among devices that have been used to store antimatter, Penning-Malmberg trap has become the device of choice because of its simplicity and versatility. However, the challenge involved in these traps is when the number of particles increases inside the trap to the densities of energy harvesting interest, the confining fields rise to unpractical values. One of the authors has proposed a design of microtube arrays with much lower end barrier potentials. The microtraps are designed for non-neutral plasma storage such as positrons. Here, we present fabrication, simulation studies, and trapping milestones so far. The fabrication involved advanced MEMS techniques including photolithography, deep reactive ion etching of silicon wafers, sidewalls smoothening, gold sputtering, wafers aligning, and thermo-compression gold bonding. Alignment of less than 2 microns was achieved using a micro-machined jig and precision ground sapphire rods. Simulation using a WARP Particle-In-Cell code showed that density of $1.6 \times 10^{11} \text{ cm}^{-3}$ is achievable with the new trap design while the end barrier potentials are several order of magnitudes smaller compared to the conventional traps. However, positron losses occur in experimentation by both trap imperfections such as misalignment of wafers, asymmetries, and physical imperfections on the surface, and also field misalignment and perturbations. The loss rates were also compared to the results from simulation in order to study and distinguish each effect. This project will open the door to a wide range of new and exciting research areas. The size of these traps along with the low confining potentials is a big step to make them portable. It could be used as a source of energy or in propulsion system where alternate sources are not feasible.

Thin Film

Room: 305 - Session TF+AS+EM-TuA

Thin Film: Growth and Characterization II

Moderator: Mark Davidson, University of Florida

2:20pm **TF+AS+EM-TuA1 A Statistical Optimization of Perpendicular Anisotropy and Damping for Ta-Inserted Double CoFeB/MgO Interface MTJ's**, S. Gupta, Samuel Schwarm, B. Clark, University of Alabama

A statistical Design of Experiments was conducted on double-interface Ta-inserted CoFeB-MgO magnetic tunnel junctions (MTJ's). These MTJ's were deposited using a Shamrock planetary sputtering system. The thicknesses of the inserted Ta and the CoFeB electrodes were varied using Response Surface Methodology. The responses measured using magnetometry and ferromagnetic resonance were a) effective magnetization, b) damping constant and c) perpendicular anisotropy. The effect of annealing on the perpendicular anisotropy was also observed for these devices. As the Ta thickness is increased for fixed CoFeB thickness, the M-H loops indicate that the anisotropy is becoming perpendicular. After annealing, both magnetometry and FMR results show that the MTJ's indicate full perpendicular anisotropy. Interfacial perpendicular anisotropy, which can be extracted from the FMR measurements, scales with the inserted Ta thickness for both as-deposited and annealed samples.

2:40pm **TF+AS+EM-TuA2 1D Matlab Modeling of the Reaction-Diffusion System during the Selenization Process in the Two-Step CIGS Solar Cells Production Process**, Jurjen Emmelkamp, A. Mannheim, TNO Technical Sciences, Netherlands

Introduction

In the two-stage fabrication process of CIGS thin-film solar cells first copper, indium and gallium precursor layers are deposited, followed by the selenization process where selenium vapor is provided at high temperature to form CIGS. Despite of the literature, many stages of the reaction-diffusion process are still a mystery. Several experimental techniques exist to analyze the selenization process, however, most of them are only useful to analyze the post-selenization product. In-situ XRD can be used to analyze the crystal structure during the selenization process, but the information is limited because depth profiles and amorphous intermediates are not measured. Modeling of the reaction-diffusion system during the selenization process can result in deeper understanding of the process and in a predictive model for the optimal process conditions that can lead to cheaper and more efficient CIGS solar cells.

The model

A relative simple 1D mathematical Matlab model is developed. Since many intermediate products and the CIGS end-product are crystals, and thus 3D

systems, an 1D approach is very simplified. Intensive evaluation with experimental in-situ XRD and cross section EDX, as well as literature values, are used to tune the model specific parameters. Main parameters include diffusion and reaction constants of the different elements and binaries/ternaries, as well as the sticking factor at the surface for the uptake of selenium from the vapor phase. Using these parameters the (intermediate) reactions can be derived and fitted to the data from experiments and literature studies.

First the process temperature profile is calculated as function of time, followed by the calculating the uptake of selenium from the vapor phase. Additionally, the diffusion and reactions are modeled, using Fick's second law, error functions and multiple reflections at the solid interfaces. Based on phase diagrams the reaction kinetics of the most important reaction products are derived and are included into the model.

For reasons of memory limitations, the time and spatial mesh need to be relative coarse. For the spatial mesh this requires adaptive meshing, in order to adapt to small spatial variations and to mimic the overall and the specific layer growth well at small time changes.

Conclusions

The development of the model is still in progress, but the first results show good approximation of the selenium uptake and the formation of the first binaries and ternaries, such as $\text{Cu}_{11}\text{In}_9$, Cu_{2-x}Se , In_4Se_3 and InSe . This can be expanded easily to other intermediates, CIS, CGS and CIGS. However, further parameter fitting is required to mimic the experimental data better.

3:00pm TF+AS+EM-TuA3 TiSiO Thin Films Deposited by Plasma Enhanced Chemical Vapor Deposition for Optical and Electrical Applications, Antoine Goullet, S. Elisabeth, D. Li, M. Carette, A. Granier, IMN, France

INVITED

TiO_2 thin films are good candidates for the development of passive optical or electrical integrated devices. They exhibit high optical refractive index ($1.8 < n < 2.7$ at 633 nm) in combination with high transparency in the visible range and high dielectric constant ($50 < k < 100$). They are compatible with semiconductor technologies and can be synthesized at low temperature by plasma processes such as plasma enhanced chemical vapor deposition (PECVD). This technique is very attractive to tune film composition and properties such as film refractive index. PECVD is also known for its ability to prepare good quality amorphous or partially crystalline films at low temperature.

Titanium-silicon mixed oxide (TiSiO) materials can overcome some of the limitations given by TiO_2 material, e.g. columnar morphology and relatively low band gap energy.

In this study, TiSiO thin films are prepared without any intentional heating in low pressure inductively coupled discharges from titanium tetraisopropoxide (TTIP- $\text{Ti}(\text{OC}_3\text{H}_7)_4$) and hexamethyldisiloxane (HMDSO - $\text{SiO}_2(\text{CH}_3)_6$) precursors mixed with oxygen.

Structure and chemical composition of the films are investigated by X-ray diffraction (XRD) and X-ray photoelectron spectroscopy (XPS). Information about film chemical bonds is also obtained from Fourier transform infrared spectroscopy (FTIR). Film morphology is characterized by scanning electron microscopy (SEM) and atomic force microscopy (AFM). Optical properties are mainly investigated by spectroscopic UV-Visible ellipsometry.

Capacitance-voltage ($C-V$) and current-voltage ($I-V$) measurements are performed by using MIS capacitors for evaluation of the mixed oxide film electrical performances.

TiO_2 thin films characteristics are investigated as a function of the plasma ion energy in the 25 – 175 eV range. Increasing the ion energy leads to more homogeneous and organized films with the transformation from anatase to rutile. To account for the columnar morphology of TiO_2 films, a gradient optical layer model was developed. The thin layer dispersion functions were described satisfactorily with the Tauc-Lorentz dispersion law.

TiSiO have been deposited by varying the HMDSO flow rate in the plasma operated in continuous or pulsed mode.

The thin films can be described as a mixture of silicon and titanium oxide at the atomic scale rather than two separate SiO_2 and TiO_2 phases. These mixed oxide layers are basically amorphous and exhibit good morphological properties provided the titanium content is lower than the silicon one.

On the whole these TiSiO layers offer a good compromise in terms of morphological, optical and electrical properties.

4:20pm TF+AS+EM-TuA7 Kinetically-Limited Lattice Relaxation in Linearly- and Non-Linearly- Compositionally-Graded $\text{In}_x\text{Ga}_{1-x}\text{As}/\text{GaAs}$ (001) Metamorphic Heterostructures, Tedi Kujofsa, J.E. Ayers, University of Connecticut

Metamorphic buffer layers allow tremendous flexibility to design novel $\text{InGaAs}/\text{GaAs}$ semiconductor heterostructures for application in various microelectronic and optical devices. However, device fabrication, reliability and performance are limited by dislocation defects associated with the growth of highly mismatched systems such as InGaAs on GaAs substrate. Thus, understanding kinetically-limited lattice relaxation and development of a plastic flow model applicable to multilayered and compositionally graded heterostructure is desirable to provide guidance in designing $\text{InGaAs}/\text{GaAs}$ devices. Previously, we reported a plastic flow model for $\text{ZnS}_y\text{Se}_{1-y}/\text{GaAs}$ (001) heterostructures which predicts the non-equilibrium strain relaxation as well as misfit dislocation and threading dislocation densities. Here, we have extended our model to $\text{In}_x\text{Ga}_{1-x}\text{As}/\text{GaAs}$ (001) metamorphic buffer layers with arbitrary compositional grading profile. In addition, we have investigated the evolution of the kinetically limited in-plane strain of $\text{In}_x\text{Ga}_{1-x}\text{As}/\text{GaAs}$ (001) heterostructures with an emphasis on grading schemes employing a step, linear-, S- and power-law- lattice mismatch compositional profile. For each structure, we have studied the thickness and grading coefficient dependence on the average and surface kinetically-limited in-plane strain. In addition, we show that the use of compositionally graded buffer layers enables the design of $\text{In}_x\text{Ga}_{1-x}\text{As}/\text{GaAs}$ (001) heterostructures with high surface strain values which enhance the sweeping of threading defects and therefore yielding device structures with minimal defect.

5:00pm TF+AS+EM-TuA9 Superconducting Properties of NbN and NbTiN Thin Films, Matthew Burton, M.R. Beebe, R.A. Lukaszew, D. Beringer, College of William and Mary

Thin films of NbN and NbTiN are promising materials currently researched for improvements in superconducting radio frequency (SRF) technology and applications. At present, bulk niobium SRF accelerating cavities suffer from a fundamental upper limit in maximally sustained accelerating gradients; however, a scheme involving multi-layered superstructures consisting of superconducting-insulating-superconducting (SIS) layers has been proposed to overcome this fundamental material limit of 50 MV/m [1]. The SIS multi-layer paradigm is reliant upon implementing a thin shielding material with a suitably high H_{c1} which may prevent early field penetration in a bulk material layer and consequently delay the high field breakdown. It has been predicted that for thin superconducting films — thickness less than the London penetration depth (~ 200 nm in the case of NbN) — the lower critical field H_{c1} will be enhanced with decreasing thickness. Thus, NbN thin films with a high H_{c1} value are possible candidates for such SIS structures. We note though that since the intrinsic resistivity of NbN is rather large, efforts are also devoted to NbTiN which has similar superconducting properties but much lower intrinsic resistivity which is preferable for this application. Here we present our study on the structure and superconducting properties of a series of NbN and NbTiN thin films and correlate the effects of film microstructure and surface morphology on relevant superconducting properties such as the critical temperature, T_c , the lower critical field, H_{c1} , and the residual resistance ratio.

[1] A. Gurevich, Appl. Phys. Lett., 88, 012511 (2006).

5:40pm TF+AS+EM-TuA11 High-Throughput Assessment of the Composition Dependence of Initial Passivating- Al_2O_3 -Scale Establishment in $\text{Al}_x\text{Fe}_y\text{Ni}_{1-x-y}$ Alloy Thin Films, Matthew Payne, J. Miller, A.J. Gellman, Carnegie Mellon University, DOE - National Energy Technology Laboratory

AlFeNi -containing alloys capable of forming passivating Al_2O_3 scales are designed for high-temperature structural applications requiring robust oxidation resistance. Mechanical considerations typically dictate that Al content be minimized, but a critical concentration, N_{Al}^* , is minimally required to promote the initial establishment of a continuous Al_2O_3 layer. Current understanding of how N_{Al}^* evolves across multi-component composition spaces is limited, being based largely on experiments that are constrained by the need for meticulous preparation and characterization of large numbers of single-composition samples. The study of properties across alloy composition space can be greatly accelerated using composition spread alloy films (CSAFs), materials libraries comprised of continuous lateral composition gradients. Properly designed CSAFs can contain every possible composition of a ternary alloy. In this work, ~ 120 nm-thick $\text{Al}_x\text{Fe}_y\text{Ni}_{1-x-y}$ CSAFs spanning the entire ternary range ($x = 0 \rightarrow 1$, $y = 0 \rightarrow [1-x]$) over an area of ~ 1 cm^2 were prepared. A variety of spatially resolved techniques were developed for effective, high-throughput characterization of early oxidation behaviors in the CSAFs. Energy-dispersive X-ray spectroscopy was used to measure changes in CSAF oxygen content as a function of both alloy composition and oxidation time. Raman spectroscopy allowed specific oxide phases formed in different

regions of the composition space to be identified. X-ray photoemission depth profiling was performed at select locations of interest to determine composition and chemical state in CSAF cross-sections. These methods were used to study oxidation across $\text{Al}_x\text{Fe}_y\text{Ni}_{1-x-y}$ composition space in both dry and moist air at 700 K, and have enabled the identification of continuous boundaries separating regions of phenomenologically unique oxidation behaviors, including the $N_{\text{Al}}^*(x,y)$ boundary for each environment. The results enhance fundamental understanding of early-stage $\text{Al}_x\text{Fe}_y\text{Ni}_{1-x-y}$ oxidation and can contribute to the accelerated design of next-generation alloys.

6:00pm **TF+AS+EM-TuA12 Structural, Electrical, and Optical Characterization of Impurity-Dependent, Ultra-Low-Dislocation-Density Ge Epitaxially Grown on Si and Characterization of MOSFETs Fabricated on Ge-on-Si, Swapnadip Ghosh, S.M. Han, University of New Mexico**

Building on a simple two-step MBE growth technique, we have investigated possible dislocation locking mechanisms by dopant impurities, coupled with artificially introduced oxygen (O). In the case of n-type Ge grown on Si, our materials characterization indicates that the dislocation density (DD) can reach the $\sim 10^5 \text{ cm}^{-2}$ level, compared to p-type and undoped Ge on Si (GoS). We note that our Ge film covers the entire underlying Si substrate at the wafer scale without mesas or limited-area growth. In this presentation, we will focus on the use of n-type impurity (phosphorus) diffusion from the Si substrate and the introduction of O at the Ge-Si interface. The O is introduced by growing a thin chemical SiO_2 layer on top of the Si substrate before Ge epitaxy begins. Z-contrast cross-sectional TEM images suggest the presence of O precipitates in n-type Ge, whereas these precipitates appear absent in p-type Ge. These O precipitates are known to lock the dislocations. Supporting the argument of precipitate formation, the TEM shows Moiré fringes due to various phase boundaries that exist at the precipitate/Ge-crystal interface. We speculate that the formation of phosphorus (P) segregation resulting from slow diffusion of P through precipitates at the precipitate/Ge-crystal interface facilitates dislocation locking. Impurity segregation in turn suppress O concentration in n-type Ge leading to the reduced DD that appears on the top surface of n-Ge compared to p-Ge film. The O concentrations (10^{17} to 10^{18} cm^{-3}) in the n- and p-type GoS films are measured using secondary ionization mass spectroscopy. We have then compared the structural and electrical characteristics of n-type Ge films with its p-type counterparts. In n-type Ge, the DD decreases from $\sim 10^9 \text{ cm}^{-2}$ near the Ge-Si interface to $\sim 10^5 \text{ cm}^{-2}$ at the film surface. In contrast, we observe $5 \times 10^7 \text{ cm}^{-2}$ DD at the film surface in p-type Ge. The full width at half-maximum for our n-type Ge(004) XRD peak is 100 arcsec, compared to 230 arcsec of p-type Ge. As a stringent test of the dislocation reduction, we have also fabricated and characterized high-carrier-mobility MOSFETs on GoS substrates. We also report p- and n-MOSFETs with μ_{eff} of 401 and $940 \text{ cm}^2/\text{V}\cdot\text{s}$ and a subthreshold slope of 100 and 200 mV/decade, respectively. These effective mobilities show an exceptional 82 and 30% improvement over that of conventional Si channel MOSFETs. We also investigate the optical quality of ultra-low DD GoS film by measuring photoluminescence (PL). n-type Ge PL main peak shows pronounced tensile-strain ($\times 0.8\%$) than that of p-type, which is an indicator of direct bandgap shrinking at the Γ band-edge.

Tuesday Evening Poster Sessions

Electronic Materials and Processing

Room: Hall D - Session EM-TuP

Electronic Materials and Processing Poster Session

EM-TuP1 Growth of AlN Nanowires on Sapphire and Silicon using the Pulsed Electron Beam Deposition (PED) Process. *N. Arefin, P. Larson, University of Oklahoma, Matthew Kane, Texas A&M University, M.B. Johnson, P.J. McCann, University of Oklahoma*

This poster will describe results recently obtained with pulsed electron beam deposition (PED) of AlN on sapphire and silicon substrates. The PED technique is potentially useful for growth of III-nitrides at lower substrate temperatures, a capability that can allow use of new buffer layer materials, integration of chemically dissimilar materials, and help solve wafer bowing issues. In addition, PED has the advantage to deposit materials that are transparent to the Kr-F excimer lasers used in pulsed laser deposition and would thus be suitable for ultra-wide bandgap materials. Systematic studies are needed to explore the growth regimes for various materials as a function of processing conditions and sample preparation techniques. AlN was deposited on sapphire and silicon (111) at a substrate temperature of 500°C and 550°C, respectively, in a UHP N₂ (15 mTorr) environment (without any surface pre-treatment, i.e., pre-nitridation). A high power electron gun pulse was used to ablate the AlN target (1" dia. x 0.250" thick, 99.8% pure) stationed at 5 cm vertical distance from the substrate. The electron pulses were generated at 15KV, 0.3 J/pulse at 1 Hz for one hour. No post growth processing was performed following the growth. Scanning electron microscopy (SEM), Electron back scattered diffraction (EBSD), and X-ray diffraction (XRD), and various optical characterization techniques were performed on the as-grown material. SEM imaging confirms hexagonal faceted high aspect ratio AlN nanowires on both sapphire and silicon substrates. The nanowire lengths ranged from 10-100 μm with average diameter of 2.5 μm on the sapphire substrate, while on the silicon (111) substrate the nanowire dimensions ranged from 200 nm-10 μm in length, and the average diameter was 0.5 μm. EBSD scan over the nanowires identified the structures as c-plane oriented AlN. XRD θ-2θ scans from 20 = 30° to 2θ = 50° showed only one peak other than those from the sapphire substrate, at 2θ = 37.56°. We had insignificant contribution from the AlN NWs in the XRD scan due to limited quantity of the NWs on the sample. The obtained peak at 2θ = 37.56° represents Al (111) suggests that during the initial growth phases Al was accumulated as metal on the substrate which acted as a precursor in initiating the nanowire growth afterwards. This finding was also verified with EBSD scans, as it also detected presence of Al crystallites on the sample surface as well as highly c-axis oriented AlN nanowires.

EM-TuP2 Passivation of InSb(100) with 1-Eicosanethiol Self-Assembled Monolayers. *Y.D. Contreras, Pablo Mancheno, A.J. Muscat, University of Arizona*

III-V semiconductors have the potential to replace Si to make faster computer processors due to their higher charge mobility. In particular, the bandgap of InSb (0.17 eV, the smallest of the III-V group) makes this semiconductor an absorber and emitter in the infrared region, suitable for infrared detectors. III-V semiconductors oxidize rapidly when exposed to air after etching, and have complex oxide layers. It has been shown that sulfur-containing molecules can passivate and enhance the electrical properties of III-V semiconductors. In this study, InSb(100) was chemically passivated for 3 min after native oxide etching by liquid-phase deposition of an alkanethiol self-assembled monolayer (SAM) on the surface of the semiconductor. The SAM contained 1-eicosanethiol (ET, 20 C atoms). The passivated surface was characterized with atomic force microscopy (AFM), spectroscopic ellipsometry, X-ray photoelectron spectroscopy (XPS) and FTIR. Tapping Mode AFM images of InSb native oxide showed that the starting surface was rough (RMS 2.25 nm), which could limit the formation of a dense and ordered alkanethiol SAM. The thickness of the overlayer (both InSb oxides and ET) measured by spectroscopic ellipsometry was 35 Å immediately after passivation. XPS analysis showed that the passivation process with a 1.0 M HCl last step and 20 h passivation yielded no detectable oxygen in the Auger region for 3 min of air exposure, but the surface was completely oxidized after 4 h of exposure. As a comparison, passivation of GaAs(100) (bandgap of 1.4 eV) with an ET SAM maintained oxygen below detection limits after 30 min, but the surface still oxidized after 4 h. When the passivation of InSb(100) was performed with different preparation conditions (HCl and thiol concentrations, solvent type, and deposition time), the largest bulk InSb to Sb₂O₃ 3d + O 1s XPS peak area ratio (minimum Sb oxidation) was achieved by using 1.0 M HCl in the oxide etching steps, 0.1 mM ET in ethanol and long thiol deposition times

(~20 h). FTIR analysis of an InSb sample passivated for 20 h in 0.1 mM ET showed the presence of peaks characteristic of methyl and methylene stretches at 2963 cm⁻¹, 2925 cm⁻¹ and 2847 cm⁻¹. The position and width of these peaks indicates the presence of a partially ordered alkanethiol layer. These results demonstrate that physically blocking O₂ diffusion with alkyl chains is possible on the surface of a narrow band-gap semiconductor, even on a surface with a relatively high average roughness.

EM-TuP3 Electric Measurements of RF SOI MOSFET using CMOS Technology. *William Mariano, UNICAMP, Brazil*

The aims of this work is the development of a 2 μm SOI CMOS process. The manufacturing of the devices was carried out using processes based on SOI CMOS technology. The characteristics of the fabricated devices in a SOI Silicon are compared in order to obtain its parameters, as well as with the results published in the literature. Besides is to present the electric measurements of n and p channel RF MOSFET fabricated on Silicon substrates of type SOI – Silicon On Insulator. The different structures of the devices had been fabricated and their physical and electrical characterizations performed. In addition, there will be a sequence of the process steps involved in building the CMOS chips. The devices are part of an academic chip, which will be used in disciplines of engineering courses and in research activities of the Microelectronics area.

EM-TuP5 Fabrication of Inverse Opal Structures by Langmuir-Blodgett Silica Microsphere Assembly and Germanium Back Filling by Molecular Beam Epitaxy. *M. Zhou, Sarun Atiganyanun, S. Ghosh, J. Chavez, S.E. Han, S.M. Han, University of New Mexico*

Photonic crystals give rise to a variety of applications such as absorbers, waveguides, and light filters. One of the common examples is an inverse opal structure made of semiconductors. This structure, unlike its counterpart opal structure, exhibits a complete photonic band gap. In this study, we investigate a low-cost and scalable fabrication of an inverse opal structure via self-assembly of colloidal silica microspheres and Ge molecular beam epitaxial (MBE) back filling, followed by buffered HF etching. First, silica microspheres are functionalized with allyltrimethoxysilane and dispersed in chloroform. Langmuir-Blodgett (LB) method is then used to self-assemble silica microspheres with a diameter of ~800 nm onto Si(100) substrates. By optimizing the pulling speed of the substrate and surface pressure within the trough, a hexagonally closed-packed opal structure is achieved. Scanning electron microscopy (SEM) images have shown domain size of the monolayer assembly to be approximately 10 μm by 10 μm. By repeating LB coating for *n* times, an *n*-multilayer assembly is formed, creating an opal template structure. After assembling silica microspheres on Si substrates, Ge MBE is used to back fill the voids between microspheres. The effusion cell temperature ranges from 1150 to 1000°C, which corresponds to the Ge flux of 6.44*10¹⁴ to 1.83*10¹³ Ge atoms/cm²-sec, respectively. When the substrate temperature is held constant at 580°C, the SEM characterization shows that the low Ge flux at 1000°C reduces random nucleation on top of the microspheres by approximately one order of magnitude compared to the high Ge flux at 1150°C. Following the backfill, the silica microspheres are removed by immersing the substrate in a buffered HF solution, creating a single-crystalline Ge inverse opal structure. In this presentation, we will further discuss the optimization of Ge flux and substrate temperature, examination of crystal quality of Ge by X-ray diffraction and Ge/Si interface by transmission electron microscopy, and the structure's optical properties with Fourier transform infrared spectroscopy.

EM-TuP7 Formation of AlN Thin Films by Direct Nitridation of Aluminum Thin Films and Their Visible Photoluminescence Property. *Shun Kajihara, M. Hamasaki, H. Katsumata, Meiji University, Japan*

AlN has the widest band-gap of 6.3 eV among the direct band-gap semiconductors and is therefore suitable for shorter wavelength light emitting devices and power devices. AlN thin films have been prepared by MOCVD and reactive sputtering with the deposition rate of about 0.1-10 nm/min. Meanwhile, AlN powders and AlN bulks have been prepared by reducing nitridation and direct nitridation methods. In this study, AlN thin films were formed by direct nitridation (DN) of Al thin films and their properties were compared with those formed by reactive sputtering (RS). For photoluminescence (PL) measurements, doping of Eu into AlN was performed to observe visible PL from Eu ions in AlN films.

Al thin films with a thickness of 150 nm were deposited on c-axis sapphire substrates by radio frequency (RF) magnetron sputtering using an Al target (φ4 inch, Koujundokagaku, Japan) in constant Ar (8.0 sccm) flow. Co-sputtering of Eu₂O₃ and Al was performed by placing 2 pieces of Eu₂O₃ tablets on the Al target for PL measurements. The films were subsequently annealed at 900°C for 15 sec in N₂ or NH₃ gas using a conventional electric quartz tube furnace, which can form AlN films with a theoretical thickness

of 300 nm. On the other hand, AlN thin films with a thickness of 500-700 nm were deposited on c-axis sapphire substrates by RS using an Al target in constant N₂ (5.6 sccm) and Ar (2.4 sccm) flow. Co-doping of Eu₂O₃ and Si during the formation of AlN films by RS was performed by placing several pieces of Eu₂O₃ and Si tablets on the Al target. Doping of Si was to observe the blue luminescence from Eu²⁺ in AlN by replacing Al atoms by Si atoms in AlN, which can prevent the formation of Eu³⁺. RF sputtering power was set at 200 W through this study. The films were subsequently annealed at 900°C for 30 min in N₂ with rapid thermal annealing system. Growth time of AlN films with a thickness of 300 nm by RS was approximately 30 times longer than that by DN. These samples were analyzed by X-ray diffraction (XRD), PL, optical transmittance and energy dispersive X-ray spectrometry. The wurtzite AlN (002) XRD peak appeared from the samples formed by DN. PL spectra of Eu₂O₃ doped AlN films formed by DN exhibited broad emissions at 400 nm and 530 nm, which were assigned to oxygen defect and Eu²⁺, respectively. The optical direct band-gap of AlN films doped with Eu₂O₃ was calculated to be 5.85 eV from their optical transmission spectra. These results were also obtained from the samples formed by RS. It is interesting to note that the PL spectral features of Eu₂O₃ doped AlN films formed by DN resembles those of Eu₂O₃ and Si co-doped AlN films formed by RS.

EM-TuP8 Improvement of Effective Work Function and Transmittance of ITO/Ultra-Thin In_{1-x}Ru_xO_y Stack Structure, Ippei Yamamoto, Shibaura Institute of Technology, Japan, *T. Kattareeya,* Chulalongkorn University, Thailand, *T. Chikyo, K. Tsukagoshi,* NIMS, Japan, *T. Ohishi,* Shibaura Institute of Technology, Japan, *T. Nabatame,* NIMS, Japan

The indium tin oxide (ITO), which is one of most attractive anode materials in organic electroluminescent, has a big issue of low work function (WF) of 4.7 eV. Several approaches have been proposed to improve the WF of ITO and/or develop new anode materials. We pay attention to RuO₂ material because of high WF (> 5 eV) and low resistivity. In this paper, we systematically investigate the characteristics of the In_{1-x}Ru_xO_y films. We also compare characteristics of ITO/ultra-thin RuO₂ (3 nm) and ITO/ultra-thin In_{1-x}Ru_xO_y (3 nm) stack structures.

The In_{1-x}Ru_xO_y films were prepared under Ar/O₂ (25 vol. %) by co-sputtering using Ru and In₂O₃ targets. The Ru composition ratio of the In_{1-x}Ru_xO_y films was varied from 0 to 1.0 by changing each sputtering power. A 150-nm-thick ITO film was deposited on RuO₂ (3 nm) or In_{1-x}Ru_xO_y (3 nm) film to fabricate ITO/RuO₂ or ITO/In_{1-x}Ru_xO_y stack structure by RF sputtering using an In_{0.9}Sn_{0.1}Ox target, respectively. The SiO₂ metal-oxide-semiconductor (MOS) capacitors with ITO/RuO₂ or ITO/In_{1-x}Ru_xO_y gate electrode were fabricated to obtain effective work function (EWF).

The In_{1-x}Ru_xO_y film consists of amorphous structure in x range from 0.3 to 0.83. The In_{0.38}Ru_{0.62}O_y film shows a lowest specific resistivity and smooth surface of small RMS (0.69 nm) value using atomic force microscopy. The maximum transmittance increased more than 80 % by reducing thickness less than 3 nm.

The ITO/RuO₂ (3 nm) stack structure shows a high EWF value (5.3 eV) and a slightly low transmittance (77 % in 600 nm) because the RuO₂ film has tetragonal crystal structure. On the other hand, the transmittance (80 % in 600 nm) of ITO/In_{0.38}Ru_{0.62}O_y (3 nm) is superior to that of ITO/RuO₂ stack structure. Furthermore, the ITO/In_{0.38}Ru_{0.62}O_y stack structure shows a high EWF (5.3 eV) and a low specific resistivity (9.2 × 10⁻⁵ Ω·cm). This suggests that the interface between ITO and In_{0.38}Ru_{0.62}O_y is kept to be clear because of same dominant element of indium and amorphous structure of In_{0.38}Ru_{0.62}O_y film.

EM-TuP9 Solid Phase Growth of Mg₂Si Thin Films on Poly-Si/Glass Substrates Prepared by Aluminum Induced Crystallization, Satoru Kawaguchi, A. Kusunoki, S. Yoshida, H. Katsumata, Meiji University, Japan

Aluminum induced crystallization (AIC) is a method of crystallizing amorphous Si (a-Si) by the interaction of Al and Si during the heat treatment. Polycrystalline Si (poly-Si) can be formed at lower temperature by AIC compared to solid phase growth techniques, since AIC can crystallize amorphous Si below the eutectic temperature of Al and Si at 577 °C. Poly-Si formed by AIC usually exhibits p-type conductivity with a high carrier concentration due to existence of residual Al. On the other hand, it has been difficult to form n-type poly-Si by metal induced crystallization using n-type doping materials as Sb. The purpose of this study is to fabricate a pn junction for light-receiving device consisting of AIC p-type poly-Si and n-type Mg₂Si. Mg₂Si (Eg: 0.6-0.7 eV) was selected as a candidate of n-type layers because Al atoms are considered to act as an n-type dopant in Mg₂Si.

The substrates used in this study were glass or p-Si (100) substrates. Al films with a thickness of 500 nm were deposited on the glass substrate by resistive evaporation. After deposition, they were exposed in the air for

more than 2 hours to form native Al oxide films. Subsequently, a-Si films with a thickness of 500 nm were deposited on the Al films by radio frequency (RF) magnetron sputtering. These samples were annealed at 450-500 °C for 3-12 hours in N₂ for AIC. After the AIC, Al top layer was removed with diluted HCl. Then, Mg films with a thickness of 100-300 nm were deposited either on AIC poly-Si films or p-type Si (100) substrates by resistive evaporation. These samples were annealed at 400 °C for 5 hours in Ar for solid phase growth of Mg₂Si.

Optical microscope images of surface of AIC poly-Si showed that the grain size of poly-Si increased with increasing AIC temperature. All sample showed Si (111) XRD peaks at 2θ = 28 degrees and Si Raman peaks at 520 cm⁻¹, which can be an evidence of formation of (111) preferentially oriented poly-Si by AIC. We investigated the correlation between grain size of poly-Si observed with optical microscope and FWHM of Raman peak at 520 cm⁻¹. As a result, it was found that the AIC at higher temperature decreased grain size and increased FWHM, while the AIC for longer time increased grain size and decreased FWHM. Optical band-gap of AIC poly-Si formed at 500 °C for 12 hours was determined to be 1.1 eV from optical transmittance spectra. Hall effect measurements of AIC poly-Si showed p-type conductivity with a hole concentration of 4.0×10¹⁷ cm⁻³ and a hole mobility value of 1.56 cm² · V⁻¹ · s⁻¹. Mg₂Si films formed both on AIC poly-Si/glass and p-Si (100) substrates showed Raman peaks at around 256 cm⁻¹, which originate from Mg₂Si.

EM-TuP11 The Effect of Vacuum-Ultraviolet Irradiation on Copper Diffusion into Low-k Dielectrics, Xiangyu Guo, University of Wisconsin-Madison, *Y. Nishi,* Stanford University, *J.L. Shohet,* University of Wisconsin-Madison

Cu diffusion into low-k dielectrics can cause serious reliability issues in on-chip interconnect systems. A considerable attention in the research community had been devoted to understanding the effect of Cu diffusion in the electrical breakdown properties of low-k dielectrics, while Cu-induced diffusion from vacuum-ultraviolet (VUV) irradiated low-k dielectrics has received only minimal attention. This work is aimed at determining the nature of copper interactions with VUV irradiated low-k dielectrics in integrated circuits. The effects of VUV irradiation on the Cu diffusion into low-k organosilicate glass (SiCOH) dielectric films were investigated. X-ray photoelectron spectroscopy depth profiling was used to assess Cu diffusion in the dielectric in the presence of a bias-temperature stress. After 12-eV photon irradiation under bias-temperature stressing at 3.5 MV/cm and 225°C respectively, Cu penetrates farther into the SiCOH, compared to that of an unirradiated sample. Further examination of the VUV photon-exposed SiCOH shows that the Cu distribution profile in the dielectric after bias-temperature stressing is different from the profile after the same temperature annealing but without electrical bias. In addition, no such enhanced phenomenon was observed in unexposed dielectrics, suggesting that Cu ion drift can occur in VUV-irradiated SiCOH. The implication of these findings on time-dependent dielectric breakdown in Cu/VUV irradiated low-k dielectrics is discussed.

This work has been supported by the Semiconductor Research Corporation under Contract No. 2008-KJ-1871 and the National Science Foundation under Grant No. CBET-1066231.

EM-TuP12 Electronic and Vibrational Structures in Photoemission Spectra for Dibenzopentacene on Au(111), Masaru Aoki, A. Suzuki, H. Sato, The University of Tokyo, Japan, *K. Shudo,* Yokohama National University, Japan, *S. Masuda,* The University of Tokyo, Japan

Electronic properties of dibenzopentacene (DBP) thin films on Au(111) were examined by ultraviolet photoemission spectroscopy (UPS), metastable atom electron spectroscopy (MAES),^{1,2} and first-principles DFT calculation. The UPS and MAES spectra for DBP multilayer show four bands near the Fermi level (E_F) due to π-derived 8b_g(HOMO), 7b_g+7a_u, 6a_u, and 6b_g states, in agreement with an earlier study.³ The corresponding bands emerge in the monolayer region, but the bandwidth of the HOMO band is much narrower than that in the multilayer. Furthermore, the HOMO band consists of three peaks with interval of ~160 meV, which is attributed to the vibrational structure of the CC stretching modes of DBP⁺ ion produced by photoionization. A similar vibronic coupling has been reported for organic molecules on inert surfaces such as phthalocyanine on graphite⁴ and pentacene on graphite,⁵ but to our knowledge there is no report in the organic-metal system. In the conference, we will introduce the weak interactions between DBP and Au(111) based on our DFT calculation, temperature-dependent (50-273 K) vibronic structure, and lifetime of photohole in organic-metal system.

References

- [1] Y. Harada, S. Masuda, H. Ozaki, *Chem. Rev.* **97**, 1897 (1997).
- [2] S. Masuda, *Appl. Surf. Sci.* **256**, 4054 (2010).

[3] B. Mahns, F. Roth, A. König, M. Grobosch, M. Knupfer, T. Hahn, *Phys. Rev. B* **86**, 035209 (2012).

[4] S. Kera, H. Yamane, I. Sakuragi, K. K. Okudaira, N. Ueno, *Chem. Phys. Lett.* **364**, 93 (2002).

[5] H. Yamane, S. Nagamatsu, H. Fukagawa, S. Kera, R. Friedlein, K. K. Okudaira, N. Ueno, *Phys. Rev. B* **72**, 153412 (2005).

EM-TuP13 Evolution of Gap States in Potassium-Doped Dibenzopentacene, *Hirofumi Sato, S. Mihara, M. Aoki*, The University of Tokyo, Japan, *K. Shudo*, Yokohama National University, Japan, *K. Akimoto*, University of Tsukuba, Japan, *S. Masuda*, The University of Tokyo, Japan

Electronic properties of potassium-doped dibenzopentacene (DBP) thin films on Au(111) were studied by ultraviolet photoemission spectroscopy (UPS), metastable atom electron spectroscopy (MAES),^{1,2} and first-principles DFT calculation. The UPS and MAES spectra for K_xDBP (0 ≤ x ≤ 3.5) films show three types of gap state (GS1~GS3) in the HOMO-LUMO gap of pristine DBP. The GS1 and GS2 emerge at the initial stage of deposition and are attributed to the modified HOMO state and partially-filled LUMO state, respectively. The threshold of electron emission for K₁DBP is located ~0.1 eV below the Fermi level (E_F) with no metallic feature, suggesting that K₁DBP is a Mott-Hubbard insulator. At the formation of K₂DBP, the GS1 and GS2 saturate in intensity and shift to the higher binding energy. This indicates that the native LUMO state is fully occupied by electron transfer, resulting in a wide-gap insulator. Upon further deposition, the GS3 appears near E_F and is attributed to partial electron filling in the LUMO+1~LUMO+3 states. For K_{3.5}DBP, the leading edge of GS3 is located ~0.1 eV below E_F without a metallic feature. Therefore, the heavily doped species transfers to a Mott-Hubbard insulator again. The GS3 plays a key role in superconductivity of K₃DBP at low temperature.³

The interaction of alkaline-metal atoms with aromatic hydrocarbons could be classified into three categories, i.e., weak interaction,⁴ simple charge transfer,⁵ and heavy mixing of mutual wave functions. The K-doped DBP belongs to third category, and the detail will be discussed in the conference.

References

[1] Y. Harada, S. Masuda, H. Ozaki, *Chem. Rev.* **97**, 1897 (1997).

[2] S. Masuda, *Appl. Surf. Sci.* **256**, 4054 (2010).

[3] M. Xue, T. Cao, D. Wang, Y. Wu, H. Yan X. Dong, J. He, F. Li, G. F. Chen, *Sci. Rep.* **2**, 1 (2012).

[4] M. Sogo, Y. Sakamoto, M. Aoki, S. Masuda, *J. Chem. Phys.* **133**, 134704 (2010).

[5] F. Bussolotti, S. Kera, N. Ueno, *Phys. Rev. B* **86**, 155120 (2012).

EM-TuP15 In Situ Metrology during GaN and InGaN Growth by Remote Plasma-assisted MOCVD, *Daniel Seidltz, R.L. Samaraweera*, Georgia State University, *I.T. Ferguson*, University of North Carolina at Charlotte, *A. Hoffman*, Technical University Berlin, Germany, *N. Dietz*, Georgia State University

Using real-time optical diagnostics during the GaN and InGaN growth progress in a remote plasma-assisted Metal Organic Chemical Vapor Deposition (RPA-MOCVD) reactor provides details in the precursors' decomposition processes and epitaxial layer growth mechanisms. Growth process control provisions in the RPA-MOCVD reactor enable a temporal and spatial controlled injection of metal organics (MO) as well as ammonia (N₂) plasma activated hydride precursors such as hydrogen (H₂) or ammonia (NH₃). Remote activated hydride precursor fragments (e.g. N*/NH*/NH₂*) are generated using a hollow cathode driven by a tunable radio frequency (rf) power source up to 600W. The radicals are directed to the substrate surface by the remote plasma afterglow regime. Plasma Emission Spectroscopy (PES) and UV-Absorption spectroscopy (UV-AS) are used to identify the active species in the plasma and determine their concentrations in dependence of the injected precursors N₂, H₂ and NH₃. Plasma emission spectroscopy during the growth run allows also a time dependent recording of the quantitative behavior of the reactive particles inside the plasma. In addition, real-time measurements and analysis of reflection spectroscopy at normal incidence on the growth surface contribute sub-monolayer growth rates for GaN and InGaN. In this report we will present and discuss results of in-situ Plasma emission spectroscopy, UV-Absorption spectroscopy and Normal incidence reflection spectroscopy (NI-RS). The combination of these real-time characterization methods provides qualitative and quantitative identification of active species in the gas phase and determination of growth rates at the growth surface. The in-situ obtained growth rates are compared with ex-situ thickness measurements (e.g. Transmission and reflection spectroscopy) and results of layer structural characterization methods (Raman spectroscopy, PL). These studies will aid our understanding of how process growth parameter such as substrate

temperature, plasma-assisted precursor generation/defragmentation, or the quantity of active species concentrations influence the growth and properties of binary and ternary group III-nitride alloys.

EM-TuP16 AFM Study on the Structural Properties of Gold Thin Films by RF Magnetron Sputtering, *Moniruzzaman Syed*, Lemoyne-Owen College, *C. Glaser, M. Schell, I. Senevirathne*, Lock Haven University

Gold (Au) thin films offer a wide range of applications in many fields such as memory storage, energy harvesting and storage, nanosensors, optics, biosensing devices and catalysis. Au film is paying more attention in many critical applications as it is highly conductive and is not easily oxidized. Therefore, it is necessary to understand the growth mechanism of film on various substrates. The structural properties of gold thin films are also playing very important role on the film quality which may affect optical properties as well as the sensing capabilities of the devices. In this study, Gold (Au) thin films were deposited on both glass and Si (100) substrates at room temperature (RT) with Ar gas atmosphere as a function of deposition time. The structural properties and surface morphology of Au thin film has been studied using Atomic Force Microscope (AFM). The deposition rate was found to be increased with increasing time of those films deposited on glass substrate. The effect of annealing temperature on the structural properties of Au film deposited on various substrates will also be discussed.

EM-TuP17 Influence of Plasma-Activated Nitrogen Species in MOCVD Grown GaN/GaN Epilayers, *Rasanga Samaraweera, D. Seidltz*, Georgia State University, *B. Hussain*, University of North Carolina at Charlotte, *M.K.I. Senevirathna*, Georgia State University, *I.T. Ferguson*, University of North Carolina at Charlotte, *N. Dietz*, Georgia State University

This contribution will present results on the influence of remote plasma activated nitrogen containing precursor species on the physical properties of GaN and ternary GaInN layers grown by plasma-assisted metal organic chemical vapor deposition (PA-MOCVD). A hollow cathode rf-plasma source (13.65 MHz, 50-500 W) was used to generate reactive nitrogen plasma species in which hydrogen (H₂) and ammonia (NH₃) are added downstreams to tailor the reactive nitrogen species (N*/NH* etc.) interacting at the growth sites.

Growth parameters such as: H₂, N₂, NH₃ flows, metalorganic (MO) flows, plasma power, reactor pressure, and/or substrate temperature have been varied to assess their influence on the physical layer properties. The plasma species and its compositions have been analyzed using plasma emission spectra and absorption spectra. The structural and optoelectronic properties of the epilayers have been studied by x-ray diffraction (XRD), Raman spectroscopy, Fourier transform infrared reflectance (FTIR) and Photoluminescence (PL) spectroscopy. The optical analysis of the GaN layers by Infrared (IR) reflectance reveals the optical dielectric function around ε_∞= 5.35, which is comparable with the reported bulk values. The growth rates vary up to 200 nm/hour for GaN.

EM-TuP18 The Electrical Properties of a Bimodal Nb Nanocluster Distribution Formed Through Plasma Gas Condensation, *Kevin Bray, C.Q. Jiao*, UES, Inc., *J.N. DeCervo, J.N. Merrett*, Air Force Research Laboratory

Nanocluster growth and characterization is an expanding field of research due to the promising catalytic, electrical, magnetic, mechanical, and optical properties exhibited by these materials. The properties of nanoclusters vary from the bulk material and can be tuned by varying the nanocluster size. The ability to obtain desired nanocluster sizes and distribution is an important step in effectively utilizing these materials. Transition metal clusters have received considerable interest due to their wide range of applications. Niobium has attracted attention due to observations of ferroelectric properties at low temperature. In this work, Nb nanoclusters are deposited using a plasma gas condensation process which involves the sputtering of a Nb target to create a dense metallic vapor where clusters are formed. Changes in the nanocluster nucleation and growth are influenced through modifications of the process parameters such as carrier gas composition and flow rate, sputter source ion current, and aggregation length. The formation of a bimodal cluster distribution under select process conditions has been observed, with the smaller cluster diameter near 1 nm and the larger cluster diameter varying from 2 to 10 nm. The larger cluster forms as a simple condensation product while the smaller cluster appears to arise from a different nucleation and growth mechanism. The effects of differing argon and helium carrier gas ratios on cluster formation in conjunction with varying sputter source currents and aggregation lengths will be discussed. The effect of the cluster size on the electrical properties will be examined.

EM-TuP20 Electron-Hole Exchange Energy in PbS and PbSe Nanocrystals, Joseph G. Tischler, E.E. Foos, D. Placencia, W. Yoon, J.E. Boercker, Naval Research Laboratory

Lead chalcogenides (PbS, PbSe and PbTe) nanocrystals (NC) possess outstanding optical properties such as broad optical absorption from the ultraviolet to the near infrared (NIR), bandgap tunability in the NIR, efficient multiple exciton generation and relatively high quantum yield luminescence. Such properties can be exploited in a variety of optoelectronic applications including biological tags, lasers, photodetectors, LEDs and photovoltaics. Thus, the electron-hole pair (or exciton) ground state electronic structure and dynamics is of particular interest. In particular, it has been reported that the luminescence of PbS nanocrystals is produced by two electronic states. A higher energy state with a lifetime of the order of tens of nanoseconds and a lower energy state with a lifetime of a few microseconds. Competition between these two levels have been reported in dynamics as a function of temperature and nanocrystal size. Furthermore, these two states have been invoked to explain the seemingly large Stokes shift dependence with nanocrystal size. Although there has been a lot of consensus on these observations, the origin of these states has been highly controversial. Some of the explanations utilized to explain the observed structure and dynamics include: a dark-exciton state, a hybrid state consisting of a trapped electron and hole in the conduction band, a trapped exciton state, an exciton state split-off due to the intervalley interaction, and shallow trap surface states.

In this work, we show that both the Stokes shift and splitting between the two energy states scale as d^3 , where d is the diameter of the NC. These findings imply that these two states correspond to the singlet "bright" state and the triplet "dark" state respectively. Furthermore we demonstrate that the Stokes shift is mainly given by the electron-hole exchange energy, and that opposite to what it was previously believed, the exchange energy is determined by the short-range interaction instead of the long-range interaction. Also, from these measurements we determined for the first time the bulk exchange interaction strength constant (J) for both PbSe and PbS.

EM-TuP22 Ultrasound Treatment Influence on the Si-SiO₂ interface defects structure, Daniel Kropman, Tallinn University of Technology, Estonia, T. Laas, Tallinn University, Estonia

The effect of ultrasonic treatment (UST) on the defect structure of the Si-SiO₂ system by means of electron spin resonance (ESR), selective etching, MOS capacitance technique and secondary ions mass spectroscopy is presented. The non-monotonous dependence of the defect densities on the US wave intensity has been observed. The influence of the UST frequency on the ESR signal intensity of the defect centres depended on the defects type and may be caused by vibration energy dissipation, which are a function of defect centres type. In the ESR spectra of Si samples a signal with $g=1.9996$ (P a centers) connected with vacancy complexes is observed. After UST appears another signal with $g=2.0055$ (broken bonds of Si atoms). The influence of the US frequency and sample orientation on the ESR signal intensity varies for different centres. The frequency and orientation dependence of the ESR signal with $g=1.9996$ and the lack of this dependence for the centres with $g=2.0055$ show that vibration energy dissipation depends on the type of defect centers. Defect density at the interface grows with an increase of US wave intensity or changes non-monotonously depending on the oxide thickness and crystallographic orientation. In the samples with thick oxide there is a maximum in the dependence of the charge carriers lifetime on the US wave amplitude and in the samples with thin oxides there is a minimum. This shows that the structural defects form electrically active centers and their density can be varied by US. The density of point defects and absorbed impurities at the Si-SiO₂ interface can be reduced and its electrical parameters improved by an appropriate choice of the UST and oxidation condition. US is widely used not only for materials treatment but in medicine as well (cancer treatment).

References:

[1] D.Kropman, V.Poll, L.Tambek, T.Karner, U.Abru. Ultrasonics 36(1998)1021-1025.

[2] D.Kropman, S.Dolgov. Physica status Solidi (c) v.9, issue 10-11, pp.2173-2176, 2012.

EM-TuP24 Low Temperature Growth of High-Quality SiO₂ Gate Dielectric by Atomic Layer Deposition, Sangram Pradhan, E. Tyani, A.K. Pradhan, Norfolk State University

A novel as well as simple method preparation of atomic layer deposited high quality SiO₂ gate dielectrics were fabricated using highly reactive ozone and tris (dimethylamino) silane. Small frequency dispersion and hysteresis behavior of SiO₂ MOS capacitor shows an ideal C-V behavior, suggesting excellent interfacial quality as well as purity of SiO₂ film. The flat-band voltage of the samples shifted from negative to positive sweep voltage region with increase in TDMAS pulse from 0.2 to 2 seconds. Based

on EOT point-of-view, the ALD SiO₂ has gate leakage current density as well as electrical fields of all ALD SiO₂ samples are nearly very good and more than (~ 10 MV/m) which is better comparable to that of thermal silicon oxide grown at temperatures above 800°C. The appealing electrical properties of thin ALD SiO₂ enable its potential applications as high-quality gate insulators for thin-film MOS transistors, and insulators for sensor structures and nanostructures on non-silicon substrates.

EM-TuP25 Surface Temperature and Kinetic Energy Dependence of SiGe Growth, Sang Choi, NASA Langley Research Center, H.J.K. Kim, National Institute of Aerospace

Silicon-germanium (SiGe) is an important semiconductor alloy for high-speed field effect transistors (FETs), high-temperature thermoelectric devices, photovoltaic solar cells, and photon detectors.[1] Semiconductor chipsets and devices require a single-crystalline phase of material without defects, while thermoelectric materials need granulated domains of poly crystalline structure with an interfacing boundary electrically connected but causing phonon scattering.[2] The structural formation between SiGe and substrate can be tailored for either single crystal or twin lattice structure.

Highly ordered single crystals with rhombohedral epitaxy using an atomic alignment of the [111] direction in cubic SiGe with the [0001] direction in the sapphire basal plane (c-plane) have been successfully grown at the NASA Langley Research Center. The changes in the growth temperature (from 820°C to 890°C) strongly influence the shape, size and density of the SiGe nuclei in the early growth stage and eventually the film morphology and defect density in the final growth stage. Annular bright field (ABF) and high angular dark field (HAADF) scanning transmission electron microscopy (STEM) were used to investigate the atomic structure and chemistry of SiGe and sapphire (Al₂O₃) interfaces, sapphire substrate reconstruction, and defects for studying the film growth mechanism. The best growth condition can be achieved by choosing the suitable substrate temperature and kinetic energy of impinging Si and Ge atomic flux. By controlling the kinetic energy of the surface atoms, either a dominant twin crystal or dominant single crystal was steadily formed. The kinetic energy of surface atoms is determined at the growth temperature between 820°C and 890°C.

[1] D. L. Hareme and B. S. Meyerson, IEEE Transactions on Electron Device, 48 (11), 2555 (2001).

[2] C. Gui, M. Elwenspoek, N. Tas, and J. G. E. Gardeniers, J. Appl. Phys. 85 (10), 7448 (1999).

EM-TuP26 TiN/Ag Multilayers made by dc Magnetron Sputtering for Patch Antennas Applications, José Ampuero, A.F. Talledo, V. Peña, C. Benndorf, Universidad Nacional de Ingeniería, Peru, M. Yarlequé, R. Cerna, Pontificia Universidad Católica del Peru

Titanium nitride has excellent physical properties such as high hardness, high abrasion wear resistance, as well as, high corrosion resistance, however, its electrical conductivity is poor compared to that of noble metals such as copper, silver or gold. On the other hand, silver films show excellent conductivity but in contact with normal atmosphere they are spoiled rapidly.

We have found that multilayers of silver and titanium nitride show high conductivity, high hardness and high corrosion resistance which make them useful for electrical and electronic applications.

In this paper we report (i) the production of silver-titanium nitride multilayers made by dc magnetron sputtering, (ii) structural and stoichiometry characterization made by X-ray diffraction and Auger electron spectroscopy. We also report the performance of patch antennas made of TiN/Ag multilayers deposited by dc magnetron sputtering on alumina plates. The analysis was made by using a Vector Network Analyzer. Typical bandwidth was in the range 3.3-3.4 GHz.

EM-TuP28 Quantum Effects Produced by Silicon Nanoparticles Embedded in Stacks of Silicon Rich Oxide Obtained by Low Pressure Chemical Vapor Deposition, Karim Monfil-Leyva, Benemerita Universidad Autónoma de Puebla, Mexico, M. Aceves-Mijares, Instituto Nacional de Astrofísica Óptica y Electrónica, A.L. Muñoz-Zurita, Universidad Autónoma de Coahuila, J.A. Luna-López, Benemerita Universidad Autónoma de Puebla, R.C. Ambrosio-Lázaro, Universidad Autónoma de Ciudad Juárez

Currently, new electronic and optoelectronic applications are using stacked arrays of different films, like superlattices, multilayers, tandem solar cells, etc. This work shows results and discussion of the structural and electrical properties from stacks of silicon rich oxide (SRO) films with different silicon excess. SRO films were deposited on *n*-type silicon (Si) substrate with low resistivity ($2\sim 3 \Omega\cdot\text{cm}$) using the low pressure chemical vapor deposition (LPCVD) technique. Two different stacks of SRO (SSRO) were formed varying the flow ratio (Ro) between N₂O and SiH₄ with Ro=10

(SRO₁₀) and Ro=30 (SRO₃₀). Also, low and high Si-implantation, 5×10^{15} and 2×10^{16} at/cm² doses respectively, were applied to SSRO. A thermal annealing was applied to all SSRO at 1100°C for 3 hours. Metal-oxide-semiconductor (MOS) structures were fabricated using the SSRO as dielectric layer with Aluminium (Al) on top and back contacts obtained by thermal evaporation. Cross section images of the Al/SSRO/Si structures were obtained by Transmission Electron Microscopy (TEM). The thickness of SSRO and diameters of embedded Si-nanoparticles (Si-Np's) were calculated from TEM images. The Si-implantation increases the size and density of Si-Np's in the SSRO. Current vs. Voltage ($I-V$) measurements of the Al/SSRO/Si structures showed current oscillations, staircases and bumps at room temperature. High frequency Capacitance vs. Voltage ($C-V$) measurements exhibited little jumps in the accumulation region due to charge trapping and de-trapping effect produced by the presence of Si-nPs. A group of SSRO structures showed a large hysteresis related to traps density in the SRO₁₀ films. The current oscillations and the other anomalies from electrical characterization were related with quantum effects like tunneling and Coulomb blockade between on and off states of the conductive paths as a result of Si-nPs embedded in the SSRO.

EM-TuP30 Tuning A Strong Photoluminescence Using Thin Silicon Rich Oxide And Silicon Rich Nitride Films Obtained By Low Pressure Chemical Vapor Deposition. *K. Monfil-Leyva*, Benemerita Universidad Autónoma de Puebla, Mexico, *A. Morales-Sánchez*, Centro de Investigación en Materiales Avanzados, S.C., *A.L. Muñoz-Zurita*, Universidad Autónoma de Coahuila, *F.J. Flores-Gracia*, Benemerita Universidad Autónoma de Puebla, *M. Moreno-Moreno*, Instituto Nacional de Astrofísica Óptica y Electrónica, *Esteban Ojeda-Durán*, Benemerita Universidad Autónoma de Puebla

Luminescent process in materials based on silicon nanostructures has attracted a great effort to overcome the intrinsic disadvantages of bulk-Si to develop optoelectronic devices. Nowadays, the Silicon Rich Oxide (SRO) and Silicon Rich Nitride (SRN) arise as a cheap and effective alternative to develop ultraviolet absorbers or silicon-based light emitters. SRO and SRN films can be deposited by several techniques but homogeneous layers can be easily obtained by low pressure chemical vapor deposition (LPCVD) using N₂O and NH₃ respectively mixed with SiH₄ as reactive gases. Silicon excess in SRO and SRN is well controlled by $Ro = N_2O/SiH_4$ and $Ro_n = NH_3/SiH_4$.

In this work, we report a wide study of the optical properties of thin SRO and SRN films obtained by LPCVD where silicon excess was changed by the pressure ratio Ro in the range of 15 and 45 (SRO15 to SRO45) and Ro_n in the range of 4 to 80 (SRN4 to SRN80). The effect of annealing at high temperature was studied at 1100 °C. Ellipsometry measurements were done on each sample to calculate the thickness and the refractive index. Fourier transform infrared (FTIR) measurements were applied on SRO and SRN films to confirm a change on stoichiometry. Absorbance spectra of SRO films showed the four characteristic peaks of non-stoichiometric silicon dioxide (SiO_x) after annealing. The as-deposited SRN films showed the characteristic peaks of a hydrogenated SiN_x matrix. However, the Si-H and N-H stretching peaks (2210 and 3315 cm⁻¹) disappeared after applying the annealing. SRN films showed a transmittance of 40 up to 90 % in the visible to near infrared region (400 to 900 nm). SRO films showed a strong photoluminescence (PL) at room temperature (RT) on two bands, a blue band from 400 to 550 nm or a red band from 575 nm to 875 nm depending on Ro. Blue and red emission bands were related to donor acceptor decays between traps promoted by defects. SRN films with high Si excess showed a wide PL from 450 to 850 nm. PL intensity from SRN was reduced when annealing temperature was increased, then the PL was also related to defects in the SiN_x matrix.

EM-TuP31 High Spatial Resolution Mass Spectrometry Imaging of Electronic Devices by Femtosecond Laser Desorption. *Yang Cui*, *M. Majeski*, *L. Hanley*, University of Illinois at Chicago

A variety of methods beyond secondary ion mass spectrometry are now available to molecularly image electronic devices and materials structures. Previous studies have shown the advantages of femtosecond laser desorption by removing sample without damaging remaining material, potentially allowing three dimensional imaging of molecular species [S. Milasinovic, et al., Anal. Chem. 84 (2012) 3945; Ibid, J. Phys. Chem. C (2014) <http://dx.doi.org/10.1021/jp504062u>]. Vacuum ultraviolet radiation has been added to femtosecond laser desorption to facilitate molecular detection [Y. Cui, ACS Appl. Mater. Interf. 5 (2013) 9269]. Nonlinear excitation by 800 nm, <100 fs laser pulses may also allow sampling of an analyte within a region smaller than the laser focus size. We explore this strategy to demonstrate mass spectrometry imaging by operating laser just above the ablation threshold. A USAF resolution test target and organic compound pattern were used for testing resolution. A simulated organic electronic device structure was then analyzed by depositing pentacene through a 1500 mesh electron microscopy grid onto a silicon wafer. The

sample was analyzed after the grid was removed, allowing collection of a mass spectrometric image of the pentacene grid as represented by signal from the intact pentacene ion. Overall, the method demonstrated a ~2-4 micron spatial resolution with the capability to maintain significant molecular information on an intact electronic device structure.

Wednesday Morning, November 12, 2014

2D Materials Focus Topic

Room: 310 - Session 2D+EM+NS+SS+TF-WeM

Novel 2D Materials

Moderator: Evan Reed, Stanford University

8:00am **2D+EM+NS+SS+TF-WeM1 Silicene and Germanene: Novel Graphene-like Artificial Silicon and Germanium Allotropes, Guy Le Lay, Aix-Marseille University, France** **INVITED**

Silicene, graphene's cousin, and germanene, a new born in Terra Plana, are predicted to combine the unique electronic properties of graphene associated to quasiparticles behaving as massless Dirac fermions to a character of two-dimensional topological insulators, and, even, possibly, high temperature superconductors. In this talk, I will present fundamental results on these novel synthetic 2D materials, which do not exist in nature, but which might open the way to practical applications, because of their expected direct compatibility with the current nano/micro electronic technologies.

8:40am **2D+EM+NS+SS+TF-WeM3 Silicon Growth at the Two-Dimensional Limit on Ag(111), Andrew Mannix, B.T. Kiraly, Northwestern University, B.L. Fisher, Argonne National Laboratory, M.C. Hersam, Northwestern University, N.P. Guisinger, Argonne National Laboratory**

Bulk silicon has played a dominant role in the growth of microelectronics over the past 50 years. Considering the immense interest in two-dimensional (2D) materials (e.g., graphene, MoS₂, phosphorene, etc.), the growth of Si in the 2D limit is of high relevance to the evolution of electronic materials. Utilizing atomic-scale, ultra-high vacuum (UHV) scanning tunneling microscopy (STM), we have investigated the 2D limits of Si growth on Ag(111). In agreement with previous reports of *sp*²-bonded silicene,^{1,2} we observe the evolution of ordered 2D phases, which we attribute to apparent Ag-Si surface alloys. At sufficiently high Si coverage, we observe the precipitation of crystalline, *sp*³-bonded Si(111) domains. These domains are capped with a $\sqrt{3}$ honeycomb phase that is indistinguishable from the $\sqrt{3}$ honeycomb-chained-trimer (HCT) reconstruction of Ag on Si(111).^{3,4,5} Additional evidence suggests that silicon intermixing with the Ag(111) substrate is followed by the precipitation of crystalline, *sp*³-bonded silicon nanosheets. These conclusions are supported by *ex-situ* atomic force microscopy (AFM), Raman spectroscopy, and X-ray photoelectron spectroscopy (XPS). Even at the 2D limit, scanning tunneling spectroscopy shows that the *sp*³-bonded silicon nanosheets exhibit semiconducting electronic characteristics.

[1] Vogt, P., *et al.* Silicene: Compelling Experimental Evidence for Graphene-like Two-Dimensional Silicon. *Phys. Rev. Lett.*, 108(15), 155501 (2012).

[2] Feng, B., *et al.* Evidence of silicene in honeycomb structures of silicon on Ag(111). *Nano Lett.*, 12(7), 3507–11 (2012)

[3] Le Lay, G. Physics and electronics of the noble-metal/elemental-semiconductor interface formation: A status report. *Surf. Sci.*, 132(1-3), 169–204 (1983).

[4] Aizawa, H., Tsukada, M., Sato, N., & Hasegawa, S. Asymmetric structure of the Si(111)- $\sqrt{3}\times\sqrt{3}$ -Ag surface. *Surf. Sci.*, 429 (0–5) (1999).

[5] Ding, Y., Chan, C., & Ho, K. Structure of the ($\sqrt{3}\times\sqrt{3}$) R30° Ag/Si(111) surface from first-principles calculations. *Phys. Rev. Lett.*, 67(11), 1454–1458 (1991).

9:00am **2D+EM+NS+SS+TF-WeM4 Growth, Structure, and Properties of 2D SiO₂ Polymorphs, Eric Altman, J. Götz, X. Zhu, A. Sonnenfeld, U.D. Schwarz, Yale University**

Recently it has been shown that SiO₂ can form closed 2D bilayers; because the layers have no dangling bonds they are expected to interact solely through van der Waals interactions. Despite the expected weak interactions, hexagonal crystalline bilayers on Pd(100) are stretched 4% to match the lattice constant of the substrate. Both electron diffraction and STM reveal that the size of the crystalline domains is limited along Pd[011] and one of the other bilayer close-packed directions but was long along the third one. The formation of regular domain boundaries on the square Pd substrate is attributed to stress relief in the crystalline layer. *Ab initio* calculations indicate that much of the remaining strain energy can be relieved by allowing the film to relax along the incommensurate direction. In this way the square substrate actually aids the templating of the overlayer despite the severe geometric mismatch. The calculations also indicate that the bilayer is surprisingly compliant, explaining the lattice matching despite the weak

interaction and poor match. Amorphous bilayers could also be prepared on Pd(100). Atomic-scale features in STM images of the amorphous film could be associated with 4-9 membered rings of corner-sharing SiO₄ tetrahedra. In addition to the structural heterogeneity, spectroscopic STM imaging revealed electronic heterogeneity with oxygen sites joining larger rings of corner-sharing SiO₄ tetrahedra fading at low bias; spectra revealed two distinct electronic states responsible for this phenomenon. MBE growth of silica bilayers on graphene layers grown on epitaxial Ru on sapphire will also be discussed.

9:20am **2D+EM+NS+SS+TF-WeM5 Layer-dependent Electronic and Vibrational Properties of SnSe₂ and SnS₂ 2D Materials, Joseph Gonzales, R. Schlaf, I.I. Oleynik, University of South Florida**

Layered metal chalcogenides possess a wide range of unique electronic properties, which are currently explored for applications as novel two-dimensional electronic materials. SnS₂ and SnSe₂ layered materials consist of covalently bonded S-Sn-S (Se-Sn-Se) sheets bonded together by weak van der Waals interactions. The atomic, electronic and vibrational properties of SnS₂ and SnSe₂ thin films are investigated using first-principles density functional theory (DFT). The accurate prediction of electronic and optical properties of SnS₂ and SnSe₂ layered 2D materials is achieved by applying state of the art many-body perturbation theory in GW approximation followed by solving the Bethe-Salpeter equation (BSE) to take into account excitonic effects. The evolution of the thickness-dependent band structure, optical and Raman spectra are discussed. The strain effects due to interactions with the substrate are also considered. The first-principles results are compared with available experimental data.

9:40am **2D+EM+NS+SS+TF-WeM6 Synthesis and Properties of Large Scale, Atomically Thin Tungsten Diselenide (WSe₂), Sarah Eichfeld, Y.C. Lin, L. Hossain, The Pennsylvania State University, A. Piasecki, The Pennsylvania State University, A. Azcatti, University of Texas, Dallas, S. McDonnell, R.M. Wallace, University of Texas at Dallas, J.A. Robinson, The Pennsylvania State University**

Transition metal dichalcogenides (TMDs), such as tungsten diselenide (WSe₂) are of interest due to their intriguing properties including the transition from indirect gap to direct gap as the material is thinned to a single atomic layer. Stacking of these layered TMDs also allows for the possibility of bandgap tuning. These properties can suit a large range of flexible and low temperature electronic and optoelectronic devices. Current methods of WSe₂ research involve exfoliation or vaporization of WO₃ and Se powder, which limits industrial scalability. This work is focused on development of a metal-organic chemical vapor deposition process that can controllably produce highly-crystalline, atomically thin WSe₂ on large area substrates.

Growth of controlled monolayer tungsten diselenide (WSe₂) was carried out using chemical vapor deposition in a cold wall vertical reactor. Tungsten hexacarbonyl (W(CO)₆) and dimethylselenium (DMSe) served as the tungsten and selenium precursors, respectively. Use of MOCVD precursors provides a means to independently control the W and Se precursors allowing for more precise control of the individual species during growth. Process variables including temperature (500-950°C), pressure (100-700 Torr), and carrier gas, which were correlated with grain size, growth rate, and nucleation density of the WSe₂ to identify optimal parameters for atomically controlled synthesis. Increasing the growth pressure from 100-700 Torr results in a decrease in growth rate and nucleation density, leading to a >50x increase in grain size. Increased growth temperatures yield an increase in grain size, however, it was found that above temperatures of 800 °C the sapphire substrate begins to decompose in the growth environment, resulting in a degradation of WSe₂ above 800°C. Synthesis using 100% hydrogen, and also hydrogen/nitrogen mixtures was carried out. It was found that 100% hydrogen was necessary in order to achieve low carbon incorporation in the WSe₂ films. Characterization of these samples via Raman and photoluminescence spectroscopy verified that high quality, monolayer WSe₂ is readily achievable. Additional characterization (i.e. scanning electron microscopy, atomic force microscopy, etc.) verify the quality, grain size, and nucleation density of the atomic layers. Finally, we will discuss the impact of substrate choice on the quality of the WSe₂ atomic layers, as well as providing direct evidence that synthesis on graphene results in highly textured films, with nearly 100% commensurability to the underlying graphene.

11:00am **2D+EM+NS+SS+TF-WeM10 Growth of Transition Metal Dichalcogenides and their Alloys and on Flat and Patterned Substrates.** *E. Preciado, A. Nguyen, D. Barroso, V. Klee, S. Bobek, I. Lu, S. Naghibi, G. Von Son Palacio, T. Empante, K. Brown, K. Yang, A. Nguyen, J. Mann, Ludwiy Bartels*, University of California - Riverside

The use of organic chalcogen precursors permits the CVD growth of $\text{MoS}_{2(1-x)}\text{Se}_{2x}$ alloys of any composition between pure MoS_2 and MoSe_2 on SiO_2 . Spatially resolved vibrational and photoluminescence (PL) spectroscopy is used to characterize our samples: while we observe a continuous transition of the PL maximum with S: Se ratio, the vibrational modes behave in a more complicated, 2-mode fashion. Depending on growth conditions, compositional homogeneous and heterogeneous films can be prepared.

We present details of our growth processes and show to which extend patterns on the substrates can affect the resultant structures. The patterns range from simple hole and pillar arrays to complex waveguide structures. We find that holes to an underlying reducing substrate (silicon) are effective in seeding growth. In contrast, protrusions on the substrate have little effect, so that complex devices can be overgrown.

Ref: Mann et al., 2-Dimensional Transition Metal Dichalcogenides with Tunable Direct Band Gaps: $\text{MoS}_{2(1-x)}\text{Se}_{2x}$ Monolayers, *Advanced Materials* 26, 1399 (2014)

11:20am **2D+EM+NS+SS+TF-WeM11 Synthesis, Characterization and Radiation Response of Boro-Carbon-Oxy-Nitride: A Heterogeneous 2D Material.** *GaneshRahul Bhimanapati, M. Wetherington, M. Kelly, J.A. Robinson*, The Pennsylvania State University

Since graphene, there have been many other two-dimensional materials systems (e.g., boron nitride (hBN), borocarbon nitride (BCN), transition-metal dichalcogenides) that provide an even wider array of unique chemistries and properties to explore future applications. In fact, these other 2D materials, are sometimes far better suited for many optoelectronic and mechanical applications. Specifically, tailoring graphene/boron nitride heterostructures, which retain the character of single-atom thick sheets that can withstand large physical strains, are easily functionalized, and have entirely different optical and mechanical properties compared to graphene can provide the foundation for entirely new research avenues. In recent years, it has been shown that because of the similar crystal structure, carbon, boron, and nitrogen can coexist as atomic sheets in a layered structure. Thus, combining these materials to form a new heterogeneous material system known as boro-carbon-oxy-nitride (BCON) for potential nano-mechanical and electronic applications and to study its fundamental property relations is necessary. Here, we present the fundamental property relations of BCON and its structural response to various radiation sources such as alpha, beta and gamma particles thereby providing a means for potential radiation sensing applications.

We have developed a facile method of integrating boron nitride and graphene oxide (GO) via chemical exfoliation. Chemical exfoliation of graphene oxide and boron nitride powders is accomplished via oxidation in strong acids, as we find previous methods of sonication in polar solvents does not yield stable solutions of hBN. Upon exfoliation, GO and hBN are mixed, and the resulting BCON material can be suspended in DI water, with suspension stability depending on the pH of the GO. The study of the stability of this material at different pH conditions indicates a stable and a uniform solution is achievable at pH 4-7. Fourier transform infrared spectroscopy (FTIR) indicates the B-N-B bending in the BCON is decreased as an effect of parent GO. Further, radiation response of this material to various radiation sources such as alpha, beta and gamma radiation are studied using In-Situ X-Ray Photoelectron Spectroscopy (XPS). The structural changes of carbon 1s peak in the BCON even for very low doses of radiation energy indicate potential applications in radiation sensing.

11:40am **2D+EM+NS+SS+TF-WeM12 The Structure of 2D Glass.** *Christin Büchner*, Fritz-Haber-Institut der Max-Planck-Gesellschaft, Germany, *L. Lichtenstein*, Lawrence Berkeley National Laboratory, *M. Heyde, H.-J. Freund*, Fritz-Haber-Institut der Max-Planck-Gesellschaft, Germany **INVITED**

For the first time, the structure of an amorphous network is imaged in real space.[1] Through a thin film approach, silica is made accessible for investigation with scanning tunneling microscopy (STM) and atomic force microscopy (AFM). Physical vapor deposition with subsequent annealing is employed to create an atomically flat bilayer of SiO_2 , supported on a Ru(0001) single crystal. Atomic positions of oxygen and silicon can be visualized, as well as ring structures with their distributions and local neighborhoods. All atomic species on the surface can be directly assigned with chemical sensitivity imaging.[2] This allows for statistical analysis of the building units, comparing amorphous to crystalline regions, as well as experiment to theory. Pair correlation functions of the 2D film structure are

set against diffraction data of bulk silica, revealing very similar bond distributions.

Coexisting crystalline and amorphous areas allow imaging of a topological transition region.[3] The understanding of glassy structures gained from these experiments is the starting point for more in-depth structural investigations[4], but also for investigating thin films with modified composition. Al-doping or Fe-doping can be employed to create 2D-Aluminosilicates or 2D-Clays, respectively.[5] Adsorption properties of the film can be probed using single metal atoms which migrate through the film, exhibiting ring-size-selectivity.[6]

[1] L. Lichtenstein, et al., *Angew. Chem., Int. Ed.* 51, 404 (2012)

[2] L. Lichtenstein, et al., *J. Phys. Chem. C* 116, 20426 (2012)

[3] L. Lichtenstein, et al., *Phys. Rev. Lett.* 109, 106101 (2012)

[4] C. Büchner, et al., *Z. Phys. Chem.*, DOI: 10.1515/zpch-2014-0438 (2014)

[5] J. A. Boscoboinik, et al., *Angew. Chem. Int. Ed.* 51, 6005 (2012)

[6] W. E. Kaden, et al., *Phys. Rev. B* 89, 115436 (2014)

Electronic Materials and Processing

Room: 311 - Session EM1-WeM

Materials and Devices for High Power Electronics (8:20-11:00 am)/Two Dimensional Electronic Materials & Devices (11:00 am - 12:20 pm)

Moderator: Andrew Antonelli, Lam Research, Rachael Myers-Ward, U.S. Naval Research Laboratory

8:00am **EM1-WeM1 Commercialization of High Voltage GaN HEMT.** *P. Parikh, Rakesh Lal*, Transphorm Inc. **INVITED**

With its proven ability to reduce size (improved form factor) and save energy (improved efficiency) Gallium Nitride (GaN) is now no longer a nice to have, it is a must have for power conversion. In applications have emerged ranging from sub 100 watt ultra-compact high frequency adapters to multi kilowatt highly efficient PV Inverters, GaN makes it possible to do what Silicon cannot. High voltage GaN on Silicon HEMT switches are now a reality, following successful completion of JEDEC qualification as well as establishment of a high voltage lifetime of 100M hours. A large area (6inch) Silicon substrate, epitaxial processes that promise to leverage the commercial success of the well established GaN LED & lighting products and the ability to manufacture in existing high volume Silicon foundries makes GaN commercially attractive. Successful companies need to deliver high quality product with a deep understanding of how the GaN switch is best utilized in applications. We will discuss the commercialization of the GaN power HEMT by Transphorm - enabled by execution on the above fronts, a strong intellectual property across the full value chain and a strong team with deep rooted experience in GaN technology and business. Ultimately GaN is expected to significantly reduce conversion losses endemic in all areas of electricity conversion, ranging from power supplies to PV inverters to motion control to electric vehicles, enabling consumers, utilities and Governments to contribute towards a more energy efficient world.

8:40am **EM1-WeM3 Progress and Future Challenges in SiC Material for High-Voltage Power Devices.** *Tsunenobu Kimoto*, Kyoto University, Japan **INVITED**

Silicon carbide (SiC) is an emerging wide bandgap semiconductor, by which high-voltage, low-loss power devices can be realized owing to its superior properties. SiC unipolar devices such as Schottky barrier diodes and MOSFETs will replace Si unipolar/bipolar devices in the blocking-voltage range from 600 V to about 6500 V. Regarding SiC power MOSFETs, the authors developed vertical trench MOSFETs in collaboration with ROHM. The trench MOSFETs with cell miniaturization exhibited extremely low on-resistances of 0.79 $\text{m}\Omega\text{cm}^2$ and 1.4 $\text{m}\Omega\text{cm}^2$ for 630 V and 1260 V devices, respectively, with normally-off characteristics [1]. After reliability tests, all-SiC power modules (1200 V – 180 A) are now commercial products.

For ultrahigh-voltage applications above 6500 V, SiC bipolar devices such as PiN diodes and IGBTs are promising. Major technological challenges include fast epitaxy of thick (> 100 μm) and high-purity epilayers, stress control, reduction of basal-plane dislocations and stacking faults, enhancement and control of carrier lifetimes. The authors succeeded in fast epitaxial growth of 100-200 μm -thick SiC at a growth rate of 40-85 $\mu\text{m}/\text{h}$ with a high purity ($1 \times 10^{13} \text{ cm}^{-3}$) and reduced density of basal-plane dislocations. Through elimination of the $Z_{1/2}$ center, a lifetime killer in SiC,

via thermal oxidation, the authors obtained about 200 μm -thick, $Z_{1/2}$ -free n-type SiC epilayers, where the bulk lifetime reaches 30 μs or even longer [2]. The carrier lifetimes can be controlled by low-energy electron irradiation, which can preferentially generate the $Z_{1/2}$ center (carbon vacancy) in SiC.

Ultrahigh-voltage PiN diodes were fabricated by using lightly-doped ($2\text{-}3 \times 10^{14} \text{ cm}^{-3}$) SiC epilayers with different thicknesses (50-260 μm). The breakdown voltage was scaled with increasing the epilayer thickness, as simulated. The maximum breakdown voltage experimentally obtained exceeded 27 kV, which is the highest blocking voltage among any solid state devices. The differential on-resistance was remarkably reduced by enhancement of carrier lifetimes, being $2 \text{ m}\Omega\text{cm}^2$ and $10 \text{ m}\Omega\text{cm}^2$ for 13 kV and 27 kV devices, respectively. A SiC bipolar junction transistor with a blocking voltage over 21 kV and current gain over 60 was also demonstrated [3].

This work was supported by the Funding Program for World-Leading Innovative R&D on Science and Technology (FIRST Program) and a Grant-in-Aid for Scientific Research from JSPS. The authors acknowledge Dr. T. Nakamura with ROHM for the MOSFET collaboration.

- [1] T. Nakamura et al., Tech. Digest. 2011 IEDM, 26.5.1.
- [2] S. Ichikawa et al., Appl. Phys. Exp., **5**, 101301 (2012).
- [3] H. Miyake et al., IEEE Electron Device Lett., **33**, 1598 (2012).

9:20am **EM1-WeM5 4H-SiC Epilayers Grown on 2° Offcut Substrates**, *Rachael Myers-Ward, Z.R. Robinson, V.D. Wheeler, P.B. Klein, N.A. Mahadik, R.E. Stahlbush, C.R. Eddy, Jr., D.K. Gaskill*, Naval Research Laboratory

Silicon carbide is a material of interest for high-voltage, high-power switching device applications. Basal plane dislocations (BPDs) are a major concern for SiC bipolar devices as they source Shockley-type stacking faults in the presence of an electron-hole plasma and reduce minority carrier lifetimes [1]. Many researchers have investigated methods to reduce BPD densities by experimenting with pre-growth treatments [2-4], substrate orientation [5], growth parameters [5, 6] and growth interrupts [7]. This work investigates extended defects, morphology and lifetime in 4H-SiC epilayers grown on substrates offcut 2° toward the [11-20].

Epilayers were grown in a horizontal hot-wall reactor using silane (2% in H_2) and propane. Hydrogen etching was conducted to determine the morphology of the substrate during the ramp to growth temperature; temperatures explored were 1400, 1450 and 1500 °C. Epilayers were grown at various growth rates of 1, 5 and 10 $\mu\text{m/hr}$ and C/Si ratios from 1.0 to 1.55. The influence of doping with ultra-high purity nitrogen was investigated. Ultraviolet photoluminescence (UVPL) imaging was used to identify BPDs in low doped epilayers. Time resolved photoluminescence measurements were performed to determine the minority carrier lifetime of the layers and Raman spectroscopy was used to analyze polytype inclusions. Surface roughness was measured by atomic force microscopy and Nomarski microscopy was also used to characterize morphology.

No step bunching was found when the temperature was raised to 1400 °C in H_2 and cooled down immediately. However, intermittent step bunching formed when the temperature was raised to 1500 °C. When a 15 μm epilayer was introduced, step bunching was observed and the surface roughness was 6.0 nm RMS. For comparison, a standard 4° offcut sample typically has 3.0 nm RMS for a 20 μm epilayer. Using UVPL, it was found that after 4 μm of epi, 90% of the BPDs had converted in the epilayer as compared to 70% in a 4° offcut sample, indicating the conversion is faster in the lower offcut material. Epilayers without any BPDs were observed; however, 3C-SiC inclusions were present as verified by Raman spectroscopy. BPD densities and carrier lifetimes of the epilayers will also be reported.

- [1] J.P. Bergman, et al. Mater. Sci. Forum Vol. **353-356**, 299 (2001).
- [2] Z. Zhang, et al., Appl. Phys. Lett. **89**, 081910 (2006).
- [3] J.J. Sumakeris, et al., Mater. Sci. Forum **527-529**, 529 (2006).
- [4] H. Tsuchida, et al., Mater. Sci. Forum **483-485**, 97 (2005).
- [5] W. Chen and M.A. Capano J. Appl. Phys. **98**, 114907 (2005).
- [6] T. Ohno, et al., J. Cryst. Growth **271**, 1 (2004).
- [7] R.E. Stahlbush, et al., Jr., Appl. Phys. Lett. **94**, 041916 (2009).

11:00am **EM1-WeM10 Recent Progress in Graphene and Heterostructure RF Electronics**, *Jeong-Sun Moon, H.-C. Seo, K.A. Son, B. Yang, M. Antcliff, A. Schmitz, D. Le*, HRL Laboratories, LLC, *L.O. Nyakiti, V.D. Wheeler, R.L. Myers-Ward, C.R. Eddy, D.K. Gaskill*, Naval Research Laboratory, *K.-M. Lee, P. Asbeck*, University of California at San Diego

INVITED

Graphene is a truly 2D electronic material with a very high intrinsic saturation velocity (V_{sat}) of $\sim 5 \times 10^7 \text{ cm/sec}$, which has great potential for high-speed RF applications. In addition, graphene offers unique properties,

such as high mobility, excellent scalability, symmetry in electron or hole channel, its ability to be integrated into any substrate, and its potential compatibility with CMOS.

The material quality and fabrication process for graphene have improved with sheet resistance of $\sim 200 \text{ ohm/sq}$, ohmic contact resistance of $\sim 0.03 \text{ W}\times\text{mm}$, the lowest on-state resistance of $0.13 \text{ W}\times\text{mm}$, and the highest saturated source-drain current of $\sim 3 \text{ A/mm}$ at $V_{\text{ds}} = 1 \text{ V}$. Recently, graphene FETs (GFETs) demonstrated zero-bias resistive FET mixer operation up to 20 GHz [1] with 10 times improvement in the mixer quality factor (IIP3/total power) over state-of-the-art (SOA) resistive FET mixers; these GFETs also demonstrated zero-bias in power detectors and radiometers (up to 220 GHz) [2] with linear-in-dB dynamic range with $>20 \text{ dB}$ improvement over SOA FETs. Graphene heterostructure-based FETs have been developed as enhancement-mode FETs with an Ion/Ioff ratio of $>10^5$ and excellent pinch-off and I-V saturation [3]. Graphene varactors have been demonstrated on glass substrates, expanding graphene's potential to be integrated with arbitrary substrates, and potentially enabling active and tunable antenna surfaces beyond wafer-scale.

In this talk, we present recent progress in graphene material, GFETs, graphene heterostructure FETs, circuit applications for mixers, radiometers, detectors, varactors, and progress toward integrating graphene with active antennas. Continuous development of this emerging material would potentially enable RF systems on nonconventional surfaces.

This material is partially based upon work supported by the Government under Contract No. N66001-08-C-2048. Any opinions, findings and conclusions or recommendations expressed in this material are those of the author(s) and do not necessarily reflect the views of the Contracting Agency.

- [1] J.S. Moon et al., IEEE Electron Device Letters., vol 34, p465, 2013; J. S. Moon and D. Kurt Gaskill, IEEE Trans. Microwave Theory and Tech., vol. 52, pp 1014-1024, 2011.
- [2] J. S. Moon et al., IEEE Electron Device Letters., vol 33, p1357, 2012.
- [3] J.S. Moon et al., IEEE Electron Device Letters., vol 34, p1190, 2013

11:40am **EM1-WeM12 High-Field and Thermal Transport in 2D Atomic Layer Devices**, *Eric Pop, C.D. English*, Stanford University, *V.E. Dorgan, A. Behnam*, University of Illinois at Urbana-Champaign, *Z. Li*, Stanford University, University of Illinois, Urbana-Champaign, *S. Islam*, University of Illinois at Urbana-Champaign

INVITED

Two-dimensional (2D) materials like graphene and transition metal dichalcogenides (TMDs) are uniquely suited for nanoscale field-effect transistors (FET) due to sub-nm channel thickness and lack of dangling surface bonds. Thus, unlike three-dimensional (3D) materials such as Si, FETs based on 2D materials would be more resilient to short-channel effects and would suffer less mobility degradation from carrier-surface scattering. Nevertheless, most existing studies of 2D materials have focused on large devices and low-field transport. By contrast, highly scaled 2D-FETs will require very good understanding of electric transport at high fields and thermal transport as relevant for large scale device integration.

In this talk we will describe our recent progress in optimizing transport at 2D-3D material contacts, examining high-field transport, FET scaling and thermal measurements at sub-100 nm device dimensions. For instance, we have recently uncovered transport physics at TMD and 2D graphene contacts with metal electrodes, including the roles of metal deposition conditions during fabrication and that of thermoelectric (Peltier) effects during transistor operation [1,2]. We will also describe our understanding of high-field transport in MoS₂ and graphene, including the importance of self-heating effects on various substrates such as SiO₂, BN and HfO₂ [3,4]. Finally, we will describe our thermal measurements in suspended graphene [5] and in graphene devices with dimensions comparable to the electron and phonon mean free paths ($\sim 100 \text{ nm}$) [6]; the former yield the intrinsic behavior of this material, while the latter show quasi-ballistic thermal transport near room temperature, as well as significant phonon-edge scattering in narrow devices. The results are of importance for both electronic and thermal applications of 2D materials.

References

- [1] K.L. Grosse, M.-H. Bae, F. Lian, E. Pop, W.P. King, Nature Nano. **6**, 287 (2011)
- [2] C.D. English, V.E. Dorgan, G. Shine, K. Saraswat, E. Pop, IEEE Device Research Conf. (2014)
- [3] M.-H. Bae, S. Islam, V.E. Dorgan, E. Pop, ACS Nano **5**, 7936 (2011)
- [4] S. Islam, Z. Li, V.E. Dorgan, M.-H. Bae, E. Pop, IEEE Electron Device Lett. **34**, 166 (2013)
- [5] V.E. Dorgan, A. Behnam, H. Conley, K. Bolotin, E. Pop, Nano Lett., **13**, 4581 (2013).

Electronic Materials and Processing Room: 314 - Session EM2-WeM

High-K Dielectrics from Non-Classical Channels

Moderator: Christopher Hinkle, University of Texas at Dallas

8:00am EM2-WeM1 The Influence of Surface Preparation pre-Atomic Layer Deposition of Al₂O₃ on GaN Metal Oxide Semiconductor Capacitors, *Dmitry Zhernokletov*, Stanford University

High-k gate dielectrics have been proposed as a means of producing high performance field effect devices with low gate leakage on GaN-based substrates for low static power consumption, improved transconductance, and higher output power capabilities [1-3]. However, because the surface of GaN may contain defects such as dangling bonds and contaminants [4], understanding the effect of varying surface preparation prior to atomic layer deposition (ALD) of the high-k gate dielectrics on GaN is of great importance for the advancement of field effect devices. Surface defects and contaminants such as carbon and oxygen may have detrimental effects on optical quality and device performance of GaN based devices. Several methods to improve GaN surface and interface quality have been proposed [4-8]. They include surface cleaning procedures using aqueous (NH₄)₂S, and acid/base treatments such as HCl, HF, NaOH and NH₄OH.

We present a detailed study on the influence of surface preparations pre-atomic layer deposition of Al₂O₃ on GaN metal oxide semiconductor capacitors. The electrical, chemical, and luminescence characteristics of MOS structures prepared on both chemically treated and as-received GaN substrates are reported. Aqueous NH₄OH cleaning shows promise for providing an enhanced starting surface for atomic layer deposition of Al₂O₃ layers on GaN.

- [1] P.D. Ye et al., *Appl. Phys. Lett.* 86, 063501 (2005).
- [2] O.I. Saadat et al., *IEEE Electron. Dev. Lett.* 30 1254-1256 (2010).
- [3] D.J. Meyer et al., *Solid-State Electron.* 5 1098 (2010).
- [4] R.D. Long et al., *Materials.* 5, 1297-1335 (2012).
- [5] Diale et al., *Appl.Surf.Sci.* 246, 279–289 (2005).
- [6] Lee et al., *J. Electrochem. Soc.* 147, 3087–3090 (2000).
- [7] Hattori et al. *Surf. Sci.* 2010, 604, 1247–1253.
- [8] Y. Koyama et al., *Solid State Electron.* 43, 1483–1488 (1999).

8:20am EM2-WeM2 Low Voltage Nonlinearity Metal-Insulator-Insulator-Metal (MIIM) Capacitors using Plasma Enhanced Atomic Layer Deposition of SiO₂ and Al₂O₃, *Dustin Austin*, Oregon State University, *D. Allman, D. Price, S. Hose*, On Semiconductor, *J.F. Conley*, Oregon State University

Back end of line (BEOL) metal-insulator-metal (MIM) capacitors reduce the need for discrete off-board components and have become a core passive device in integrated circuits. Applications include analog-to-digital converters, analog noise filters, DC voltage decoupling, and electrostatic discharge (ESD) protection. To enable continued scaling, capacitance density must be increased, either by introducing higher dielectric constant (κ) materials or by reducing the insulator film thickness. However decreasing insulator film thicknesses increases both leakage current density and voltage nonlinearity (characterized by the quadratic voltage coefficient of capacitance or α VCC). In addition high- κ materials typically have a large positive α VCC. Although a promising route to simultaneously meeting these competing requirements is to use a nanolaminate of insulators, which allows for combining of layers with complementary properties. Previous work has demonstrated nanolaminate MIIM devices with high capacitance density, low leakage current density, and low α VCC using PECVD SiO₂ or uncommon materials.¹⁻³

In this work, MIIM capacitors using bilayers of Al₂O₃ and SiO₂ were deposited sequentially using plasma enhanced atomic layer deposition (PEALD). PEALD allows for low deposition temperatures, precise thickness control, and conformal coverage over high aspect ratio structures. Al₂O₃ and SiO₂ are attractive due to their common usage in IC fabrication, large metal-insulator barrier heights, and high dielectric breakdown strength. In addition SiO₂ is one of the few materials that exhibits a negative α VCC. Spectroscopic ellipsometry was used to characterize the growth rate and nucleation delay on TaN and Si substrates. The dielectric constants of Al₂O₃ and SiO₂ were found to be 4.6 and 8.7, respectively. α VCC values were plotted as a function of thickness and fit with a power law.

Appropriate layer thicknesses were chosen to offset the negative α VCC of SiO₂ with the positive α VCC of Al₂O₃ in order to minimize the effective α VCC for a given capacitance density. The initial results for 8 nm Al₂O₃ / 3.5 nm SiO₂ MIIM devices show capacitance density of 5.4 fF/ μ m², 2 nA/cm² leakage at 1V, and α VCC of 70 ppm/V², simultaneously meeting the ITRS 2014 requirements for capacitance density (> 5 fF/ μ m²), leakage current density (< 10 nA/cm² at 1V), and voltage nonlinearity (< 100 ppm/V²). Current work is underway to optimize this nanolaminate to meet the ITRS 2017 requirements.

- ¹ S. Van Huynenbroeck et al, *Electron Device Lett. IEEE* 23, 191 (2002).
- ² S.J. Kim et al, *Electron Device Lett. IEEE* 25, 538 (2004).
- ³ T.H. Phung et al, *Electrochem. Soc.* 158, H1289 (2011).

8:40am EM2-WeM3 Metal-Insulator Transitions, Resistive Switches and Oxide Electronics, *Shriram Ramanathan*, Harvard University **INVITED**

There is growing interest in the exploring complex oxide semiconductors as functional elements in solid state devices. This is in part created by the inevitable limits to use of traditional semiconductors in highly scaled devices and also expanding interest in integrating multiple functionalities at the chip-level. Dielectrics with engineered defects and correlated oxides could be potentially interesting in this regard as switchable, adaptive materials for interconnects, logic and memory. There are a number of fundamental issues from the materials and interface aspects that remain poorly understood. For example, how can we develop a quantitative understanding of the electrical aspects of the high-k / correlated oxide interface where in almost all cases, such phase change materials show drastic frequency dependent properties? How can we design gate stacks to modulate carrier density approaching that of metallic state in such oxides? In this presentation, I will address these problems, with emphasis on studies conducted in our laboratory on rutile (e.g. VO₂) and perovskite (e.g. SmNiO₃) structured oxide thin films that undergo insulator-metal transitions.

9:20am EM2-WeM5 Complex Oxide Devices, *Suman Datta*, Penn State University **INVITED**

Strongly correlated electronic phases encountered in complex oxides exhibit collective carrier dynamics that if properly harnessed can enable novel functionalities and perhaps even new computation paradigms. In this talk, we will present our recent understanding of electronically triggered charge oscillations in a prototypical metal insulator transition (MIT) system, vanadium dioxide. We show that the key to such oscillatory behavior lies in the ability to stabilize a spontaneously reversible phase transition in the complex oxide devices using a negative feedback mechanism. We also explore the synchronization dynamics of such oscillators via experiment and simulation, and investigate its potential for coupled oscillator based non-Boolean associative computing.

11:00am EM2-WeM10 Ferroelectric Devices, *Alexander Demkov*, The University of Texas at Austin **INVITED**

Novel methods of deposition developed over the past decade or so, enabled fabrication of thin films of ferroelectric materials, such as BaTiO₃ (BTO), of very high crystal quality. This has resulted in renewed interest in ferroelectric field effect transistors and in addition, led to new device architectures, such as negative capacitance devices. Thanks to very high Pockels coefficient, thin films of BTO may find applications in Si nanophotonics.

In this talk I will describe our recent efforts on integration of BTO (and other ferroic oxides) on semiconductors using a SrTiO₃ (STO) buffer. More specifically, I will describe integration of BaTiO₃ on Si (001) and Ge (001) using molecular beam epitaxy (MBE) and atomic layer deposition (ALD). We employ first principles modeling to both guide the crystal growth and analyze the characterization data. By modeling core level spectroscopy and comparing it with the x-ray photoemission data we are able to identify the Zintl growth template for STO on Si and Ge. Comparing theoretical spectral functions with the angle resolved photoemission spectra (ARPES), provides us with a better understanding of the SrTiO₃ buffer surface. Using this strategy we stabilized ferroelectric state with out-of-plane polarization in BaTiO₃ (BTO) grown on Si with an STO buffer. And we demonstrate both out-of-plane in-plane polarized BTO growth on Ge (001). Annular dark field microscopy is used to elucidate the atomic structure of the semiconductor/oxide interface that is used in subsequent first principles calculations of the band alignment at the interface. We use a combination of polarization force and microwave impedance microscopies to investigate the ferroelectric response and field effect in our structures.

This work is done in collaboration with Patrick Ponath, Kurt Fredrickson, Agham Posadas, John Ekerdt, David Smith, Martin Frank, Vijay Narayanan, Catherine Dubourdieu, Sergei Kalinin and Keji Lai. It is

supported by the Air Force Office of Scientific Research under grant FA9550-12-10494, Office of Naval Research (ONR) under grant N000 14-10-1-0489, National Science Foundation under grant DMR- 1207342, and Texas Advanced Computing Center.

11:40am **EM2-WeM12 Enhanced Performance Metal/Insulator/Insulator/Metal (MIIM) Tunnel Diodes**, *N. Alimardani, John F. Conley, Jr.*, Oregon State University

Thin film metal-insulator-metal (MIM) tunnel devices are gaining interest for applications such as hot electron transistors, diodes for optical rectenna based IR energy harvesting, IR detectors, large area macroelectronics, and selector diodes to avoid the sneak leakage in RRAM crossbar arrays. For many of these applications, figures of merit include high asymmetry and strong nonlinearity of current vs. voltage (I-V) behavior at low turn on voltages (V_{ON}). The common strategy to achieving rectification in MIM devices relies on Fowler-Nordheim tunneling (FNT) conduction in conjunction with the use of dissimilar work function metal electrodes to produce an asymmetric, polarity dependent electron tunneling barrier. The properties of single layer MIM diodes are dominated by the choice of insulator. Performance is limited by the workfunction difference that can be achieved between the electrodes as well as the metal-insulator band offsets. Wide bandgap oxides are limited by high V_{ON} . Narrow bandgap dielectrics such as Ta_2O_5 and Nb_2O_5 are attractive because the small barrier heights allow for low turn-on voltages. However, because conduction in these materials is based on emission rather than tunneling, they may not be suitable for high speed rectification. Recently, we showed that a nanolaminate pair of insulators (Al_2O_3/HfO_2) can be used to form MIIM diodes with enhanced performance over single layer MIM diodes and demonstrated that observed enhancements in low voltage asymmetry are due to "step tunneling," a situation in which an electron may tunnel through only the larger bandgap insulator instead of both.¹

In this work, we show that MIIM diodes may require only one of the insulators to be dominated by tunneling and thus allow use of narrow band gap insulators for tunnel devices. Atomic layer deposition (ALD) was used to deposit nanolaminate insulators on smooth amorphous metal bottom electrodes. We demonstrate that Ta_2O_5 , a narrow bandgap dielectric dominated by thermal emission, may be combined with Al_2O_3 , a wide bandgap dielectric dominated by tunneling, to achieve high asymmetry, low V_{ON} MIIM diodes whose overall performance is dominated by tunneling. The performance of a variety of other bilayer MIIM diodes (HfO_2/Ta_2O_5 , ZrO_2/Ta_2O_5 , Al_2O_3/ZrO_2 , and HfO_2/ZrO_2) will be discussed as well. These results advance the understanding needed to engineer thin film tunnel devices for microelectronics applications.

1. N. Alimardani and J.F. Conley, Jr., Appl. Phys. Lett. 102, 143501 (2013).

12:00pm **EM2-WeM13 Assessment of Barrier Heights between ZrCuAlNi Amorphous Metal and SiO_2 , Al_2O_3 , and HfO_2 using Internal Photoemission Spectroscopy**, *Tyler Klarr*, Oregon State University, *L. Wei, N.V. Nguyen, O.A. Kirillov*, National Institute of Standards and Technology (NIST), *J. McGlone, J. Wager, J.F. Conley*, Oregon State University

As scaling of Si based devices approaches fundamental limits, thin film metal-insulator-metal (MIM) tunnel diodes are attracting interest due to their potential for high speed operation. Because operation of these devices is based on tunneling, electrode / interfacial roughness is critical. Recently, we showed that combining ultra-smooth bottom electrodes with insulators deposited via atomic layer deposition (ALD) enabled reproducible fabrication of MIM diodes with stable I-V behavior.¹ Key performance parameters of MIM diodes include high I-V asymmetry and low turn-on voltage. The standard way to achieve asymmetry relies on the use of non-equivalent workfunction metal electrodes to induce a built-in field that creates polarity dependent electron tunneling barrier.² Assessment of metal-insulator barrier heights is therefore critical for predicting diode performance.

In this work, we report the first use of internal photoemission spectroscopy (IPE) to measure barrier heights between an amorphous ZrCuAlNi (ZCAN) metal bottom electrode and several high-k dielectrics. MIM stacks were fabricated on Si substrates capped with 100nm of thermally grown SiO_2 and a 150nm thick ZCAN amorphous metal bottom electrode deposited via DC magnetron sputtering. Al_2O_3 and HfO_2 were deposited via thermal ALD at 250°C using H_2O and TMA or TEMA-Hf, respectively. SiO_2 was deposited using plasma-enhanced ALD (PEALD) at 200°C using O_2 and bis-diethylaminosilane (BDEAS). For IPE measurements, semitransparent top electrodes were formed by electron beam evaporation of Al (0.04mm²) and patterned by a multistep photolithography process. In IPE, the conduction band offset between two materials is characterized by measuring the additional current created by photo-excitation of carriers under an applied bias (V_{app}). Devices were tested in a custom built IPE system in which incident photon energy (E_{ph}) from a broadband 150W xenon lamp source

was swept from 1.5 to 5eV while the increase in current (photoemission yield) was monitored. The V_{app} polarity was such that photoemission occurs at the ZCAN/insulator interface. The photoemission yield^{1/2} was plotted vs. E_{ph} to determine the spectral threshold at each V_{app} . Finally, a Schottky plot of spectral threshold vs. V_{app} ^{1/2} was used to estimate the zero field barrier heights from the y-axis intercept. Initial analysis indicates barriers of 3.4, 3.2, and 2.7 eV for SiO_2 , Al_2O_3 , and HfO_2 , respectively. Additional dielectrics and metals are under investigation. IPE results will be compared to electrical methods of barrier extraction.

1. N. Alimardani et al, JVSTA 30, 01A113 (2012).

2. J.G. Simmons, JAP 34, 2581 (1963); JAP 34, 1793 (1963).

Energy Frontiers Focus Topic

Room: 315 - Session EN+AS+EM+SE-WeM

Thin Film Photovoltaics

Moderator: Rachel Morrish, Colorado School of Mines

8:20am **EN+AS+EM+SE-WeM2 Epitaxy and Nanochemistry of CdS on Cu(In,Ga)Se₂ for Photovoltaic Devices**, *X. He*, University of Illinois at Urbana Champaign, *H. Tellez, J. Druce*, Kyushu University, Japan, *K. Demirhan, Miasole, P. Ercius*, Lawrence Berkeley National Laboratory, *V. Lordi*, Lawrence Livermore National Laboratory, *J. Kilner*, Imperial College London, UK, *T. Ishihara*, Kyushu University, Japan, **Angus Rockett**, University of Illinois at Urbana Champaign

Cu(In,Ga)Se₂ (CIGS) photovoltaics are very promising candidates for high-performance energy generation from sunlight. They typically include a heterojunction between CdS and CIGS. The nature of that heterojunction is critical to the performance of the devices. We present experimental results on the nanochemistry of CIGS and CIGS/CdS heterojunctions and the nanostructure of the junctions. In particular we present low energy ion scattering (LEIS) results on epitaxial single crystal CIGS and CIGS/CdS heterojunctions formed by chemical bath deposition of CdS. Also shown are results of high-resolution transmission electron microscopy (TEM) studies of the CIGS/CdS heterojunction where the junction is formed by physical vapor deposition. LEIS has single-atomic-layer chemical sensitivity that provides a unique ability to distinguish the nanochemical nature of CIGS surfaces and heterojunctions. TEM provides both nanostructural information and the possibility to determine the chemistry of the junction on the nanoscale by energy dispersive spectroscopy and energy filtered imaging. Complete epitaxy of the CdS throughout its ~50 nm thickness is observed in the physical-vapor-deposited CdS. Domains of cubic zincblende and hexagonal wurtzite structure CdS have been observed. Twins in the CIGS grains were found to propagate into and often through the CdS layer, resulting in a twin or grain boundary in the CdS. The CdS epitaxial relationship and the effect of surface steps on the CIGS surface are shown. The nanochemical analysis results show significant penetration of Cu into the CdS layer, although no alteration in the CdS nanostructure is observed. The other elements show an abrupt nanochemical junction. LEIS results show the presence of segregated layers on the CIGS surface and further refine the nature of the nanochemical intermixing across the interface.

8:40am **EN+AS+EM+SE-WeM3 Microstructure Development in Cu₂ZnSn(S_xSe_{1-x})₄ Thin Films During Annealing of Colloidal Nanocrystal Coatings**, *B.D. Chernomordik, M. Ketkar, K. Hunter, A.E. Beland, Eray Aydil*, University of Minnesota

A potentially high-throughput and inexpensive method for making Cu₂ZnSn(S_xSe_{1-x})₄ (CZTSSe) thin film absorber layers for solar cells is annealing of coatings cast from colloidal dispersions of CZTS nanocrystals (NCs). The nanocrystal coatings can be annealed in sulfur or selenium atmosphere to make CZTS or CZTSSe, respectively. During annealing, the nanocrystal films can transform into polycrystalline thin films with micrometer size grains. Understanding the roles of key annealing parameters in the development of microstructure in CZTSSe thin films is critical for achieving inexpensive and high-efficiency CZTSSe solar cells. In this presentation, we will discuss the effects of parameters such as selenium vapor pressure, annealing temperature, substrate, and heating ramp-rate on the microstructure development in CZTSSe films and contrast the results with films annealed in sulfur. By using a closed system, rather than a flow furnace, we can quantify and systematically control selenium pressure. Annealing films at high selenium pressure (450 Torr) leads to the formation of a layer of 2-5 μm size CZTSSe grains on top of a nanocrystalline layer that is rich in carbon. This segregation of carbon at the CZTSSe-substrate interface is commonly ascribed to the immediate formation of a capping/blocking layer of CZTSSe grains, which trap the carbon, originating from the ligands on NC surfaces, beneath these grains.

However, we found that a continuous layer of CZTS_xSe grains is not necessary to observe carbon segregation to the film-substrate interface. In contrast, films annealed with sulfur do not show such distinct carbon-rich layers and most of the carbon volatilizes from the film during annealing. Increasing the heating ramp-rate to the annealing temperature eliminates the formation of the carbon-rich layer and results in grains that are approximately 500 nm. We will discuss the results of a series of experiments which led us to conclude that Se condensation during annealing may play a key role in grain growth and carbon segregation.

9:00am EN+AS+EM+SE-WeM4 Effect of Chemical Wet Cleaning on Surface Composition and Work Function of Thin Film CZTS_xSe, Kasra Sardashti, University of California at San Diego, E.A. Chagarov, T. Kaufman-Osborn, University of California, San Diego, S.W. Park, University of California San Diego, R. Haight, W. Wang, D.B. Mitzi, IBM T.J. Watson Research Center, A.C. Kummel, University of California at San Diego

Polycrystalline Copper-tin-zinc-sulfide/selenide (CZTS_xSe) compounds have received wide research interest due to their potential as inexpensive absorber materials composed of earth-abundant elements. Photovoltaic devices fabricated on CZTS_xSe have reached the highest (or record) conversion efficiency of the 12.6%. One of the key parameters to further boost the conversion efficiency is to control the concentration of recombination sites at the surface, in the grain boundaries, and in the bulk. Surface states formed on the sample surface as a result of carbon and oxygen contamination can act as non-radiative recombination sites which limit the ultimate cell efficiency. Therefore, a surface-cleaning method which can effectively reduce the amount of surface oxygen and carbon is necessary for CZTS_xSe processing. In this work, 2 μm thick CZTS_xSe films were prepared by spin coating hydrazine-based precursor solutions onto Mo-coated soda lime glass substrates in a nitrogen-filled glove box. To clean the CZTS_xSe surfaces, three different wet cleaning recipes were used: a) NH₄OH only; b) HCl followed by NH₄OH; 3) H₂O₂ followed by NH₄OH. The effect of the wet cleaning on the surface composition including carbon and oxygen content has been studied via X-ray photoelectron spectroscopy (XPS) and femtosecond ultraviolet photoelectron spectroscopy (fs-UPS). Spatial variation of work function over the surface upon surface cleaning was measured via Kelvin Probe Force Microscopy (KPFM). The stability of the clean surface against reoxidation in ambient was modeled by density functional theory (DFT). The H₂O₂/NH₄OH recipe showed the best result reducing the amount of surface O and C down to 5% and 20%, respectively. This is due to the oxidizing effect of H₂O₂ which converted the carbonaceous surface contaminants into oxides which were later removed by NH₄OH. DFT calculations are consistent with a group VI surface being stable against oxidation by ambient moisture. KPFM measurements showed strongly non-homogeneous surfaces after both NH₄OH-only and H₂O₂/NH₄OH clean. Areas with work function different from CZTS could be the binary chalcogenides formed during the growth and were covered by the native oxide. NH₄OH etch successfully removed the covering oxide and made those phases visible to KPFM.

9:20am EN+AS+EM+SE-WeM5 Phase Transformation, Surface States, and Electronic Structures of Pyrite Thin Films Under In Situ Heating and Oxygen Gas Exposure, Yu Liu, N. Berry, Y.N. Zhang, University of California Irvine, C.-C. Chen, Argonne National Laboratory, H. Bluhm, Z. Liu, Lawrence Berkeley National Laboratory, R.Q. Wu, M. Law, J.C. Hemminger, University of California Irvine

Iron pyrite (cubic FeS₂) with its exceptional optical absorption and suitable band gap is a promising earth-abundant semiconductor for thin film solar cells. Using ambient pressure synchrotron x-ray spectroscopies, we report the nanoscale depth profiles of surface and electronic structures for phase-pure pyrite thin films under *in situ* heating and oxygen gas exposure. Polarized x-ray absorption spectra show that the absorption edge of Fe L₂-edge shifts closer to the Fermi surface with increasing temperature. The XAS line shapes of Fe and S L-edge provide the information of ligand crystal field environment and the phases of the FeS₂ particles. We also report the non-destructive photoemission depth distributions of sulfur defects, vacancies, impurities and oxide as a function of temperature and oxygen dose. Valence band spectra indicate a band gap narrowing related to the creation of surface states at elevated temperature. An irreversible phase transition from pyrite (FeS₂) to pyrrhotites (Fe_{1-x}S) occurs above 430 °C. In addition, our results under *in situ* oxygen gas exposure suggest that the surface monosulfide species is oxidized first, and the reduction in the total density of states near the Fermi surface is caused by oxide layers of sulfate like and iron oxide products on the top ~2 nm.

9:40am EN+AS+EM+SE-WeM6 Improvement of SnS-based Photovoltaic Devices via Reverse Engineering of the V_{oc} and Study of Optimal n-Type Material, Rona Banai, N.J. Tanen, J.J. Cordell, J.R. Nasr, R.E. Urena, H. Lee, J.R.S. Brownson, M.W. Horn, Penn State University

Tin (II) Monosulfide (SnS) has theoretical promise as a new material for thin film photovoltaics (PV). Despite a full decade of rigorous research to develop SnS-based devices, improvement beyond single-digit percent efficiencies seems unattainable. Engineering this material into a usable device is crucial for future development. Our group has been investigating the optical and structural properties of magnetron sputtered SnS_x thin films [1,2,3]. This work will investigate the properties that govern open-circuit voltage, including band gap, series resistance, carrier concentration and built-in potential. Some of these parameters are directly related to the junction material paired with SnS. Several partner materials will be presented with p-SnS including, but not limited to highly doped n-ZnO and n-SnS. Current work is underway to produce n-type SnS as well which would have potential to produce a homojunction.

The optoelectronic properties of SnS make it a suitable material for PV. Its high absorption coefficient, greater than 10⁴ cm⁻¹, and band gap near 1.3 eV are well matched with the solar spectrum. SnS also has a carrier concentration greater than 10¹⁵ cm⁻³ and potential to be both n-type and p-type. Our group is able to produce dense SnS thin films with optimal electronic properties. Sputtering the material gives great control over the material properties and recent work optimizing post-deposition heat treatment has shown great promise for improving the material.

Tin sulfide thin films were sputtered on glass and oxidized silicon substrates at varying substrate-to-target distances, substrate temperature, target power, and chamber pressure. The sputter target was a 3" SnS₂ with 99.999% purity (LTS Research Laboratories, Inc.). These sulfur-rich samples were then annealed under medium vacuum (<2x10⁻⁶ Torr) in the deposition chamber at 400°C to produce a uniform α-SnS, which is most likely to be p-type. Producing n-type SnS is possible via annealing of the films in a methanol/SnCl₄ solution. Production of homojunction SnS-based thin film devices is not found in the literature. Our work aims to produce these devices for the first time and compare them to a well-known partner material such as ZnO.

- [1] R. E. Banai, et al., in *Proceedings of 2012 38th IEEE Photovoltaics Specialists Conference*, Austin, 2012, pp. 164-169.
- [2] R. E. Banai, et al., *IEEE Journal of Photovoltaics*, vol. 3, no. 3, pp. 1084-1089, 2013.
- [3] R. E. Banai, et al., in *Proceedings of 2013 39th IEEE Photovoltaic Specialists Conference*, Tampa, 2013, pp. 2562-2566.

11:00am EN+AS+EM+SE-WeM10 Advanced Contacts for High Efficiency CdTe Solar Cells, D. Meysing, J.J. Li, J. Beach, T.R. Ohno, Colorado School of Mines, M.O. Reese, T.M. Barnes, National Renewable Energy Laboratory, Colin Wolden, Colorado School of Mines

Record CdTe device efficiency has recently surpassed 20%, and it is the leading thin film photovoltaic technology in terms of commercial installation with current manufacturing capacity exceeding 1 GW/year. However, with a Shockley-Queisser limit of ~33% there remains substantial room for additional improvements in efficiency. The quality of both the front and back contacts has substantial influence on CdTe solar cells device efficiency, impacting the current and voltage respectively. This talk will focus on recent work directed at understanding the materials science of both the front and back contact interfaces and optimizing their performance.

Cadmium sulfide is the most commonly employed window layer in the front contact, and its properties can greatly affect cell performance through optical absorption and the quality of the CdS-CdTe junction. In this work, we develop reactive sputtering as an alternative to chemical bath deposition (CBD) for the production of oxygenated cadmium sulfide (CdS:O) to enable high efficiency CdTe solar cells. The intrinsic properties of CdS:O as well as their impact on device performance were studied by varying the oxygen content in the Ar sputtering ambient over the range of 0-10%. XRD, RBS, XPS, and spectrophotometry were used to measure the crystal structure, composition, bonding, and optical properties, respectively. The variation in properties is unsurprisingly non-linear, and optimal performance is attributed to a compromise between optical transmission, which improves monotonically with oxygen content, and band alignment which sharply attenuates device performance beyond a critical threshold.

It is notoriously difficult to make a good ohmic contact to CdTe using conventional metals, because this requires a work function of greater than 5.7 eV. Copper-doped zinc telluride (ZnTe:Cu) is one of the most commonly employed buffer layers to mitigate this issue. ZnTe was identified due to its valence band alignment and compatibility with CdTe. Copper has both positive and deleterious effects and it is critical to precisely control both its amount and spatial distribution in order to obtain high

efficiency. We have developed a back contacting procedure that employs rapid thermal processing (RTP) to deliver precise control over the activation and distribution of Cu. The RTP process is coupled with atom probe tomography and advanced optoelectronic characterization to improve our understanding of the structure-property-performance relationships in this system. The advances achieved here using commercially scalable processes are combined to produce devices with $V_{oc} > 850$ mV and efficiencies exceeding 16%.

11:20am **EN+AS+EM+SE-WeM11 Structural Variations and their Effects on the Fundamental Bandgap of $ZnSnN_2$** , *Nathaniel Feldberg*, University at Buffalo-SUNY, *Y. Yang*, University of Michigan, *W.M. Linhart*, *T.D. Veal*, University of Liverpool, UK, *P.A. Stampe*, *R.J. Kennedy*, Florida A&M University, *D.O. Scanlon*, University College London, UK, *L.F.J. Piper*, Binghamton University, *N. Senabulya*, *R. Clarke*, University of Michigan, *R.J. Reeves*, University of Canterbury, New Zealand, *S. Durbin*, Western Michigan University

In recent years Zn-IV-N₂ compounds have seen increased interest as potential earth abundant element semiconductors for photovoltaic and solid state lighting applications. Several reports of successful growth for the Ge and Si containing compounds are extant as well as more recent publications on the Sn containing member of the family. This material offers a possible alternative to indium containing materials which have experienced large price fluctuations due to limited domestic supply, lack of recycling and heightened demand. Our films were grown by plasma assisted molecular beam epitaxy on (111)-yttria stabilized zirconia. In the case of an ordered lattice, density functional theory (DFT) predicts an orthorhombic structure; however, the disordered lattice is predicted to be pseudo-hexagonal. Reflection high energy electron diffraction patterns for these films indicate single crystal structure with hexagonal symmetry, consistent with X-ray diffraction measurements. Hall effect indicates carrier concentrations in the $3\text{-}10 \times 10^{21} \text{ cm}^{-3}$ range for which we would expect a significant Burstein-Moss shift. Contrary to expectations, optical measurements of absorption onset occur at higher energy in films with lower carrier concentrations. As in $ZnSnP_2$, the bandgap is expected to narrow with the introduction of disorder for this material; this narrowing behavior is consistent with observed variations in absorption spectra. Of practical interest is the possibility of a material with a tunable bandgap without the need for traditional alloying. $Zn\text{-}Sn\text{-}N_2$ is expected to have a bandgap varying from 1.1 to 2 eV controlled by the continuous degree of order in the cation sublattice. Although hard X-ray diffraction measurements of these films do not show any variation from a hexagonal structure, Hall measurements of carrier concentrations compared with absorption data indicates that our samples vary their absorption onset, not as would be expected from Burstein-Moss Shift, but in a manner consistent with a variation in the lattice order. DFT calculations indicate that there is a variation in the Density of States between the ordered and disordered films. Films which were consistent with increased order absorption are also consistent with an increased order density of states measured by HAXPES.

This project is supported by NSF grant DMR1244887 (Program Director Charles Ying), and EPSRC grant EP/G004447/2.

11:40am **EN+AS+EM+SE-WeM12 Inhomogeneity of $p\text{-}n$ Junction and Grain Structure of Thin Film CdTe Solar Cells Studied by Electron Beams**, *Heayoung Yoon*, *P. Haney*, NIST, *P. Koirala*, University of Toledo, *J.I. Basham*, *Y. Yoon*, NIST, *R.W. Collins*, University of Toledo, *N.B. Zhitenev*, NIST

Thin film CdTe solar cells are a promising photovoltaic (PV) technology in today's market due to their high optical absorption and inexpensive fabrication processes. However, the current module efficiency is well below the theoretically estimated maximum efficiency (13% vs. 30%). Recent studies have suggested that inhomogeneity of the PV materials is mainly responsible for the low power conversion efficiency. In this work, we investigate the variation of local PV properties of CdTe solar cells, focusing on grain bulk, grain boundaries, and $n\text{-}CdS$ / $p\text{-}CdTe$ junctions. The window (≈ 120 nm thick CdS) and absorber (≈ 2.2 μm thick CdTe) layers were sputtered on a TCO (transparent conductive oxide) coated glass substrate followed by CdCl₂ treatment. The back contact metals (3 nm Cu / 30 nm Au) were deposited and annealed, creating 256 devices in a 15 cm by 15 cm solar panel. Following light and dark current-voltage measurements, we performed local characterizations using electron beams for high (> 13%) and low efficiency (< 6%) devices within the panel. Electron beam induced current (EBIC) was used to measure the local carrier collection efficiency with a spatial resolution of ≈ 20 nm exciting carriers either from the top surface or the cross-sections of the devices. Cross-sectional EBIC data reveals that the peak of efficiency is in the middle of CdTe layer in the low efficiency devices, while the carrier collection is maximal near the $p\text{-}n$ junction in the high efficiency devices. The EBIC contrasts at grains/grain boundaries in these devices are also compared. The measured local electronic properties are correlated to microstructural morphology

(Transmission Electron Microscopy), orientation (Electron Back Scattered Diffraction), and chemical composition (Energy Dispersive X-ray spectroscopy). We perform 2D model drift-diffusion simulations to determine the magnitude of downward band-bending near grain boundaries (with typical magnitude of 0.2 eV). We will discuss the impact of carrier generation rate (high level injection vs. low level injection) in EBIC analysis.

12:00pm **EN+AS+EM+SE-WeM13 Micro-Structural Activation Mechanisms in Thin Film CdTe Photovoltaic Devices**, *John Walls*, *A. Abbas*, *J.W. Bowers*, *P.M. Kaminski*, Loughborough University, UK, *K. Barth*, *W. Sampath*, Colorado State University

Thin Film CdTe photovoltaics is a commercially successful second generation technology now used extensively in solar energy generation at the utility scale. Although the cadmium chloride treatment is a process that is essential to produce high efficiency devices, the precise mechanisms involved in the re-crystallization and associated improvement in electronic properties have not been fully understood. In this paper we report on the application of advanced micro-structural characterization techniques to study the effect of the cadmium chloride treatment on the physical properties of the cadmium telluride solar cell deposited by both close space sublimation (CSS) and magnetron sputtering and relate these observations to device performance. In particular, High Resolution Transmission Electron Microscopy (HRTEM) reveals that the untreated material contains high densities of planar defects which are predominantly stacking faults and that the optimized cadmium chloride treatment removes these completely with only twins remaining. Parallel theoretical studies using Density Functional Theory (DFT) shows that certain types of stacking fault are responsible for the poor performance of the untreated material. Extending the treatment time or increasing the annealing temperature above $\sim 400^\circ\text{C}$ improves the microstructure but results in lower efficiency devices. Composition -depth profiling using XPS and SIMS reveals that this deterioration in performance is linked with chlorine build up at the CdS/CdTe junction. These experiments and parallel theoretical studies have improved our understanding of the mechanisms at work in the cadmium chloride assisted re-crystallization of CdTe and could lead to further increases in device efficiency

Wednesday Afternoon, November 12, 2014

2D Materials Focus Topic

Room: 310 - Session 2D+AS+EM+MI+MN+NS+TF-WeA

Properties of 2D Materials

Moderator: Guy Le Lay, Aix-Marseille University

2:20pm **2D+AS+EM+MI+MN+NS+TF-WeA1 Tuning Excitons in Two-Dimensional Semiconductors**, Kirill Bolotin, Vanderbilt University
INVITED

Monolayer molybdenum disulfide (MoS₂) is a two-dimensional crystal comprising a single layer of molybdenum atoms sandwiched between two layers of sulfur atoms. Monolayer MoS₂ differs from its celebrated all-carbon cousin, graphene, by the presence of a direct band gap leading to robust light absorption and by strong electron-electron interactions leading to formation of rightly bound excitons. In this talk, we demonstrate that both electrical and optical properties of MoS₂ can be widely tuned via external influences.

In the first part of the talk, we study changes in the bandgap and phonon spectra in strained MoS₂. We investigate the transition from direct to indirect band gap in MoS₂ under uniaxial strain. The experimental signatures of this transition include strain-induced changes in the PL wavelength and intensity.

Second, we examine the influence of the environment of MoS₂ on its properties. We demonstrate substrate-induced scattering is suppressed in suspended MoS₂ specimens. We use photocurrent spectroscopy to study excitons in pristine suspended MoS₂. We observe band-edge and van Hove singularity excitons and estimate their binding energy. We study dissociation of these excitons and uncover the mechanism of their contribution to photoresponse of MoS₂.

3:00pm **2D+AS+EM+MI+MN+NS+TF-WeA3 Electron-Phonon Coupling and Photoluminescence in Single Layer Transition Metal Dichalcogenides**, Neha Nayyar, V. Turkowski, D.T. Le, T.S. Rahman, University of Central Florida

Single layer MoS₂ and other transition metal dichalcogenides have been the subject of numerous investigations because of their unusual optical, electronic and transport properties. To understand and thereby tune their photoluminescent properties, we have analyzed the role of electron-phonon interactions. Density functional perturbation theory is used to calculate the dispersion of system phonons, while electron-phonon coupling is obtained using the Eliashberg approach. Time-dependent density-functional theory based calculations using the density-matrix approach is employed to study the exciton and trion excitations which are found to appear as peaks in the absorption spectrum in the visible range with binding energy ~0.5 – 1 eV and ~0.02-0.03 eV, correspondingly. The emission peak is found to also lie in the visible spectrum and is sensitive to the value of the electron-phonon coupling, which depends on the nature and extent of doping. The position of the spectral peaks may thus be manipulated by doping. Calculations of the self-energy and spectral functions of doped systems show excitations to have 10-100 fs lifetime, which makes the system interesting for ultrafast applications. Comparison will be made of these optical properties of several single layer dichalcogenides and contact will be made with available experimental data. Work supported in part by DOE Grant No. DOE-DE-FG02-07ER46354

3:20pm **2D+AS+EM+MI+MN+NS+TF-WeA4 Temperature Dependent Photoluminescent Spectroscopy of MoS₂**, Michael Watson, J.R. Simpson, Towson University & NIST, R. Yan, H. Xing, University of Notre Dame, S. Bertolazzi, J. Brivio, A. Kis, EPFL, Switzerland, A.R. Hight-Walker, NIST

We report temperature and power dependent photoluminescence (PL) of molybdenum disulfide (MoS₂). Mechanical exfoliation of MoS₂, from bulk provides single-layer flakes which are then transferred either to sapphire substrates or suspended over holes in Si/SiO₂. We measure temperature dependence from ~100K to 400K and power dependence from ~6μW to ~7mW using an Argon laser at 514.5nm and a HeNe laser at 632.8 nm. The PL spectrum exhibits a main excitonic peak(A) at ~1.87eV which consist of both neutral excitons and charged trions (A⁻ or A⁺) [1]. The A exciton peak and the A⁻ exciton peak redshift and broaden with increasing temperature and power. Along with the A peak, we observe a lower energy bound exciton (BE) that is likely related to defects. The BE, a broad peak centred at ~1.7eV, linearly redshifts and narrows with increasing power. The power dependence of both the main and bound peak saturates above 0.5mW. Raman temperature and power dependence will also be discussed [2].

[1] K.F. Mak et al. Nat. Mat 12,207(2013)

[2] R.Yan and J.R.Simpson, S. Bertolazzi and J. Brivio, M. Watson, X.Wu and A. Kis, T.Luo, H.G.Xing, A.R. Hight Walker, ACS Nano 8,1 (2013)

4:20pm **2D+AS+EM+MI+MN+NS+TF-WeA7 Effects of Dimensionality on the Raman and Photoluminescence Spectra of and TaSe₂ and TaS₂ Dichalcogenides**, Danilo Romero, University of Maryland, College Park, M. Watson, J.R. Simpson, Towson University, H. Berger, Ecole Polytechnique Federale de Lausanne, Switzerland, A.R. Hight Walker, NIST

We investigate the effects dimensionality on the electronic properties through the optical spectra of the transition-metal dichalcogenides 2H-TaSe₂ and 1T-TaSe₂, and 1T-TaS₂. In bulk, these materials exhibit electronic states from Mott insulator, commensurate and incommensurate charge-density phases, and superconducting ground state as function of temperature. We explore the evolution of these properties as the materials approach a few layers, achieved via mechanical exfoliation of bulk single-crystals. Raman and photoluminescence spectroscopy of 2H-TaSe₂ and 1T-TaSe₂, and 1T-TaS₂, carried out over a wide-range of temperature, were used as a probe of the change of the electronic properties from the bulk to single-layer phases of the materials. Comparison of the phonon and excitonic transitions as a function of temperature and dimensionality will be presented.

4:40pm **2D+AS+EM+MI+MN+NS+TF-WeA8 Few-Layer and Symmetry-Breaking Effects on the Electrical Properties of Ordered CF₃Cl Phases on Graphene**, Josue Morales-Cifuentes, T.L. Einstein, Y. Wang, J. Reutt-Robey, University of Maryland, College Park

An effective potential mechanism for breaking the inherent sublattice symmetry of graphene has been studied using DFT calculations on hexagonal boron nitride.¹ Electrical detection of CF₃Cl phase transitions on graphene shows the existence of a commensurate ordered phase in which this can be tested.² We study the electronic properties of similar phases varying coverage and orientation of CF₃Cl with respect of the graphene substrate using VASP ver 5.3.3, with ab initio van der Waals density functionals (vdW-DF1, vdW-DF2).^{3,4} Consistent with a physisorbed phase, binding energies are calculated to be on the order of 280meV, and insensitive to coverage and orientation of the CF₃Cl molecules. Charge transfer was calculated to be sensitive with coverage, but not orientation, which is qualitatively consistent with experiment. For low coverages, sublattice symmetry breaking effects are responsible for gap openings in the order of 4meV, whereas for large coverages it is the formation of ordered overlayers that opens gaps of 15meV. Furthermore, in bilayer graphene at low coverage we estimate an enhanced gap of 20meV.

[1] Gianluca Giovannetti et al. , PRB **76**, 073103(2007)

[2] Yilin Wang et al. , APL **103**, 201606 (2013)

[3] Jiri Klimes et al. , PRB **83**, 195131 (2011)

[4] Kyuho Lee et al. , PRB **82**, 081101(R) (2010)

5:00pm **2D+AS+EM+MI+MN+NS+TF-WeA9 Optical Anisotropies in Layered Nanomaterials**, Jon Schuller, UC Santa Barbara
INVITED

In nanomaterials optical anisotropies reveal a fundamental relationship between structural and optical properties. In layered materials, optical anisotropies may result from in-plane and out-of-plane dipoles associated with intra- and inter-layer excitations respectively. In this talk, I describe a novel method wherein we resolve the orientation of luminescent excitons and isolate photoluminescence signatures from distinct intra- and inter-layer excitations, respectively. We compare photoluminescence anisotropies in materials with weak or strong interlayer coupling, MoS₂ and the organic semiconductor PTCDA respectively. We demonstrate that photoluminescence from MoS₂ mono-, bi- and trilayers originates solely from in-plane excitons, whereas PTCDA supports distinct in-plane and out-of-plane exciton species with different spectra, dipole strengths and temporal dynamics. The insights provided by this work are important for understanding fundamental excitonic properties in layered nanomaterials and designing optical systems that efficiently excite and collect light from exciton species with different orientations.

5:40pm **2D+AS+EM+MI+MN+NS+TF-WeA11 Mechanical Properties of 2D-Materials**, J.M. Gonzales, University of South Florida, R. Perriot, Los Alamos National Laboratory, Ivan Oleynik, University of South Florida

Graphene and other two-dimensional (2D) materials possess extraordinary mechanical properties, which are currently being explored in various novel applications. Atomic force microscopy (AFM) nanoindentation experiments

on both pristine and polycrystalline samples of 2D materials, while being successful in measuring overall mechanical performance of graphene, require some theoretical input to extract the important mechanical properties. Large-scale atomistic molecular dynamics simulations are used to predict the mechanical properties of 2D materials, such as the elastic moduli, breaking strength, stress/strain distributions, and mechanisms of fracture under conditions of AFM nanoindentation experiments. Perfect, defective, and polycrystalline samples are investigated using large-scale molecular dynamics simulations with a screened environment-dependent bond order (SED-REBO) potential. The mechanisms of crack propagation in both perfect and defective samples will also be presented.

6:00pm **2D+AS+EM+MI+MN+NS+TF-WeA12 Mechanical Control of Structural Phase Transitions in Two-Dimensional Mo- and W-Dichalcogenide Monolayers**, *Evan Reed, K.-A.N. Duerloo, Y. Li*, Stanford University

Mo- and W- dichalcogenide compounds have a two-dimensional monolayer form that differs from graphene in an important respect: it can potentially have more than one crystal structure. Some of these monolayers exhibit tantalizing hints of a poorly understood structural metal-to-insulator transition with the possibility of long metastable lifetimes. If controllable, such a transition could bring an exciting new application space to monolayer materials beyond graphene. Here we discover that mechanical deformations provide a route to switching the thermodynamic stability between a semiconducting and a metallic crystal structure in these monolayer materials. We employ density functional and hybrid Hartree-Fock/density functional calculations including vibrational energy corrections to discover that single layer MoTe₂ is an excellent candidate phase change material. We identify a range from 0.3% to 3% for the tensile strains required to transform MoTe₂ under uniaxial conditions at room temperature. We elucidate the appropriate thermodynamic constraints for monolayers, which can differ from bulk materials. The potential for mechanical phase transitions is predicted for all six studied compounds. The potential application space ranges from catalysis to information storage and nanoscale electronics.

Electronic Materials and Processing Room: 311 - Session EM+EN+TF-WeA

Thin Films and Materials for Energy Storage

Moderator: Christopher Hinkle, University of Texas at Dallas

2:20pm **EM+EN+TF-WeA1 Investigation of Composite Dielectric Materials for Energy Storage**, *Kimberly Cook-Chennault, U. Sundar, W. Du*, Rutgers, the State University of New Jersey

Electrical energy storage plays a key role in electronics, stationary power systems, hybrid electric vehicles and pulse power applications. Traditionally, bulk ceramic dielectric oxides are used for these applications, though they suffer from inherently low breakdown field strength, which limits the available energy density and increases the dielectric loss. On the other hand, polymers have high break down field strengths, low dielectric losses and can be readily processed into thin films, but suffer from relatively low dielectric permittivity, and thus low energy densities. As a result, contemporary materials have become a limiting factor to the realization of miniaturized devices, due to Moore's Second law, in terms of size, cost and parasitic impedances. Realization of micrometer to sub-micrometer scale commercial and industrial devices such as, high density DRAM (dynamic access memory), non-volatile memory (NRAM) and capacitors, require advanced materials that can both accumulate and deliver vast amounts of energy nearly instantaneously with minimal dielectric losses. This work focuses on examination of piezoelectric-epoxy based composites for dielectric materials, and explores the interrelationship processing plays on realized electrical and dielectric properties. Materials under investigation include lead-zirconate-titanate, and barium titanate – epoxy composites.

2:40pm **EM+EN+TF-WeA2 Preparation and Characterization of ZnO Nano Rods**, *P. Thamaraiselvan*, Selvam Arts and Science College, India, *M. Saroja, M. Venkatachalam, P. Gowthaman*, Erode Arts and Science College, India, *S. Ravikumar*, Sengunthar Arts and Science College, India, *S. Shankar*, Erode Arts and Science College, India

ZnO nano rods were prepared using chemical bath deposition technique. ZnO seed layer thin films were deposited on glass substrates by dip coating method. Subsequently, ZnO seed-coated glass substrates were immersed in aqueous solution of zinc nitrate and hexamethylenetetramine (HMT) at three different growth time of 3, 4 and 5 hours at low temperature of 90°C.

0.02 mol of Zinc nitrate and 0.2 mol of Hexamethylenetetramine (HMT) on 1:10 molar concentration were used for the growth of Zinc oxide nano rods. The structure and surface morphology of the ZnO nano rod were studied using X-ray diffraction Scanning Electron Microscopy (SEM), respectively.

3:00pm **EM+EN+TF-WeA3 Rational Design of Energy Storage Materials from Earth Abundant Elements**, *Kyeongjae Cho*, UT Dallas
INVITED

As a part of global scale renewable energy technology solutions, large scale energy storage system (ESS) would be critical in mediating the gaps between cycles of energy demands and intermittent solar and wind energy generations. Furthermore, electric vehicles (EV) require significantly larger energy storage capacity compared to the batteries used electronic device applications. There are significant challenges in extending the current Li ion battery (LIB) technology (based on graphite anode, organic liquid electrolyte, and Co oxide cathode) to EV and ESS applications. Many different approaches are currently investigated to overcome the capacity, safety and cost issues of LIB in EV and ESS applications, and new battery technology researches include Si anode, Na and Mg batteries, metal-air batteries, over-lithiated-oxide (OLO) [1] and silicate cathodes [2] for LIB. OLO and silicate cathode materials provide two times larger charge storage capacity (~300 mAh/g) compare to current commercial LiCoO₂ (LCO) or Li(Ni,Co,Mn)O₂ (NCM) cathodes. Both Li₂MnO₃ and Li₂FeSiO₄ are based on earth abundant transition metals of Mn and Fe so that a successful development of these cathode materials would improve cathode capacity and cost problems. In order to achieve the short term goal of OLO and silicate cathode development and the long term goal of EV and ESS material development, we have applied the rational material design and development framework developed for pollution control technology in which Pt catalysts are replaced by PdAu alloy and Mn-mullite catalysts. [3-5] In this talk, we will discuss the current status of OLO and silicate cathode material research based on the integrated material design-synthesis-characterization framework.

This work was supported by Samsung GRO project.

1. R. C. Longo et al., "Phase stability of Li-Mn-O oxides as cathode materials for Li-ion Batteries: insights from ab initio calculations" (submitted)
2. R. C. Longo, K. Xiong and K. Cho, "Multicomponent Silicate Cathode Materials for Rechargeable Li-ion Batteries: An ab initio study," Journal of the Electrochemical Society 160, A60 (2013).
3. X. Hao et al., "Experimental and Theoretical Study of CO Oxidation on PdAu Catalysts with NO Pulse Effects," Top. Catal. 52, 1946 (2009).
4. B. Shan et al., "First-principles-based embedded atom method for PdAu nanoparticles," Phys. Rev. B 80, 035404 (2009).
5. W. Wang, G. McCool, N. Kapur, G. Yuan, B. Shan, M. Nguyen, U. M. Graham, B. H. Davis, G. Jacobs, K. Cho, X. Hao, "Mixed-Phase Oxide Catalyst Based on Mn-Mullite (Sm, Gd)Mn₂O₅ for NO Oxidation in Diesel Exhaust," Science 337, 832-835 (2012).

4:20pm **EM+EN+TF-WeA7 Transferring Environmentally Sensitive Battery Materials between GloveBox and UHV Surface Analysis Chamber: Composition Study of Model Battery Interfaces and their Controlled Oxidation**, *Hugo Celio*, University of Texas at Austin

Environmentally sensitive battery materials prepared in an inert environment (e.g., Argon filled glovebox containing trace levels of water and oxygen at ~1 part-per-million) are often difficult to transfer to an ultra-high vacuum (UHV) chamber for surface analysis. While minimizing additional oxidant(s) exposure, three challenging factors arise from transferring environmentally sensitive materials: 1) Engineering a pump-down load-lock to transition from atmospheric pressure to UHV regime, 2) developing a method to generate a set of figures of merit (FOMs) that allows a user to evaluate transfer reliability, and 3) evaluating of the amount of material that subsequently undergoes, due to reaction with trace ppm levels of oxidants in the Argon gas, oxidation during transfer. To target these issues a novel transfer load-lock/capsule was built and directly coupled to a UHV surface analysis chamber, equipped with X-ray photoelectron spectrometer (XPS). This new load-lock/capsule has lead to a new capability to study the composition of model battery materials (e.g., silicon anode and metal oxide cathode) at the solid electrolyte interfacial (SEI) layer, including their controlled oxidation post-transfer.

4:40pm **EM+EN+TF-WeA8 Development of Thin Film Si-C Based High Temperature Microsupercapacitor Devices**, *J.P. Alper, C.-H. Chang, C. Carraro, Roya Maboudian*, University of California at Berkeley
On-chip integrated energy storage and delivery at high power is an important aspect in realizing the full potential of microsystems technology such as remote mobile sensor platforms. One promising high power device which has garnered much attention is the supercapacitor. Energy is stored in

SC's at the electrode-electrolyte interface, making the high specific surface area of thin films of 1-d materials particularly attractive for application to these devices. However many operations such as in the chemical process industries which could benefit from remote sensor deployment reach temperatures beyond current electrode and electrolyte material constraints. Here we report on the use of bottom-up chemical vapor deposition based silicon carbide (SiC) nanowires and top-down chemically etched SiNWs passivated with an ultrathin carbon sheath as thin film micro-SC electrodes. The electrochemical performance of the two nanowire types in high temperature compatible electrolytes such as ionic liquids and yttria stabilized zirconia (YSZ) are presented. The materials are stable during cycling and achieve specific capacitance values comparable to or better than previously reported carbon electrodes. Operation at temperatures above those attainable with standard electrode-electrolyte systems is also demonstrated. Current challenges for the methods presented and strategies for overcoming them are discussed.

5:00pm **EM+EN+TF-WeA9 Rate Capability of Silicon Carbon Nanotube Anodes for Lithium Ion Batteries**, *Lawrence Barrett, R. Fan, R.C. Davis, K. Hinton, R.R. Vanfleet*, Brigham Young University

Research has shown stable high capacity lithium ion battery anodes can be made from silicon deposited on carbon nanotubes (CNTs). However, rate capability remains a challenge. We have explored two potential limiting factors: diffusion from the top of the forest down and diffusion into the silicon coating. To probe top down diffusion, we compared a uniform CNT forest to a forest with an array 10 um holes spaced 10 um apart to allow channels for faster top down diffusion and found rate capability was unaffected, indicating top down diffusion is not a limiting factor. We also probed diffusion through the silicon coating by changing the thickness and morphology of the coating.

5:20pm **EM+EN+TF-WeA10 Characterization and Optimization of Interface Engineering on Li Metal Anode Using Atomic Layer Deposition and In Situ Electrochemical AFM**, *Chuan-Fu Lin, A.C. Kozen, A.J. Pearse, M. Noked, M.A. Schroeder, S.B. Lee, G.W. Rubloff*, University of Maryland, College Park

Rechargeable Li-metal anode batteries could be considered the holy grail of energy storage systems because Li offers extremely high theoretical specific capacity (3860 mAh/g), low density (0.59 g/cm³), and the lowest negative electrochemical potential (-3.040 V vs. standard hydrogen electrode). However, Li is thermodynamically unstable with organic solvents, inviting serious capacity degradation as well as safety concerns such as Li dendrite growth. The prognosis for Li anodes would be profoundly enhanced for next generation batteries if suitable passivation schemes could be developed to protect Li anodes without significantly reducing ion transport between Li and electrolyte.

In our laboratory, we use atomic layer deposition (ALD) to precisely deposit very thin layer of aluminum oxide (Al₂O₃) on Li foils, using glove box and UHV environments to avoid air exposure while depositing passivation layers on the Li metal surface. We then characterize the surface morphology of the passivated Li by AFM at varying stages of electrochemical reaction and as a function of time and film thickness. We observed the growth of defects on ALD-passivated Li metal surface, decorated by AFM structures indicative of localized electrochemical reactions. The resulting defect density decreased as the film thickness increased.

For thinner ALD protection layers, EC-AFM showed bubble-like structures decorating the steps and boundaries of ALD/Li metal surface in electrochemical system, suggesting mechanisms associated with volatile products. While thin ALD layers suppress charge transfer processes which lead to electrolyte decomposition and formation of solid electrolyte interphase (SEI) [1-2], defects in the ALD passivation layer may cause localized SEI formation, which in turn involves volatile products (e.g., C₂H₄, CO). Alternatively, trace H₂O in the propylene carbonate electrolyte may react with Li metal through pinholes in the ALD layer, leading to LiOH and volatile H₂ products. We are working to differentiate between these by applying in-situ mass spectroscopy to monitor the gas formation in the cell as a function of controlled water content and ALD film thickness. The identification of passivation layer degradation mechanisms and the development of robust approaches to metal anode protection have profound benefit to a variety of beyond-Li-ion batteries.

References:

1. Kevin Leung, J. Phys. Chem. C, 2012, 117, 1539-1547.
2. Kevin Leung et al., JACS, 2011, 133, 14741-14754.

5:40pm **EM+EN+TF-WeA11 The Road to Next-Generation Energy Storage is Paved with Zinc**, *Joseph Parker, C.N. Chervin*, Naval Research Laboratory, *I.R. Pala*, National Research Council postdoc working at Naval Research Laboratory, *E.S. Nelson*, Pathways Student working at Naval Research Laboratory, *J.W. Long, D.R. Rolison*, Naval Research Laboratory

While Li-ion batteries presently dominate the energy-storage landscape, zinc-based batteries offer a compelling alternative due to the earth-abundance of zinc, innate safety and cost advantages that arise from using aqueous electrolytes, and device-realized specific energy that is comparable to or higher than Li-ion. Yet the performance of present-day Zn-based batteries is hindered by suboptimal Zn utilization (typically <60% of theoretical capacity) and poor rechargeability—a consequence of the complex dissolution/precipitation processes that accompany Zn/Zn²⁺ cycling and the ad hoc construction of conventional powdered-bed Zn anodes. We address these limitations by designing and fabricating highly conductive, porous, and 3D-wired Zn “sponge” electrodes from emulsion-cast, consolidated Zn powders that are thermally treated to produce rugged monolithic forms. With this 3D Zn architecture, we achieve >90% Zn utilization when discharged in primary Zn–air cells with retention of the 3D framework of the Zn sponge and uniform deposition of charge/discharge products at the surfaces of the Zn sponge, as verified by scanning electron microscopy and impedance spectroscopy. We further show that the structural characteristics of the Zn sponge promote greater rechargeability when cycled in prototype Ag–Zn and Ni–Zn cells. Our results demonstrate that all Zn-based chemistries can now be reformulated for next-generation rechargeable batteries.

Electronic Materials and Processing

Room: 314 - Session EM-WeA

High-K Dielectrics for 2D Semiconductor

Moderator: Andrew C. Kummel, University of California at San Diego

2:20pm **EM-WeA1 Adding New Functionalities to CMOS Integrated Circuits Via Directed Self-Assembly**, *Theresa Mayer*, Penn State University

INVITED

With CMOS nearing the physical limits of scaling, the future of the semiconductor industry is at a critical point. The International Technology Roadmap for Semiconductors identifies the growing need to interface new nanoscale materials and devices with Si CMOS architectures to sustain nanoelectronic circuit scaling (more-of-Moore) and to discover entirely new electronic systems (more-than-Moore). This talk will describe new directed self-assembly process to position large, diverse, and interchangeable arrays of nanowire sensors or sheets of alternative electronic materials onto fully-processed Si CMOS circuits. The wires or sheets are fabricated off-chip from many different materials tailored for a specific function. Electric-field forces are then used direct different populations of these materials to specific regions of the chip, while also providing accurate registry to a predefined feature on the chip. Following assembly, conventional lithographic processes can then be used to define the nanodevices and connect them to the Si circuit. Several material and device integration examples will be discussed, including the directed assembly of metal-oxide nanowire device arrays as well as monolayer 2D transition metal dichalcogenide crystal materials.

3:00pm **EM-WeA3 Band Gap Engineering of 2D Semiconductor Materials via Atomic Layer Deposition of TiOPc on Graphene and MoS₂**, *Pabitra Choudhury*, New Mexico Institute of Mining and Technology, *A.C. Kummel*, University of California at San Diego

Metal phthalocyanine (MPc) molecules are composed of a metal atom and a surrounding phthalocyanine ligand ring. The metal-ligand interaction and molecule-surface interaction are the two most important parameters, which controls the various physical and chemical properties of this adsorption system of MPc molecules onto the substrate. MPc molecules can potentially be employed for electrostatic doping of non-reactive substrates (for example 2D semiconductor materials), will lead to various applications such as sensors and electronics, and hence MPc become a model system for surface chemistry and nanotechnology. Tytanyl phthalocyanine (TiOPc) is another interesting molecule of phthalocyanine family having anisotropic intermolecular interactions. In this study, TiOPc electrostatic interactions with two nonreactive 2D semiconductor substrates, graphene and MoS₂, were studied. We have carried out first principle density functional theory (DFT) calculations and theoretical analysis to explore the structural and electronic properties of mono- and bi-layer of TiOPc molecule on both graphene and MoS₂. The adsorption of mono- and bi-layer films of TiOPc on graphene shows that there is a net 0.047 electrons and 0.016 electrons

per TiOPc molecule charge transfer takes place from the graphene surface, respectively. Conversely, a net amount of 0.058 electrons and 0.029 electrons per TiOPc molecule charge transfer take place to the MoS₂ surface in case of mono- and bi-layer of TiOPc, respectively. Moreover, we find that the bandgaps of graphene/TiOPc(mono-and bi-layer) and MoS₂/TiOPc(mono-and bi-layer) heterostructures decrease with increasing number of TiOPc layers. Our results suggest that the band gap of 2D semiconductors, MoS₂/TiOPc and graphene/TiOPc heterostructures, could be engineered with atomic layer precision by controlling the number of TiOPc layer deposited on the 2D substrate, which could serve as a potential candidate for both sensor and advanced electronics applications.

3:20pm EM-WeA4 HfSe₂ Thin Films: 2D Transition Metal Dichalcogenides Grown by MBE, Ruoyu Yue, A. Barton, X. Peng, N. Lu, R. Addou, S. McDonnell, L. Chen, J.Y. Kim, University of Texas at Dallas, L. Colombo, Texas Instruments, M. Kim, R.M. Wallace, C.L. Hinkle, University of Texas at Dallas

The growth of high-quality, layered HfSe₂ thin films by molecular beam epitaxy (MBE) on a variety of substrates is demonstrated for the first time. The cross-section of HfSe₂ thin films on highly ordered pyrolytic graphite (HOPG) shows the layered structure of crystalline HfSe₂ with an atomically sharp interface between the HfSe₂ and HOPG, verifying the van der Waals epitaxy. Crystalline HfSe₂ thin films with preferred orientation and hexagonal top surface symmetry are characterized by RHEED, STM, and XRD with a measured lattice constant consistent with the theoretical prediction of the 1-T phase. The stoichiometry (Hf: Se) of crystalline HfSe₂ on HOPG, measured by XPS, is very close to 1:2 and the in-plane and out-of-plane vibration mode peaks of the 1-T structure of HfSe₂ is confirmed by Raman spectroscopy. It is also noted that the crystal quality of the HfSe₂ changes as a function of substrate with the best growth results obtained on inert, hexagonal symmetry surfaces. These results indicate that the growth of novel TMDs by MBE is achievable and opens the possibility for exciting new 2D heterostructures and devices.

4:20pm EM-WeA7 Phonons, Scattering, and Semiclassical Transport Studies in 2D Materials and Devices, Massimo Fischetti, W.G. Vandenberghe, The University of Texas at Dallas **INVITED**

Basic ideas from pseudopotentials and semiclassical-transport will be used to discuss the properties of some novel 2D materials considered for post-Si-CMOS applications. First, it will be shown that in order to scale devices to 5 nm, simple electrostatic scaling laws demand the use of these two-dimensional materials, despite the daunting processing challenges they pose. Graphene will be considered discussing how its outstanding electronic properties become much less interesting when used as a component of some non-ideal structure, such when supported and gated and/or in nanoribbon form. A couple of very interesting ideas will be discussed next: 1. The Bose-Einstein condensation in bilayer systems (motivating UT-Austin's BiSFETs) as an example of how issues of practical implementation may regrettably transform an excellent idea into a pure academic exercise; and 2. Monolayer tin ("stannanane") as a 2D topological insulator with potential applications in spintronics and low-power high-performance devices. Besides discussing its potential electronic properties, the likelihood of actually fabricating such a material will be discussed on the basis of *ab initio* thermodynamics.

5:00pm EM-WeA9 In Situ Transmission Electron Microscopy of Oxides on TMDs, Moon Kim, N. Lu, J. Oviedo, X. Peng, J. Wang, G. Lian, A. Azcatl, S. McDonnell, R.M. Wallace, The University of Texas at Dallas, S. Vishwanath, H. Xing, University of Notre Dame **INVITED**

Over the past two years, transition metal dichalcogenide (TMD) materials, as 2-D crystals, have attracted much interest for a wide range of electronic and optoelectronic device applications. Yet, uniform deposition of sub-10 nm dielectrics on 2-D materials remains challenging. There is a great demand for the visualization and analysis of interfaces and defects in 2-D crystals and gate oxides, which play an important role in the growth and properties of heterostructures. Site-specific cross-sectional TEM imaging and associated techniques have become essential in providing detailed atomic scale information. High angle angular dark field (HAADF)-scanning transmission electron microscopy (STEM) can be used to investigate the atomic structure and chemistry of TMD-oxide interfaces and defects. *In-situ* TEM techniques such as heating and electrical/mechanical probing can also provide information regarding the dynamic behavior of the materials/devices of interest.

Herein, we report our results on HfO₂ and Al₂O₃ thin films deposited on MoS₂ by atomic layer deposition and SnSe₂ FETs with an Al₂O₃ gate oxide. Our *in-situ* TEM work on 2-D materials will also be presented. Based on our study, a possible growth mechanism of oxides on TMD with different surface treatments has been proposed [1,2]. These unique and effective site-

specific and *in-situ* analysis tools can be widely applied to other gate oxides of interest.

This work was supported in part by the Center for Low Energy Systems Technology (LEAST), one of six centers supported by the STARnet phase of the Focus Center Research Program (FCRP), a Semiconductor Research Corporation program sponsored by MARCO and DARPA.

[1] ACS Nano, 7, 10354–10361, 2013.

[2] Applied Physics Letters, 104, 111601, 2014.

5:40pm EM-WeA11 Effects of Neutron Irradiation of Ultra-Thin HfO₂ Films, Kai-wen Hsu, University of Wisconsin-Madison, H. Ren, Applied Materials, R.J. Agasie, University of Wisconsin-Madison, L. Zhao, Y. Nishi, Stanford University, J.L. Shohet, University of Wisconsin-Madison

In order to investigate neutron-induced effects on HfO₂ resistive random-access memory (RRAM), HfO₂ films are subjected to irradiation by neutrons with energies above 1 MeV. Changes in the defect state concentrations of HfO₂ may lead to changes in the states of memory which has the potential to convert a "0" into a "1" in RRAM or vice versa.

Electron-spin resonance (ESR) is used to detect defect-state concentrations of the HfO₂ film deposited on high-resistivity substrates. Additionally, leakage currents of HfO₂ films are also measured to support the ESR data.¹

Neutron irradiation at low fluence decreases the Pb-type and E' defect levels in ultra-thin HfO₂ films because electrons can fill existing states. These electrons come from electron-hole pairs generated by neutron interactions with silicon and oxygen. Thus, a low fluence of neutrons "anneals" the sample. However, when neutron fluence increases, more neutrons collide with oxygen atoms and cause them to leave the lattice or to transmute into different atoms. This causes the E' state concentration to increase. The changes in the number of defect states lead to changes in leakage currents.

This work was supported by the Semiconductor Research Corporation under Contract 2012- KJ-2359 and by the National Science Foundation under Grant CBET-1066231.

¹K-W Hsu, H. Ren, R.J. Agasie, S. Bian, Y. Nishi, and J.L. Shohet, *Applied Physics Letters* 104 032910 (2014)

6:00pm EM-WeA12 Nucleation of Low Temperature HfO₂ Atomic Layer Deposition on InGaAs using Various Native Oxide Removal Techniques, Tyler Kent, University of California at San Diego, K. Tang, Stanford University, S. Lee, C.Y. Huang, V. Chobpattana, University of California at Santa Barbara, K. Sardashti, M. Edmonds, University of California at San Diego, R. Droopad, Texas State University, P.C. McIntyre, Stanford University, A.C. Kummel, University of California at San Diego

One of the major obstacles impeding the advancement of III-V MOSFETs is the large density of interfacial trap states (D_{it}) at the high-k/III-V interface. Poor nucleation of the gate oxide can lead to dangling bonds, strained bonds, and metallic bonds which contribute to D_{it}; additionally, low nucleation density requires a thicker oxide to avoid pinholes which increase gate leakage. The nucleation of HfO₂ was studied using tetrakis(ethylmethylamino)hafnium (TEMAH) and H₂O on the InGaAs (001) and InGaAs (110) surfaces at low temperature, 120 °C, using atomic layer deposition (ALD). Low temperature ALD reduces subcutaneous oxidation of the channel when this is an activated process. The pulse and purge times of the oxidant and reductant were varied and their impact on the nucleation of HfO₂ were studied by fabricating MOSCAPs and extracting the D_{it} using the full interface surface state model. All samples had 10 cycles of an in-situ pre-ALD surface clean developed by Choptabanna and Carter which utilizes atomic H and TMA. The effectiveness of the ex-situ buffered oxide etch (BOE) was examined by fabricating samples with and without this clean. The BOE was more effective on the (001) samples since the non-BOE samples had a larger D_{it} and a higher C_{max} indicating poor nucleation of the HfO₂. The dispersion in accumulation remained constant indicating the BOE had an immediate effect on the interface, rather than deep traps in the oxide. The BOE and non-BOE (110) samples had a nearly identical C_{max}, D_{it}, and dispersion in accumulation indicating the nucleation of HfO₂ is not as dependent on the BOE as the (001) surface. This result obviates the need for the BOE allowing an all dry process on InGaAs(110) and is likely a result of the inherent stability of the (110) surface compared to the (001) surface.

Energy Frontiers Focus Topic

Room: 315 - Session EN+AS+EM-WeA

Organic-Inorganic Interfaces for Energy

Moderator: Ramana Chintalapalle, University of Texas at El Paso

2:20pm EN+AS+EM-WeA1 Towards Efficient Solution Processed Organic Photovoltaic Devices, *Elsa Reichmanis*, Georgia Institute of Technology **INVITED**

Solution-processed π -conjugated semiconductors exhibit potential in the development of low-cost, light-weight and large-area flexible plastic optoelectronics, particularly photovoltaics (OPVs). However, one drawback to current OPVs is their limited efficiency. We have explored the use of donor-acceptor (D-A) hybridization to tailor HOMO/LUMO energy levels and thus the band gap. Materials exhibiting high charge carrier mobility and strong low-energy absorption profiles have been synthesized and characterized. Coupled with materials structure, the performance of devices fabricated using polymeric semiconductors depends critically upon alignment of the polymer chains at the nano- through meso- and macro-scales. Significant structure-process-property relationships that allow for enhancement of long-range order will be discussed. For instance, a lyotropic liquid crystalline (LC) phase has been observed in poly-(3-hexylthiophene) (P3HT) via solvent-evaporation induced self-assembly. The lessons learned through these studies may allow for simple, controllable, and cost-effective methodologies for achieving high performance flexible plastic electronic devices.

3:00pm EN+AS+EM-WeA3 Understanding Carrier Dynamics in $\text{Cu}_2\text{ZnSn}(\text{S,Se})_4$ Using Time-Resolved Terahertz Spectroscopy, *G.W. Guglietta*, Drexel University, *K. Roy Choudhury, J.V. Caspar*, DuPont Central Research and Development, *Jason Baxter*, Drexel University

We have used time-resolved terahertz spectroscopy (TRTS) to measure lifetimes and determine recombination mechanisms in $\text{Cu}_2\text{ZnSn}(\text{S,Se})_4$ (CZTSSe) thin films fabricated from nanocrystal inks. TRTS probes photoconductivity on femtosecond to nanosecond time scales that are relevant for recombination in thin film photovoltaics. Terahertz frequencies (0.2-2.5 THz) correspond to typical scattering rates in semiconductors, enabling determination of carrier density and mobility. Ultrafast time resolution permits tracking the evolution of carrier density to determine recombination mechanisms. By manipulating the photoexcitation wavelength and fluence, we can tailor the generation profile of photoexcited carriers to distinguish between surface, Shockley-Read-Hall (SRH), and Auger recombination mechanisms and determine rate constants.

TRTS experiments and modeling were used to understand the role of recombination mechanisms and their contribution to CZTSSe photovoltaic performance. TRTS photoconductivity shows an instrument-limited onset within 1 ps of an ultrafast pump pulse, followed by a slow decay over nanoseconds. Photoconductivity decay kinetics were fit with a bi-exponential model with two time constants and a weight fraction. The short time constant is typically ~200 ps and roughly corresponds to diffusion to and recombination at the surface. The long time constant is typically ~2 ns and is attributed to SRH recombination. Assignment of these mechanisms is supported by the dependence of kinetics upon excitation fluence and wavelength. Normalized kinetics are independent of fluence over a range of 40x, indicating that no Auger recombination is occurring. Without Auger recombination, we can distinguish between surface and SRH rates by tuning the pump wavelength. As the excitation wavelength is shifted towards the blue, carriers are generated nearer to the front surface and the photoconductivity kinetics are sensitive to the surface recombination velocity. With blue excitation, we see that a larger fraction, ~0.5, of carriers recombine with a short time constant. With redder excitation wavelengths, the carriers are generated more evenly throughout the film and the kinetics are dominated by SRH recombination with the long time constant having a majority of the weight fraction, ~0.8. TRTS provides a pathway to determine performance-limiting recombination mechanisms and measure key parameters like SRH lifetime and surface recombination velocity, helping to direct the design of efficient thin film photovoltaics.

3:20pm EN+AS+EM-WeA4 Comparative Study of the Doping Effects of Titanium and Nitrogen into Tungsten Oxide (WO_3) Thin Films for Photovoltaic Device Applications, *Mirella Vargas, C.V. Ramana*, The University of Texas at El Paso

Tungsten oxide (WO_3) is a technologically important n-type semiconductor that is extensively studied in the fields of electronic and opto-electronic devices. Due to its unique properties such as a high work function and high-coloration efficiency, WO_3 is attractive for electrochromic and memory

devices including large area information displays, smart-windows, and optical heat-mirrors. Low-dimensional structures of WO_3 coupled with an ideal band gap ($E_g \sim 2.8$ eV) have been employed as materials for the photocatalyst driven by visible light irradiation in dye-sensitized solar cells. In addition, WO_3 has also become a strong contender to replace indium-doped tin oxide or ITO thin films in transparent electrode applications. The present work is focused on WO_3 thin films characterized as promising transparent conducting oxide (TCO) materials by investigating doping effects on the structural, chemical, and optical properties. The incorporation of titanium (Ti) was achievable by depositing the films through co-sputtering of W and Ti metal targets. The sputtering powers to the W and Ti were kept constant at 100 W and 50 W, respectively, while varying the growth temperature (T_s) in the range of 25-500 °C. While all the samples are optically transparent, the structural quality of Ti-doped WO_3 films is dependent on T_s . Ti-doped WO_3 films grown at $T_s < 400$ °C were amorphous. A temperature of 400 °C is critical to promote the structural order and formation of nanocrystalline films in the monoclinic phase. The optical constants and their dispersion profiles determined from spectroscopic ellipsometry indicate that there is no significant inter-diffusion at the film-substrate interface for W-Ti oxide film growth of ~40 nm. The index refraction (n) at $\lambda = 550$ nm vary in the range of 2.15-2.40 with a gradual increase in growth temperature. Nitrogen (N_2) incorporation was made through a post-deposition anneal in an ammonia environment on WO_3 films. The un-doped WO_3 films grown by variable growth temperature will be annealed at high temperatures for various rates to accommodate a strong N_2 incorporation. The tungsten oxynitride films will be characterized by various analytical techniques to compare the doping effects of Ti and N_2 on the structural, electronic, and optical properties of WO_3 thin films.

5:00pm EN+AS+EM-WeA9 Engineering Exciton Recombination in Organic Light-Emitting Devices, *Russell Holmes*, University of Minnesota **INVITED**

While capable of realizing very high peak efficiency, many organic light-emitting devices (OLEDs) suffer a significant reduction in efficiency under large injected current densities. This efficiency roll-off can limit device brightness and potentially compromise operational stability. Much previous work has identified the key contributing factors to the efficiency roll-off in phosphorescent OLEDs as triplet-triplet annihilation and triplet-polaron quenching. Here, the parameters associated with these quenching processes are independently measured, and the impact of the exciton recombination zone width on the quenching processes in various OLED architectures is examined directly. In high efficiency devices employing a graded-emissive layer (G-EML) architecture the roll-off is due to both triplet-triplet annihilation and triplet-polaron quenching, while in devices which employ a double-emissive layer (D-EML) architecture, the roll-off is dominated by triplet-triplet annihilation. Overall, the roll-off in G-EML devices is found to be much less severe than in the D-EML device. This result is well accounted for by the larger exciton recombination zone that is experimentally measured in G-EML devices, serving to reduce exciton density-driven loss pathways. Indeed, a predictive model of the device efficiency based on the quantitatively measured quenching parameters shows the role a large exciton recombination zone plays in mitigating the roll-off.

5:40pm EN+AS+EM-WeA11 Interface Engineering to Control Magnetic Field Effects of Organic-based Devices by using a Self-Assembled Monolayer, *Hyuk-Jae Jang*, NIST & WFU, *S.J. Pookpanratana*, NIST, *A.N. Brigeman*, Wake Forest University, *R.J. Kline*, NIST, *J.I. Basham*, NIST & PSU, *D.J. Gundlach*, *C.A. Hacker*, *O.A. Kirillova*, NIST, *O.D. Jurchescu*, Wake Forest University, *C.A. Richter*, NIST

Magnetic field effects (MFEs) in non-magnetic organic semiconductors provide a non-contact approach to control electronic and optoelectronic properties of organic-based devices by using a sub-tesla magnetic field and thus they have been of great interest to industry as well as academia around the world.^{1,2} However, there is no consensus on the physical mechanism(s) causing the MFEs in organic semiconductors even though a variety of fundamental models have been proposed to explain the effects.² Studies on many different organic semiconductors and organic-based structures have shown that the magnitude and even the sign of the MFEs can vary by changing the measurement and fabrication conditions such as bias voltage, film thickness, and temperature. Therefore, it is suggested that there can be multiple origins inducing the MFEs and the outcome may result from a competition between different MFE mechanisms.²

In this presentation, we report a novel method of manipulating the MFEs on electrical resistance of organic semiconductors, namely organic magnetoresistance in Alq_3 (tris-(8-hydroxyquinoline) aluminum) – based devices by simply adding a molecular self-assembled monolayer (SAM) between a metal electrode and an organic semiconductor. SAMs have been known for their versatile use in various technological applications.³

Particularly, SAMs can alter the physical property of an inorganic solid surface and thus modify the interface between an electrode and an organic thin film when a SAM is inserted between them.³ We show for the first time that the interfacial modification by simply inserting a fluorinated SAM (heptadecafluoro-1-decanethiol [$\text{CF}_3(\text{CF}_2)_7(\text{CH}_2)_2\text{SH}$] or F-SAM) in organic-based devices changes the sign of organic magnetoresistance due to the change in relative strength of different MFE mechanisms coexisting in organic-based devices. In addition, we utilize different MFE mechanisms coexisting in organic-based devices by adding a thin TPD (N,N' -Bis(3-methylphenyl)- N,N' -diphenylbenzidine) layer to create a system whose organic magnetoresistance can be tuned by an external bias voltage.

References

1. J. Kalinowski, M. Cocchi, D. Virgili, P. Di Marco, and V. Fattori, *Chem. Phys. Lett.* vol. 380, pp. 710-715, 2003.
2. W. Wagemans, P. Janssen, A. J. Schellekens, F. L. Bloom, P. A. Bobbert, and B. Koopmans, *SPIN* vol. 1, pp. 93-108, 2011.
3. J. C. Love, L. A. Estroff, J. K. Kriebel, R. G. Nuzzo, and G. M. Whitesides, *Chem. Rev.* vol. 105, pp. 1103-1169, 2005.

6:00pm **EN+AS+EM-WeA12 Study on the Correlation between Electrode-Active Layer Interfaces and Performance of Polymer Solar Cells, Huanxin Ju, J.F. Zhu, University of Science and Technology of China**

The PSCs were fabricated with different cathodes (Ca/Al and Al) as the electron-collection layers and with PCDTBT (poly[N-9'-hepta-decanyl-2,7-carbazole-alt-5,5-(4',7'-di-2-thienyl-2',1',3'-benzothiadiazole)]) and PC70BM ([6,6]-phenyl-C71-butyric acid methyl ester) as the active layers. The Ca/Al interlayer significantly improves the open circuit voltage (VOC), short circuit current (JSC), fill factor (FF) so as to improve the PCE in comparison with Al as the cathode. In order to understand how the electrodes affect the device performance, the Ca/PCDTBT and Al/PCDTBT interfaces were investigated by transient photovoltage (TPV), charge extraction (CE) and synchrotron radiation photoemission spectroscopy (SRPES). The TPV and CE measurements were used to determine the charge carrier lifetime and density. Charge carrier recombination rate constant was found to be much smaller in the device with Ca/Al cathode as compared to that with Al cathode. Energy band diagrams and interfacial chemical reactions were characterized using high-resolution SRPES. The results indicate that the Ca interlayer can induce the stronger dipole moment, which facilitates electrons collection and drives holes away at the cathode/polymer interface. The device performance was improved because of the lower recombination.

Thin Film

Room: 307 - Session TF+EM+EN-WeA

Thin Film and Nanostructured Coatings for Light Trapping, Extraction, and Plasmonic Applications

Moderator: Tansel Karabacak, University of Arkansas at Little Rock

2:20pm **TF+EM+EN-WeA1 Enhanced Light Trapping by Glancing Angle Deposited Semiconductor and Metallic Nanostructure Arrays, Hilal Cansizoglu, R. Abdulrahman, M.F. Cansizoglu, University of Arkansas at Little Rock, M. Finckenor, NASA Marshall Space Flight Center, T. Karabacak, University of Arkansas at Little Rock**

Management of light trapping in nano materials has recently got attention owing to altering optical properties of materials commonly used in potential applications such as photovoltaics and photonics. Trapping the light inside the semiconducting nanostructure coating can increase optical absorption capacity of the material dramatically. Meanwhile, metallic nanostructures can serve as individual back reflectors if the light is achieved to be trapped among metallic nanostructures, which results in enhanced optical absorption of the possible surrounding absorber material around metallic structures. In this study, we examine light trapping in arrays of zig-zags, springs, screws, tilted rods, and tapered vertical rods of indium sulfide (In_2S_3) and aluminum (Al) as the model semiconducting and metallic materials, respectively. Nanostructures of different shapes were produced by glancing angle deposition (GLAD) technique. We investigated the effect of size and shape of the arrays on light trapping properties using ultraviolet-visible-near-infrared (UV-VIS-NIR) spectroscopy and finite difference time domain (FDTD) simulations. Optical characterization results show that light trapping by GLAD nanostructures can strongly depend on their shapes. Under normal incidence of light, 3D geometries of semiconducting nanostructures such as springs, screws, and tapered vertical rods can

provide an enhanced optical absorption compared to zigzags, and tilted rods. In addition, total reflectance measurements reveal that reflectance is inversely proportional to metallic nanorod length in the wavelength range of 200-1800 nm. Meanwhile, FDTD optical modelling indicates an enhanced diffuse light scattering and light trapping through uniform distribution of diffracted light within the 3D In_2S_3 nanostructure geometries such as springs, screws and vertical rods. On the other hand, zigzags and tilted rods show light absorption at relatively low level similar to the experimental results. In addition, simulations reveal that average reflectance of Al nanorods can drop down to as low as ~50%, which is significantly lower than the ~90% reflectance of conventional flat Al film at similar wavelengths. Our results demonstrate that GLAD nanostructures can provide efficient light trapping through the control of their shapes and size.

2:40pm **TF+EM+EN-WeA2 Enhanced Photoresponsivity of Conformal TiO_2/Ag Nanorod Arrays Fabricated via (Successive) Glancing Angle and Atomic Layer Deposition, Ali Haider, N. Biyikli, A.K. Okyay, Bilkent University, Turkey, T. Karabacak, H. Cansizoglu, University of Arkansas at Little Rock, B. Teckcan, Bilkent University, Turkey, M.F. Cansizoglu, University of Arkansas at Little Rock**

Improved charge carrier collection and optical absorption are two main techniques to enhance the photocurrent of a nanostructured photodetector. In a nanostructured photodiode, longer carrier life time and shorter transit time of the photo-generated carriers provides efficient charge carrier collection while the nanostructured device architecture contributes towards trapping the light by diffuse light scattering and enhancing optical absorption. However, efficient charge carrier collection is limited by the random and non-uniform nano-network. For nanostructured Schottky photodetectors, uniform nanostructured geometries with larger aspect ratio can enhance the interface of the Schottky junction which in turn decreases the transit time of generated carriers. In addition, most of the nanofabrication methods that can produce uniform nanostructure geometries are limited to certain materials. Therefore, it is an overwhelming demand to develop innovative low-cost nanostructured photodetector fabrication methodologies which enables the use of a variety of semiconductor alloy families with uniform and optimized geometries for improving photoresponsivity performance. In this work, we demonstrate a proof-of-concept nanostructured Schottky photodiode fabrication method combining glancing angle deposition (GLAD) and atomic layer deposition (ALD) to fabricate metal-semiconductor radial junction nanorod arrays, which offers significantly enhanced photoresponse compared to conventional planar counterpart. Firstly, silver (Ag) nanorod (NR) arrays were deposited on Ag thin film/Si templates by utilizing glancing angle deposition (GLAD) technique. A conformal and thin titanium dioxide (TiO_2) coating was deposited on silver nanorods via ALD. ALD emerge as highly attractive deposition technique for coating of nanorods due to its remarkable conformality and uniformity on the densely packed NR structures. Moreover, ALD also facilitates the ultra-precise control of deposited film thickness in the sub-nm scale. Following the growth of TiO_2 on Ag NRs, aluminum (Al) metallic top contacts were deposited by thermal evaporation to complete the fabrication of NR-based Schottky photodiodes. Due to the improved charge carrier collection and optical absorption, the resulting nanostructured detector exhibits a more-than two orders of magnitude photoresponsivity enhancement factor (3.8×10^2) under 3V reverse bias when compared to the corresponding thin film counterpart device with the same TiO_2 thickness. Our preliminary structural, optical, electrical, and photoresponse characterization results are presented.

3:00pm **TF+EM+EN-WeA3 Nanostructured Photonic Materials for Light-Trapping and Photon Management in Solar Energy Conversion, Koray Aydin, Northwestern University**

INVITED
Nanophotonics, the emerging field of photon-material interactions at the nanoscale, poses many challenges and opportunities for researchers both in the basic and applied sciences. In this talk, I will describe our efforts in designing, realizing and characterizing nanostructured photonic materials including metals, transparent conductive oxides and inorganic semiconductors. By shaping materials at the nanoscale, one can drastically increase absorption in and/or scattering from nanostructures that could provide significant performance enhancements in solar energy conversion processes including photovoltaics and photocatalysis. First, I will discuss our research efforts on realizing broadband plasmonics absorbers enabled by nanophotonic light-trapping approaches in metal-insulator-metal resonators. By using reflective metals and transparent dielectrics, we have achieved significant absorption enhancement in the metallic parts opening routes for spectrally and spatially selective light-absorbing devices that could find use in thermophotovoltaics and hot-electron collection devices. Then, I will describe light-trapping in nanostructured inorganic silicon ultrathin films which results in drastic absorption enhancement over the entire solar spectrum and over the wide range of incident angles. This approach does not involve any plasmonic components and based solely on

localized and delocalized resonances in semiconductor nanostructures. This novel resonant light absorption phenomenon in semiconductors could find use in photocatalytic and photovoltaic applications of inorganic semiconductors. Finally, I will talk about our results on nanostructured transparent conductive oxide contacts, which is capable of light trapping over broad range of wavelengths. Nanostructured TCO contacts could benefit both organic and inorganic photovoltaic materials, offering significant absorption and short circuit enhancements.

4:20pm **TF+EM+EN-WeA7 Porous Solid Phase Microextraction (SPME) Fibers by Oblique Angle Deposition, Anubhav Diwan, B. Singh,** Brigham Young University, *M. Kaykhali, Sistan & Baluchestan University, Iran (Islamic Republic of), B. Paul, P. Nesterenko,* University of Tasmania, Australia, *M.R. Linford,* Brigham Young University

Solid phase microextraction (SPME) is a solvent-free technique used for extracting organic compounds from matrices such as air or wastewater. It involves a fiber coated with a liquid or solid stationary phase that extracts target compounds directly from a solution or from the head space above a solution or material. Solid stationary phases provide faster extraction than liquid phases, but exhibit lower capacities. Porous solid phases have been able to overcome these issues by providing large surface areas for analyte adsorption. Commercial SPME fibers are rather expensive, swell in many solvents, and often extract limited numbers of compounds (show limited selectivity). Herein, we discuss the preparation of porous SPME fibers by oblique angle deposition (OAD) of sputtered silicon or other materials onto a fiber. OAD involves deposition of materials onto substrates placed at steep angles with respect to the direction of the incoming species, creating porous structures. The resulting nanoporous coatings can be modified with different functional groups to enhance selectivity of the phase towards target compounds. If normalized for thickness, our fibers show ca. three times the capacity of a commercial, 7 μm PDMS fiber. To confirm their morphologies, new OAD-based fibers have been characterized by scanning electron microscopy (SEM). Various silane coatings can be applied to our fibers, which will offer a range of selectivities. These coatings, e.g., a C18 silane, have been characterized on model planar substrates by X-ray photoelectron spectroscopy (XPS) and contact angle goniometry (wetting).

4:40pm **TF+EM+EN-WeA8 Chiral Patchy Particle Arrays: A Simple Fabrication Method to Achieve Plasmonic Circular Dichroism in the Visible Region, George Larsen, Y. He, W. Ingram, Y.P. Zhao,** University of Georgia, Athens

An object is said to be “chiral” if it cannot be made superimposable upon its mirror image solely by rotations and translations. That is, chiral objects do not exhibit reflective symmetry. By combining self-assembled colloid monolayers and glancing angle deposition (GLAD), we can create chiral patchy particle thin films that exhibit plasmonic activity in the visible region. Due to their chirality, these patchy particle films exhibit circular dichroism, i.e., they absorb right- and left-circular polarized light to different degrees. Interestingly, we find that the GLAD method relaxes requirements on the template quality, allowing for the production strongly chiral films from polycrystalline colloidal monolayers with randomly oriented domains. It is determined that the rotation direction during GLAD breaks the racemic symmetry of the templates by creating a chiral distribution of material which enhances the chirality of one set of enantiomers relative to the other. Microscopic analysis and geometric chirality calculations confirm that the optical chirality of the bulk film results from incomplete cancellations of even stronger local chiralities. By improving the quality of the colloidal monolayers and intentionally creating a chiral material distribution, we seek to use these chiral patchy particle arrays as plasmonic biosensors that are sensitive to the handedness of the target molecule.

5:00pm **TF+EM+EN-WeA9 Tunable Three-Dimensional Helically Stacked Plasmonic Layers on Nanosphere Monolayers, Yizhuo He*, G.K. Larsen, W. Ingram, Y.P. Zhao,** University of Georgia, Athens

Chiral metamaterials are artificial materials designed to interact with left- and right-handed circularly polarized light in different ways. Such a unique optical property enables applications such as negative refractive index, circular polarization, enantiomer sensing, etc. Practical applications usually require the fabrication of large-area chiral metamaterials on substrates with tunable chiroptical properties, especially in visible to near infrared wavelength region. We report a simple and scalable method to fabricate three-dimensional chiral metamaterial combining glancing angle deposition and self-assembled colloidal monolayers. Ag and SiO₂ are deposited alternately on colloidal monolayers. By controlling the azimuthal rotation of substrates between depositions, Ag and SiO₂ layers can be helically stacked in left-handed and right-handed fashions to form continuous

helices. These helically stacked plasmonic layers (HSPLs) exhibit localized surface plasmon resonances (LSPR) and strong chiroptical responses in visible to infrared region, which is also confirmed by finite-difference time-domain simulations. The most important feature of HSPLs is the great tunability of chiroptical spectra. By increasing the nanosphere diameter from 200 nm to 500 nm, the HSPL structure can be scaled up and thus the LSPR peak redshifts from 520 nm to 1000 nm. Since the chiroptical response originates from the strong interaction of metal layers with light, i.e. LSPR, the chiroptical spectra also redshifts accordingly without a significant change in magnitude. With such flexibility in the design, HSPLs may act as tunable chiral metamaterials, as well as serve as different building blocks for chiral assemblies.

5:20pm **TF+EM+EN-WeA10 Co-deposition of Mixed-Valent Oxides of Molybdenum and Germanium (Mo_xGe_yO_z): A Route to Tailored Optical Absorption, Neil Murphy,** Air Force Research Laboratory, *L. Sun,* General Dynamics Information Technology, *J.G. Jones,* Air Force Research Laboratory, *J.T. Grant,* General Dynamics Information Technology

Mixed-valent oxides of molybdenum and germanium were deposited simultaneously using reactive magnetron co-deposition within an oxygen-argon environment. The films' stoichiometry, optical and physical properties were varied through changes in oxygen partial pressure induced by systematic variation of the potential applied to the molybdenum cathode. The oxygen partial pressure was determined from the drop in pressure as measured by a capacitance manometer, assuming constant argon partial pressure. To facilitate deposition, a constant power of 100 W DC was applied to the germanium cathode, while power was applied to the molybdenum target using a modulated pulse power supply. Modulated pulse power magnetron sputtering was used due to its ability to generate high target power densities, allowing for rapid reduction of oxygen on the surface of the “oxygen poisoned” molybdenum cathode, as well as for its highly metallic plasma resulting in increased oxygen-gettering capability. Changes in the modulated pulse power supply's capacitor bank charge, stepped from settings of 300 to 380 V, resulted in films ranging from mixtures of transparent GeO₂ (Ge⁴⁺) and MoO₃ (Mo⁶⁺) to the introduction of various absorptive ionic species including Mo³⁺, Mo⁴⁺, Ge²⁺ and Ge⁰, as determined from X-ray photoelectron spectroscopy. The presence of each of the aforementioned ions results in characteristic changes in the films' band energies and optical absorption, measured using UV-VIS-NIR optical spectroscopy. As deposited Mo_xGe_yO_z thin films grown using this method have been shown to have band gaps that are able to be tailored between 2.8 eV and 0.6 eV, spanning useful ranges for devices operating in the visible and near-infrared.

5:40pm **TF+EM+EN-WeA11 Permanent Optical Tape and Solid State Data Storage Devices, Hao Wang, R. Gates, N. Madaan, J. Bagley, A. Diwan, A. Pearson, S. Jamieson, K. Laughlin,** Brigham Young University, *Y. Liu,* Lehigh University, *B. Lunt, M. Asplund,* Brigham Young University, *V. Shutthanandan,* Pacific Northwest National Laboratory, *R.C. Davis, M.R. Linford,* Brigham Young University

Recently we have prepared novel write–once–read–many (WORM) optical stacks on Mylar for archival data storage in an optical tape format.¹ Here, a nanoscale, co-sputtered bismuth–tellurium–selenium (BTS) alloy was employed as the write layer with carbon protective layers on both the top and bottom of the BTS film. We have successfully written information (matrix of marks) on the C/BTS/C optical stack using a 532 nm laser. Both the optical stack structure (film thickness) and writing conditions (laser power and laser spot size) have been optimized. Films were characterized by X-ray diffraction, X-ray photoelectron spectroscopy, time-of-flight secondary ion mass spectrometry, scanning electron microscopy, spectroscopic ellipsometry, and atomic force microscopy.^{2,3}

We have also recently developed novel WORM solid-state memory elements. These consisted of nanoscale, bowtie-like sputtered carbon films to which a voltage (ca. 10 V) is applied. These fuses have been successfully blown, and the carbon fuse shape, thickness of the carbon layer, and writing voltage have been optimized. Other aspects of the device are currently being optimized.

References

- [1] Wang, H.; Lunt, B.M.; Gates, R.J.; Asplund, M.C.; Shutthanandan, V.; Davis, R.C.; Linford, M.R. Carbon/ternary alloy/carbon optical stack on Mylar as an optical data storage medium to potentially replace magnetic tape, *ACS Appl. Mater. Interfaces*, **2013**, *5*, 8407–8413.
- [2] Wang, H.; Diwan, A.; Lunt, B.M.; Davis, R.C.; Linford, M.R. XPS and SIMS characterization of a BiTeSe write layer for permanent optical tape storage, *Proceedings of ISOM 2013*, ISOM 2013 International Conference, Incheon, South Korea, 2013.
- [3] Wang, H.; Lunt, B.M.; Davis, R.C.; Linford, M.R. Simulation of laser writing on Bi-Te-Se alloy/carbon/Mylar permanent optical storage tape, ISOM 2013 International Conference, Incheon, South Korea, 2013.

* TFD James Harper Award Finalist

Spectroscopic Ellipsometry Focus Topic

Room: 304 - Session EL+AS+EM+EN+SS-ThM

Spectroscopic Ellipsometry for Photovoltaics and Instrument Development

Moderator: Mariadriana Creatore, Eindhoven University of Technology, Netherlands, Tino Hofmann, University of Nebraska-Lincoln

8:00am **EL+AS+EM+EN+SS-ThM1 Spectroscopic Ellipsometry Characterization in the Photovoltaic Device Configuration, Nikolas Podraza, University of Toledo** **INVITED**

Thin film large area photovoltaics (PV) are a maturing field, yet challenges remain in manufacturing and fundamental research. Even the simplest thin film PV devices consist of multiple layers of doped or undoped semiconductors, transparent conducting front contacts, and metal back contacts. Characteristics of each layer, along with the interfaces between layers, all have an impact upon device performance. Within each layer, the material may evolve with thickness or exhibit spatial non-uniformity. Furthermore, studies of each thin film material can be difficult, as fundamental property measurements on special substrates may not accurately represent the characteristics of the material in the final device configuration. Spectroscopic ellipsometry (SE) data, collected over the infrared to ultraviolet, is sensitive to layer thicknesses, interface formation, and surface roughness as well as the optical response of each component in the form of the complex dielectric function spectra ($\epsilon = \epsilon_1 + i\epsilon_2$) for samples deposited on arbitrary reflective substrates. Variations in ϵ for a given layer can be linked to order (amorphous vs. crystalline, grain size, crystal phase), composition, and characteristics of opto-electronic response (band gap, dc electrical properties). In situ real time SE (RTSE) is now often applied to study the growth evolution of component materials within device configurations for hydrogenated silicon (Si:H), cadmium telluride (CdTe), and copper indium gallium diselenide (CIGS) PV. This utilization of RTSE provides a means of monitoring layer characteristics as materials are being processed in the device structure and generates appropriate structural models for analysis of similar samples when only ex situ SE measurements are available. Appropriate structural models derived from RTSE have been applied to analyze ellipsometric spectra collected over 6 inch x 6 inch rigid substrates and assess the spatial uniformity in characteristics of each layer in the sample. These maps of optically derived material properties can be compared to electrical device performance (efficiency, open circuit voltage, short circuit current, fill factor) and used to guide PV optimization principles. The optical (ϵ) and structural (layer thickness) information gained from SE is input into quantum efficiency simulations for comparison with experimental PV device measurements. These comparisons are used to assess both opto-electronic performance of devices and validity of models used in SE data analysis as well as further guide device development by identifying sources of optical and electrical losses.

8:40am **EL+AS+EM+EN+SS-ThM3 Application of Pseudo-Bulk Approach in Ellipsometric Studies of Polycrystalline Photovoltaic Thin Films, Sukgeun Choi, National Renewable Energy Laboratory, J. Li, University of Toledo, I. Repins, National Renewable Energy Laboratory**

Fundamental band gap is one of the key properties of semiconducting materials, which directly influences the functionality and performance of many photonic and photovoltaic (PV) devices. Photoluminescence (PL) and optical absorption spectroscopies are widely used to determine the band-gap energy E_g . For polycrystalline thin-film PV materials, however, it is often challenging to unambiguously interpret PL data owing to the presence of multiple peaks associated with various types of defect structures. To estimate E_g from optical absorption spectrum, on the other hand, a straight segment of the absorption coefficient curve needs to be chosen. But this selecting procedure is somewhat arbitrary, which leads to an inaccurate E_g value.

Spectroscopic ellipsometry (SE) accurately determines material's optical function spectra over a wide spectral range. For semiconductor thin-film structures, a multilayer analysis is generally used to extract the optical information from SE data. Although mainly surface overlayer artifacts need to be corrected for SE data well-above the band gap in the analysis, several contributions should be considered for those near (and below) the band gap, such as the optical characteristic of substrate, presence of interfacial layers, and finite thickness of film in addition to the artifacts from surface overlayers. As a result, the obtained optical function spectrum and E_g value become somewhat model dependent with an increased uncertainty.

To reduce complications in mathematical modeling of SE data and improve the accuracy of resulting near-band-gap optical function spectrum, we introduce the *pseudo-bulk* approach, where SE measurements are performed on thin films grown on macroscopically roughened substrate surface. The essence of this approach is in suppressing the reflection of probing light from the film/substrate interface and below. Thus, no thickness fringes appear in the SE data, despite the thin-film nature of sample, and the band-gap onset can be clearly observed with a post-growth chemo-mechanical polishing of the film surface. We apply the *pseudo-bulk* approach to study near-band-gap optical properties of $\text{Cu}_2\text{ZnSnSe}_4$ and related PV absorber materials. We present a non-monotonic temperature-dependence of E_g for $\text{Cu}_2\text{ZnSnSe}_4$ and the clear band-gap onset of Cu_2SnSe_3 at around 0.45 eV for the first time. SE results are explained by the results from the electronic structure calculations. The applicability and limit of this approach are also discussed.

9:00am **EL+AS+EM+EN+SS-ThM4 Real-Time and Through-the-Glass Mapping Spectroscopic Ellipsometry for Analysis and Optimization of CdS:O Window Layers of CdTe Superstrate Solar Cells, Xinxuan Tan, R.W. Collins, P. Koirala, J. Li, N.J. Podraza, University of Toledo**

In-situ real-time spectroscopic ellipsometry (RT-SE) has been applied for the analysis of CdS:O films sputter deposited on c-Si substrates from a CdS target using different flow ratios of $\text{O}_2/(\text{Ar}+\text{O}_2)$ from 0 to 0.05. RT-SE studies of the CdS:O layers from the film side provide the complex dielectric function spectra of each the layers over a spectral range of 0.75 to 6.5 eV and its dependence on oxygen content in the material as deduced by energy dispersive X-ray spectroscopy (EDS). Ex-situ infrared ellipsometry of these samples enables extension of the dielectric function data to ~ 0.04 eV and provides information on free carrier conduction and chemical bonding in the material. In similar RT-SE studies, data acquired during the growth of CdS:O/CdTe layers on transparent conducting oxide (TCO) coated glass superstrates have been analyzed to determine the structural evolution of the layers in the configuration used for CdTe solar cells, with the CdS:O serving as an n-type window layer for the p-type CdTe absorber. The results of this analysis assist in the development of a realistic optical model for the multilayer structure of the solar cell. Using this optical model ex-situ through-the-glass spectroscopic ellipsometry (TG-SE) has been implemented toward the analysis of glass/(TCO-stack)/CdS:O/CdTe solar cells in the superstrate configuration.

For the solar cells, CdS:O layers with different oxygen contents were deposited on 15 cm x 15 cm TCO coated glass superstrates. A 16 x 16 array of dot cells each with an area of 0.125 cm² was fabricated on the superstrate in order to optimize efficiency improvements through combinatorial methods. Because the as-deposited superstrate/film-structure undergoes additional processing steps during device fabrication, three sets of TG-SE mapping data were acquired on (i) as-deposited, (ii) CdCl₂-treated (an activation step), and (iii) back-contact coated device structures. With an optical database that has been established for both as-deposited and CdCl₂ treated CdS:O, CdTe, and back contact materials, each of the TG-SE mapping data sets were analyzed based on an optical model deduced from RT-SE studies of the CdS:O and CdS:O/CdTe depositions. Thickness and compositional non-uniformity observed over the area by mapped by TG-SE enables correlations between solar cell performance and basic property parameters of the component layers including layer thicknesses and compositions. The resulting correlations provide a pathway to expedite solar cell optimization.

9:20am **EL+AS+EM+EN+SS-ThM5 Combined Optical Emission Spectroscopy and Spectroscopic Ellipsometry Collected During Thin Film Deposition, Anna Barnes, M.M. Junda, N.J. Podraza, University of Toledo**

Plasma processes are commonly used to deposit thin film layers for a variety of optical, electronic, and coating applications. Two common processes widely used in the fabrication of thin films are physical vapor deposition (sputtering) and plasma enhanced chemical vapor deposition (PECVD). Non-contacting optical probes, such as spectroscopic ellipsometry (SE) and optical emission spectroscopy (OES), are particularly attractive techniques to study these deposition processes in situ during film growth. Connecting studies involving SE and OES offers the ability to observe and interpret the growth of thin films from plasma over time using variant parameters, though in different ways. Real time SE (RTSE) provides a means of monitoring the deposited material itself, while OES can be used to track variations in the plasma employed for the deposition. Tracking the time dependence of both film and plasma properties is desirable as variations in material properties resulting from changes in plasma conditions may impact the final device performance. In this particular

study, we look at the growth evolution of semiconductor, transparent conducting oxide (TCO), and metal contact layers commonly used in thin film photovoltaic devices. Case studies involve undoped, n-type, and p-type hydrogenated amorphous silicon prepared by PECVD, as well as zinc oxide, indium tin oxide, and silver prepared by magnetron sputtering on either smooth test substrates (glass, crystal silicon wafers) or in the full device configuration. Variations in thin film structure (bulk layer thickness, surface roughness) and optical properties in the form of the complex dielectric function spectra ($\epsilon = \epsilon_1 + i\epsilon_2$) are obtained as a function of time by RTSE. Results from RTSE (ϵ , structure) are interpreted to determine order (grain size, amorphous vs. nanocrystalline), electronic transitions (band gap, free carrier absorption characteristics), and morphology evolution as appropriate for the given material layer. OES indicates the presence and relative strength of plasma emission peaks, which correspond to the species present in the plasma and their relative concentrations. Analysis of RTSE and OES data collected simultaneously is sought to identify links present between these plasma and film characteristics.

9:40am **EL+AS+EM+EN+SS-ThM6 Optical Insights into Graphene Functionalized by Atoms, Biomolecules and Metal Nanoparticles, Maria Losurdo, M. Giangregorio, G.V. Bianco, P. Capezzuto, G. Bruno, CNR-IMIP, Italy**

New opportunities for energy production and storage, catalysis, biosensing, drug delivering and plasmonics are offered by graphene-based materials. In order to make all these applications viable technologies, it is mandatory to functionalize graphene for modulating reproducibly its properties and for better understanding the surface and interfacial electronic phenomena in graphene hybrids.

To this aim, this contribution discusses the optical properties measured by spectroscopic ellipsometry in the 0.6-6.5 eV of graphene functionalized by:

- (1) the covalent attachment of hydrogen, nitrogen, oxygen, and fluorine atoms, which strongly affect the optical properties of graphene through a partial sp²-to-sp³ conversion of carbon.
- (2) the non-covalent interaction with organic molecules such as porphyrins that interact with graphene through p-systems.
- (3) a variety of metals nanoparticles, like Au, Ag, Ga, to create a versatile graphene-based platform for plasmonics in frequency range from the terahertz to the visible.
- (4) plasmonic nanoparticles and subsequent proteins to create an electro-optical sensing graphene platform.

The graphene is grown by chemical vapor deposition (CVD) and transferred to glass substrates with coverage higher than 98%. This assures large area graphene samples that can easily accommodate the ellipsometric probing light spot avoiding uncontrolled effects due to undefined substrate/graphene boundaries. With the availability of high quality samples, effect of thickness and anisotropy, which have been debated for a while, are clarified.

Data on the real time monitoring of graphene optical properties by spectroscopic ellipsometry that allows for an unprecedented control over the degree of functionalization will also be presented.

The perspective of this work is twofold. From the fundamental point of view, in the investigated spectral range, the band structure of graphene has saddle van Hove-like singularities at the M points of the Brillouin zone, with possible excitonic effects. Focusing on the analysis of these singularities, many-body effects for all the graphene-derivates mentioned above are described.

From the technological point of view, it will be shown how the optical measurements can serve to clarify and explain the occurrence and stability of the doping of graphene by the various heteroatoms and molecules, the electron transfer between graphene and metals and molecules, and finally the sensitivity of the graphene-platform in sensing gases and biomolecules.

Spectroscopic ellipsometry data of functionalized graphene are corroborated by Raman spectroscopy, microscopies and electrical characterizations.

11:00am **EL+AS+EM+EN+SS-ThM10 Enhanced Sensitivity to Surface-Normal Dielectric Function of Uniaxial-Anisotropic Materials via Attenuated Total Reflection Ellipsometry, Thomas Tiwald, J.A. Woollam Co., Inc., J. VanDerslice, Z. Xiao, J.S. Huang, University of Nebraska Lincoln**

It is often difficult to determine the surface-normal dielectric functions of anisotropic materials, because of lack of sensitivity to optical properties out of the surface plane[1][2]. The primary cause is the large angle of refraction that occurs as the light enters from low index medium like air. In these circumstances, the penetrating light beam bends strongly towards surface normal, resulting in electric fields that are oriented primarily in the surface plane. This is a particular problem for absorbing films, since most of the light collected by the detector is reflected from the ambient/film interface. We use a total internal reflection method to enhance ellipsometric

sensitivity to optical properties of uniaxial absorbing materials in the out-of-plane direction. This non-destructive technique is illustrated using a P3HT poly(3-hexylthiophene) film on fused silica, and the results are compared to the standard air/film/substrate method.

[1] D.E. Aspnes, *J. Opt. Soc. Am.*, **70**, 10, 1275 (1980).

[2] G. E. Jellison Jr. and J. S. Baba, *J. Opt. Soc. Am. A*, **23**, 2 468 (2006).

11:20am **EL+AS+EM+EN+SS-ThM11 Infrared to Ultraviolet Optical Properties of Gadolinium Gallium Garnet (Gd₃Ga₅O₁₂) and Bismuth Germanate (Bi₄Ge₃O₁₂) Single Crystals, Kiran Ghimire, H. Haneef, N.J. Podraza, University of Toledo**

The optical properties of commercially available oxide single crystals gadolinium gallium garnet (Gd₃Ga₅O₁₂) and bismuth germanate (Bi₄Ge₃O₁₂) have been studied over a maximum spectral range of 0.034 to 6.5 eV by multiple spectroscopic ellipsometry and transmittance measurements, via a multichannel ellipsometer from the near infrared to ultraviolet, a Fourier transform infrared (FTIR) ellipsometer, and a spectrophotometer. Spectroscopic measurements from each instrument and over the respective spectral ranges have been analyzed differently yet yield optical properties over the full measured range. Near infrared to ultraviolet ellipsometric spectra are analyzed using a divided spectral range procedure whereby information below and above the band gap are fit to models with separate physically realistic parameterizations of the complex dielectric function spectra ($\epsilon = \epsilon_1 + i\epsilon_2$) that share the same structural parameters—surface roughness thickness in these cases. The surface roughness thicknesses are then fixed and direct numerical inversion is used to determine ϵ over the continuous spectral range. Analysis of transmittance and FTIR ellipsometric spectra also relies upon fixing surface roughness from near infrared to ultraviolet spectroscopic ellipsometry analysis and either direct numerical inversion or parametric models to determine ϵ . In the vicinity of the band gap, the absorption coefficient (α) obtained from ϵ is then combined with low values of ϵ obtained from transmittance below the absorption edge, where ellipsometry lacks sensitivity. The combined α from transmission and ellipsometry is used to determine the band gap of the materials. Unlike Gd₃Ga₅O₁₂, the band gap of the Bi₄Ge₃O₁₂ is sufficiently within the measured spectral range so critical point analysis has been performed on Bi₄Ge₃O₁₂ by extending the measured spectral range up to 6.5 eV, where the material was found to have additional critical points. FTIR ellipsometric spectra are analyzed with a parametric model combining Gaussian and Lorentzian broadened resonance features to represent modes attributed to chemical bonding and lattice vibrations. The results of these analysis procedures yield ϵ from the infrared to ultraviolet, from which information on the band gap, electronic transitions, and vibrational modes are obtained.

11:40am **EL+AS+EM+EN+SS-ThM12 Cu surface reactions in hydrochloric solution probed on the atomic scale by polarization optical methods and STM, Christoph Cobet, Gh. Barati, V. Solokha, K. Hingerl, Johannes Kepler University, Austria**

Electrochemical reactions on metal electrodes have been in the focus of many scientific studies and Cu is probably the most investigated example. Mainly, the interest on Cu is motivated by questions concerning e.g. the corrosion behavior or the optimization of electro-polishing procedures. Classical electrochemical approaches contain usually a description of the occurring reaction products and concentrations. However, it is evident that a fundamental understanding also requires knowledge about the microscopic occurrence of the metal-electrolyte interface. Desirable is a fundamental knowledge as it is obtained already for surfaces in UHV. But unfortunately, most of the classical surface sensitive techniques cannot be applied in liquid environments. Thus it is not surprising that many fundamental issues in electrochemical reactions are still unsolved.

In our work we combine reflection anisotropy spectroscopy, spectroscopic ellipsometry, and a homemade electrochemical scanning tunneling microscope to study Cu single crystals in hydrochloric solutions. With these methods we enabled monitoring of the local appearance as well as the dynamics of interface transformations/reactions on the atomic scale. In particular it was possible to explain for the (110) surface in more detail the correlation of Faraday-current and structural transformation. Here, the Cl adsorption minimizes the surface energy by a formation of monoatomic steps parallel to the [001] direction which finally ends in a faceting of the surface. It turns out that characteristic redox peaks in cyclic voltammograms correlate with the stabilization of certain arrangements of these steps. The structures are formed first by Cu dissolution and at higher anodic potentials by rearrangement of Cu atoms in the surface. It is remarkable that the latter process compares nicely with oxide/chloride induced surface transformations which are observed in UHV. The comparison with the UHV results in turn is used to achieve a more comprehensive model for the processes in electrochemical environment.

Electronic Materials and Processing Room: 311 - Session EM1-ThM

Materials for Light Management

Moderator: Sang M. Han, University of New Mexico

8:40am **EM1-ThM3 Thin Film c-Si Solar Cells – Detailed Understanding from Light Trapping to Carriers Collection**, *M.S. Branham, W.-C. Hsu*, Massachusetts Institute of Technology, *S. Yerci*, Middle East Technical University, Turkey, *Gang Chen*, Massachusetts Institute of Technology **INVITED**

Crystalline silicon (c-Si) is the dominant material in photovoltaic industry. However, it contributes ~40% of the total module cost of c-Si solar cells, and a thin-film device has been one strategy to reduce the usage of material. Here, we demonstrate experimentally that an inverted nanopyramid light-trapping scheme for a 10 μ m-thick c-Si thin-film solar cell can achieve an absorptance value comparable to that of a 300 μ m-thick planar device and its efficiency higher than 13%. To reach the high efficiencies necessary for a commercial product, we constructed a multi-physics optimization tool incorporating both optical absorption and electronic carrier collection to understand in detail loss mechanisms including incomplete photonic absorption, contact losses, surface, Schottky-Read-Hall and Auger recombination. Our model predicts that a 10 μ m-thick thin-film c-Si solar cell with an inter-digitated back contact scheme can have an efficiency higher than 20%. Finally, we calculated the optimum height to period ratio of light-trapping structures around 0.7 for a fixed period of 700nm. This structure can be obtained in crystalline silicon using a well-known potassium hydroxide anisotropic etching. These multi-physics simulation results can provide design insights for flexible and high efficiency thin silicon solar cells.

9:20am **EM1-ThM5 Symmetry-Breaking in Light Trapping Nanostructures on Silicon for Solar Photovoltaics**, *SangEon Han, S. Ghosh, T. Cai, B.R. Hoard, S.M. Han*, University of New Mexico

In thin-film photovoltaics, highly absorptive materials are conventionally used. However, these materials except gallium arsenide have achieved efficiencies that are not comparable to those of thick crystalline silicon (c-Si) photovoltaics and, in some cases, suffer from their toxicity and low supply. A viable solution to these problems would be to use c-Si for thin-film photovoltaics. However, thin c-Si films absorb sunlight weakly because of its indirect band gap, and highly efficient light-trapping should be provided to achieve high efficiency. For thin-film photovoltaics, nanoscale structures are typically involved for light trapping because the film thickness becomes comparable to the wavelength of sun light. While diverse nanostructures have been studied to break the light-trapping limit of geometric optics, known as the Lambertian limit, highly efficient nanostructures that can be easily manufactured have not been demonstrated. We have previously predicted that symmetry-breaking in light-trapping periodic nanostructures on thin films can approach the Lambertian limit very closely. Herein, we will present how the systematic symmetry-lowering increases light-trapping in thin-film photovoltaics. Further, we will demonstrate the experimental realization of such low-symmetry structures using simple wet etching methods on c-Si(100) wafers without any off-cut, tilt angle.

9:40am **EM1-ThM6 Suppressing Optical Absorption in Nanostructured Metal Electrodes in Photovoltaics**, *Samuel Clark, S.E. Han*, University of New Mexico

Electrodes are ubiquitously used in optoelectronic devices such as solar cells, infrared detectors, and light emitting diodes. Typically, metals exhibit good electrical conductivity due to their free electrons and are suitable for electrodes in these devices. However, metal electrodes cause inefficiency in the devices by absorbing light as their free electrons suffer from collisions. To circumvent this problem, nanostructured metals are being explored to realize low optical losses while maintaining large electrical conductivity. Here, we study optical absorption in helical metal nanocoils and find that absorption can be dramatically decreased when the metal is suitably nanostructured. Theoretical modeling showed that this effect is due to the increase in effective mass of free electrons in nanostructured metals. Heavy electrons suffer a decreased rate of collision and emulate dielectric materials where optical losses are negligible. Calculations showed that, when metal electrodes are used in semiconductor devices, suitably chosen nanostructures can increase the fractional absorption in semiconductors more than 60 times by reducing losses in the metal. Further, we show that a two-dimensional analogue to nanocoil, namely serpentine structure, exhibits optical losses of less than 7 % in the infrared even at a large metal area fraction of 0.3. We will discuss the different physics of optical losses between the coil and the serpentine structures.

11:00am **EM1-ThM10 High Efficiency Si Cells and the Challenges to Integrate the Light Management**, *Paul Stradins, B.G. Lee*, National Renewable Energy Laboratory **INVITED**

In this talk, we discuss the stringent requirements that enable the high efficiency, industrially relevant, Si solar cells, and show that the light management approaches need to be developed integral to the whole device. The highest efficiencies known today are obtained with PERL (UNSW), IBC (SunPower) and IBC Heterojunction (Panasonic) device architectures. The challenge is to balance the excellent bulk, surface, and contact passivation leading to high Voc, with light management features leading to high Jsc. For example, pyramid-texturing the front of the cell leads to an excellent visible range response and near-Lambertian light trapping in near-infrared, but the associated 1.7x increase in the front surface area increases the recombination current prefactor. The IBC approaches significantly restrict any light management structures on the back of the cell (e.g. plasmonics, gratings). Novel passivated contact approaches currently pursued by NREL [1] and others [2] show promise to significantly enhance cell efficiencies in an industrially relevant way. In particular, we have developed [1] high performance tunneling passivated full area back contact for the n-CZ based cell. Because of the high-low junction induced by a deposited n+ poly-Si contact layer, there is no P-doping involved in BSF formation. The contact itself provides better BSF passivation than currently used nitride-passivated BSF surface, has low contact resistance, and does not need patterning as in PERT or PERL structures. We then discuss of how advanced optics and light trapping can fit into this device architecture and are there viable alternatives to the near-Lambertian pyramid texturing. With near-perfect bulk and surface/contact passivation, the importance of light management increases. However, it becomes increasingly more challenging to justify much thinner wafer cells even with perfect Lambertian light trapping. For high efficiency, passivated contact wafer cells, additive light management structures provide potential efficiency improvements and will be discussed. Finally, we will briefly discuss numerous light management approaches examined in the course of our previous Si program that focused on <10 micron thin c-Si devices (small pyramids, black Si, dielectric nanoparticle backscatters), and their potential to high efficiency Si cells.

1.D. L. Young et al., SiliconPV conference proceedings 2014.

2.F. Feldmann et al, Sol. En. Mat. Sol. Cells (2014) 120, pp. 270-274.

11:40am **EM1-ThM12 Developing Periodically Oriented Gallium Nitride for Frequency Conversion**, *Jennifer Hite, R. Goswami, J.A. Freitas, Jr., M.A. Mastro, I. Vurgaftman, J.R. Meyer*, U.S. Naval Research Laboratory, *C.G. Brown*, Sotera Defense Solutions, *S.R. Bowman, C.R. Eddy*, U.S. Naval Research Laboratory

Gallium nitride is a semiconductor widely used in both optical and electronic devices. The polarity of GaN (+/- c-direction) influences many properties of the resultant material, including chemical reactivity and electric field in these 'spontaneously polarized' materials. By engineering inversion layers, we have demonstrated control of GaN polarity on both polar faces of GaN. By employing a selective growth method to deposit the IL, the lateral polarity of the GaN can be alternated, thus enabling structures referred to as periodically oriented (PO) GaN.

In previous work on N-polar substrates, we demonstrated that optimization of the MOCVD growth rates resulted in sharp, vertical interfaces and smooth surfaces. The present work has moved the technology substantially closer to practical non-linear optic emitters by using HVPE to extend the PO GaN templates on N-polar substrates to total thicknesses of up to 80 μ m, while faithfully maintaining the pattern of alternating polarity. Additionally, cross-sectional cathode-luminescence (CL) imaging of such an extension shows that the large initial dislocation densities occurring in the original inversion layers greatly decreased after about 25 μ m of regrowth.

For growth on Ga-polar substrates, we have demonstrated that inversion layers can be created using atomic layer deposition (ALD) of Al₂O₃. This new capability is especially relevant because Ga-polar films are more prominent in devices, as they result in lower impurities, higher quality and smoother films. In this case, GaN grown over the inversion layer is N-polar. This inversion layer was used to form laterally-patterned stripes of alternating Ga- and N-polar films. We find that annealing the ALD films crystallizes the Al₂O₃, thereby allowing N-polar GaN to be grown over the new sapphire-like surface. Transmission electron microscopy shows that the inversion layer in a PO GaN structure is crystalline, a-plane oriented, and a-phase. TEM characterization further indicates that the GaN layers, both above and below the Al₂O₃ inversion layer, are c-oriented without any rotation between them. The optimization of this process has enhanced the surface smoothness.

These methods of GaN polarity inversion offer the promise of engineered materials with custom lateral and vertical polarity variations for applications in novel electronic and optoelectronic devices, a subset of which are expected to be suitable for non-linear optics.

12:00pm **EM1-ThM13 White-Light Emission from Amorphous ZrHfO_x/AlO_x/ZrHfO high-*k* Stack**, C.-C. Lin, Yue Kuo, Texas A&M University, X. Zhang, Xi'an Jiaotong University, China

LEDs has the low energy consumption, compact size, and long-lifetime [1]. Since the white light cannot be emitted from a single LED, a combination of red, green, and blue LEDs or an UV or blue LED with a yellow phosphor has to be used. Kuo and Lin proposed a new type of single-chip, white-light emission LED that is made of the amorphous high-*k* dielectric thin film on a Si wafer [2-5]. The light emission is from the thermal excitation of nano-size conductive paths formed during the dielectric breakdown, which is similar to the principle of the incandescent device. Its energy efficiency is expected to be much higher than that of the incandescent light bulb because of the small size conductive path. The emission light intensity and wavelength range of the LED were enhanced with the embedding of a nanocrystal layer in the high-*k* film paths [2]. Authors investigated optical and electrical characteristics of the ZrHfO_x/AlO_x/ZrHfO LED.

The following results were obtained from this study. First, the AlO_x embedded ZrHfO LED emits the broad band light including the visible to near IR wavelengths. Second, the emitted light falls into the warm white light region of the CIE 1931 color chart with a high color rendering index (CRI) of ~98. Third, the LED has a larger leakage current than the control sample, i.e., ZrHfO without the embedded AlO_x layer, which is due to the stress mismatch between these two materials film [6]. Fourth, both the emission light intensity and the number of the bright dots increase with the inclusion of the AlO_x layer and the increase of the magnitude of the stress voltage ($|V_g|$). These phenomena can be explained by the mechanism of thermal excitation of the conductive path. The large current density causes the high thermal excitation efficiency of the conductive path for the high intensity light emission. The larger number of conductive paths also contribute to the high emission intensity. Fifth, light emission was studied with the pulsed V_g driving method, i.e., at 1 kHz and -40 V, at various duty cycles (DCs). The spectrum wavelength range was independent of the change of DC. However, the peak height decreases with the decrease of the DC. It can be explained by the fast thermal excitation process of the extremely short conductive path, i.e., ~8.7 nm. The new LED can be an important white light source for many industrial, medical, etc. applications.

[1] N. Kimura, APL 90 051109 (2007)

[2] Y. Kuo et al., APL 102, 031117 (2013).

[3] Y. Kuo et al., Electrochem. Solid-State Lett. 2, Q59 (2013).

[4] Y. Kuo et al., Solid-State Electron. 89, 120 (2013).

[5] C.-C. Lin et al, JVSTB 32, 011208 (2014).

[6] C.-C. Lin et al, JVSTB 32, 03D116 (2014).

Electronic Materials and Processing

Room: 314 - Session EM2-ThM

High-K Dielectrics for ReRAM and RAM

Moderator: John Conley, Oregon State University

8:00am **EM2-ThM1 Challenges and Materials Solutions for Memristive Devices (ReRAM)**, Jianhua(Joshua) Yang, HP Labs
INVITED

Memristive devices (also known as RRAM when used for memory) are electrical resistance switches that can retain a state of internal resistance based on the history of applied voltage or current, which can be used to store and process information for computing systems beyond CMOS technologies. These devices have shown great scalability, switching speed, non-volatility, analogue resistance change, non-destructive reading, 3D stack-ability, CMOS compatibility and manufacturability. However, there are still a number of challenges facing memristive devices for real applications, including device variability and isolation in a crossbar array. This talk will discuss and address these challenges from the materials perspective.

8:40am **EM2-ThM3 Physical Mechanisms and Scaling of the Resistive Memory (ReRAM)**, Daniele Ielmini, S. Balatti, S. Ambrogio, Politecnico di Milano, Italy
INVITED

The resistive memory (ReRAM) is attracting strong interest from the industry and academia for its low-power, high-speed and nonvolatile behavior. ReRAM properties are compatible with many of the requirements of storage (e.g., the solid state drive, or SSD) and memory (e.g., SRAM or DRAM), thus ReRAM may potentially revolutionize computing architectures in the future. While ReRAM has been recently introduced in the ITRS, the industrial programs for device development, volume

production and commercial exploitation are still challenged by the lack of understanding about device physics, reliability and scaling.

This work will discuss the recent progress on the understanding of ReRAM physics. First, a numerical model for ReRAM switching will be described, highlighting the primary role of defect migration driven by Joule heating and electric field. The model will be tested under several conditions of voltage and currents, showing the model capability to identify new operation modes for self-select ReRAM and enhanced multilevel operation. Finally, the scaling issues will be addressed, explaining the device variability data with the aid of a Monte Carlo model for discrete defect migration. The fundamental tradeoff between power reduction and device reliability will be finally discussed.

9:20am **EM2-ThM5 Variability of Metal Oxide Based RRAM: Challenges and Opportunities**, An Chen, GLOBALFOUNDRIES
INVITED

Recently, metal-oxide based resistive-RAM (RRAM) has emerged as a promising nonvolatile memory (NVM) candidate. However, it is also recognized that the stochastic RRAM switching mechanisms inevitability introduce large variability in device parameters, which impose severe challenges for memory applications especially in high-density arrays. RRAM variability can be attributed to the microscopic variation of dimension and/or composition of the filamentary conductive paths during the switching process. Variability in switching voltage/current reduces safe operation margin and resistance variation degrades sensing margin. Cell-to-cell and cycle-to-cycle variability has different origins and needs to be differentiated in RRAM characterization. Resistance variability measured by σ/μ (deviation/mean) has to be controlled within target ranges determined by device and array specifications. Mechanism and typical characteristics of RRAM variability will be reviewed in this presentation. Although variability is undesirable for memory arrays, security applications embrace truly random variations. Pervasive and ubiquitous computing requires robust light-weight security technologies at low cost. Physical unclonable functions (PUF) exploit physical randomness and variability as security primitives. RRAM variability may be utilized for PUF implementation, which may achieve much smaller footprint than existing PUF solutions. Feasibility of PUF designs based on RRAM variability will be analyzed based on measured device properties

11:00am **EM2-ThM10 High-K Development for DRAM, NAND, and ReRAM Applications**, Nirmal Ramaswamy, Micron Technology
INVITED

DRAM, NAND and ReRAM utilize high-K oxides to enable high performance devices. High-K oxides are deployed as capacitor dielectrics in DRAM, blocking dielectrics in NAND and solid state electrolytes to enable ion motion in ReRAM. The material and electrical properties required to enable these different technologies are widely different. Several critical parameters such as dielectric constant, band offset, trap density, modulus, crystallinity and texture have to be simultaneously optimized for each technology. This talk highlights the performance requirements of advanced memory devices and the high-K materials engineering required to enable these devices.

11:40am **EM2-ThM12 Resistive Switching Characteristics and Mechanism in Oxide Conductive-Bridge RAM**, Ming Liu, Q. Liu, H.B. Lv, S.B. Long, Chinese Academy of Sciences, China
INVITED

Conductive bridging RAM (CBRAM) has been intensively investigated for the application of next generation nonvolatile memories due to its excellent scalability and superior switching performances [1-2]. Generally, the device forms by an ion-conducting insulator sandwiched between an oxidizable electrode (i.e. Cu or Ag) and an inert electrode (i.e. Pt or W). The resistance switching is based on the the formation and annihilation of nanoscale metallic conductive filament (CF) in the ion-conducting insulator under the external power. This kind of filament utilizes composition of metal ions transferring from the oxidizable electrode to the inert electrode due to cation redox reaction [2]. Deep understanding of the CF dynamic growth mechanism and development of controllable CF growth method will help to guide the design of CBRAM devices with desirable properties. Using binary oxide, such as ZrO and HfO₂, we successfully obtained some CBRAM devices with excellent resistive switching performances [3-4]. Based on the variable temperature testing and the advanced SEM and TEM analysing, some fundamental issues related to the resistive switching effect, including the morphologies, chemical compositions and dynamic growth/dissolution of CFs were directly addressed in various CBRAM systems [5]. In addition, using "electrical engineering", we demonstrated that the CF growth process can be controlled by modulating distribution electric field inside ion-conducting insulator, which greatly improving the uniformity of the CBRAM device [6].

Reference:

- [1]. R. Waser, M. Aono, Nat. Mater. 2007, 6, 833.
- [2]. J. J. Yang, D. B. Strukov, D. R. Stewart, Nat. Nanotechnol. 2013, 8, 13.
- [3]. Q. Liu, S. Long, W. Wang, S. Tanachutiwat, Y. Li, Q. Wang, M. Zhang, Z. Huo, J. Chen, M. Liu, IEEE Electron Device Lett. 2010, 31, 1299.
- [4]. Y. Li, H. Lv, Q. Liu, S. Long, M. Wang, H. Xie, K. Zhang, Z. Huo, M. Liu, Nanoscale 2013, 5, 4785.
- [5]. Q. Liu, J. Sun, H. Lv, S. Long, K. Yin, N. Wan, Y. Li, L. Sun, M. Liu, Adv. Mater. 2012, 24, 1844.
- [6]. Q. Liu, S. long, H. Lv, W. Wang, J. Niu, Z. Huo, J. Chen, M. Liu, ACS Nano 2010, 4, 6162.

Scanning Probe Microscopy Focus Topic

Room: 312 - Session SP+2D+AS+EM+MC+NS+SS-ThM

Probing Electronic and Transport Properties

Moderator: An-Ping Li, ORNL, Corentin Durand, ORNL

8:00am **SP+2D+AS+EM+MC+NS+SS-ThM1 Investigation of the Electronic and Structural Properties of Metal Free Naphthalocyanine Vapor Deposited on Au(111)**, *Bryan Wiggins*, University of Chicago, *K.W. Hipps*, Washington State University

Naphthalocyanines (Ncs) are promising candidates for future components in electronic devices and applications. To maximize the efficiency of Nc devices, it is critical to understand their structural and electronic properties and how these are impacted by deposition methods. The formation of a metal free naphthalocyanine (H_2Nc) self-assembled monolayer on a Au(111) crystal was investigated by scanning tunneling microscopy under ultra-high-vacuum conditions at room temperature. A rigorous purification and processing procedure was developed to produce high purity, low defect, and well-ordered monolayers. High-resolution STM images reveal epitaxial growth of H_2Nc on Au(111) with the observed structure having a molecular spacing of 1.6 ± 0.05 nm, with molecules orientated slightly off (roughly 2.5°) the low density packing direction of Au(111). A commensurate structure having 4 molecules per unit cell and unit cell parameters of $A = 3.25 \pm 0.05$ nm, $B = 3.17 \pm 0.05$ nm, and $\alpha = 87.5 \pm 2^\circ$ is proposed. Orbital-mediated tunneling spectroscopy was used to examine the electronic properties of individual molecules within the thin film. The first ionization potential and electron affinity of H_2Nc adsorbed on Au(111) were measured to be -0.68 ± 0.03 and 1.12 ± 0.02 eV, relative to the Fermi energy.

8:20am **SP+2D+AS+EM+MC+NS+SS-ThM2 The Fundamentals of Charge Transport at Oxide and Ferroelectric Interfaces**, *Ramsey Kraya*, *L.Y. Kraya*, University of Pennsylvania

Here we investigate how charge transport properties at metal-semiconductor interfaces scale down to the nanoscale regime, comparing the properties to macroscopic interfaces and providing a perspective on what it means to device manufacturing. Strontium titanate - the prototypical oxide material - has been widely studied for applications in thermoelectrics, nanoelectronics, catalysis, and other uses, and behaves as an n-type semiconductor when doped. We investigated how charge transport is effected at interfaces to strontium titanate under a wide range of conditions - by varying contact size, interface shape, dopant concentration, and surface structure and in various combinations. The results of the analysis have wide ranging implications, especially for ferroelectric oxide materials and serves as the basis for understanding and controlling switching effects - both polarization and oxygen migration based switching.

8:40am **SP+2D+AS+EM+MC+NS+SS-ThM3 Epitaxial Graphene on Nanostructured Silicon Carbide**, *Phillip First*, Georgia Institute of Technology

INVITED

Graphene grown epitaxially on silicon carbide conforms to nanofaceted step edges, even for step heights of many nanometers. The "sidewall" nanoribbons that result show astounding transport characteristics (~ 15 um ballistic length at room temperature), as demonstrated by others,¹ but the physical basis for these results is still not certain. In our STM measurements of sidewall nanoribbons, we find an extended 1D region with electronic structure much different than 2D graphene. Spectroscopic results on graphene near nanofacet corners indicate a strain gradient and a rapid change in the doping. Such strong gradients may be key to understanding the ballistic transport in this system. P

¹J. Baringhaus, M. Ruan, F. Edler, A. Tejada, M. Sicot, Amina Taleb-Ibrahimi, A.-P. Li, Z. Jiang, E. H. Conrad, C. Berger, C. Tegenkamp and

W. A. de Heer, "Exceptional ballistic transport in epitaxial graphene nanoribbons," *Nature*, **506**, 349 (2014).

9:20am **SP+2D+AS+EM+MC+NS+SS-ThM5 Conductivity of Si(111) - 7 x 7: The Role of a Single Atomic Step**, *B. Martins*, University of Alberta and The National Institute for Nanotechnology, Canada, *M. Smeu*, *H. Guo*, McGill University, Canada, *Robert Wolkow*, University of Alberta and The National Institute for Nanotechnology, Canada

The Si(111) - 7×7 surface is one of the most interesting semiconductor surfaces because of its

complex reconstruction and fascinating electronic properties. While it is known that the Si - 7×7 is

a conducting surface, the exact surface conductivity has eluded consensus for decades as measured

values differ by 7 orders of magnitude. Here we report a combined STM and transport measurement

with ultra-high spatial resolution and minimal interaction with the sample, and quantitatively determine the intrinsic conductivity of the Si - 7×7 surface. This is made possible by the capability of

measuring transport properties with or without a single atomic step between the measuring probes:

we found that even a single step can reduce the surface conductivity by two orders of magnitude.

Our first principles quantum transport calculations confirm and lend insight to the experimental

observation.

9:40am **SP+2D+AS+EM+MC+NS+SS-ThM6 Asymmetric Electron Transport Revealed at Monolayer-Bilayer Graphene Junctions by Atomic-Scale Scanning Tunneling Potentiometry**, *K. Clark*, *X. Zhang*, *J. Park*, Oak Ridge National Laboratory, *G. Gu*, University of Tennessee, *G. He*, *R.M. Feenstra*, Carnegie Mellon University, *An-Ping Li*, Oak Ridge National Laboratory

The quest for novel two-dimensional (2D) materials has led to the discovery of hybrid heterostructures of graphene and other 2D atomic films [1]. These heterojunctions provide us fascinating playground for exploring electronic and transport properties in 2D materials. Even in graphene itself, there usually exist large amount of extended topological defects, such as grain boundaries, changes in layer thickness, and substrate steps, which divide graphene into grains and domains. These interfaces and boundaries can break the lattice symmetry and are believed to have a major impact on the electronic properties, especially the transport, in 2D materials.

Here, we present our recent study on an asymmetric electron transport upon bias polarity reversal at individual monolayer-bilayer (ML-BL) boundaries in epitaxial graphene on SiC (0001), revealed by multi-probe scanning tunneling potentiometry [2,3]. A greater voltage drop is observed when the current flows from monolayer to bilayer graphene than in the reverse direction, and the difference remains nearly unchanged when bias exceeds a threshold. A thermovoltage is measured across the boundary due to the thermopower difference between the two sides, which however is too small to account for the observed asymmetry. Interestingly, this asymmetry is not from a typical nonlinear conductance due to electron transmission through an asymmetric potential. Rather, it indicates the opening of an energy gap at the Fermi energy. Our theoretical analysis finds that Friedel charge oscillation opens a gap for electrons with wave vectors perpendicular to the boundary. The Friedel gaps are different on the monolayer and bilayer sides, which can shift under bias and lead to asymmetric transport upon reversing the bias polarity. A quantitative agreement is seen between experiment and theory on both the sign and the magnitude of the asymmetry.

1 "Heteroepitaxial Growth of Two-Dimensional Hexagonal Boron Nitride Templated by Graphene Edges", L. Liu, J. Park, D. A. Siegel, K. F. McCarty, K. W. Clark, W. Deng, L. Basile, J.-C. Idrobo, A.-P. Li, G. Gu, *Science***343**, 163-167 (2014).

2 "Spatially Resolved Mapping of Electrical Conductance around Individual Domain (Grain) Boundaries in Graphene", K. W. Clark, X.-G. Zhang, I. V. Vlassiuk, G. He, R. M. Feenstra, and A.-P. Li, *ACS Nano*. **7** (9), 7956-7966 (2013).

3 "Friedel Oscillation-Induced Energy Gap Manifested as Transport Asymmetric at Monolayer-Bilayer Graphene Boundaries", K. W. Clark, X.-G. Zhang, G. Gu, G. He, R. M. Feenstra, and A.-P. Li, *arXiv*: 1401.1796, *Physical Review X***4** (1), 011021 (2014).

11:00am **SP+2D+AS+EM+MC+NS+SS-ThM10 Defect-mediated Transport in CVD-grown Monolayer MoS₂**, *Corentin Durand, J. Fowlkes, Oak Ridge National Laboratory, S. Najmaei, J. Lou, Rice University, A.P. Li, Oak Ridge National Laboratory*

Transition metal dichalcogenides like molybdenum disulphide (MoS₂) have attracted great interest as candidate to fill the need of 2 dimensional semiconductor materials. By controlling the thickness, the bandgap of MoS₂ thin films can be tuned from 1.2 eV (bulk material, indirect bandgap) to 1.8 eV (monolayer film, direct bandgap). Recently, researchers succeeded in growing monolayered MoS₂ by chemical vapor deposition (CVD) on silicon dioxide (SiO₂) substrate, showing the possibility of low cost scalable device fabrication. However, the mobility reported on exfoliated MoS₂ monolayers exceeds 200 cm².V⁻¹.s⁻¹, whereas the measurements realized on CVD growth MoS₂ monolayers reveal a mobility value that is usually 1-2 orders of magnitude lower. Here, we study the transport properties of CVD-grown monolayer on SiO₂/Si substrate. We directly measure the resistivity and the mobility of the material with a field-effect transistor architecture by using a cryogenic four-probe scanning tunneling microscope (STM), the Si substrate being used as back-gate. In order to ensure reliable electrical contacts, we fabricate platinum pads (4x4 μm²) on individual MoS₂ crystal domains by using an electron-beam induced deposition technique. The combination of the STM scanners and a scanning electron microscope (SEM) enables us to connect the STM tips on those pads and thereby establish the contacts on this material without any subsequent lithography process, avoiding contaminations introduced by other technological steps. An electron hopping process in localized charge trapping states appears to dominate the transport behavior. We performed temperature-dependent measurements in the range of 82 K to 315 K which demonstrate a variable range hopping (VRH) transport with a very low mobility. Furthermore, the effects of electronic irradiation are examined by exposing the film to electron beam in the SEM in an ultra-high vacuum environment. We found that the irradiation process affect the mobility and also the carrier concentration of the material, with conductance showing a peculiar time-dependent relaxation behavior. It is suggested that the presence of defects such as vacancies and antisites create charge trapping states, leading to the low mobility. This is consistent with recent density functional theory calculations where these defects are shown to create localized gap states that can act as scattering centers and thereby reduce the mobility.

11:20am **SP+2D+AS+EM+MC+NS+SS-ThM11 Coherent One Dimensional Boundaries in Graphene and Hexagonal Boron Nitride Heterostructures**, *Jewook Park, Oak Ridge National Laboratory, L. Liu, The University of Tennessee Knoxville, D.A. Siegel, K.F. McCarty, Sandia National Laboratories, L. Basile, J.-C. Idrobo, K. Clark, ORNL, W. Deng, The Univ. of Tennessee Knoxville, C.P. Durand, ORNL, G. Gu, The Univ. of Tennessee Knoxville, A.P. Li, ORNL*

The quest for novel two-dimensional (2D) materials has led to the discovery of hybrid heterostructures where graphene and other atomic layer films such as monolayer hexagonal boron nitride (hBN) form phase-separated domains or both materials grow epitaxially onto a common crystalline substrate. By implementing the concept of epitaxy to 2D space, we developed and applied a new growth technique to hybrid isostructural but electrically dissimilar materials, such as the 2D epitaxial growth of hBN templated by graphene edge [1]. Scanning tunneling microscopy and spectroscopy measurements revealed a single-atomic-layer, in-plane heterostructure between graphene and hBN, as well as an abrupt 1D zigzag oriented boundary. In addition, the dI/dV conductance map unveiled the 1D interfacial states that are extended along, but localized at the boundary. We investigated spatial and energetic distributions of 1D boundary states. Also, low-energy electron microscopy and micro low-energy electron diffraction confirmed the heterostructure at mesoscopic scale and established that the graphene edge solely determines the crystallography of the hBN regardless of underlying the Cu(100) lattice. The Z-contrast scanning transmission electron microscopy further indicates an atomically sharp interface with a transition width of ~0.5 nm. We suggest that the graphene-hBN epitaxial heterostructure provides an excellent platform to explore heteroepitaxy in 2D space, and the unique functionalities at the 1D interface. [1] Lei Liu *et al. Science* **343** 163 (2014)

11:40am **SP+2D+AS+EM+MC+NS+SS-ThM12 Charge and Spin Density Waves in Quasi One-Dimensional Atomic Wires**, *Herbert Pfnür, Leibniz Universität, Germany* **INVITED**

Although free one-dimensional (1D) objects should exist only at T=0, atomic single wires or arrays embedded into a two- or three-dimensional environment exist even at room temperature and above, since they are stabilized by lateral interactions. These interactions not only stabilize, but also strongly modify the properties of the wires. Their 2D or 3D coupling, however, does not generally prevent observation of 1D properties with their complex variety of instabilities. Furthermore, these coupling can result in special 1D behavior not predicted by standard theories either in 1D or 2D. I will show several examples how atomic wires and wire arrays grown by

self-assembly on semiconducting surfaces of Si and Ge acting as insulating substrates can be used to study in detail fundamental aspects of low-dimensional physics, such as charge density waves [1] and Luttinger liquid behavior [2], partially under explicit control of the atomic structure. Due to the low symmetry in these structures, large Rashba-type spin-orbit coupling is expected to lift the spin degeneracy of the metal-induced surface states. In this context new types of spin order were proposed, e.g. for Au/Si(553) [3] and found to be consistent with experiment. As a further example, the Pb/Si(557) system close to monolayer coverage turned out to be an intriguing model system that demonstrates the wealth of phenomena to be expected in quasi-1D physics. Adsorbate induced electronic stabilization leads to (223) refaceting of the (557) surface, to opening of a band gap, to Fermi nesting normal to the steps [4], and to the formation of a charge density wave. Rashba splitting is so large that it causes in-plane anti-ferromagnetic spin polarization along the steps with twice the step periodicity resulting in a combined spin-charge density wave. New superstructures are formed by an excess Pb coverage up to 0.1ML due to ordered step decoration indicating strong electron-electron correlation across steps. This leads to new long range ordered states and formation of a sequence of 1D charge density waves up to a concentration of 1.5 ML, but also, as very recent angular and spin resolved photoemission studies show, to new ordered spin states.

[1] T. Tanikawa *et al. Phys. Rev. Lett.* **93**, 016801 (2004).

[2] C. Blumenstein *et al. Nat. Phys.* **7**, 776 (2011).

[3] S.C. Erwin, F. J. Himpsel, *Nature Communications* **1**, 58 (2010); J. Aulbach *et al. Phys. Rev. Lett.* **111**, 137203 (2013)

[4] C. Tegenkamp, D. Lükermann, H. Pfnür, B. Slomski, G. Landolt H. Dil, *Phys. Rev. Lett.* **109**,

266401 (2012).

Thursday Afternoon, November 13, 2014

2D Materials Focus Topic

Room: 310 - Session 2D+EM+MI+MN+NS+SS+TF-ThA

Novel Quantum Phenomena in 2D Materials

Moderator: Alexander Sinitskii, University of Nebraska-Lincoln

2:20pm **2D+EM+MI+MN+NS+SS+TF-ThA1 Optoelectronics of Two-Dimensional Semiconductors, Xiaodong Xu**, University of Washington
INVITED

Two dimensional transition metal dichalcogenides are a recent addition to the 2D electronic materials family. They have shown outstanding electrical and optical properties for new optoelectronic device concepts. In this talk, we will first discuss the unique interplay between spin, valley, and layer pseudospins in bilayer WSe_2 . Such coupling effects lead to electrical control of spin states and optical generation of valley coherence through interlayer triions, where electrons and holes are localized in different layers. We will then talk about optoelectronic devices based on monolayer WSe_2 , including p-n junctions as light emitting diodes and hybrid monolayer semiconductor/photonic crystal cavity devices. We will conclude the talk with a discussion of the optoelectronic properties of MoSe_2 - WSe_2 heterostructures.

3:00pm **2D+EM+MI+MN+NS+SS+TF-ThA3 Theory of Graphene Transport Barriers in the Specular Limit, Daniel Gunlycke, C.T. White**, Naval Research Laboratory

Offering room-temperature ballistic electron transport well over one micron, while being atomically thin and planar, graphene is undeniably a promising material for future nanoelectronic devices. Presently, however, switchable devices have normally low on-off ratios, a reflection of the challenge of selectively blocking electron and hole carriers from propagating across the graphene surface. This has stimulated a lot of research on different methods for making graphene nanoribbons that exhibit suitable band gaps. An alternative way to obtain a controllable gap takes advantage of resonant tunneling across a pair of transport barriers. For the latter approach, the key is to find a barrier that is fairly reflective but not so much as to effectively cut off all transport across it.

In this presentation, we present a model for straight transport barriers in graphene in the specular limit. Using the Lippmann-Schwinger equation, we obtain the wave function, from which we derive the reflection and transmission probabilities, as well as the local density of itinerant states. This local density of states exhibits fluctuations arising from quantum interference between incoming and outgoing matter waves that allow the transport properties of a barrier to be estimated without explicitly probing the current across the barrier. Our model is tested against exact multi-channel, tight-binding quantum transport calculations for graphene with weak local potentials, local strain, local adsorption, and a locally defective structure. As the model parameters are related to observable quantities, they could be obtained from theory and/or experiment, allowing the model to be adopted even when the precise details of the barrier are unknown.

3:20pm **2D+EM+MI+MN+NS+SS+TF-ThA4 Tip-induced Potential Confinement on Graphene in Scanning Tunneling Microscopy Measurement, Yue Zhao, J. Chae, J.E. Wyrick, NIST/CNST, F.D. Natterer**, Ecole Polytechnique Fédérale de Lausanne (EPFL), France, S. Jung, Korea Research Institute of Standards and Science (KRISS), A.F. Young, C.R. Dean, L. Wang, Y. Gao, Columbia University, J.N. Rodrigues, Graphene Research Centre, NUS, Singapore, K. Watanabe, T. Taniguchi, National Institute for Materials Science (NIMS), Japan, S. Adam, Graphene Research Centre, NUS, Singapore, J.C. Hone, K. Shepard, P. Kim, Columbia University, N.B. Zhitenev, J.A. Stroscio, NIST/CNST

Graphene is a two-dimensional-electron-gas(2DEG) system with exposed surface, which allows scanning tunneling microscopy (STM) to investigate the electron-electron interaction associated with the Dirac nature on a local scale, with a variety of tuning knobs, such as carrier density, spatially varying disorder potential, and applied magnetic field. However, the electron-electron interaction in graphene is sensitive to the disorder details. Moreover, tip induced potential confinement can significantly complicate the interpretation of STM experiment. Utilizing a high mobility graphene device with low residual disorder, we can minimize the effect of local potential fluctuation, to better understand the role tip-induced potential plays in the measurement. We observed the emergency of large spectra gaps, modification to graphene Landau levels (LLs), and quantum dots with changing size due to the spatially inhomogeneous tip gating.

4:00pm **2D+EM+MI+MN+NS+SS+TF-ThA6 Topological Phase Transitions and Spin-orbit Density Waves, Hugo Dil**, Ecole Polytechnique Fédérale de Lausanne (EPFL), Switzerland
INVITED

In recent years systems where the spin-orbit interaction (SOI) is not just a perturbation but the main energy scale have received increasing attention. In combination with a broken inversion symmetry in the crystal structure or at interfaces, SOI will lift the spin degeneracy and induce a complex Fermi surfaces and spin textures with spin momentum locking [1,2]. Furthermore, the SOI can drive the system through a phase transition to a so-called topological insulator. Being an insulator in the bulk these systems are characterized by spin-polarized, topologically protected interface states.

After a short introduction to the role of topology in the band structure of solids I will give an overview of our main spin- and angle-resolved photoemission (SARPES) results on a variety of non-interacting topological insulators [3]. One of the questions is how the spin texture evolves around a topological transition. We explored the occurrence of spin polarized states around a SOI driven topological transition [4] and around a structure driven topological transition [5]. In both cases we observe spin-polarized precursor states, which indicate that although the topological transition is sharp, the response of the system is more gradual.

From a fundamental point of view the truly interesting aspect of non-trivial spin textures lies in their combination with other interactions. This can result in a variety of phenomena, cumulating in the creation of the elusive Majorana Fermion. An example of a combination of interactions is our recent verification with SARPES of SbB_6 as a topological Kondo insulator [6]. In topologically trivial systems, interactions can lead to the formation of a so-called spin-orbit density wave. I will show how the combination of a large spin-splitting and Fermi nesting leads to the formation of such a state and can explain the anisotropic behavior of Pb nanowires [7]. Furthermore, I will present our recent SARPES results for transition metal oxide surfaces where a subtle interplay between ferroelectricity and magnetic order results in the formation of a single spin-polarized energy contour. The occurrence of superconductivity in such systems could render it a 2D Majorana platform.

[1] J.H. Dil, J. Phys: Cond. Mat. 21, 403001 (2009)

[2] G. Landolt et al. Phys. Rev. Lett. 109, 116403 (2012)

[3] D. Hsieh et al. Science 323, 919 (2009); D. Hsieh et al. Nature 460, 1101 (2009); S.Y. Xu et al. Science 332, 560 (2011); S. Ereemeev et al. Nature Comm. 3, 635 (2012)

[4] S.Y. Xu et al. arXiv:1204.6518

[5] G. Landolt et al. Phys. Rev. Lett. 112, 057601 (2014)

[6] N. Xu et al. Nature Materials (2014)

[7] C. Tegenkamp et al. Phys. Rev. Lett. 109, 266401 (2012)

4:40pm **2D+EM+MI+MN+NS+SS+TF-ThA8 The Symmetry Dependent Band Structure of MoS_2 , Duy Le**, University of Central Florida, T. Komesu, University of Nebraska-Lincoln, Q. Ma, University of California, Riverside, E.F. Schwier, H. Iwasawa, Hiroshima University, Japan, M. Shimada, Higashi-Hiroshima, Japan, T.S. Rahman, University of Central Florida, L. Bartles, University of California, Riverside, P.A. Dowben, University of Nebraska-Lincoln

We will present results of density functional theory (DFT) based calculations of symmetry dependent band structures of single crystal $\text{MoS}_2(0001)$ surface together with symmetry-polarized angle resolved photoemission spectroscopy (ARPES) derived experimental band structure. The good agreement of the DFT band structure with the experimentally derived bands with even and odd symmetries, attests to the reliability of the results. We performed ARPES at the Hiroshima Synchrotron, determining the MoS_2 band structure separately for both p- and s-, polarized to distinguish even and odd symmetry, and the experimentally determined dispersion, in accordance with expectations and experimental confirmation of C_{3v} symmetry, argues in favor of an experimental band structure obtained from single domains. The comparison of theory and experiment provides strong indications that the bands at the top of the valence band are dominated by Mo 4d states. These states and indeed placement of the valence band can be perturbed by adsorbates. Indeed, we find that, under the effect of Na adsorption, the changing placement of the valence band structure of MoS_2 clearly indicate the Na atoms donate electrons to MoS_2 and that the Fermi energy level shifts as much as 0.5 eV with respect to the top of MoS_2 's valence band. Surprisingly, Na adsorption does not perturb the MoS_2 band dispersion significantly. We will discuss these results in the light of those obtained for single layer MoS_2 for insights and clarity.

5:00pm **2D+EM+MI+MN+NS+SS+TF-ThA9** **CuIn₁₁₁P₂S₆ - Room Temperature Layered Ferroelectric**, Alex Belianinov, P. Maksymovych, Oak Ridge National Laboratory, A. Dziugys, Vilnius University, Lithuania, Q. He, Oak Ridge National Laboratory, E. Eliseev, National Academy of Sciences of Ukraine, A. Borisevich, Oak Ridge National Laboratory, A. Morozovska, NAS of Ukraine, J. Banys, Vilnius University, Lithuania, Y. Vyschanskii, Uzhgorod University, Ukraine, S.V. Kalinin, Oak Ridge National Laboratory

We have utilized ambient and Ultra High Vacuum Scanning Probe Microscopy tools to explore ferroelectric properties in cleaved 2D flakes of copper indium thiophosphate, CuIn₁₁₁P₂S₆ (CITP), and report on size effect and presently achievable limits of ferroelectric phase stability. CITP is an unusual example of a layered, anti-collinear, uncompensated, two-sublattice ferroelectric system. These are the only materials known to display “2-D” ferroelectric semiconductor behavior in a van-der-Waals crystal. The material exhibits a first-order phase transition of order–disorder type from the paraelectric to the ferroelectric phase at $T_c = 315$ K. Our observations suggest the presence of stable ferroelectric polarization as evidenced by domain structures, rewritable polarization, and hysteresis loops. These observations suggest that flakes above 100 nm have bulk-like polarization and domain structures, whereas below 50 nm polarization disappears. Furthermore, the materials have measurable ionic mobility, as evidenced both by macroscopic measurements and by formation of surface damage above tip bias of 4 V, likely due to copper reduction. We ascribe this behavior to well-known instability of polarization due to depolarization field, along with internal screening by mobile Cu ions, as suggested by their high ionic mobility.

Acknowledgement:

Research for (AB, PM, QH, AB, SVK) was supported by the US Department of Energy, Basic Energy Sciences, Materials Sciences and Engineering Division. Research was conducted at the Center for Nanophase Materials Sciences, which is sponsored at Oak Ridge National Laboratory by the Scientific User Facilities Division, Office of Basic Energy Sciences, US Department of Energy.

5:20pm **2D+EM+MI+MN+NS+SS+TF-ThA10** **Doping Efficiency and Mechanisms of Single and Randomly Stacked Bilayer Graphene by Iodine Adsorption**, Hokwon Kim, A. Tyurnina, Univ. Grenoble Alpes/CEA, LETI, France, J.-F. Guillet, J.-P. Simonato, J. Dijon, Univ. Grenoble Alpes/CEA, LITEN, France, D. Rouchon, D. Mariolle, N. Chevalier, O.J. Renault, Univ. Grenoble Alpes/CEA, LETI, France

The precise control of graphene's conductivity and work function is crucial in developing practical applications of graphene based electronics. In order to enhance the conductivity of graphene, we employed a simple doping method where graphene films produced by chemical vapor deposition and transferred onto SiO₂, Al₂O₃, and WO₃ substrates are p-doped with iodine vapor through physisorption at temperature of ~ 100 °C [1-3]. The work function values and iodine to carbon ratios of the one-layer (1L) and two-layer (2L) folded regions were analyzed by high spatial- and energy resolution X-ray photoelectron emission microscopy (XPEEM) on a NanoESCA instrument. After the iodine doping, the work function values were significantly increased up to ~0.4 eV and ~0.5 eV, respectively, for 1L and 2L graphene on SiO₂/Si. This higher degree of doping by iodine was corroborated by I 3d_{5/2} core level imaging of the same area where the 2L graphene exhibited significantly larger concentration of iodine (2 at. % versus 1 at. %) likely due to the intercalation of iodine at the inter-layer space.

The main iodine species identified by high resolution core level X-ray photoemission spectroscopy and Raman spectroscopy were I₃⁻ and I₅⁻ polyiodide anionic complexes with slightly higher concentration of I₃⁻ in 2L than 1L graphene possibly due to different doping mechanisms. Temperature dependent ultra-high-vacuum, in-situ annealing of the doped films has demonstrated that most of iodine is removed above 300 °C for the both 1L and 2L regions, although a significant removal of iodine is observed for 2L graphene at temperature as low as 100 °C. Surprisingly, after the complete removal of iodine by annealing, the work function value did not return to the original one before the doping treatment and remained at a much higher value. This can be ascribed to the residual hydrocarbon contaminations interacting with the atomic defects within the graphene layer that lead to unintentional n-type doping in our samples[4].

Acknowledgement: The XPEEM and KFM measurements were performed at the Nanocharacterization Platform (PFNC).

References

- [1] L. Grigorian, K.A. Williams, S. Fang, G.U. Sumanasekera, A.L. Loper, E.C. Dickey, S.J. Pennycook, P.C. Eklund, Phys. Rev. Lett., (1998) 5560-5563.
- [2] A.B. Kaiser, Rep. Prog. Phys., (2001) 1.

[3] S.W. Chu, S.J. Baek, D.C. Kim, S. Seo, J.S. Kim, Y.W. Park, Synth. Met., (2012) 1689-1693.

[4] B.H. Kim, S.J. Hong, S.J. Baek, H.Y. Jeong, N. Park, M. Lee, S.W. Lee, M. Park, S.W. Chu, H.S. Shin, J. Lim, J.C. Lee, Y. Jun, Y.W. Park, Sci. Rep., (2012).

5:40pm **2D+EM+MI+MN+NS+SS+TF-ThA11** **Use of XPS for Device Characterization**, P. Aydogan, E.O. Polat, C. Kocabas, Sefik Suzer, Bilkent University, Turkey

A noncontact chemical and electrical measurement technique of XPS is utilized to investigate a number of devices made of graphene. The main objective of the technique is to trace chemical and location specific surface potential variations as shifts of the XPS peak positions under operating conditions. Devices consisting of graphene; (i) acting as a simple resistive element between two gold electrodes, (ii) a semiconducting sheet controlled by a back-gate, and (iii) between the source and the drain metal electrodes in a full transistor geometry, have been analyzed by recording the Au4f of the metal electrodes, the C1s of the graphene layer, and the O1s (or N1s) peaks of the silicon oxide (or nitride) of the substrate. The advantage of this technique is its ability to assess element specific surface electrical potentials of devices under operation based on the deviations of the core level peak positions in surface domains/structures. Detection of the variations in electrical potentials and especially their responses to various stimuli gives unprecedented information about the chemical nature as well as the location of structural and/or other types of defects as a result of doping, oxidation, reduction, etc.

Spectroscopic Ellipsometry Focus Topic Room: 304 - Session EL+AS+EM+MC+SS-ThA

Optical Characterization of Nanostructures and Metamaterials

Moderator: David Aspnes, North Carolina State University, Mathias Schubert, University of Nebraska-Lincoln

2:20pm **EL+AS+EM+MC+SS-ThA1** **The Optical Properties of Metallic Nanostructures**, Bruno Gompf, Universität Stuttgart, Germany
INVITED

The entire optical response of a homogenous reciprocal sample can be characterized by eight basic physical properties: mean absorption, mean refraction, circular birefringence and circular dichroism, linear birefringence and linear dichroism (0°, 90°), linear birefringence and linear dichroism (±45°). Always two out of the three main birefringence-dichroism pairs (basic anisotropies) are sufficient to jump from any point of the Poincare-sphere to any other. A common example is the Soleil-Babinet compensator. This implies that always two of the basic anisotropies generate artificial signals of the third [1]. Therefore even for perfect crystals it is hard to judge, what optical property lead to an observed polarization change.

In the case of inhomogeneous materials the permittivity additionally becomes k-dependent $\epsilon_{ij}(\omega, k)$; it exhibits spatial dispersion. For most artificial nanostructures, dubbed metamaterials, the building blocks are in the range $l/10 < P < l/2$. During the last couple of years it has become clear that in general it is not possible for these kinds of materials to define effective optical parameters, which are independent of the angle of incidence of the probing light. There optical response is intrinsically k-dependent.

With Mueller-matrix spectroscopic ellipsometry the entire optical response of artificial nanostructures can be characterized. For this the Mueller-matrix elements $m_{ij}(\theta, \alpha, \omega)$, which depends on the angle of incidence θ , the azimuth orientation α and the energy, had to be measured over the complete angular and a wide frequency range. Visualizing the results in polar contour plots enables a detailed analysis of how nanostructures influence the polarization state of light [2-4]. Most importantly, immediate experimental evidence is obtained for deviations from pure dielectric behaviour; i.e. the optical response cannot be explained by an effective $\epsilon_{ij}(\omega)$ alone but requires spatial dispersion.

In the talk the entire optical response of a some artificial nanostructures will be presented and some generalizations will be discussed, when spatial dispersion becomes important and how it can be distinguished from other optical properties leading to a mixing of polarization states, like birefringence and optical activity.

[1] J.Schellman and H.P.Jensen, Chem. Rev., 87, 1359 (1987.))

[2] B. Gompf, J. Braun, T. Weiss, H. Giessen, M. Dressel, U. Huebner, Phys.Rev.Lett. 106,

185501 (2011).

[3] B.Gomph, B. Krausz, B. Frank, M. Dressel, Phys.Rev.B. **86**, 075462 (2012).

[4] A. Berrier, B. Gomph, Liwei Fu, T. Weiss, H. Schweizer, Phys.Rev.B. in print

3:00pm EL+AS+EM+MC+SS-ThA3 Mueller Matrix Ellipsometry As a Powerful Tool for Nanoimprinted Grating Structure Metrology, Xinguo Chen, C.W. Zhang, S.Y. Liu, Huazhong University of Science and Technology, China

Compared with conventional ellipsometric scatterometry, which only obtains two ellipsometric angles, Mueller matrix ellipsometry (MME, sometimes also referred to as Mueller matrix polarimetry) based scatterometry can provide up to 16 quantities of a 4 by 4 Mueller matrix in each measurement. Consequently, MME can acquire much more useful information about the sample and thereby can achieve better measurement sensitivity and accuracy. In this talk, we will demonstrate MME as a powerful tool for nanoimprinted grating structure metrology. We will show that MME-based scatterometry at least has the following three aspects of advantages over conventional ellipsometric scatterometry.

(1) More accurate characterization of line width, line height, sidewall angle, and residual layer thickness of nanoimprinted grating structures can be achieved by performing MME measurements in the optimal configuration. In contrast, conventional ellipsometric scatterometry can only be conducted in the planar diffraction configuration, i.e., with the plane of incidence perpendicular to grating lines, which is not necessarily the optimal measurement configuration for nanostructures in general.

(2) Not only further improvement in the measurement accuracy and fitting performance can be achieved, but also the residual layer thickness variation over the illumination spot can be directly determined by incorporating depolarization effects into the interpretation of measured data. The depolarization effects, which are demonstrated to be mainly induced by the finite bandwidth and numerical aperture (NA) of the instrument, as well as the residual layer thickness variation of the nanoimprinted grating structures, can be only handled by MME.

(3) Conventional ellipsometric scatterometry has difficulties measuring asymmetric grating structure due to the lack of capability of distinguishing the direction of profile asymmetry. In contrast, MME not only has good sensitivity to both the magnitude and direction of profile asymmetry, but also can be applied to accurately characterize asymmetric nanoimprinted gratings by fully exploiting the rich information hidden in the measured Mueller matrices.

3:20pm EL+AS+EM+MC+SS-ThA4 Vector Magneto-Optical Generalized Ellipsometry on Sculptured Thin Films with Forward Calculated Uniaxial Response Simulation, Chad Briley, T. Hofmann, University of Nebraska-Lincoln, D. Schmidt, National University of Singapore, E. Schubert, M. Schubert, University of Nebraska-Lincoln

We present the vector magneto-optical generalized ellipsometric (VMOGE) response and forward calculated simulations of ferromagnetic slanted columnar thin films. Directional hysteresis magnetization scans were performed with an octu-pole vector magnet at room temperature on slanted columnar thin film samples of permalloy grown by glancing angle deposition passivated by an atomic layer deposited Al₂O₃ conformal coating. Model analyses of the measured Mueller matrix ellipsometric data through a point-by-point best match model process determines the magneto-optical (MO) dielectric tensor. Three dimensional rendering of the anti-symmetric off-diagonal elements of the MO dielectric tensor reveal a uniaxial magnetic response of the thin film along the long axis of the columns. The magnetic response was subsequently modelled by a best match model process with uniaxial hysteretic response governed by the shape induced anisotropy from the physical geometry and orientation of the nano-columns. By using model parameters for normalized saturation $\|M_s\|=1$, coercivity $\|H_c\|=50$ mT, and remanence $\|M_r\|=0.9999*\|M_s\|$ the forward calculated magnetic simulations described the observed magneto-optical response for all measured orientations of the nano-columns with respect to all magnetizing field directions generated by the vector magnet.

1) D. Schmidt, C. Briley, E. Schubert, and M. Schubert Appl. Phys. Lett. **102**, 123109 (2013)

4:00pm EL+AS+EM+MC+SS-ThA6 In Situ Generalized Ellipsometry Characterization of Silicon Nanostructures during Lithium-ion Intercalation, Derek Sekora, R.Y. Lai, T. Hofmann, M. Schubert, E. Schubert, University of Nebraska-Lincoln

Nanostructured silicon has emerged as a leading candidate for improved lithium-ion battery electrode design. The combined highly accessible surface area and nanoscale spacing for volumetric lattice expansion of nanostructured thin films have shown improved cycle lifetime over bulk-

like silicon films. Additionally, ultra-thin passivation layers have been reported to increase the longevity and stability of silicon thin film electrodes. Very little *in-situ* information has been reported on silicon films during the complicated lithiation process. Furthermore, what information available has been limited to the study of bulk-like thin films. The advantageous geometry of glancing angle deposited (GLAD) thin films allows for the strain from lithiation to affect individual nanostructures in comparison to the bulk response. For this reason, alumina passivated GLAD silicon films were grown for use as working electrodes in half cell electrochemical experiments.

The spatially coherent silicon GLAD nanostructures have intrinsic biaxial optical properties. Therefore, generalized ellipsometry was employed to investigate the silicon film's physical response to lithium intercalation during an electrochemical cyclic voltammogram cycled against pure lithium metal in a conductive anhydrous electrolyte solution. *In-situ* ellipsometric monitoring of directional optical constant changes determined by the homogeneous biaxial layer approach are presented. The optical response expresses a morphologic conversion from a highly anisotropic film to a pseudo-isotropic lithium concentrated form and subsequently, its return to the original anisotropic state. The ability to nondestructively monitor complex nanostructured thin films during lithium-ion processes provides new avenues for high storage battery electrode design.

4:20pm EL+AS+EM+MC+SS-ThA7 Characterization of SiO₂ Nanoparticle Layers on a Glass Substrate by Spectroscopic Imaging Ellipsometry and AFM, Peter H. Thiesen, Accurion GmbH, Germany, G. Hearn, Accurion Inc., C. Röling, Accurion GmbH, Germany

The well-directed organization of nanoparticles is of increasing technical and scientific interest. One approach is the organization of nanoparticles at the air/water interface for applications, like producing 2D colloidal crystals or nanowires. For example, Gil et al. (2007) monitored the formation of 2D colloidal crystals by Langmuir-Blodgett technique. They used Brewster angle microscopy to observe the film quality. Zang et al. (2009) have also studied silica nanoparticle layers at the air/water interface by multiple angle of incidence ellipsometry. For data interpretation, a two-layer model was introduced. With this model, the radius of interfacial aggregates and the contact angle of the nanoparticle surface at the air/water interface were obtained.

In this paper different line shaped pattern of SiO₂ nanoparticles were characterized by spectroscopic imaging ellipsometry in the wavelength range between 360 and 1000 nm and by AFM. The samples were provided by the research group of Professor Y. Mori, Doshisha University, Japan.

The work shows the unique capability of imaging ellipsometry in characterizing patterned surfaces. We started with a pre inspection of the surface by imaging ellipsometric contrast microscopy. Tiny regions of interest (ROIs) were placed on interesting areas like on different steps of the stripes and Delta and Psi spectra were recorded. The next step in characterization was the mapping of Delta and Psi with pixel resolution of the detector. The same samples were also characterized with an AFM. The results optical modelling are in good agreement with the results of the scanning method.

A. Gil, M. Vaupel, F. Guitiana, D. Möbius (2007) *Journal of Materials Chemistry* **17**: 2434-2439.

D. Zang, A. Stocco, D. Langevin, B. Weib, B.P. Brinks (2009) *Phys. Chem. Chem. Phys.* **11**: 9522-9529.

5:00pm EL+AS+EM+MC+SS-ThA9 Dielectric Tensor Model for Inter-Landau-level Transitions in Highly Oriented Pyrolytic Graphite and Epitaxial Graphene – Symmetry Properties, Energy Conservation and Plasma Coupling, Philipp Kühne, Linköping University, Sweden, T. Hofmann, M. Schubert, University of Nebraska-Lincoln, C.M. Herzinger, J.A. Woollam Co., Inc., V. Darakchieva, Linköping University, Sweden

We report on polarization sensitive, magneto-optic, reflection-type Landau level (LL) spectroscopy at low temperatures by using the integrated optical Hall effect instrument¹ in the mid-infrared spectral range (600 – 4000 cm⁻¹) on highly oriented pyrolytic graphite (HOPG) and epitaxial graphene grown on C-face silicon carbide by thermal decomposition. In both sample systems we observe a multitude of inter-LL transitions. Inter-LL transitions in HOPG possess polarization mode mixing polarization selection rules characteristics, while polarization mode conserving and polarization mode mixing inter-LL transitions are observed in epitaxial graphene which can be assigned to single- and Bernal stacked (ABA) multi-layer graphene, respectively.² We present a new dielectric tensor model for inter-LL transitions which explains all experimentally observed line-shapes. For inter-LL transitions in multi-layer graphene and HOPG we employ this new model together with energy conservation considerations, to show that these polarization mode mixing inter-LL transitions couple with a free charge carrier plasma. Finally, inter-LL transition energy parameters are determined and discussed.

¹) P. Kühne, et. al., Rev. Sci. Instrum., accepted (2014)

²) P. Kühne, et. al., Phys. Rev. Lett. **111**, 077402 (2013)

5:20pm **EL+AS+EM+MC+SS-ThA10 Characterization of Exfoliated 2D Nano Materials with Imaging Spectroscopic Ellipsometry**, *P.H. Thiesen*, Accurion GmbH, Germany, *Greg Hearn*, Accurion Inc., *B. Miller*, Technische Universität München, Germany, *C. Röling*, Accurion GmbH, Germany, *U. Wurstbauer*, Columbia University, *E. Parzinger*, *A.W. Holleiner*, *U. Wurstbauer*, Technische Universität München, Germany

In the initial period of graphene research, the issue was to identify and characterize crystallites of microscopic scale. Imaging ellipsometry is a nondestructive optical method in thin film metrology with a lateral resolution down to 1 μm . In a number of papers, imaging ellipsometry has been applied to characterize graphene flakes of few micrometer size. Ellipsometric contrast micrographs, delta and Psi maps as well as wavelength spectra [1],[2] and single layer steps in multilayer graphene/graphite stacks [3] have been reported.

Molybdenum disulfide is a layered transition metal dichalcogenide. From the point of current research, 2D-nano materials based on MoS₂ are very promising because of the special semiconducting properties. The bulk material has an indirect 1.2 eV electronic bandgap, but single layer MoS₂ has a direct 1.8 eV bandgap. The monolayer can be used in prospective electronic devices like transistors (MOSFETs) or photo detectors. Delta and Psi Spectra of MoS₂ monolayers as well as maps of the ellipsometric angles will be presented. The practical aspect of single layer identification will be addressed and the capability of ellipsometric contrast micrographs as a fast tool for single layer identification will be demonstrated.

An additional focus will be on the modelling of the optical properties of 2D nanomaterials.

[1] Wurstbauer et al., Appl. Phys. Lett. 97, 231901 (2010)

[2] Matkovic et al. J. Appl. Phys. 112, 123523 (2012)

[3] Albrektsen O. J. Of Appl. Phys. 111, 064305 (2012)

Electronic Materials and Processing

Room: 311 - Session EM1-ThA

Materials for Quantum Computation

Moderator: Sang M. Han, University of New Mexico

2:20pm **EM1-ThA1 Mos Quantum Bits for Adiabatic and Non-Adiabatic Quantum Computing**, *Malcom Carroll*, Sandia National Laboratories **INVITED**

This talk will describe silicon nanostructures that confine electrons at the SiO₂/Si interface and produce quantum dot behavior. These structures combined with single ion implantation provide a platform for silicon quantum bits. Application of these structures towards circuit model and ground state quantum computing approaches will be discussed. We acknowledge the research funding support provided by the laboratory directed research and development (LDRD) program at Sandia National Laboratories. Sandia National Labs is a multi-program laboratory operated by Sandia Corporation, a Lockheed Martin Company, for the United States Department of Energy's National Nuclear Security Administration under contract DE-AC04-94AL85000.

3:00pm **EM1-ThA3 ²⁸Si Enriched In Situ to 99.9998 % for Quantum Computing Devices**, *Kevin Dwyer*, University of Maryland, College Park, *J. Pomeroy*, *D. Simons*, National Institute of Standards and Technology (NIST)

We are enriching *in situ* and depositing epitaxial thin films of ²⁸Si in support of quantum computing devices. Highly enriched ²⁸Si is a critical material for quantum computing as removal of ²⁹Si spins provides a non-interacting "semiconductor vacuum" medium for qubits such as ³¹P donors which have electron and nuclear coherence (T₂) times of seconds and minutes respectively even up to room temperature. ³¹P donors can also be addressed optically due to hyperfine transitions not normally resolvable in natural Si. Starting with natural abundance silane, we have used mass filtered ion beam deposition to produce ²⁸Si films enriched to > 99.9998 % with a residual ²⁹Si isotope fraction < 1 ppm (40 times less than previously reported ²⁸Si sufficient for optical addressing). Using our ion beam system we have grown crystalline ²⁸Si films and are pursuing characterization of their structural properties using *in situ* reflection high energy electron diffraction (RHEED), *in situ* scanning tunneling microscopy (STM), and transmission electron microscopy (TEM). Secondary ion mass spectrometry (SIMS) is used to determine enrichment of crystalline ²⁸Si films. As we move away from silane towards a solid sputtering source, enrichment may be improved

even further and the use of additional materials such as Ge can become possible. Numerous experimental systems can take advantage of ²⁸Si as a medium for qubits including STM based hydrogen lithography devices, single donors coupled to single electron transistors, and quantum wells. We have demonstrated the ability to produce isotope heterostructures with applications including fully enriched ²⁸Si/²⁸Si⁷⁴Ge quantum wells. The importance of ²⁸Si to quantum information systems and the scarcity of such material make clear the critical need for an alternate source of enriched silicon such as the one we demonstrate.

3:20pm **EM1-ThA4 Computational Analysis of Interdiffusion in Silicon-Germanium Alloy Films Subject to Patterned Stress Fields**, *Daniel Kaiser*, University of Pennsylvania, *S. Ghosh*, *S.M. Han*, University of New Mexico, *T.R. Sinno*, University of Pennsylvania

In this talk we present a multi-element computational approach for quantitatively describing atomic interdiffusion within a random-alloy SiGe wafer subject to a patterned stress field imposed by an indenter array applied to its surface. The model, and the associated parametric investigations we carry out, are motivated by a recently-proposed approach for forming ordered arrays of heteroepitaxial Ge quantum dots (QD) on semiconductor substrates in a scalable and robust manner. In this approach, patterned compositional redistribution of Si and Ge atoms is driven by an applied stress field under thermal annealing. The resulting compositional heterogeneity is shown to induce an internal stress field in the SiGe substrate wafer that persists after the indenter array is removed, thereby effectively "transferring" the stress pattern of the indenter into the substrate. The transferred stress pattern, which we study in detail as a function of several parameters including indenter geometry and thermal annealing schedule, is then used to drive patterning in a subsequent Ge deposition step.

The interdiffusion model is based on a combination of lattice kinetic Monte Carlo (LKMC) and static energy minimization. The LKMC simulation is propagated using rates for atomic diffusion that depend explicitly on local values of stress, composition, and temperature. The dependence of atomic diffusion on composition is regressed to experimental data while the stress dependence is described using the theory of activation volumes [1]. The stress field is updated quasi-statically using a separate energy minimization routine with forces computed based on a Tersoff interatomic potential for the Si-Ge system [2]. The atomic stresses and identities are then smoothed to generate continuous fields that are used as input into the LKMC simulation.

Using our model, we establish that atomic redistribution is feasible for reasonable indenter forces and annealing times and temperatures. We compute the corresponding internal stresses in the compositionally patterned film for several different annealing conditions and show that these stresses are likely to be large enough to influence subsequent Ge quantum dot nucleation and growth. We also compare our results to recent experimental measurements.

References:

[1] M. J. Aziz, Applied Physics Letters 70, 2810 (1997).

[2] J. Tersoff, Physical Review B 39, 5566 (1989).

4:00pm **EM1-ThA6 Scanning Capacitance Microscopy of Atomically-Precise Donor Devices in Si**, *Shashank Misra*, *E. Bussmann*, *M. Rudolph*, *S.M. Carr*, *G. Subramania*, *G. Ten Eyck*, *J. Dominguez*, *M.P. Lilly*, *M. Carroll*, Sandia National Laboratories

Recently, a scanning tunneling microscopy (STM) technique to fabricate atomically-precise dopant-based nanoelectronics in Si has been developed. Phosphorus donors are placed via an atomic-precision template formed by STM H-depassivation lithography, then capped with epi-Si and lastly metal contacts are made to the buried donor layer using conventional microfabrication. New challenges are introduced with this approach that center around difficulties to locate and characterize the pattern of buried donors. In this talk, we show that scanning capacitance microscopy (SCM) can image these buried donor nanostructures with sub-100-nm tip-limited resolution. The technique is used to successfully locate and characterize buried donor nanostructures relative to surface alignment marks. This approach relaxes alignment requirements for the STM lithography step and can offer improved alignment of subsequent metallization steps. The SCM technique is also used to nondestructively image the shape of the electronic carrier distribution and characterize the relative doping levels. This work, performed in part at the Center for Integrated Nanotechnologies, a U.S. DOE Office of Basic Energy Sciences user facility, was supported by Sandia's Lab Directed Research and Development Program. Sandia is a multi-program lab operated by Sandia Corp, a Lockheed-Martin Company, for U. S. DOE under Contract DE-AC04-94AL85000.

4:20pm **EMI-ThA7 SiGe on sSOI: Nanoscale Engineering of Structures and Devices on Surfaces**, *Esmeralda Yitamben, E. Bussmann*, Sandia National Laboratories, *R. Butera*, Laboratory for Physical Sciences, *S. Misra, M. Rudolph, S.M. Carr, M. Carroll*, Sandia National Laboratories
The relentless increase in both density and speed that has characterized microelectronics, and now nanoelectronics, will require a new paradigm to continue beyond current technologies. One proposed such paradigm shift demands the ultimate control over the number and position of dopants in a device, which includes quantum information processing and variety of semiconductor device materials and architectures aimed at solving end-of-Moore's law issues.

Such a work requires the development of a tool for the design of atomically precise devices on silicon and other surfaces, in hope of studying the effect of local interactions between atomic-scale structures, their microscopic behavior, and how quantum mechanical effects might influence nano-device behavior in very small structures. Demonstrations of remarkable 2D nanostructures down to single atom devices are reported here thanks to the development of scanning tunneling microscopy (STM) as an imaging and patterning tool. These include atomic-scale depassivation of a hydrogen terminated surface with an STM, toward the incorporation of dopants in silicon, and SiGe growth on strained silicon on insulator (sSOI). sSOI has been shown to be relatively insensitive to thermal relaxation and thereby provides a starting material that satisfies the requirements of both enabling high temperature surface preparation steps combined with providing a strained layer that can be capped with relaxed SiGe forming a high quality interface for gate tunable channel formation. In this talk we will present, STM and other characterization results on cleaning, hydrogen lithography, dopant incorporation and SiGe growth on sSOI.

Acknowledgments: This work was performed, in part, at the Center for Integrated Nanotechnologies, a U.S. DOE, Office of Basic Energy Sciences user facility. The work was supported by the Sandia National Laboratories LDRD Program. Sandia National Laboratories is a multi-program laboratory operated by Sandia Corporation, a Lockheed-Martin Company, for the U. S. Department of Energy under Contract No. DE-AC04-94AL85000.

4:40pm **EMI-ThA8 Creating a Responsive SiGe Substrate to Form 2D Array of Ge Quantum Dots Using Stress-induced Near-surface Compositional Redistribution**, *S. Ghosh*, University of New Mexico, *D. Kaiser, T.R. Sinno*, University of Pennsylvania, *Sang M. Han*, University of New Mexico

A well-defined array of Ge quantum structures possesses unique electronic properties for a variety of applications, including quantum-computers and infrared photodetectors. Herein, we use simulation to predict and experiment to demonstrate the compositional redistribution of Si and Ge in the near-surface region of $\text{Si}_{0.8}\text{Ge}_{0.2}$ substrates by applying a spatially structured compressive stress to the substrate and thermally annealing the substrate under stress. The primary advantage of the proposed approach is that a single, reusable template is used to induce the compositional variation for multiple substrates. The compositional redistribution of Ge is predicted under purely elastic deformation, using a lattice kinetic Monte-Carlo simulation that accounts for the influence of composition, temperature, and stress on the diffusion kinetics of Ge in SiGe alloy. Atomistic stress field in a SiGe slab is computed using the Tersoff empirical potential and static relaxation. This compositional variation in turn can be used to selectively grow a 2D array of Ge quantum dots upon Ge exposure. To complement the computational prediction, the compressive stress is applied by pressing a 2D array of Si pillars against the $\text{Si}_{0.8}\text{Ge}_{0.2}$ substrate. Hertz contact model is used to calculate the compressive stress applied to the $\text{Si}_{0.8}\text{Ge}_{0.2}$ substrate under the Si nanopillars. We observe that the magnitude of compressive stress and annealing temperature determine the nature of deformation (elastic or plastic) in the $\text{Si}_{0.8}\text{Ge}_{0.2}$ substrate. Corresponding energy dispersive x-ray spectroscopy (EDS) shows that the compositional redistribution of Si and Ge in the near-surface region of $\text{Si}_{0.8}\text{Ge}_{0.2}$ substrates results from elastic deformation within a thermal annealing temperature range of 950 to 1000 °C and an applied stress range of 15 to 18 GPa. Based on nano-probe EDS, the elastically deformed compressed region shows near-complete Ge depletion and Si enrichment in atomic concentration. However, the temperature and stress exceeding the aforementioned ranges result in plastic deformation with no compositional variation. The plastic deformation depth is ~30 nm according to scanning transmission electron microscope images. We attribute the plastic deformation to (1) the localized pressure applied to the substrate under the contact area, (2) the near-surface substrate stiffness at substrate temperature, and (3) the tensile biaxial stress under the compressed region due to different thermal expansion rates of Si vs. $\text{Si}_{0.8}\text{Ge}_{0.2}$.

5:00pm **EMI-ThA9 DFTMD Modeling of Atomic Scale Structure Requirements for amorphous Sub 0.5 EOT Gate Oxides**, *T. Kent, T. Kaufman-Osborn, M. Edmonds, S.W. Park, J.H. Park, L.J. Kwak, E.A. Chagarov*, University of California, San Diego, *P. Choudhury*, New Mexico Institute of Mining and Technology, *R. Droopad*, Texas State University, *Andrew C. Kummel*, University of California, San Diego

For EOT scaling below 0.5 nm on FinFETs, it is necessary to nucleate the ALD in 99% of the unit cells on multiple crystallographic faces to obviate the requirement that the oxide overgrow non-reactive unit cells. (1) DFTMD calculations of high- k /InGaAs stacks annealed at 700K show that oxide bonding to each InGaAs surface atom in each cell is critical to avoid dangling bonds creating conduction band edge states; this requires high ALD nucleation by a metal precursor density follow by oxidation of any metal-metal bonds formed during nucleation. For III-V semiconductors, experimental STM and STS studies show the in-situ exposure of just a few hundred Langmuirs of atomic H readily removes both group V and group III oxides from 001 and 110 surfaces allowing high nucleation density of metal ALD precursors. Concurrent MOSCAP studies show demonstrate sub 0.5 nm EOT gate oxides with low defect densities on InGaAs after in-situ cleaning and high nucleation density ALD. (2) DFTMD studies of the $\text{a-Al}_2\text{O}_3/\text{SiGe}(001)$ stack show that the SiGe(001) interface with Si termination ($\text{a-Al}_2\text{O}_3/\text{Si-SiGe}(001)$) has a superior electronic structure to the interface with Ge termination ($\text{a-Al}_2\text{O}_3/\text{Ge-SiGe}(001)$). Silicon termination of SiGe should also be highly favorable for forming gas passivation of dangling bonds. For SiGe(001) a novel technique has been developed to produce surface which will mimic the good passivation properties of Si(001) by terminating the surface in a monolayer of Si-OH which will react with nearly any metal ALD precursor. (3) While group IV and III-V semiconductors can be nucleated by covalent bonds, 2D semiconductors require a different approach. DFTMD simulation studies show the metal coordination complexes can readily chemisorb on 2D semiconductor via non-bonding interaction and they can covalent bond multiple TMA molecules consistent with a submolecular nucleation density. A technique has been developed for functionalize 2D semiconductors with a phthalocyanine, and it has been demonstrated it can nucleate insulation sub 1nm gate oxide growth.

5:20pm **EMI-ThA10 Crystalline SrHfO₃ Grown Directly on Ge (001) by Atomic Layer Deposition as a Gate Oxide for High-Mobility Ge-based Transistors**, *Martin McDaniel, T.Q. Ngo, A.B. Posadas, C. Hu, S.N. Chopra, E.T. Yu, A.A. Demkov, J.G. Ekerdt*, The University of Texas at Austin

Crystalline strontium hafnate, SrHfO₃ (SHO), is an ideal candidate to study as a suitable high- k gate dielectric on Ge. SHO ($a \sim 4.069$ Å) has a reasonable lattice match to the Ge (001) surface ($a/\sqrt{2} \sim 3.992$ Å), yielding a ~1.9% compressive strain in the epitaxial film. SHO shows a high permittivity ($k \sim 20$) with appropriate band alignment (~1 eV offset) to Ge. In addition, the crystalline nature of the SHO film is expected to drastically reduce the interface trap density at the oxide-Ge interface. We will report our recent results on the growth, characterization, and electrical performance, of epitaxial SHO films and heterostructures for next-generation high- k dielectrics on Ge.

In our recent publication, we reported on the direct growth of crystalline strontium titanate, SrTiO₃ (STO), on Ge via atomic layer deposition.^[1] Electrical measurements of a 15-nm thick undoped STO film show a large dielectric constant ($k \sim 90$), but high leakage current (~10 A/cm² at +1 eV). In the present work, the unfavorable conduction band offset (and high leakage current) of STO on Ge is circumvented by growing the HF-based perovskite, SHO. For the growth of SHO, we employ the commercially available strontium bis(triisopropylcyclopentadienyl) and hafnium formamidate precursors. After thermal deoxidation, the Ge substrate is transferred *in vacuo* to the deposition chamber where a thin film of SHO (2-4 nm) is deposited by ALD at 225 °C. Following post-deposition annealing at 700 °C, the perovskite film becomes crystalline with epitaxial registry to the underlying Ge (001) substrate. *In situ* x-ray photoelectron spectroscopy confirms stoichiometric to Sr-rich films with no GeO_x formation or carbon impurities.

Ex situ x-ray diffraction confirms the perovskite structure and orientation of the SHO film. Thicker SHO films (above 2 nm) appear to show a relaxed lattice constant, indicating relaxation of the epitaxial film above the critical thickness. The electrical performance of several SHO films and heterostructures will be presented. In general, the leakage current is reduced by several orders of magnitude for the SHO films versus STO on Ge. The current work demonstrates the promise for crystalline oxides grown by ALD on Ge for advanced semiconductor devices, including high-mobility Ge-based transistors.

[1] M. D. McDaniel *et al.*, "A Chemical Route to Monolithic Integration of Crystalline Oxides on Semiconductors," accepted to *Adv. Mater. Interfaces* (2014), doi: 10.1002/admi.201400081.

5:40pm **EM1-ThA11 The Influence of Carbon Incorporation into Gd₂O₃ High-k Gate Dielectric on the Electronic Behavior of the MOS Stack**, *Pini Shekhter*, Technion Israel Institute of Technology, Israel, *A.R. Chaudhuri*, Leibniz University, Germany, *A. Laha*, Indian Institute of Technology Bombay, India, *H.J. Osten*, Leibniz University, Germany, *M. Eizenberg*, Technion Israel Institute of Technology, Israel

High k dielectric materials receive great attention in recent years due to the downscaling of metal-oxide-semiconductor (MOS) devices leading to the need in replacing the traditionally used SiO₂ gate oxide. Rare earth oxides are leading candidates as high-k dielectrics. Introduction of different elements into the bulk of such oxides can drastically alter the behavior of the MOS stack.

Here we present the results of incorporation of carbon into the bulk of Gd₂O₃ on the electrical properties of the Pt/Gd₂O₃:C/Si stack. Crystalline layers of stoichiometric Gd₂O₃ were MBE deposited together with elemental C on Si (100) substrates. Four samples with different concentration of elemental C were prepared: 0%, 0.10%, 0.67% C and 1.89%. MOS capacitors were prepared by in-vacuo (in the MBE tool) evaporating Pt through a shadow mask.

Capacitance voltage (C-V) measurements revealed an increase in the flatband voltage (V_{fb}) for the carbon rich sample. While the three samples with the lower carbon content all showed V_{fb} voltages of $-0.1 \div +0.2$ V, the sample with 1.89% carbon presented a significant increase to 2.25 V.

X ray diffraction (XRD) revealed that all the layers hold the same structure and that no orientation differences are present in the layers, ruling out the option of structural differences leading to such a change in V_{fb} . Time of flight secondary ion mass spectroscopy (ToF-SIMS) depth profiles revealed an uneven concentration profile for the carbon in the 0.67% and 1.89% samples. For both samples, the same concentration was found in the bulk of the layer, indicating the existence of a certain solubility limit that had been exceeded. This led to some segregation for the 0.67% sample to the inner interface while substantial segregation was observed in the 1.89% sample to the inner interface and some to the outer surface. Transmission electron microscope (TEM) micrographs show a thin amorphous interface layer that is formed between the Gd₂O₃ and Si that most likely plays a role in the capturing of the segregating carbon atoms.

We propose that the carbon segregation causes a modification of V_{fb} which is an important property of the MOS stack. By using carbon incorporation it might be possible to develop an effective method for controlling V_{fb} without changing the process or materials for any of the MOS gate components.

Electronic Materials and Processing

Room: 314 - Session EM2-ThA

Hybrid and Organic Electronics

Moderator: Sean King, Intel Corporation, Rachael Myers-Ward, U.S. Naval Research Laboratory

4:00pm **EM2-ThA6 Innovating Organic Electronics and Photonics**, *Bernard Kippelen*, Georgia Institute of Technology **INVITED**

Printed organic electronics, a technology based on organic semiconductors that can be processed into thin films using vacuum processing or conventional printing and coating techniques, has been the subject of active research and development over the past decades. A range of solid-state devices, including organic light-emitting diodes (OLEDs), organic field-effect transistors (OFETs), photodiodes, and solar cells, have been demonstrated with this new class of materials. However, despite a steady progress in performance, many challenges remain and further scientific and technological advances are required before this emerging technology can unleash its full potential.

In this talk, we will review recent advances both in materials and device architectures in a series of organic semiconductor devices. First, we will present progress in organic light-emitting devices with an unconventional architecture that yield current efficacies of 200 cd/A at a luminance of 1000 nits and 100 cd/A at 100,000 nits. Next, we will discuss a new organic field-effect transistor geometry that yield unprecedented environmental stability and allows for continuous reversible sensing in aqueous media. In a third part, we will discuss recent advances in organic photovoltaic devices. A new method to produce air-stable low work function electrodes as a substitute for Ca will be presented. This method is based on surface modification by water-soluble polymers that physisorb to the surface of

various conductors and lead to large surface dipoles that shift the vacuum level (> 1 eV) reducing the injection or collection barrier for electrons. We will show that these advances in interface modification can be used to design organic solar cells with novel architectures that can overcome some of the economic hurdles of current approaches and accelerate the deployment of these technologies. We will show that the current-voltage characteristics of organic solar cells can be modeled with engineering-inspired equivalent circuit models. Strategies based on transfer lamination will be presented that allow for a drastic reduction of parasitic shunt effects, enabling solar cells with unprecedented dynamic range. Finally, we will discuss how to minimize the environmental footprint of organic electronic technologies.

4:40pm **EM2-ThA8 Role of Light Scattering in Hybrid Solar Cells**, *James Dorman*, *M. Noebels*, *T. Pfadler*, *J. Weickert*, *L. Schmidt-Mende*, University of Konstanz, Germany

Hybrid solar cells, with an inorganic/organic interface for charge separation, have been extensively investigated in the past decade in order to replace the expensive Si based technology with an inexpensive alternative. Typically, these devices incorporate a mesoporous TiO₂ film which is decorated with dye molecules and filled with a hole transport material, to conduct the electrons and holes, respectively. Recently, devices with an liquid electrolyte have been able to reach up to 13% conversion efficiency. However, the TiO₂ mesoporous films used for solid state dye sensitized solar cells and hybrid solar cells have a limited light absorption due to thickness of the film (500 nm – 2 μ m) required for efficient charge transportation. An elegant approach to increase the light absorption is to induce "defects" within the mesoporous film, causing light to scatter within the active layer of the device. In this work, we combine the commonly used 25 nm particles with other nanostructures, including 200 nm TiO₂ particles, TiO₂ nanowires, and Sn doped nanowires, all of which produce light scattering due to their dimensions and disorder within the active layer. Through this approach, we are able to correlate an improvement in conversion efficiencies of around 25 % to the light scattering. Furthermore, the incorporation of these nanowire structures increases the mobility of the electrons, allowing for increased charge extraction and reduced recombination. These two phenomena can be simultaneously engineering due to the crystallinity of the "defects" within the films and the cascading conduction bands produced with the incorporation of the doped TiO₂ wires. The extent of the reduction in recombination is quantified through photovoltage decay and impedance spectroscopy measurements and compared to the standard mesoporous TiO₂ devices.

5:00pm **EM2-ThA9 The Structure and Energetics of the Calcium / Phenyl-C₆₁-butyric Acid Methyl Ester Interface**, *James Lownsbury*, *C.T. Campbell*, University of Washington

The vapor deposition of metal films onto the surfaces of organic semiconductors, especially fullerene derivatives and π -conjugated polymers, plays an important role in the fabrication and long-term stability of organic electronic, optoelectronic and photovoltaic devices. Nevertheless, the strength and structural details of metal-organic bonding at such interfaces is not well known. We report here measurements of the interface structure and adsorption energies of calcium metal films grown by vapor deposition on phenyl-C₆₁-butyric acid methyl ester (PCBM). PCBM is a much studied electron acceptor material used in a vast array of organic electronic devices, most notably organic photovoltaics, and Ca metal is often used as the cathode material for such devices due to efficient electron collection at the cathode-active layer interface. Structural details of the interface and the morphology of the evolving metal film were measured using low-energy ion scattering spectroscopy and X-ray photoelectron spectroscopy. The energetics of interfacial bonding were measured using an adsorption microcalorimeter which is unique in the world, and which has been applied previously to the adsorption of Ca on common and well-researched electron donor materials including derivatives of poly(phenylene-vinylene), polyfluorene, and polythiophene. Spin-cast PCBM samples were prepared under nitrogen environment and transferred to our ultrahigh vacuum chamber without exposure to atmosphere. There, a pulsed beam of calcium atoms was directed at the sample surface. By simultaneously measuring the heat of adsorption and the sticking probability of the metal atoms as a detailed function of metal coverage, we obtain interfacial bonding energies for Ca on PCBM.

Work supported by the National Science Foundation under grant CHE-1010287

5:20pm **EM2-ThA10 Controlling the Electronic Structure of Organic Semiconductors via Doping**, *Antoine Kahn*, Princeton University **INVITED**

Typical organic (molecular and polymer) semiconductors (OSC) used in organic light emitting diodes, field-effect transistors or photovoltaic cells

have energy gaps upwards of 1.5-2 eV and have very low conductivity due to the exceedingly small density of “free” carriers and the localized nature of these carriers. Chemical doping has proven to be an extremely powerful tool for controlling the electronic structure of these materials, in particular for improving charge carrier injection at contacts. This talk will review recent developments in the area of chemical doping of OSCs [1,2]. The reducing or oxidizing power of a number of n- and p-type organic dopants are reviewed, along with their impact on the electronic structure and conductivity of both vacuum- or solution-processed OSC films. In particular, the talk will outline recent work aimed at passivating, or compensating, deep electronic gap states, or traps, which are due to structural or chemical imperfections and profoundly affect interface energetic and carrier transport [3]. The process implies the control of ultra-low concentrations of dopants just sufficient to fill traps states and render them inactive, without adding significant densities of “free” carriers in the system. Impact on device characteristics will be reviewed [4].

[1] C. K. Chan et al. *Org. Elect.* **9**, 575 (2008)

[2] G. Song et al. *Adv. Mat.* **24**, 699 (2012)

[3] S. Olthof et al., *Phys. Rev. Lett.* **109**, 176601 (2012)

[4] S. Olthof et al., *Appl. Phys. Lett.* **101**, 253303 (2012)

Scanning Probe Microscopy Focus Topic Room: Hall D - Session SP+AS+EM+NS+SS-ThP

Scanning Probe Microscopy Poster Session

SP+AS+EM+NS+SS-ThP2 Fabrication of Single-Walled Carbon Nanotube Probe and Processing of Single Nanometer Scale Pit with High-Aspect-Ratio of Highly Oriented Pyrolytic Graphite Using by STM, *Syun Ohsumimoto, A. Matsumuro*, Aichi Institute of Technology, Japan

Our unique fabrication methods of high-aspect-ratio nanometer scale three-dimensional structures of pits, lines and convex parts using a multi-wall carbon nanotube (MWNT) with diameter of about 50 nm as a STM probe have been developed successfully. It turns out that this method has been applicable to surfaces of various conducting materials, such as noble metal thin films, low-resistivity single crystalline silicon wafer and highly oriented pyrolytic graphite (HOPG). We also have clarified that the physical origin of this nanometer-scale pit processing using STM must be the field evaporation mechanism by the results of TEM *in-situ* observations during fabrication process. In order to realize further ultra-precise three dimensional structures with high aspect ratio, it is surely required that a innovative ultimate ultra-precision processing technology needs fabrication size below several nm, i.e. single nanometer scale.

This study paid great attention to realize the ultimate processing of single nanometer scale structures using a single-wall carbon nanotube (SWNT) probe as our original STM processing. The most important problem was to overcome to much difficulty in synthesis of SWNT probes with high probability. Then, the application of mixed dispersion liquid containing both MWNTs and SWNTs could be devised at the process of producing SWNT probes. In this process, it was clarified that the SWNT easily attached to the point of the MWNT, which was easily adhered to the apex of the conventional tungsten needle through the pulling method that we developed originally. The success rate for synthesis of the SWNT probes with diameters of about 2 nm and 10 nm were drastically increased up to about 10 % and 14 %, respectively. As compared with the case where the dispersion liquid of only SWNT is used, success fabrication rate has been nearly equal to 0 %. Single nanometer scale pits were actually fabricated on HOPG in atmosphere and room temperature condition. The SWNT probe with diameter of about 2 nm under the conditions of a bias voltage of 5 V, tunnel current of 1 nA and fabrication time of 60 s could realize a single nanometer scale pit with the diameter of 9 nm and the depth of 13 nm. The aspect ratio with SWNT probes increased up to about 5 times in the case of MWNT probes. These demonstrate that these STM fabrications by using SWNT probes with several diameters must give a remarkable effect in fabricating three-dimensional high-aspect-ratio structures with single nanometer-scale.

SP+AS+EM+NS+SS-ThP3 Probing the Electronic Structure of the Layered Electride Ca₂N, *Jeonghoon Ha*, NIST/Maryland Nano Center, University of Maryland, *H. Baek*, NIST & Seoul National University, Republic of Korea, *D. Zhang*, NIST/Maryland Nano Center, University of Maryland, *Y. Kim, S. Kim, Y.J. Song*, Sungkyunkwan University, Republic of Korea, *Y. Kuk*, Seoul National University, Republic of Korea, *J.A. Stroscio*, NIST

Electrides are electronic materials in which excessive electrons are confined into cavities defined by the crystal structure. These excessive electrons take the place of negatively charged ions in an ionic crystal. The geometry of the cavities confining these anionic electrons determines the electronic properties of the material and provides a platform to study various interaction physics [1]. A previous study reported the inorganic electride Ca₂N to have a layered structure with anionic electrons confined to 2-dimensional cavities between the cationic crystal layers [2]. In this previous study, transport measurements showed high electron mobility and long mean scattering time, and magneto-resistance measurements confirmed diffusive 2-dimensional transport in the electron layers.

In the present work, we use an ultra-low temperature scanning tunneling microscope to investigate the local electronic structure of a cleaved surface of a Ca₂N single crystal. An energy gap was observed in the tunneling spectrum with a gap size of 0.4 meV. The spectra contain multiple coherence-like peaks which are equally spaced in energy, suggestive of possible multi-band superconductivity or quantum confinement in the electron layers. Temperature-dependent tunneling spectroscopy measurements show a gradual suppression of the energy gap up to 2.5 K. An interesting observation is that the gap structure and the peak features do not get suppressed in the presence of a perpendicular magnetic field up to

14.5 T, suggesting if the crystal is in a superconducting state, then the critical field is extremely large compared to the transition temperature. These observations and further discussion of possible unconventional superconductivity will be discussed in this presentation.

[1] J. Dye, *Science* **301**, 607 (2003)

[2] K. Lee *et al*, *Nature* **494**, 336 (2013)

SP+AS+EM+NS+SS-ThP5 Improving the Accuracy of Atomic Force Microscopy in Nanometrology for Linewidth Measurements, *James Su, N.N. Chu, M.H. Shiao, C.N. Hsiao*, Instrument Technology Research Center, National Applied Research Laboratories, Taiwan, Republic of China

Atomic force microscopy (AFM) has an important role in dimensional metrology especially in the nanoscale. The morphology image processed by the AFM is the interaction between the tip and the sample surface. The result of the interaction may cause broadening of peaks and shrinking of valleys in the scanning process caused by tip effects. It would be impossible to differentiate the portion due to the tip and the portion due to the sample surface without determining the tip geometry which is a key role in AFM-image quality. As a case study, AFM measurements of nanowires (NW), carbon nanotubes (CNT) and nano-honeycombs fabricated by nanosphere lithography (NSL) technology are examined. Line width measurement results may expand up to 39.5% by adopting a conventional pyramid-shaped probe and 17.5% by using a conical-shaped one as the dimensions of the scanned features approaches to the order of magnitude of the tip apex. The uncertainty of measurement would expand if tip wear occurs during image scan. Calculation for surface reconstruction has been developed to extract the part related to the tip from the SPM image. The SPM used for these measurements is equipped with a highly accurate scanning system, which employs closed-loop capacitive feedback control to ensure outstanding linearity and position accuracy. To identify the geometry of the tip, a silicon tip characterization grating was imaged between the measurements. Deconvolution process were carried out for topography image corrections, and the results were further compared with the ones measured from the scanning electron microscope (SEM). This process is essential to derive accurate measurement results in the nanoscale region.

SP+AS+EM+NS+SS-ThP8 The Effect of Electrochemical Potential on Single Molecule Conductance, *Esteban Sanchez, R. Aguilar*, BUAP, Mexico, *S. Afsari*, Temple University, *Z. Li*, Ball State University, *E. Borguet*, Temple University

Porphyryns have been widely studied for their electrochemical properties to understand charge transfer. The related property of charge transport can be accessed by single molecule conductance (SMC) measurements. The most common SMC studies involve transport between different anchor groups at transversal positions in the molecule [1]. Few investigations have been made using porphyryns lying flat on the substrate in electrochemical environment [2]. Recent studies have shown that the templating effect of self-assembly can be exploited to orient molecules in metal-molecule-metal junctions, so that transport perpendicular to the molecular plane can also be easily accessed [3].

This goal research is to use self assembly, verified by scanning tunneling microscopy (STM), to measure charge transport in single porphyryns adsorbed flat on the Au (111) surface. 5,10,15,20-Tetra(4-pyridyl)porphyrin (TPyP) is a good candidate for this research because it has been demonstrated that this porphyrin has a strong interaction with, and can form ordered layers on, Au (111) in electrochemical environment [4]. This control of the orientation of the porphyrin by electrochemical potential enables us to make SMC measurements perpendicular to the molecular plane.

[1] Zhihai Li, Manuel Smeu, Mark A. Ratner, and Eric Borguet, Effect of Anchoring Groups on Single Molecule Charge Transport through Porphyryns, *J. Phys. Chem. C*, **117**, 14890–14898 (2013).

[2] Quirina Ferreira, Ana M. Braganca, Luis Alcaccer, and Jorge Morgado, Conductance of Well-Defined Porphyrin Self-Assembled Molecular Wires up to 14 nm in Length, *J. Phys. Chem. C*, **118**, 7229–7234 (2014)

[3] Sepideh Afsari, Zhihai Li, and Eric Borguet, Orientation-Controlled Single-Molecule Junctions, *Angew. Chem. Int. Ed.* **53**, 9771–9774 (2014).

[4] Tao Ye, Yufan He, and Eric Borguet, Adsorption and Electrochemical Activity: An In Situ Electrochemical Scanning Tunneling Microscopy Study of Electrode Reactions and Potential-Induced Adsorption of Porphyryns, *J. Phys. Chem. B*, **110**, 6141–6147 (2006).

2D Materials Focus Topic

Room: 310 - Session 2D+EM+MS+NS-FrM

2D Materials: Device Physics and Applications

Moderator: Daniel Gunlycke, Naval Research Laboratory

8:20am 2D+EM+MS+NS-FrM1 1, 2, 3... **Ripples, Gaps and Transport in Few-layer Graphene Membranes**, *ChunNing(Jeanie) Lau*, University of California, Riverside **INVITED**

Graphene, a two - dimensional single atomic layer of carbon, has recently emerged as a new model system for condensed matter physics, as well as a promising candidate for electronic materials. Though single layer graphene is gapless, bilayer and trilayer graphene have tunable band gaps that may be induced by out-of-plane electric fields or arise from collective excitation of electrons. Here I will present our results on mechanical manipulation and transport measurements in bilayer and trilayer graphene devices with mobility as high as 400,000 cm²/Vs. We demonstrate ripple formation due to thermally or mechanically induced strain, the presence of an intrinsic gapped state in bilayer and trilayer graphene at the charge neutrality point and evidence for quantum phase transition. Our results underscore the fascinating physics in these 2D membranes, and have implications for band gap engineering for graphene electronics and optoelectronic applications.

9:00am 2D+EM+MS+NS-FrM3 **Photoinduced Doping in Heterostructures of Graphene and Boron Nitride**, *Jairo Velasco Jr., L. Ju*, UC Berkeley, *E. Huang*, Stanford University, *S. Kahn, C. Nosiola, H.-Z. Tsai*, UC Berkeley, *W. Yang*, Beijing National Laboratory for Condensed Matter Physics, Republic of China, *T. Taniguchi, K. Wantanabe*, National Institute for Materials Science (NIMS), Japan, *Y. Zhang*, Fudan University, Republic of China, *G. Zhang*, Beijing National Laboratory for Condensed Matter Physics, Republic of China, *M.F. Crommie, A. Zettl, F. Wang*, UC Berkeley

Van der Waals heterostructures (VDH) provide an exciting new platform for materials engineering, where a variety of layered materials with different electrical, optical and mechanical responses can be stacked together to enable new physics and novel functionalities. Here we report an emerging optoelectronic phenomenon (i.e. photo-induced modulation doping) in the graphene-boron nitride VDH (G/BN heterostructure). We find it enables flexible and repeatable writing and erasing of charge doping in graphene with visible light. We demonstrate that the photo-induced modulation doping maintains the remarkable carrier mobility of the G/BN heterostructure, and it can be used to generate spatially varying doping profiles like *pn* junctions. Our work contributes towards understanding light-matter interactions in VDHs, and innovates a simple technique for creating inhomogeneous doping in high mobility graphene devices. This opens the door for new scientific studies and applications.

9:20am 2D+EM+MS+NS-FrM4 **Two-dimensional Resistance Map of Graphene p-n Junction in the Quantum Hall Regime**, *Nikolai N. Klimov, S. Le, C.A. Richter*, National Institute of Standards and Technology (NIST), *J. Yan*, University of Massachusetts, Amherst, *E. Comfort, J.U. Lee*, SUNY-University of Albany, *D.B. Newell*, National Institute of Standards and Technology (NIST)

Graphene, a two dimensional (2D) electronic system with a unique band structure, is a promising material for future electronic devices, especially for electrical metrology [1]. Currently, devices based upon GaAs heterostructures 2D electron gases (GaAs-2DEG) are used to realize a single quantum resistance standard value of $(\frac{1}{2})h/e^2 = 12,906.4035 \Omega$ with metrological accuracy. It is important to realize resistance values over a wider resistance scale to expand the technical relevance of quantum resistance standards.

In the past, attempts have been made by using parallel or series GaAs-2DEG Hall bars to achieve multiple or fractional resistance values of h/e^2 . However, the difficulties of fabricating ideal contacts and metal interconnects between the Hall bars severely limit the yield of properly operating devices. Graphene, with its ability to create both electron and hole 2D gases on a single Hall bar device without metal interconnects, is an ideal platform to overcome this difficulty [2].

We have fabricated a graphene FET p-n junction device in a Hall bar geometry and experimentally characterized it at large magnetic fields to determine the range of quantized resistance values that can be obtained. The device features two doped polysilicon split gates that are buried in a SiO₂ substrate within 100 nm-150 nm from the surface of graphene. The fabrication process achieves an atomically smooth dielectric surface, which is needed to preserve the intrinsic band structure of graphene. Independent

voltage control on these gates allows separate tuning of both type and concentration of charge carriers in the two parts of graphene conducting channel. In addition, a very narrow 150 nm gap between split gates gives a very sharp junction. Measurement of the sample's resistance at different gate values and measurement configurations in the quantum Hall regime allows us to fully characterize the device and to obtain multiples or fractions of the resistance value h/e^2 . We will show that our experimental results can be explained by the Landauer-Büttiker edge-state transport model with the assumption of a partial mixing at the p-n interface. Potential application of graphene p-n junction devices for resistance standards with a wide range of resistance values other than $h/2e^2$ will be discussed.

References:

[1] A. Tzalenchuk, *et al.*, Nature Nanotech., 5, 186 (2010)

[2] M. Woszczyzna, *et al.*, APL, 99, 022112 (2011)

9:40am 2D+EM+MS+NS-FrM5 **Electrical Breakdown and Current Carrying Ability of Multilayer MoS₂ Transistors**, *Philip Feng, R. Yang, Z. Wang*, Case Western Reserve University

We report the first study of electrical breakdown of multilayer molybdenum disulphide (MoS₂) transistors through precision electrical measurements and simulation that shows the effect of varying the device size and conductivities on the breakdown limit. We demonstrate that the multilayer devices have better current carrying capabilities compared to thin layer devices. We also study the effect of varying MoS₂ thickness upon electron mobility in the channel.

MoS₂ has recently emerged as a new two-dimensional (2D) semiconducting crystal with attractive properties, such as the absence of dangling bonds, high thermal stability, and having a thickness-dependent bandgap [#_edn1]. While prototype single- and few-layer MoS₂ FETs and circuits have been demonstrated, in practice multilayer (up to 10s of nanometers) devices may be more desirable for certain applications: they can have higher carrier mobility and density of states under the same dielectric environment, greater mechanical strength, higher current limit and better manufacturability [#_edn2] [#_edn3]. While the breakdown of single layer MoS₂ transistors has been demonstrated [#_edn4], breakdown of multilayer devices has not been studied.

In this work, we study the electrical breakdown of devices with different thicknesses through experimental demonstration and simulation with finite element method (FEM). We observe that the breakdown process happens gradually with multiple voltage sweeping cycles, and thicker devices generally show higher breakdown current, which is also demonstrated in the simulation. The highest breakdown current in the measurement is 1.2mA, which is one of the highest current reported results so far for MoS₂ transistors. Simulation also shows that with higher conductivity channel, the breakdown current and breakdown current density both increase. The high field transport characteristics of multilayer MoS₂ transistors demonstrate that the devices could drive high loads in circuits and could be used for circuits that require high power or current. The thickness dependence of mobility shows that the device performance can be further improved by carefully tuning the device parameters.

[i] [#_ednref1] Q. H. Wang, *et al.*, Nat. Nanotechnol. 7, 699 (2012).

[ii] [#_ednref2] D. Jariwala, *et al.*, ACS Nano 8, 1102 (2014).

[iii] [#_ednref3] R. Ganatra, Q. Zhang, ACS Nano (2014), DOI: 10.1021/nn405938z.

[iv] [#_ednref4] D. Lembke, A. Kis, ACS Nano 6, 10070 (2012).

10:00am 2D+EM+MS+NS-FrM6 **Lithography-free Fabrication of Graphene Devices**, *Nick Thissen, R.H.J. Vervuurt*, Eindhoven University of Technology, Netherlands, *J.J.L. Mulders*, FEI Electron Optics, Netherlands, *J.W. Weber, A.J.M. Mackus, W.M.M. Kessels, A.A. Bol*, Eindhoven University of Technology, Netherlands

Graphene device fabrication on large-area graphene typically involves several patterning steps using electron beam or optical lithography, followed by graphene etching and metallization for application of metallic contacts. However, the resist films and lift-off chemicals used in lithography introduce compatibility issues, such as the difficulty of removing the resist from the graphene. This resist residue has a negative influence on the thermal and electrical properties of the graphene and interferes with functionalization of the graphene. This motivates the development of a 'bottom-up', direct-write, lithography-free fabrication method.

In this work, a lithography-free fabrication method for graphene-based devices was developed. As a first step, the method involves direct

patterning of large-area graphene by focused ion beam (FIB) in order to isolate graphene from the bulk. The patterning of the graphene is performed in a DualBeam (SEM / FIB) system, in which a 30 kV FIB is used to locally remove graphene from the substrate. An *in situ* Raman microscope allows for direct observation of the graphene quality before and after FIB processing, from which it was determined that a low Ga-ion dose of 10 C/m² is sufficient for complete graphene removal. By optimizing the pattern design, the ion beam current and the background pressure in the DualBeam system, unintentional damage of the graphene by scattered ions is almost completely prevented.

After FIB patterning, as a second step a direct-write atomic layer deposition (ALD) technique is applied in the same system to locally deposit contacts to the isolated graphene. In the direct-write ALD technique, the patterning capability of electron beam induced deposition (EBID) is combined with the material quality of ALD. A thin seed layer consisting of small Pt grains in amorphous carbon is deposited on the graphene by EBID in the desired contact pattern. Subsequently, a selective ALD process purifies the seed layers and builds them into high-quality Pt contacts. This combined approach yields virtually 100% pure Pt (resistivity of 12 μΩcm) with a lateral resolution of 10 nm¹¹. This chemical approach to contact deposition is expected to yield lower contact resistances compared to conventional physical deposition techniques.

By combining patterning and direct contact deposition in the same system, graphene devices were fabricated from large-area graphene without the use of lithography. First results from sub-optimal devices demonstrate field-effect mobilities approaching 500 cm²/Vs and contact resistances as low as (40 ± 30) Ω.

[1] A.J.M. Mackus et al., *Nanoscale* 4, 4477 (2012)

10:40am **2D+EM+MS+NS-FrM8 Electronic Transport in Transition Metal Dichalcogenides**, *Joerg Appenzeller*, Purdue University **INVITED**
Since the discovery of graphene for electronic applications, there has been a substantial worldwide effort to explore other layered materials. Transition metal dichalcogenides (TMDs) like MoS₂, MoSe₂, or WSe₂, to just name a few, not only offer the desired ultra-thin body structure that translates into superior electrostatics as desirable for nanoelectronics applications, but also exhibit a sizable band gap. While to date the ideal application space for these materials has not been identified, it is obvious that only through a detailed understanding of the underlying transport in these layered materials intrinsic properties that lend themselves to particular applications can be uncovered.

In my presentation I will first discuss the benefits of an ultra-thin body structure for scaled tunneling FET applications including tunneling devices. Contacts play a particularly crucial role in this context and can easily mask the intrinsic performance of TMDs as will be discussed based on experimental Schottky barrier tunneling data obtained from MoS₂, MoSe₂ and WSe₂ field-effect transistors. A careful analysis of all these material systems reveals details about Schottky barrier heights for electron and hole injection as well as the band gap. These findings are then put into the context of channel length scaling and layer thickness dependence of three-terminal TMD devices based on MoS₂ transistors. Last, experimental data on the band-to-band tunneling in partially gated WSe₂ device structures will be discussed and projections about the potential usefulness of TMDs for tunneling device applications will be made.

11:20am **2D+EM+MS+NS-FrM10 Controlled Synthesis and Fuel Cell Application of Carbon Nanowalls**, *Hiroki Kondo, S. Imai, K. Ishikawa, M. Sekine, M. Hori*, Nagoya University, Japan, *M. Hiramatsu*, Meiji University, Japan

Carbon nanowalls (CNWs) are one of carbon nanomaterials and contain stacks of graphene sheets vertically standing on a substrate. Each wall with the top edge is continuous crystallographically through bending or branching and composed of nanographite domains. Recently, we have developed the formation method of the ultra-high-density over 10¹³ cm⁻² Pt nanoparticles on the whole surface area of the CNWs with a diameter of 2-3 nm employing metal-organic chemical fluid deposition (MOCFD) method in supercritical fluid (SCF). They are promising as a catalytic electrodes for a polymer electrolyte fuel cell because of its high-specific-surface-area and high aspect ratio. On the other hand, while it is known that Pt nanoparticles are poisoned by CO below 100°C, it is reported that Pt-Au nanoparticles are excellent candidate for a low-temperature anode electrocatalyst. In this study, supporting processes of Pt-Au nanoparticles on the CNWs using the SCF-MOCFD method and their catalytic properties were investigated.

We used the SCF-MOCFD system to support Pt and Au nanoparticles on the CNWs. Firstly, Pt nanoparticles were supported using 1wt% (CH₃C₂H₄)(CH₃)₃Pt solution (2 ml). Then, Au nanoparticles were subsequently supported using (CH₃)₂Au(CH₃COCHCOCH₃) solution (1 ml). Both precursors were diluted by n-hexane [CH₃(CH₂)₄CH₃].

According to the SEM images of the CNWs after the supporting processes of only Pt nanoparticles and, both Pt and Au ones, the nanoparticles are supported on the entire surface area of each CNWs in the both cases. It is also found that the diameter and its distribution of the nanoparticles decrease after the second Au supporting process, while its density increases. This means that the relatively large Pt nanoparticles are effectively removed and small Au nanoparticles are simultaneously supported at the second supporting process. On the other hand, we evaluated cyclic voltammetry (CV) characteristics using CNWs with different-density Pt nanoparticles, in which density of 3.0×10¹² cm⁻² and diameter of 1.1 nm obtained for 10 min supporting and, density of 8.3×10¹² and diameter of 1.5 nm obtained for 30 min supporting. Peaks related to adsorption and desorption of hydrogen were found in both cases. With increasing the supporting time, the specific surface area of Pt evaluated from the CV about twofold increased. However, according to the TEM images, the ratio of surface area of Pt nanoparticles are about fivefold. It is deduced that some parts of Pt nanoparticles are inactive. Therefore, these results indicate that not the crystallinity control of CNWs are essential to improve the catalytic performance.

Spectroscopic Ellipsometry Focus Topic

Room: 304 - Session EL+AS+BI+EM+SS-FrM

Application of SE for the Characterization of Organic and Biological Materials

Moderator: Tino Hofmann, University of Nebraska-Lincoln

8:20am **EL+AS+BI+EM+SS-FrM1 Multimodal Optical and Mass Spectrometric Imaging of Cells and Tissues**, *DaeWon Moon*, DGIST, Republic of Korea **INVITED**

Understanding interfacial phenomena has been one of the main research issues not only in semiconductors but only in life sciences. I have been trying to meet the atomic scale surface and interface analysis challenges from semiconductor industries and furthermore to extend the application scope to biomedical areas. Optical imaging has been most widely and successfully used for biomedical imaging but complementary mass spectrometric imaging can provide more detailed molecular specific information

In this presentation, I report our recent activities of multimodal nanobio imaging of cardiovascular cells and tissues. Firstly, in atherosclerotic plaque imaging using coherent anti-stokes raman scattering (CARS) and time-of-flight secondary ion mass spectrometry (TOF-SIMS), multimodal CARS & SIMS analysis showed that increased cholesterol palmitate may contribute to the formation of a necrotic core by increasing cell death. Secondly, surface plasmon resonance imaging ellipsometry (SPRIE) was developed for cell biointerface imaging of cell adhesion, migration, and infiltration dynamics for HUVEC, CASMC, and T cells. SPRIE images were validated with confocal fluorescence microscopy. Collagen fibrils are widely used as cell adhesion substrates. Changes of surface composition and elastic modulus of collagen fibrils after thermal and acidic treatment were investigated by TOF-SIMS and non-contact force microscopy. Multimodal SPRIE & TOF-SIMS imaging would be a useful methodology for understanding cell-substrate interactions in tissue engineering.

In conclusions, multimodal optical and mass spectrometric imaging provides overall structural and morphological information with complementary molecular specific information, which can be a useful methodology for biomedical studies. Future challenges in optical and mass spectrometric imaging for new biomedical applications will be discussed regarding to *in-vivo* imaging.

9:00am **EL+AS+BI+EM+SS-FrM3 Sum Decomposition of Mueller Matrices from Beetle Cuticles**, *Hans Arwin, R. Magnusson*, Linköping University, Sweden, *E. Garcia-Caurel, A. de Martino*, LPICM-CNRS, Ecole Polytechnique, France, *K. Järrendahl*, Linköping University, Sweden, *R. Ossikovski*, LPICM-CNRS, Ecole Polytechnique, France

Spectral Mueller matrices are very rich in information about physical properties of a sample. We have recently shown that polarizing properties like ellipticity and degree of polarization, can be extracted from a Mueller matrix measured on a beetle cuticle (exoskeleton). Mueller matrices can also be used in regression analysis to model nanostructures in cuticles. Here we present the use of sum decomposition of Mueller matrices from these depolarizing biological reflectors to explore the fundamental character of these reflectors. The objective is to decompose a Mueller matrix into well-defined ideal non-depolarizing matrices corresponding to mirrors, circular polarizers, halfwave retarders etc. Generally it is possible to decompose a measured depolarizing Mueller matrix M into four (or fewer) non-

depolarizing matrices according to $\mathbf{M}=\alpha\mathbf{M}_1+\beta\mathbf{M}_2+\gamma\mathbf{M}_3+\delta\mathbf{M}_4$, where α , β , γ and δ are eigenvalues of the covariance matrix of \mathbf{M} . Two strategies for decomposition will be discussed. A Cloude decomposition will provide the eigenvalues and also the \mathbf{M}_i 's although the latter will contain severe noise in some spectral regions. However, a major advantage with the Cloude decomposition is that the number of nonzero eigenvalues is directly obtained, i.e. the number of contributing \mathbf{M}_i matrices. In an alternative decomposition, the \mathbf{M}_i 's are assumed and the eigenvalues are found by regression analysis based on \mathbf{M} . In the case with two non-zero eigenvalues we define a model Mueller matrix $\mathbf{M}_D=\alpha_R\mathbf{M}_1+\beta_R\mathbf{M}_2$ with $\alpha_R+\beta_R=1$. With α_R as adjustable parameter, the Frobenius norm $\|\mathbf{M}-\mathbf{M}_D\|$ is minimized for each wavelength in the spectral range of \mathbf{M} . For more complex structures, the regression can be extended by adding more matrices up to a total of four. Advantages with a regression approach are its simplicity and stability compared to a Cloude decomposition. The Mueller-matrix spectra of beetle cuticles are recorded with a dual rotating compensator ellipsometer in the spectral range 400 – 900 nm at angles of incidence in the range 20 - 75°. The application of decomposition on biological reflectors is demonstrated on \mathbf{M} measured on the beetle *Cetonia aurata*, which represents a narrow-band chiral Bragg reflector with two non-zero eigenvalues. A decomposition in an ideal mirror and a circular polarizer is feasible. In another example, the broad-band and gold-colored beetle *Chrysina argenteola*, we show that more than two eigenvalues can be nonzero, especially at oblique incidence, and additional matrices are involved.

9:20am **EL+AS+BI+EM+SS-FrM4 Polymer- and Ceramic-Supported Hybrid Gas Separation Membranes Characterized by Ellipsometry, Ioannis A. Mergos, H. Verweij, The Ohio State University**

Membrane structures consist of thin continuous layers deposited on porous ceramic or polymer supports. We have been developing inorganic and hybrid membranes for various applications that include gas separation (e.g. post-combustion CO₂ capture), water purification, Solid Oxide Fuel Cells (SOFC) and sensors. Spectroscopic Ellipsometry (SE) is a major non-destructive characterization tool, which can be used to obtain the thickness (typical range 50 nm...2 μm) and complex refractive index (n,k) of the supported membrane layers. This information, in turn, is used to obtain information about membrane composition, porosity and gas or water sorption. The characterization of fully-ceramic structures on optically smooth porous α-alumina surfaces (roughness ~25 nm, higher than most typical SE applications) has been employed by our group for several years. Recently we have expanded the use of SE to characterization of multi-layered membranes, and of inorganic or polymer layers on polymer supports, on coarser α alumina surfaces, and on ceramic tubes. Examples are γ- and α-alumina on polyethersulfone (PES) and poly-sulfone (PES), Ce_{0.9}Gd_{0.9}O_{1.95} on tubular α-alumina, and successive layers of amorphous microporous silica and polydimethylsiloxane (PDMS) on mesoporous intermediate layers. We have achieved signal detection and interpretation to acquire meaningful results, even in multi-layered structures and in cases with substantial interfacial of surface roughness, or curvature. Overall, the application of SE, including non-destructive characterization at intermediate stages between deposition and processing steps, can significantly facilitate the design of gas separation membrane structures that combine organic and polymer layers.

9:40am **EL+AS+BI+EM+SS-FrM5 Spectroscopic Ellipsometry Methodology for Analysis of Thin Films with Significant Surface Non-idealities: Combining Through-the-Substrate and Film-Side Measurements, Jian Li, University of Toledo, L. Mansfield, National Renewable Energy Laboratory, P. Pradhan, University of Toledo, H. Du, S. Glenn, J. Mann, A. Norman, K. Ramanathan, National Renewable Energy Laboratory, R.W. Collins, University of Toledo, G. Teeter, D. Levi, National Renewable Energy Laboratory**

Spectroscopic ellipsometry (SE) is a powerful tool for studying thin films, including the thickness and dielectric function, the latter being closely related to important properties such as composition, phase, grain size, porosity, and stress. The sub-nanometer sensitivity of SE is best exploited if all interfaces between layers, at substrate/layer and layer/ambient are abrupt and smooth. Even for the simple structure of substrate/film/ambient, however, whereby the film is fabricated in a uniform process, surface non-idealities including roughness, oxides, compositional variations, or a combination of these, are inevitable. If an accurate film dielectric function is of interest, then the widely-used effective medium approximation (EMA) treatment of the surface roughness can distort the result, especially in photon energy range of strong absorption.

In this work, an improved SE methodology has been developed, tested, and applied to study thin films with significant surface non-idealities. The investigated materials include Cu(InGa)Se₂, Zn(O,S), Cu₂ZnSnS₄, and Cu₂SnS₃ deposited on transparent substrates by co-evaporation, sputtering, or chemical bath deposition. The film thicknesses in this study range from ~20 to 4000 nm, with potential applicability of the methodology over an even

wider range. The key component of the SE methodology is integration of through-the-substrate (TS) SE with standard film-side (FS) SE. The following successes have been demonstrated.

(1) When the surface non-ideality is predominantly roughness within the EMA applicability, two-side (FS+TS) SE can minimize dielectric function distortion caused by the EMA assumptions.

(2) When the surface non-ideality is outside the EMA applicability and traditional SE methodology becomes unreliable, accurate results can be obtained using the FS+TS SE methodology, in which the dielectric functions of the surface and bulk layers can be allowed to vary wavelength by wavelength independently. Most thin films of this study fall into this category.

(3) When the surface is macroscopically rough and scatters light, films can be grown intentionally thick and hence rough enough to suppress specular reflection from the surface. In this case, through-the-substrate SE alone can be used to extract the bulk film dielectric function.

An important criterion for evaluating SE analysis on semiconductor films is that the ε₂ spectrum should be flat and essentially zero below the band gap. It is demonstrated that the dielectric functions obtained through the above SE methodology either satisfy or better satisfy this criterion compared to previous studies. The limitations of the SE methodology will also be discussed.

10:00am **EL+AS+BI+EM+SS-FrM6 A Classical Model for Depolarization through Incoherent Superposition of Dipoles Driven by Evanescent Fields, Kurt Hingerl, University Linz, Austria**

A finite spectral resolution and/or an imperfectly collimated beam /and or an (areal) extended light source / and or an (areal) extended detector and/ or a sample with a varying thickness can produce depolarization effects. However, despite these experimental findings, there are to our knowledge no physical models published which trace the origin of depolarization back to the atomic properties. Therefore, we explain depolarization by the following steps:

1) A mathematical model for cross-polarization: In structured samples the Fresnel reflectances are not correct any more, they rely on homogeneity (i.e. an arbitrary shift of the sample along any surface direction). Mathematicians are aware of this and the numerical tools developed by them, e.g. finite element methods (FEM) or rigorous coupled wave analysis (RCWA), take these effects into account, when matching boundary conditions. Mathematically the Jones matrix then possesses nondiagonal elements. This cross polarization signifies the presence of a totally polarized photon state, but takes into account that p- polarized incoming light creates s- polarized outgoing and vice versa.

2) Cross-polarization then has to take into account radiating dipoles, whose radiation create the scattered cross (and later, after incoherent superposition, partially de-) polarized field. In any structured sample there are inner boundaries present and it is straightforward to show that the usual boundary conditions on the continuity of the tangential electric field and the normal of the displacement field yield inherent contradictions at these inner boundaries. In order to fulfill the boundary conditions, close to the inner boundaries **evanescent fields** must be present, which drive the atomic dipoles in **other spatial directions than the incoming field**.

3) Depolarization: The end point of the field of unpolarized light may be assumed to move quite irregularly, and the light shows no preferential directional properties when resolved in arbitrary orthogonal directions normal to the direction of propagation. Depolarization is mathematically described by the **correlation** which exists between these two orthogonal directions. Furthermore the extension of the light source, the extension of the detector and **the extension of the illuminated sample area (especially its depth!)** are reducing the value above. The measured intensity at the detector is obtained by the **incoherent superposition** of the single waves. The mathematical formulation is given by the Cittert-Zernike theorem (M. Born & E. Wolf, *Principles of Optics*, chapter X.9).

10:40am **EL+AS+BI+EM+SS-FrM8 The Development Of Highly-Oriented 3D Nanostructures For Use With Ultra-Thin Layer Chromatography And Ellipsometry, Erika Pfaunmiller, University of Nebraska Lincoln, D. Peev, D. Sekora, University of Nebraska-Lincoln, S. Beeram, University of Nebraska Lincoln, C. Rice, M. Schubert, T. Hofmann, D. Hage, University of Nebraska-Lincoln**

Slanted columnar thin films based upon SiO₂ were deposited on glass substrates through the use of glancing angle deposition (GLAD). The typical length of these structures was between 500 nm and 2.5 μm. These thin films were then evaluated for use in ultra-thin layer chromatography (UTLC), which is a special type of thin layer chromatography (TLC) that uses supports that incorporate nanomaterials. In this work, a series of lipophilic dyes were analyzed through the use of both TLC and UTLC followed by detection through imaging ellipsometry. It has previously been

demonstrated that changes in birefringence is seen as small organic molecules attach to some of the types of nanostructures that were used in this study. The principle behind the detection of organic chemicals that attach/adsorb onto such nanostructures is based on the variation of the optical anisotropy of highly-ordered 3D nanostructures with attached or adsorbed molecules. This causes screening of the dielectric displacement charges that are produced by the incident electromagnetic fields within the nanostructures, which can be measured as a variation of the effective birefringence of the highly-ordered 3D nanostructures. Measurement of this birefringence was done through generalized imaging ellipsometry. This combined imaging and separation approach should be useful for label-free detection in UTLC and for the chromatographic analysis of a various target compounds.

Electronic Materials and Processing

Room: 311 - Session EM+EN-FrM

Nitrides for LED and PV Device Applications

Moderator: Nikolaus Dietz, Georgia State University

9:00am EM+EN-FrM3 **The Capricious Effect of Heating on the Surface Photovoltage in Si-doped GaN**, Joy McNamara, K.L. Phumisithikul, A.A. Baski, M.A. Reshchikov, Virginia Commonwealth University

Surface photovoltage (SPV) studies on gallium nitride (GaN) thin films have recently revealed much information, including the band bending at the surface, the effect of polarity on the surface potential, the role of the surface oxide layer, and many other surface related behaviors. By using the Kelvin probe method, the surface potential of GaN can be measured in respect to a vibrating metal probe. To investigate the SPV behavior of both n- and p-type GaN, several experimental conditions have been varied, such as ambient or temperature. It is expected from a thermionic model that the surface band bending decreases immediately under ultraviolet (UV) illumination with the intensity used in these measurements. This results in the production of an immediate increase in the SPV signal as measured by the Kelvin probe. In recent studies on GaN thin films grown by metal organic chemical vapor deposition (MOCVD) and doped with silicon (concentration of $\sim 10^{19}$ cm⁻³), we observed an effect of heating on the transient SPV behavior due to the history of sample preparation. For the first group of samples, a very fast rise of the SPV signal by 0.7 eV was observed at room temperature under UV illumination in vacuum, after the samples were initially exposed to air. However, after heating these samples to 600 K in vacuum before taking measurements at room temperature, the fast SPV component decreased to 0.2 eV, while a slow, logarithmic-in-time increase was observed for longer times of UV exposure, with a maximum SPV signal of only 0.4 eV after 30 min. For the second group of samples, the heating in vacuum caused the magnitude of the initial fast SPV in vacuum to be much smaller (0.7 eV after air exposure and 0.3 eV after heating), but without a slow, logarithmic-in-time increase. The SPV behavior could be reversed by UV illumination in air at room temperature. Interestingly, similar SPV behavior has also been observed in ZnO films. The reversible heating effect is preliminarily explained by assuming that the presence of an oxide layer either inhibits or allows the transfer of UV-induced charge carriers between the bulk and surface states, depending on the conditions of the measurement.

9:20am EM+EN-FrM4 **Atomic Layer Deposition of III-Nitride Alloys using Hollow-Cathode Plasma Source for Post-CMOS Processing and 3D Integration**, C. Ozgit-Akgun, A. Haider, AliKamal Okyay, N. Biyikli, Bilkent University, Turkey

Plasma-assisted atomic layer deposition (PA-ALD) is a cyclic, low-temperature thin film deposition method, in which the substrate surface is exposed to sequential pulses of precursor molecules and plasma species separated by evacuation and/or purging periods. When compared to other techniques, ALD stands out with its self-limiting growth mechanism, which enables the deposition of highly uniform and conformal thin films with sub-angstrom thickness control. These features make PA-ALD a promising and alternative technique for the low-temperature deposition of III-nitrides and their alloys in post-CMOS processing and 3D integration technology.

In our previous reports on the PA-ALD of polycrystalline wurtzite AlN thin films at temperatures ranging from 100-500 °C using trimethylaluminum as the Al precursor, films deposited at temperatures within the ALD window (100–200 °C for both NH₃ and N₂/H₂ processes) were C-free and had relatively low O concentrations (<3 at.%). Our initial efforts for depositing GaN thin films, however, resulted in amorphous thin films with high O concentrations (~20 at.%). Following experiments revealed the source of this O contamination as the quartz tube of the inductively coupled RF-

plasma source itself. In view of these circumstances, the choice of N-containing plasma gas (N₂, N₂/H₂ or NH₃) determined the severity of O incorporation into the deposited AlN and GaN thin films. As an effort to completely avoid this contamination problem, we integrated a stainless steel hollow-cathode plasma (HCP) source to the ALD system, and thereby reported on hollow cathode PA-ALD (HCPA-ALD) of nanocrystalline AlN and GaN thin films with low impurity concentrations at 200 °C using trimethylmetal precursors. Within the scope of the same study, Al_xGa_{1-x}N thin films were also deposited via digital alloying, where alloy composition was determined by the relative number of AlN and GaN subcycles in the main HCPA-ALD cycle.

In this presentation, we will review our recent efforts on the development of low-temperature HCPA-ALD processes for III-nitride alloys including GaN, InN, In_xGa_{1-x}N, and In_xAl_{1-x}N thin films. In-detail materials characterization results including structural, optical and electrical properties as well as potential device architectures for post-CMOS processing and 3D integration will be presented and discussed.

9:40am EM+EN-FrM5 **Development of Nitride Nanorod Light-emitting Diode Array**, C.G. Tu, C.H. Liao, Y.F. Yao, C.Y. Su, H.S. Chen, W.H. Chen, C. Hsieh, H.T. Chen, Y.W. Kiang, **Chih-Chung Yang**, National Taiwan University, Taiwan, Republic of China **INVITED**

With the nano-imprint lithography and the pulsed growth mode of metalorganic chemical vapor deposition, a regularly-patterned, c-axis nitride nanorod (NR) light-emitting diode (LED) array of uniform geometry with m-plane core-shell InGaN/GaN quantum wells (QWs) is formed. To grow an NR with uniform cross-sectional size, in the pulsed growth mode, the sources of groups III and V are switched on and off alternatively with fixed supply durations. By growing a p-i-n core-shell structure, an InGaN/GaN QW NR LED array can be fabricated by depositing a conformal layer of GaZnO on the NRs for serving as the transparent conductor. The electrical property of such an LED array is comparable with that of a conventional planar LED. Besides, by varying the supply duration of group III source (TMGa) in the pulsed growth process, the NR cross section can be tapered for growing another section of NR of a different cross-sectional size. Based on this growth technique, a multiple-section GaN NR of changing cross-sectional size can be obtained. When InGaN/GaN QWs are deposited on the sidewalls of the NR, the indium contents and QW thicknesses are different in different sections of different cross-sectional sizes due to different strain relaxation conditions. In this situation, the emission wavelengths of the QWs from different sections are different, leading to the multiple-color emission of such an NR array. Such an emission behavior can be used for fabricating a phosphor-free white-light LED.

10:40am EM+EN-FrM8 **Trends in Production Scale MOCVD Equipment for Nitride Semiconductors**, Alexander Gurary, Veeco Instruments, Inc. **INVITED**

Metalorganic Chemical Vapor Deposition (MOCVD) is a technology of choice for large scale production of GaN based LED and Power Electronic devices. For the last 20 years MOCVD equipment evolved from small R&D oriented deposition systems (three 50 mm wafers per run) to large industrial cluster type systems (two hundred sixteen 50 mm wafers per run) with very sophisticated in-situ devices and process control. Evolution of the production scale MOCVD equipment is driven by one major goal – Cost of Ownership (CoO) reduction. Industry is achieving this goal utilizing several trends:

Migration from R&D to production requirements. GaN MOCVD systems started as an R&D tool. Further development of these systems is the path from universality and flexibility typical for R&D tools to stability and simplicity required for production environment.

Increasing batch size. This is the most obvious way to improve CoO as the cost to manufacture system with two times more wafers per run is less than the factor of two. All major MOCVD equipment companies follow this trend and release new larger batch systems every 3-5 years. One of the most important questions for scaling up is the limit of this trend.

Move from the single reactor system to the cluster and increase level of automation. Majority of modern MOCVD systems migrated from the single reactor to the cluster type multi-reactor design with central loading module and wafer carrier transfer robot.

Increasing role of the in-situ devices for wafer parameters measurement and control. Evolution of in-situ devices for production system includes the following sequence: thermocouple - conventional pyrometer - reflectometer - emissivity compensated pyrometer - deflectometer (wafer bow measurements). There is also a trend for more sophisticated control methods that move from PID to predictive and model based algorithms.

Increased wafer carrier complexity. The wafer carrier is a unique component of MOCVD system that to a large degree defines system yield.

Complexity of the wafer carriers is constantly increasing with the goal to improve deposition uniformity. Wafer carriers are a subject of majority MOCVD equipment patents.

Increased role of process modeling. Troubleshooting and process optimization in production environment exclude “trial and error” approach and require good computational models for flow dynamic and process chemistry that are fine-tuned based on experimental data.

In this presentation we will describe above trends in detail and make an attempt to predict next steps in the development of the equipment for large scale production of GaN based materials.

11:20am EM+EN-FrM10 Growth of GaN on Sapphire, Si (111), and Ge/Si (111) using a Pulsed Electron Beam Deposition (PED) Process, Nazmul Arefin, University of Oklahoma, *M.H. Kane,* Texas A&M University, *K. Hossain,* Amethyst Research Inc, *B.N. Pritchett,* Oklahoma Geological Survey, *M.B. Johnson, P.J. McCann,* University of Oklahoma

This presentation will describe results recently obtained with pulsed electron beam deposition (PED) of GaN on sapphire, silicon (111), and 2 nm germanium coated silicon (111) substrates. The PED technique is potentially useful for growth of III-nitrides at lower substrate temperatures, a capability that can allow use of new buffer layer materials, introduction of chemically dissimilar lattice-matched materials, and help solve wafer bowing and cracking problems during growth. The introduction of this technique could lead to improvements in device quality and fabrication of vertical LED structures. In this study, GaN was deposited on sapphire at a substrate temperature of 750°C, and on silicon (111) and Ge/Si (111) at 600°C in a UHP N₂ (15 mTorr) environment (without any surface pre-treatment such as pre-nitridation). A high power electron gun pulse (Neocera, Inc) was used to ablate the GaN target (1” dia. x 0.250” thick, 99.99% pure) stationed at 5 cm vertical distance from the substrate. The electron pulses were generated at 15KV, 0.3 J/pulse at 1 Hz for initial few nm of growth, and then increase to a 3 Hz pulse rate. Scanning Electron Microscopy (SEM), X-ray Diffraction (XRD), Rutherford backscattering, and optical absorption characterization were performed. SEM imaging confirms a rough surface morphology with the presence of 30 nm to 300 nm scaled GaN crystallites (for the GaN/Sapphire sample) while smaller but more coalesced crystallites of 30-50 nm size is observed for GaN/Si (111) and GaN/Ge/Si (111) samples. The average film thickness is 350 nm for the samples, yielding a growth rate of 0.16 angstrom/pulse. From SEM, it appeared that high aspect ratio filament structures have grown over the crystallites. XRD θ -2 θ scans from $2\theta = 0^\circ$ to $2\theta = 70^\circ$ on the GaN on sapphire showed only two other peaks, besides the peaks from the sapphire, near $2\theta = 34.6^\circ$. The peaks near $2\theta = 34.6^\circ$ consist of a stronger peak at 34.668° and a much weaker peak at 36.903° . These peaks correspond to the (0002) and (10-11) orientations for GaN, respectively. XRD θ -2 θ scans from $2\theta = 0^\circ$ to $2\theta = 70^\circ$ on the GaN on Si (111) and GaN on Ge/Si (111) samples show presence of only polar GaN (0002) peak at 34.7° besides the Si (111) peak at $2\theta = 28.5^\circ$. The XRD results clearly show that the deposited GaN material is not polycrystalline. Optical absorption spectroscopy over a 1.2 eV to 6.2 eV spectral range, for the GaN/Sapphire sample, showed an abrupt absorption edge at 3.4 eV, a clear indication of interband transitions in binary GaN. These results confirm that our PED-grown GaN is highly *c*-axis oriented and suitable for the initial growth of GaN on various substrate materials.

11:40am EM+EN-FrM11 Growth Template Impact on the Properties of InN Epilayers Grown by High-Pressure CVD, Sampath Gamage, M.K.I. Senevirathna, Georgia State University, *H. Babar, I.T. Ferguson,* University of North Carolina at Charlotte, *R. Collazo,* North Carolina State University, *N. Dietz,* Georgia State University

The unique optical and electrical properties of InN and related ternary InGaIn alloys make the material system attractive for various optoelectronic device applications, including but not limited to high-speed electronics, photovoltaic solar cells, or light emitting devices. Even though progress has been made in establishing the base properties of the binaries InN and GaN, the growth of high-quality InN and indium-rich ternary InGaIn epilayers and heterostructures is an open challenge. In previous work, we demonstrated the stabilization of InN and InGaIn epilayers utilizing superatmospheric MOCVD (also denoted as HPCVD) to suppress the decomposition at higher growth temperatures.

In this contribution, we explored the influence of the growth templates (e.g. sapphire substrates, micrometer-scale patterned AlN/sapphire templates, and/or patterned GaN/AlN/sapphire) on the properties of bulk InN epilayers, keeping the reactor pressure constant at 8bar (15bar) as well as the III/V precursor ratio. The growth temperature was optimized in the range of 800°C to 900°C based on Raman E₂(high) mode evolution. The various templates are assumed to introduce different strain fields during the initial nucleation process, affecting the extended defect generation and propagation processes. To assess this effect on the bulk properties of thick

InN epilayers, Raman spectroscopy [e.g. E₂(high) and A₁(LO) mode analysis], XRD rocking and ω -2 θ scans and photoluminescence (PL) spectroscopy were performed to analyze the crystallinity as well as the extended defect and point defect densities in these layers. The free carrier concentrations in these epilayers and the mobility was determined by FTIR spectra analysis as well as Raman A₁(LO) fitting.

Electronic Materials and Processing

Room: 314 - Session EM+NS+TF-FrM

Transparent Electronics

Moderator: Lisa M. Porter, Carnegie Mellon University

9:00am EM+NS+TF-FrM3 Transparent Amorphous Oxide Semiconductors: Interfacial Chemistries and New Applications, Gregory Herman, Oregon State University **INVITED**

During the past decade research in the area of transparent amorphous oxide semiconductors (TAOS) has increased substantially due to the ability to fabricate thin film transistors (TFT) at relatively low processing temperatures while still maintaining large electron mobilities. The primary applications for these materials include active matrix displays with the possibility for integration onto flexible polymeric substrates. More recently potential applications have expanded to include non-volatile memory, sensing, and memristive neurological networks. We have studied amorphous zinc tin oxide (ZTO) and indium gallium zinc oxide (IGZO) that have been deposited by both vacuum and solution based approaches. The electrical characteristics of the films have been evaluated in both TFT and metal-insulator-metal memristive devices. Excellent device characteristics have been obtained, however we have found that surface impurities can strongly affect device stabilities. We have found that the chemistry of adsorbed species on the back-channel strongly influences the bias stress stabilities of ZTO and IGZO TFTs, while reactions at the Al/ZTO interface leads to the resistive switching characteristics of memristors, and post annealing leads to interfacial reactions and modifies the Schottky barrier for Pt/IGZO diode structures. To better understand the role of interfacial reactions on TFT and memristive devices we have developed methods to prepare clean well defined surfaces for ZTO and IGZO, and further characterized there surface and interface properties with X-ray photoelectron spectroscopy and secondary ion mass spectrometry.

9:40am EM+NS+TF-FrM5 HMDSO/O₂-Plasma-Deposited Organic-Inorganic-Hybrid Materials as Gate Dielectrics for MgZnO Thin Film Transistors and Encapsulation Layers for Solar Cells, Y.S. Li, C.H. Tsai, I.C. Cheng, Jian-Zhang Chen, National Taiwan University, Taiwan, Republic of China

Organic-inorganic hybrid materials can be deposited from hexamethyldisiloxane (HMDSO) diluted with oxidants using plasmas technology. The properties of the deposited material can be controlled by varying the dilution ratio of the oxidants. The chemical compositions can vary from polymer-like (organic-like) to SiO₂-like (inorganic-like) depending on the oxidant dilution ratio and the process power. In this paper, we report two applications of HMDSO/O₂-plasma-deposited organic-inorganic-hybrid materials developed in our group: (1) as gate dielectrics of MgZnO TFTs, and (2) as the encapsulation layers for organic-inorganic hybrid solar cells.

The inorganic/organic component ratios in hybrid films were tailored by varying the process power and the O₂/HMDSO flow rate ratio. The FTIR analysis and contact angle measurement show that higher deposition power and/or larger O₂/HMDSO flow rate ratio result in more SiO₂-like films. For rf-sputtered MgZnO TFTs, a more organic-like film affords a better interface to the MgZnO active layer and higher dielectric constant, leading to a smaller threshold voltage and a steeper subthreshold slope; while an inorganic-like film has lower leakage currents, resulting in a larger on/off current ratio in the transistors. The TFT with an organic-inorganic-hybrid gate dielectric deposited at an O₂/HMDSO ratio of 40 and process power of 30 W exhibits a threshold voltage of 6.8 V, a subthreshold slope of 0.48 V/dec, an on/off current ratio of >10⁷ and a linear mobility of ~60 cm²V⁻¹s⁻¹, respectively. We also have demonstrated that this O₂/HMDSO-plasma-deposited organic-inorganic material can be used as an efficient single-layer encapsulation technique for organic photovoltaic cells. Calcium test was used to evaluate the water vapor transmission rate (WVTR) of the barrier film deposited on a polyimide foil. A water vapor transmission rate of 3.6×10⁻⁶ g/m²-day was obtained for a 1.5 um-thick single permeation layer. Inverted type organic photovoltaic passivated by the hybrid material was used to evaluate the effectiveness of this encapsulation. Efficiency decay was not observed in the cell coated with this encapsulation layer after 3000-hour exposure to the air; on the contrary, the un-encapsulated counterpart

cell degraded rapidly and completely failed after 120-hour exposure to the air. The result shows that this single-layer hybrid material encapsulation can enhance the stability of organic photovoltaic cell. The cell life time is greatly improved.

10:00am EM+NS+TF-FrM6 Solution Processed Oxide Semiconductor and Dielectric Thin Films: Towards High Performance, Low Temperature ZnO Field-effect Transistors with Low Operation Voltage, Yu Liu, H. Katz, Johns Hopkins University

Solution processing is a preferred method for manufacturing large-area low-cost electronic devices. High performance metal oxide semiconductor-based field-effect transistors can be fabricated in this manner. For applications of flexible electronics, a low processing temperature is required to avoid overheating of the substrate material. It is a challenge to fabricate a dense impurity-free oxide semiconductor film at low temperature. A water-based ZnO precursor with ammine-hydroxo complex was introduced to decrease the processing temperature. However, repeated time-consuming centrifugation and decantation steps are required in this process.

To simplify the processing steps we discovered a new strategy to prepare aqueous ZnO precursor. Based on this precursor, ZnO FETs with a benchmark dielectric SiO₂ have been fabricated at 200 °C. The transistors exhibited promising performance with a saturation field-effect mobility of 0.7 cm²·V⁻¹·s⁻¹ and a typical on/off current ratio on the order of 10⁴. To prepare the precursor, zinc nitrate hexahydrate and acetylacetone were dissolved in ammonium hydroxide with a concentration of 0.6 M. As prepared precursor was then filtered and dilute it with DI water. A similar strategy was applied in the preparation of aqueous zinc tin oxide precursor with tin fluoride as tin source.

Based on a redox chemical reaction between fuel and highly exothermic oxidizer, a combustion processing method has been found to be promising for decreasing the annealing temperature of oxide semiconductor thin films. In this study, combustion processing strategy was used in preparing high capacitance ion-incorporated alumina dielectrics at 200 °C by using urea as the fuel and aluminum nitrate nonahydrate as oxidizer.

Both zinc tin oxide and sodium-incorporated alumina low temperature precursors showed strong exothermic reaction peaks at temperatures lower than 200 °C. This suggests a conversion from ammine-hydroxo/combustion precursor to solid zinc tin oxide/sodium incorporated alumina thin films at a temperature lower than 200 °C. A sharp (002) peak is shown in the XRD pattern of 200 °C processed ZnO thin film, which demonstrates a wurtzite crystal structure.

The high-k dielectrics exhibited a good compatibility with our low temperature ZnO precursor and excellent transistor performance has been achieved in these devices. With this, we are able to fabricate low temperature low voltage transistors on plastic substrates such as polyimide. This low temperature ZnO precursor could also be applied to fabricate flexible inverters in combination with p-type solution processed polymer semiconductors, such as PBTTT and TIPS-pentacene.

10:40am EM+NS+TF-FrM8 Metal Oxide Conductors and Semiconductors: From Materials to Device Applications, Elvira Fortunato, R. Martins, FCT-UNL and CEMOP-UNINOVA, Portugal
INVITED

Transparent electronics has arrived and is contributing for generating a free real state electronics that is able to add new electronic functionalities onto surfaces, which currently are not used in this manner and where silicon cannot contribute [1,2]. The already high performance developed n- and p-type TFTs have been processed by physical vapour deposition (PVD) techniques like rf magnetron sputtering at room temperature which is already compatible with the use of low cost and flexible substrates (polymers, cellulose paper, among others). Besides that a tremendous development is coming through solution-based technologies very exciting for ink-jet printing, where the theoretical limitations are becoming practical evidences. In this presentation we will review some of the most promising new technologies for n- and p-type thin film transistors based on oxide semiconductors and its currently and future applications.

[1] E. Fortunato, P. Barquinha, and R. Martins, "Oxide Semiconductor Thin-Film Transistors: A Review of Recent Advances," *Advanced Materials*, vol. 24, pp. 2945-2986, Jun 2012.

[2] P. Barquinha, R. Martins, L. Pereira and E. Fortunato, *Transparent Oxide Electronics: From Materials to Devices*. West Sussex: Wiley & Sons (March 2012). ISBN 9780470683736.

11:20am EM+NS+TF-FrM10 Influence of Oxygen Diffusion in Transparent In_{0.9}Sn_{0.1}O_x Film on Effective Work Function Change, Toshihide Nabatame, NIMS, Japan, H. Yamada, Shibaura Institute of Technology, Japan, A. Ohi, NIMS, Japan, T. Oishi, Shibaura Institute of Technology, Japan, T. Chikyo, NIMS, Japan

The In_{0.9}Sn_{0.1}O_x (ITO) films is widely used as transparent electrodes in optical and optoelectronic devices. The work function (WF) of the ITO film was generally evaluated by optical measurements such as ultraviolet photoemission spectroscopy and Kelvin probe. However, the optically measured WF differs from the effective work function (EWF) estimated by electrical measurement. The influence of oxygen diffusion in ITO film on EWF change has not been also understood. In this paper, we systematically investigate EWF change of ITO film by oxidation and reduction annealing. We also examine oxygen diffusion coefficient (D) of ITO film, using isotope ¹⁸O tracer, to discuss influence of oxygen diffusion of ITO film on EWF change.

The ITO films were prepared under an Ar/O₂ by sputtering using an In_{0.9}Sn_{0.1}O_x target. The ITO-gated metal-oxide-semiconductor (MOS) capacitors with HfO₂ and SiO₂ gate insulators were fabricated to estimate EWF value of ITO film. The ITO (150 nm)/SiO₂/Si films were annealed at 300 – 500 °C for 30 min under 10⁴ Pa of ¹⁸O isotope (99%) gas to obtain D value.

The resistivity of ITO film, which consists of cubic structure, shows an almost same value regardless of oxidation and reduction annealing temperatures. The EWF of ITO-gated MOS capacitors significantly changes from 4.4 to 5.2 eV as the oxidation annealing temperature increases from 250 to 350 °C. The EWF change is saturated at 350 °C. On the other hand, the EWF value decreases in reduction annealing temperature ranging from 200 to 350 °C. This must be due to oxygen introduction and removal in ITO film during oxidation and reduction annealing, respectively. To understand the mechanism of oxygen transfer in the ITO film, we examine D behavior of ITO film. The ITO film has a large D value of about a 1.1X10⁻²⁰cm²/s at 300 °C and a small activation energy (E_a) of about 1.4 eV. We found that the D and E_a values are similar to those of grain boundary in monoclinic ZrO₂. This results indicate that oxygen diffusion of ITO film occurs even at low temperature of 300 °C and affects to the EWF change during oxidation and reduction annealing at around 300 °C.

11:40am EM+NS+TF-FrM11 Transparent Conducting Films from Ultraporos Aerogels of Single-Walled Carbon Nanotubes / PEDOT:PSS Composites, Xi Liu, L.M. Porter, M.F. Islam, Carnegie Mellon University

In this study we report on the fabrication and characterization of ultralight (>99% porosity) aerogels based on single-walled carbon nanotubes (SWCNTs) and poly(ethylene dioxythiophene) : poly(styrene sulfonate) (PEDOT:PSS), that are electrically conducting and highly stretchable. The aerogels were created by critical-point drying of aqueous elastic co-gels of individually dispersed SWCNTs mixed with PEDOT:PSS to yield either free-standing films or thin films supported on flexible (PET) or glass substrates; the nanotubes substantially reduce the percolation threshold of PEDOT:PSS. These transparent conductors with sheet resistance of 35 ohm/sq and 60% transparency (at 550 nm) also proved to be highly flexible – they can be repeatedly stretched to 20% with < 1% change in resistivity. The electrical, optical, mechanical, and microstructural properties of these materials will be presented, along with their application in devices.

Scanning Probe Microscopy Focus Topic

Room: 312 - Session SP+AS+BI+EM+NS+SE+SS-FrM

Probe-Sample Interactions and Emerging Instrument Formats

Moderator: Carl Ventrice, Jr., University at Albany-SUNY

8:40am SP+AS+BI+EM+NS+SE+SS-FrM2 2013 ASSD Student Award Talk: New Insights into Nanoscale Adhesion from In Situ TEM Studies, Tevis Jacobs, J.A. Lefever, University of Pennsylvania, J. Liu, University of Wisconsin-Madison, D.S. Grierson, SysteMECH LLC, K.E. Ryan, P.L. Keating, J.A. Harrison, United States Naval Academy, K.T. Turner, R.W. Carpick, University of Pennsylvania

A fundamental understanding of adhesion is important for applications at all length scales, but is particularly critical in nanoscale devices and applications due to their high surface-to-volume ratio. Advancements in studying such tribological phenomena are typically hindered by the inaccessibility of the sliding interface. We will present nanoscale adhesion measurements conducted inside of a transmission electron microscope (TEM), using a modified in situ nanoindentation apparatus that makes

contact with atomic force microscope (AFM) cantilever tips. This tool provides new opportunities to observe, identify, and quantify tribological processes with unprecedented access and resolution. First, using ultra-strong carbon-based tip materials, we find that roughness of tips can greatly reduce the pull off force and lead to severe underestimation of the work of adhesion [1]. Furthermore, we have quantified adhesion by making and breaking contact between nanoscale silicon asperities and a flat diamond substrate. The snap-in distance and the pull-off force are measured with sub-nanometer and sub-nanonewton resolution, respectively. The shape of the Si asperity is determined with sub-nanometer resolution immediately before and after contact to verify that elastic conditions were maintained. From this, we independently determine the work of adhesion and range of adhesion. The results show that accounting for roughness has a strong effect on both parameters. These two results demonstrate the importance of applying in situ approaches to studies of adhesion. --- I. Jacobs, T.D.B., Ryan, K.E., Keating, P.L., Grierson, D.S., Lefever, J.A., Turner, K.T., Harrison, J.A. and Carpick, R.W. The Effect of Atomic-Scale Roughness on the Adhesion of Nanoscale Asperities: A Combined Simulation and Experimental Investigation. *Tribol. Lett.* 50, 81-93 (2013).

9:40am **SP+AS+BI+EM+NS+SE+SS-FrM5 Nanoscale Mapping of the W/Si(001) Schottky Barrier using Ballistic Electron Emission Microscopy**, *Christopher Durcan*, University of Albany-SUNY, *V.P. LaBella*, University at Albany-SUNY

The W/Si(001) Schottky barrier was spatially mapped using ballistic electron emission microscopy (BEEM) and ballistic hole emission microscopy (BHEM) using high resistivity *n*-type and *p*-type silicon substrates. A thin tungsten silicide is observed upon deposition utilizing transmission electron microscopy (TEM) and Rutherford backscattering spectrometry (RBS). The sum of the Schottky barrier heights from *n*-type and *p*-type silicon substrates agree with the silicon band gap. The BEEM and BHEM spectra are fit utilizing a linearization method to the power law of the BEEM model. Spatially resolved Schottky barrier maps are generated over a 1 μ m x 1 μ m area and provide insight into the spatial homogeneity of the barrier height. Histograms of the barrier heights show a Gaussian distribution, consistent with an interface dipole model.

10:00am **SP+AS+BI+EM+NS+SE+SS-FrM6 Local Probing of Superconductivity in Half Heusler Compounds**, *Hongwoo Baek*, NIST & Seoul National University, Republic of Korea, *J. Ha*, *D. Zhang*, NIST/Maryland Nano Center, University of Maryland, *Y. Nakajima*, *P.S. Syers*, *X. Wang*, *K. Wang*, *J. Paglione*, University of Maryland, *Y. Kuk*, Seoul National University, Republic of Korea, *J.A. Stroscio*, NIST

Heusler alloys have attracted interest as multifunctional experimental platforms for topological quantum phenomena ranging from magnetism to superconductivity and heavy fermion behavior. The rare-earth chalcogenide ternary half Heusler compounds were theoretically predicted to have topologically nontrivial surface states due to band inversion [1]. The lack of inversion symmetry of the crystal lattice makes unconventional pairing symmetry feasible. The superconductivity in the non-centrosymmetric half Heusler compound YPtBi was recently reported as a promising system for the investigation of topological superconductivity [2]. In this work, we use ultra low temperature scanning tunneling microscopy to investigate the superconducting properties of the ternary half Heusler compounds YPdBi and YPtBi. Both were theoretically proposed to have topological states with different band inversion strength [1], and experimentally reported as a topological insulator [3]. Strong spin-orbit coupling and the lack of inversion symmetry present the possibility of spin-triplet superconductivity in these materials. The tunneling spectra of YPdBi show two different superconducting gaps of 0.36 meV and 0.16 meV depending on the measurement location. The variation in gaps might originate from inhomogeneity in the crystal. The superconducting gap of 0.36 meV is completely suppressed above a critical magnetic field of $B=2.5$ T, in agreement with bulk transport measurements. A superconducting gap of 0.21 meV and an upper critical field of 1.25 T were measured in a circular superconducting domain of diameter ≈ 180 nm in YPtBi. Sequential addition of single vortices to the superconducting YPtBi domain could be observed with increasing magnetic field, with vortices occupying the perimeter of the island. These observations will be discussed in terms of island confinement and pairing symmetry of YPtBi.

[1] S. Chadov, X. Qi, J. Kubler, G. H. Fecher, C. Felser, and S. C. Zhang, *Nat. Mater.* **9**, 541 (2010).

[2] N. P. Butch, P. Syers, K. Kirshenbaum, A. P. Hope, and J. Paglione, *Phys. Rev. B* **84**, 220504(R) (2011).

[3] W. Wang, Y. Du, G. Xu, X. Zhang, E. Liu, Z. Liu, Y. Shi, J. Chen, G. Wu, and X. Zhang, *Scientific Reports* **3** (2013).

10:40am **SP+AS+BI+EM+NS+SE+SS-FrM8 Multimodal Intermittent Contact Atomic Force Microscopy: Topographical Imaging, Compositional Mapping, Subsurface Visualization and Beyond**, *Santiago Solares*, George Washington University

Multifrequency atomic force microscopy (AFM) refers to a family of techniques that involve excitation of the microcantilever probe at more than one frequency [R. Garcia and E.T. Herruzo, *Nature Nanotechnology* **7**, 217 (2012)]. This can be carried out in a sequential manner, varying the excitation frequency over time, as in chirp band excitation methods, or simultaneously supplying drive signals containing more than one frequency to the cantilever shaker. The latter mode of operation commonly involves the simultaneous excitation of more than one cantilever eigenmode, such that each eigenmode is used to carry out different functions. For example, in a recently developed trimodal imaging scheme for soft sample characterization [D. Ebeling, B. Eslami and S.D. Solares, *ACS Nano*, **7**, 10387 (2013)], the fundamental eigenmode is used for topographical acquisition, as in standard tapping-mode AFM, while two higher eigenmodes are used for compositional mapping and subsurface visualization, respectively. This talk presents experimental and computational results for validated multimodal imaging schemes involving one to three eigenmodes, and discusses the expected benefits and complexities of including more than three eigenmodes.

Surface Science

Room: 309 - Session SS+EM-FrM

Semiconductor Surfaces and Interfaces 2

Moderator: Robert Bartynski, Rutgers, the State University of New Jersey, Kurt Kolasinski, West Chester University

8:20am **SS+EM-FrM1 Two Dimensional Supramolecular Ordering of Oligothiophene Molecules on the Si(111)- $\sqrt{3}\times\sqrt{3}$ -Ag Surface**, *R. Liu*, Lakehead University, Canada, *C. Fu*, *D.F. Perepichka*, McGill University, Canada, *Mark Gallagher*, Lakehead University, Canada

The functionalization of semiconductor surfaces with organic molecules is a necessary step in the development of hybrid organic-semiconductor structures. A significant challenge to organic layer formation is the fact that semiconducting surfaces exhibit a large number of dangling bonds, which suppress the diffusivity of adsorbed molecules and can even break the molecules apart via the formation of Si-C bonds. Recently it has been shown that these problems can be obviated by depositing the organic molecules onto a passivated surface [1].

We have studied the adsorption of brominated π conjugated tetrathienoanthracene molecules (TBTTA) onto the Si(111)- $\sqrt{3}\times\sqrt{3}$ -Ag surface. Thiophene based molecules like TBTTA are of considerable interest in organic semiconductor research due to their efficient conjugation and the chemical stability [2]. The Si(111)- $\sqrt{3}\times\sqrt{3}$ -Ag surface has no Si dangling bonds and should provide a high mobility surface suitable for TBTTA adsorption. Scanning Tunneling Microscopy images reveal that at low coverage the molecules readily migrate to step edges and defects in the $\sqrt{3}$ overlayer, in fact many images show direct evidence of molecular mobility. With increasing coverage the molecules eventually form compact supramolecular structures. In terms of the $\sqrt{3}$ lattice vectors (*a* and *b*), the oblique unit cell of these structures is $a_m = 3a + b$, and $b_m = a + 2b$. The structures are quite fragile and can decompose under repeated STM imaging. Our results suggest that TBTTA is weakly bound to the $\sqrt{3}$ surface at room temperature and that the supramolecular structures are held together by weak van der Waals forces.

1. T. Suzuki et al., *Phys. Chem. Chem. Phys.* **11**, 6498 (2009).

2. R. Gutzler et al., *Nanoscale* **6**, 2660-2668 (2014).

8:40am **SS+EM-FrM2 Interface Formation between a Self-Assembled Monolayer and an Organic Semiconductor**, *Sujitra Pookpanratana*, *H.-J. Jang*, *A.N. Brigeman*, *J.I. Basham*, *O.A. Kirillov*, *D.J. Gundlach*, National Institute of Standards and Technology (NIST), *O.D. Jurchescu*, Wake Forest University, *C.A. Richter*, *C.A. Hacker*, NIST

Organic-based electronics are attractive because they have potential manufacturing advantages such as mechanical flexibility and simpler processing (solution-based, low temperature, and atmosphere conditions). Molecular-based semiconductors offer a nearly limitless range of possibilities in tailoring the chemical composition and structure for a desired electronic, optical, or film-processing property. Probing and understanding molecular surfaces and interfaces is essential for the further development of organic-based photovoltaics, light emitting diodes, and field-effect transistors. Organic-organic interfaces are key in some of those devices, and understanding the impact of a self-assembled monolayer

(SAM) has when an organic semiconductor is on top of it, is a complex issue.¹ This strategy is commonly implemented as a way to modify the hole injection barrier between an organic material and an inorganic substrate.

Here, we have investigated the interaction between a pi-conjugated organic semiconductor (tris-(8-hydroxyquinoline) aluminum, Alq₃) on SAM's of different tail and backbone composition. We have used ultraviolet and X-ray photoelectron spectroscopies to monitor the energy level alignment and chemical structure at the interface. The SAM's strongly interact with the Au substrate, where an interface dipole can down shift or up shift the surface work function. After Alq₃ is deposited onto the SAM-coated substrates, we find that the highest occupied molecular orbital of Alq₃ is relatively constant (with respect to the substrate Fermi level) on all surfaces, suggesting Fermi level pinning.² However, the composition of the SAM's did strongly influence the growth and chemical structure of the Alq₃ at the interface. The photoemission signal arising from the Au substrate is least attenuated when the SAM/Au surface is hydrophobic when compared to a hydrophilic SAM/Au or bare Au surface. The difference in substrate attenuation suggests that the early growth of the Alq₃ layer strongly depends on this surface property. This finding is corroborated with microscopy of the same samples. In addition, Alq₃ chemically reacts with a fluorinated SAM at the organic-organic interface as indicated by the shifting and asymmetric broadening of Al and N core levels. These results will be discussed in context of painting a comprehensive picture of the organic-organic interface formation that influences the chemical composition, electronic structure and physical structure at the interface.

[1] F. Rissner *et al*, *ACS Nano* 3, (2009) 3513.

[2] L. Lindell *et al*, *Appl. Phys. Lett.* 102, (2013) 223301.

9:00am **SS+EM-FrM3 Reactions of Benzoquinone with Hydrogen Terminated Silicon Surfaces**, R.L. Opila, Meixi Chen, N.A. Kotulak, N.J. Schreiber, University of Delaware

Quinhydrone dissolved in methanol has long been known to react with hydrogen terminated silicon surfaces to passivate electronic defects where photo-excited carriers recombine non-radiatively. The mechanism of this passivation is not well understood. We have shown that benzoquinone, C₆O₂H₄ rather than hydroquinone, C₆O₂H₆, both components of the quinhydrone mixture, is the active component. Benzoquinone reacts to abstract a hydrogen and then itself bonds with the surface. We have shown that the hydrogen can be abstracted from the solvent and that incident light is necessary for this reaction to take place. X-ray photoelectron spectroscopy and Fourier Transform Infrared Spectroscopy were used to show that the benzoquinone reacted with the surface. Photo-excited carrier lifetime is a good measure of the extent of the passivation of the surface. Density functional theory supports the proposed reaction mechanism.

9:20am **SS+EM-FrM4 High-Quality Monolayers Derived from Short Alkyne Chains on Si(111) Surfaces**, Sidharam Pujari, A. Filippov, S. Gangarapu, H. Zuillhof, Wageningen University, Netherlands

Hydrosilylation has been a key reaction in preparing monolayers on silicon surfaces. This process involves the reaction of a terminally unsaturated reactant with the Si surface. Over the past 20 years, several advances have been accomplished to obtain better (i.e. denser and more stable) monolayers with various reactants (alkenes, alkynes, dienes, etc.) under different reaction conditions (e.g. thermal initiation, ultraviolet light, etc.).^{1,2} Such a higher density is advantageous for the structural ordering, stability and a wide range of applications. The procedure used in our lab (as well as labs around the world) involves wet-chemical techniques for the surface modifications. As the name implies, the reactants with these techniques must be available as liquids under the reaction conditions. Due to this constraint, only monolayers of relatively long chain lengths have been made, because shorter chains evaporate under thermal conditions (or are even a gas). In the current project, we have prepared and characterized a new class of monolayers with (short) chain lengths that were previously inaccessible.

H-Si(111) surfaces were modified with gaseous alkynes in a pressure-resistant PARR reactor. This novel method in silicon-carbon chemistry allows the chemisorption of compounds that were previously unusable in surface modification due to its volatility. Si-C-bonded monolayers derived from propyne, 1-butyne and 5-functionalized-pent-1-yne (-COOH, -Cl, & -NH₂) were prepared and characterized using various surface-sensitive techniques. Si(111)-propenyl and butenyl silicon-monolayers display a higher packing density (up to 75%) than any wet-chemically prepared alkyne-derived monolayer. Furthermore, a combination of experimental and theoretical data shows that propyne chemisorption happens in a temperature-dependent manner, not observed for any other alkyne studied up to now: through addition of the second carbon (-*iso*) at temperatures below 90 ° C, and of the terminal carbon (-*lin*) above 90 ° C. Finally, 5-chloro-1-pentyne and 4-Pentynoic acid were shown to bind at high surface

densities and (near-)exclusively via the terminal carbon of the triple bond. These end groups allow for further functionalization of the monolayer.

(1) Rijksen, B.; Pujari, S. P.; Scheres, L.; van Rijn, C. J. M.; Baio, J. E.; Weidner, T.; Zuillhof, H. *Langmuir* **2012**, *28*, 6577-6588.

(2) Li, Y.; Calder, S.; Yaffe, O.; Cahen, D.; Haick, H.; Kronik, L.; Zuillhof, H. *Langmuir* **2012**, 9920-9929.

9:40am **SS+EM-FrM5 Surface Modification of Antimonide-Based Compound Semiconductor Superlattices using ALD**, Erin Cleveland, J. Nolde, C. Canedy, E. Aijer, Naval Research Laboratory

The use of dielectric films in device passivation is complicated by the fact that they are typically deposited on processed material surface that bear little resemblance to that of the virgin growth surface. This is particularly evident in technologically important device structures employing antimonide-based compound semiconductor (ABCS) superlattices, where the exposed mesa sidewalls may be comprised of four or more atomic species and their complex oxides. Physically, the etched surface presents a different crystallographic orientation, and may have additional structure due to variation in etch rate of superlattice layers. Since the nature of the dielectric/semiconductor interface directly impacts the density of surface states, it is critical to understand how processed, multilayer semiconductor surfaces may be modified during the initial phase of the atomic layer deposition (ALD) process.

A significant effort has been focused on surface preparations prior to ALD that removes the native oxide and passivates the III-V atoms in order to ensure the best possible interface. Current approaches typically rely upon wet-chemical etches to remove the defect-prone native oxide layer prior to dielectric deposition; however, this technique typically suffers from a lack of reproducibility, as well as potential interface contamination between processing steps. Therefore, we studied the effectiveness of using the ALD precursor, TMA, in conjunction with wet and dry pre-treatments, in removing carbon and etch precipitates, scavenging the various oxide species, and residues of excess group III and V elements on (100) surfaces of ABCS superlattices as a function of precursor choice, sequence (i.e. TMA vs oxidizer first), exposure time, as well as substrate temperature. Furthermore, surface passivation stability was investigated as a function of temperature and time. Surfaces were analyzed using XPS, AFM, and SEM both before and after ALD treatments. Results indicate that a completely oxide free surface may not be necessary to produce a good electrical interface.

10:00am **SS+EM-FrM6 Mechanism Changes Caused by Metal Catalyst During Silicon Etching in V₂O₅ + HF Solutions**, Kurt Kolasinski, W.B. Barclay, West Chester University

Etching of Si in oxidant + HF solutions can lead to a self-limiting reaction that spontaneously produces nanocrystalline porous Si – a process known as stain etching. The presence of a metal catalyzes and localizes etching such that ordered arrays of pores or nanowires can be formed depending on the structure of the metal – a process known as metal assisted etching (MAE). Ag, Au, Pd and Pt were deposited from solution onto H-terminated Si to act as catalysts for MAE. The metals all catalyzed the injection of holes into the Si. They all increased the rate of hole injection by approximately a factor of 5. The stoichiometry of MAE in V₂O₅ + HF solutions depended on the chemical identity of the metal. The stoichiometry when etching with Ag and Au was the same as for stain etching in V₂O₅ + HF solutions. However, for Pd and Pt, the stoichiometry differed significantly, consuming more V₂O₅ and producing less H₂ per mole of Si etched. This indicates that the metal catalyst can change the mechanism of etching. Etching in V₂O₅ + HF solutions was well behaved and gave consistently reproducible kinetic results. The behavior is much different when HOOH is added instead of V₂O₅. In the absence of deposited metal, no reaction occurs with HOOH. When HOOH was added to metal-coated Si samples immersed in HF(aq), etching was immediate in all cases. In contrast to V₂O₅, we were unable to obtain well-behaved stoichiometric results for HOOH + HF solutions. This is related to heightened sensitivity on reaction conditions compared to the V₂O₅ system as well as nonlinearities introduced by side reactions.

The mechanism of Si etching changes based on the presence of a metal catalyst during metal assisted etching and depends on the chemical identity of the metal. A valence 2 path dominates the formation of photoluminescent nanoporous Si in stain etching as well as MAE with Ag and Au. A valence 4 path dominates the formation of photoluminescent nanoporous Si in MAE with Pt. However for MAE with Pd, no nanoporous Si is formed initially and a mixture of valence 4 and valence 2 processes is observed. The nature of the electron transfer process and its dependence on the electronic structure of the metal/Si interface will be discussed.

10:40am **SS+EM-FrM8 Selective Wet Etching of III-V Semiconductors with HCl, H₂O₂, and α -Hydroxy Acid Mixtures**, *Pablo Mancheno-Posso, R. Jain, A.J. Muscat*, University of Arizona

The higher electron mobility of III-V semiconductors makes them suitable for NMOS devices in CMOS transistor technology. A clean, smooth and well-defined semiconductor surface is needed for epitaxial growth of heterostructures and atomic layer deposition of dielectrics. Device fabrication also requires selective etching and smooth finishing of layers composed of different materials. Wet chemical treatments enable batch processing, and aqueous mixtures containing an oxidizing agent and an etchant (acid or base) have been developed for III-V materials. The (100) face of the binary III-V semiconductors contains both group III (electron-deficient) and V (electron-rich) atoms. HCl solutions favor the removal of the latter. The addition of α -hydroxy acids (citric and tartaric acids) to the etching mixture is expected to promote a more uniform etch by chelating the group III atoms. In this study, we compare the etching rates of the (100) faces of GaAs, InAs, InP, InSb and GaSb, using aqueous solutions of HCl (0.01-4 M), H₂O₂ (0.01-8 M), and tartaric and citric acids (0.1-1.5 M). The etching rate was determined by profilometry measurements of the step height on patterned substrates. The chemical composition of the surface was studied using XPS, and the surface topography and roughness were characterized with AFM. The etching rate of GaAs in HCl-H₂O₂ mixtures was independent of HCl concentration (0.1-4 M) and showed a linear dependence on H₂O₂ concentration (0.1-8 M). Etching was limited by the removal of water-soluble Ga and As chlorides formed from GaAs oxides. InP etching was independent of HCl concentration (1-5 M), but sharply increased for 6-7 M. H₂O₂ concentration showed no significant effect on InP etching. The GaSb etching rate depended linearly on H₂O₂ concentration but in a narrower range (0.1-0.5 M). The etching of InP and GaSb is limited by the removal of the group III atoms. Etching of GaAs and InAs is limited by the removal of the group V atom. The strong bond that As makes with O drives etching. The etching selectivity of GaAs to InP increased from about 15 to 250 when the H₂O₂ concentration was raised from 1 to 8 M at a fixed 1.76 M HCl concentration. The addition of tartaric or citric acid to HCl and H₂O₂ mixtures yielded no change in the etching rate of GaAs when compared to solutions containing HCl and H₂O₂ only, but preferentially removed Ga atoms, yielding smoother surfaces at low concentrations. Using a chelator etched InAs with high selectivity relative to InP without as much roughening as with HCl. Selective etching will be discussed in the context of a set of proposed mechanisms based on the data.

11:00am **SS+EM-FrM9 Lanthanum Quantification for Optimization of Advanced High-k/Metal Gate Stacks using Low Energy Electron X-ray Emission Spectrometry**, *E. Martinez*, CEA, LETI, MINATEC Campus, France, *C. Trouiller*, STMicroelectronics, France, *M.P. Moret, N. Morel*, CAMECA, France, *Andrew Davis*, CAMECA Instruments Inc, *P. Caubet*, STMicroelectronics, France, *F. Bertin*, CEA, LETI, MINATEC Campus, France

We report about accurate monitoring of ultra-low La doses inserted in advanced high-k/metal gate stacks for threshold voltage tuning purposes. Three characterization techniques are implemented for precise and reproducible lanthanum quantification. LEXES (Low energy Electron X-ray Emission Spectrometry) capabilities are highlighted in terms of sensitivity and accuracy thanks to a comparison with reference results obtained by Rutherford Backscattering Spectrometry (RBS). The capabilities of state-of-the-art Auger nanoprobe for depth profiling in the sub-nanometer range are also illustrated.

Authors Index

Bold page numbers indicate the presenter

— A —

Abbas, A.: EN+AS+EM+SE-WeM13, 33
Abdulrahman, R.: TF+EM+EN-WeA1, 39
Aceves-Mijares, M.: EM-TuP28, 25
Adam, S.: 2D+EM+MI+MN+NS+SS+TF-ThA4, 48
Addou, R.: EM-WeA4, 37
Afsari, S.: SP+AS+EM+NS+SS-ThP8, 55
Agasie, R.J.: EM-WeA11, 37
Aguilar, R.: SP+AS+EM+NS+SS-ThP8, 55
Aifer, E.: SS+EM-FrM5, 63
Aihara, T.: EN+EM+MN+NS+TR-MoA11, 11
Akimoto, K.: EM-TuP13, 24
Albertini, D.: EM+MI+NS-MoM8, 3
Alimardani, N.: EM2-WeM12, 31
Allman, D.: EM2-WeM2, 30
Alper, J.P.: EM+EN+TF-WeA8, 35
Altman, E.I.: 2D+EM+NS+SS+TF-WeM4, 27
Ambrogio, S.: EM2-ThM3, 45
Ambrosio-Lázaro, R.C.: EM-TuP28, 25
Ampuero, J.L.: EM-TuP26, 25
Anand, B.: EN+EM+MN+NS+TR-MoA3, 10
Ando, A.: SE+EM+EN+PS+TF-MoM3, 5
Antcliffe, M.: EM1-WeM10, 29
Aoki, M.: EM-TuP12, 23; EM-TuP13, 24
Aoki, T.: EM+MI+NS-MoM3, 2
Appenzeller, J.: 2D+EM+MS+NS-FrM8, 57
Arefin, N.: EM+EN-FrM10, 60; EM-TuP1, 22
Arwin, H.: EL+AS+BI+EM+SS-FrM3, 57
Asbeck, P.: EM1-WeM10, 29
Asensio, M.C.: 2D+AS+EM+NS+SS-MoA6, 7
Asplund, M.: TF+EM+EN-WeA11, 40
Atiganyanun, S.: EM-TuP5, 22
Austin, D.Z.: EM2-WeM2, 30
Avanesian, T.: EN+AS+EM+SE-TuM3, 13
Avila, J.: 2D+AS+EM+NS+SS-MoA6, 7
Aydil, E.S.: EN+AS+EM+SE-WeM3, 31
Aydin, K.: TF+EM+EN-WeA3, 39
Aydogan, P.: 2D+EM+MI+MN+NS+SS+TF-ThA11, 49
Ayers, J.E.: TF+AS+EM-TuA7, 20
Azcatl, A.: 2D+EM+NS+SS+TF-WeM6, 27
Azcatl, A.: EM-WeA9, 37

— B —

Babar, H.: EM+EN-FrM11, 60
Bachelet, R.: EM+MI+NS-MoM8, 3
Baek, H.: SP+AS+BI+EM+NS+SE+SS-FrM6, 62; SP+AS+EM+NS+SS-ThP3, 55
Bagley, J.: TF+EM+EN-WeA11, 40
Baklanov, M.: EM-TuM6, 12
Balatti, S.: EM2-ThM3, 45
Banai, R.E.: EN+AS+EM+SE-WeM6, 32
Banys, J.: 2D+EM+MI+MN+NS+SS+TF-ThA9, 49
Barati, Gh.: EL+AS+EM+EN+SS-ThM12, 43
Barclay, W.B.: SS+EM-FrM6, 63
Barnes, A.: EL+AS+EM+EN+SS-ThM5, 42
Barnes, T.M.: EN+AS+EM+SE-WeM10, 32
Barrett, L.: EM+EN+TF-WeA9, 36
Barroso, D.: 2D+EM+NS+SS+TF-WeM10, 28
Bartels, L.: 2D+EM+NS+SS+TF-WeM10, 28
Barth, K.: EN+AS+EM+SE-WeM13, 33
Bartis, E.A.J.: SE+EM+EN+PS+TF-MoM2, 4
Bartles, L.: 2D+EM+MI+MN+NS+SS+TF-ThA8, 48
Barton, A.: EM-WeA4, 37
Bartynski, R.A.: EN+EM+NS-TuA4, 18
Basham, J.I.: EN+AS+EM+SE-WeM12, 33; EN+AS+EM-WeA11, 38; SS+EM-FrM2, 62
Basile, L.: SP+2D+AS+EM+MC+NS+SS-ThM11, 47
Baski, A.A.: EM+EN-FrM3, 59
Batzill, M.: 2D+AS+EM+NS+SS-MoA6, 7
Baumann, P.: EM+2D-TuA3, 16
Baxter, J.B.: EN+AS+EM-WeA3, 38

Bayindir, Z.: EM-TuM3, 12
Beach, J.: EN+AS+EM+SE-WeM10, 32
Beebe, M.R.: TF+AS+EM-TuA9, 20
Beeram, S.: EL+AS+BI+EM+SS-FrM8, 58
Behnam, A.: EM1-WeM12, 29
Béland, A.E.: EN+AS+EM+SE-WeM3, 31
Belianinov, A.: 2D+EM+MI+MN+NS+SS+TF-ThA9, 49
Benndorf, C.: EM-TuP26, 25
Berger, H.: 2D+AS+EM+MI+MN+NS+TF-WeA7, 34
Beringer, D.: TF+AS+EM-TuA9, 20
Berry, N.: EN+AS+EM+SE-WeM5, 32
Bertin, F.: SS+EM-FrM9, 64
Bertolazzi, S.: 2D+AS+EM+MI+MN+NS+TF-WeA4, 34
Bevan, EM+2D-TuA10, 17
Bhimanapati, G.R.: 2D+EM+NS+SS+TF-WeM11, 28
Bianco, G.V.: EL+AS+EM+EN+SS-ThM6, 43
Biyikli, N.: EM+EN-FrM4, 59; TF+EM+EN-WeA2, 39
Bluhm, H.: EN+AS+EM+SE-WeM5, 32
Bobek, S.: 2D+EM+NS+SS+TF-WeM10, 28
Boemmels, J.: EM-TuM6, 12
Boecker, J.E.: EM-MoA10, 9; EM-TuP20, 25
Bol, A.A.: 2D+EM+MS+NS-FrM6, 56
Bolotin, I.: EM-MoA9, 9
Bolotin, K.I.: 2D+AS+EM+MI+MN+NS+TF-WeA1, 34
Bonetti, S.: MI+EM-MoM11, 4
Borguet, E.: SP+AS+EM+NS+SS-ThP8, 55
Borisevich, A.: 2D+EM+MI+MN+NS+SS+TF-ThA9, 49
Bourke, P.: SE+EM+EN+PS+TF-MoM6, 5
Bowers, J.W.: EN+AS+EM+SE-WeM13, 33
Bowman, S.R.: EM1-ThM12, 44
Branham, M.S.: EM1-ThM3, 44
Bray, K.R.: EM-TuP18, 24
Brennan, B.: EM+2D-TuA3, 16
Brigeman, A.N.: EN+AS+EM-WeA11, 38; SS+EM-FrM2, 62
Briley, C.: EL+AS+EM+MC+SS-ThA4, 50
Brivio, J.: 2D+AS+EM+MI+MN+NS+TF-WeA4, 34
Brown, C.G.: EM1-ThM12, 44
Brown, K.: 2D+EM+NS+SS+TF-WeM10, 28
Browning, J.: EN+EM+MN+NS+TR-MoA9, 10
Brownson, J.R.S.: EN+AS+EM+SE-WeM6, 32
Bruno, G.: EL+AS+EM+EN+SS-ThM6, 43
Büchner, C.: 2D+EM+NS+SS+TF-WeM12, 28
Bultman, J.E.: 2D+EM+NS+PS+TF-MoM5, 1
Burger, A.: EM+MI+NS-MoM4, 2
Bursa, E.: EM+2D-TuA3, 16
Burton, M.: TF+AS+EM-TuA9, 20
Bussmann, E.: EM1-ThA6, 51; EM1-ThA7, 52
Butera, R.: EM1-ThA7, 52
Bux, S.: EN+AS+EM+SE-TuM13, 14

— C —

Cai, T.: EM1-ThM5, 44
Campbell, C.T.: EM2-ThA9, 53
Canedy, C.: SS+EM-FrM5, 63
Cansizoglu, H.: TF+EM+EN-WeA1, 39; TF+EM+EN-WeA2, 39
Cansizoglu, M.F.: TF+EM+EN-WeA1, 39; TF+EM+EN-WeA2, 39
Cao, L.: EN+AS+EM+SE-TuM6, 14
Cao, S.: EM+MI+NS-MoM10, 3
Capezzuto, P.: EL+AS+EM+EN+SS-ThM6, 43
Carette, M.: TF+AS+EM-TuA3, 20
Carpick, R.W.: SP+AS+BI+EM+NS+SE+SS-FrM2, 61
Carr, S.M.: EM1-ThA6, 51; EM1-ThA7, 52
Carraro, C.: EM+EN+TF-WeA8, 35

Carroll, M.: EM1-ThA1, 51; EM1-ThA6, 51; EM1-ThA7, 52
Caspar, J.V.: EN+AS+EM-WeA3, 38
Cassidy, C.: EM-MoA1, 8
Caubert, P.: SS+EM-FrM9, 64
Celio, H.C.: EM+EN+TF-WeA7, 35
Cerna, R.: EM-TuP26, 25
Chabal, Y.J.: EN+EM+MN+NS+TR-MoA3, 10
Chae, J.: 2D+EM+MI+MN+NS+SS+TF-ThA4, 48
Chagarov, E.A.: EM+2D-TuA4, 16; EM1-ThA9, 52; EN+AS+EM+SE-WeM4, 32
Chang, C.-H.: EM+EN+TF-WeA8, 35
Chaudhuri, A.R.: EM1-ThA11, 53
Chavez, J.: EM-TuP5, 22
Chawla, J.S.: EM-TuM12, 13
Chen, A.: EM2-ThM5, 45
Chen, C.-C.: EN+AS+EM+SE-WeM5, 32
Chen, G.: EM1-ThM3, 44
Chen, H.S.: EM+EN-FrM5, 59
Chen, H.T.: EM+EN-FrM5, 59
Chen, J.Z.: EM+NS+TF-FrM5, 60
Chen, L.: EM-WeA4, 37
Chen, M.: SS+EM-FrM3, 63
Chen, W.H.: EM+EN-FrM5, 59
Chen, X.G.: EL+AS+EM+MC+SS-ThA3, 50
Cheng, I.C.: EM+NS+TF-FrM5, 60
Cherkaoui, K.: EM+2D-TuA8, 17
Chernomordik, B.D.: EN+AS+EM+SE-WeM3, 31
Chervin, C.N.: EM+EN+TF-WeA11, 36
Chevalier, N.: 2D+EM+MI+MN+NS+SS+TF-ThA10, 49
Chikyo, T.: EM+NS+TF-FrM10, 61; EM-TuP8, 23
Cho, K.J.: EM+EN+TF-WeA3, 35
Chobpattana, V.: EM-WeA12, 37
Choi, S.: EM1-TuM3, 12
Choi, S.C.: EM-TuP25, 25
Choi, S.G.: EL+AS+EM+EN+SS-ThM3, 42
Chopra, S.N.: EM+MI+NS-MoM11, 3; EM1-ThA10, 52
Choudhury, P.: EM1-ThA9, 52; EM-WeA3, 36
Christopher, P.: EN+AS+EM+SE-TuM3, 13
Chu, N.N.: SP+AS+EM+NS+SS-ThP5, 55
Chu, S.: EN+EM+NS-TuA10, 19
Chu, Y.-H.: MI+EM-MoM2, 3
Ciobanu, C.V.: 2D+EM+NS+PS+SS+TF-MoM10, 2
Ciofi, I.: EM-TuM6, 12
Clark, B.: TF+AS+EM-TuA1, 19
Clark, K.: SP+2D+AS+EM+MC+NS+SS-ThM11, 47; SP+2D+AS+EM+MC+NS+SS-ThM6, 46
Clark, S.M.: EM1-ThM6, 44
Clarke, R.: EN+AS+EM+SE-WeM11, 33
Cleveland, E.: SS+EM-FrM5, 63
Cobet, C.: EL+AS+EM+EN+SS-ThM12, 43
Cohen, H.: EN+EM+MN+NS+TR-MoA8, 10
Colby, R.J.: EM-MoA3, 8
Collazo, R.: EM+EN-FrM11, 60
Collins, R.W.: EL+AS+BI+EM+SS-FrM5, 58; EL+AS+EM+EN+SS-ThM4, 42; EN+AS+EM+SE-WeM12, 33
Colombo, L.: EM-WeA4, 37
Comfort, E.: 2D+EM+MS+NS-FrM4, 56
Conley, J.F.: EM2-WeM13, 31; EM2-WeM2, 30
Conley, Jr., J.F.: EM2-WeM12, 31
Contreras, Y.D.: EM-TuP2, 22
Cook, B.: EN+AS+EM+SE-TuM12, 14
Cook-Chennault, K.: EM+EN+TF-WeA1, 35
Cooke, M.: EM-TuM6, 12
Cordell, J.J.: EN+AS+EM+SE-WeM6, 32
Coulter, K.: SE+EM+EN+PS+TF-MoM5, 5
Coy-Diaz, H.: 2D+AS+EM+NS+SS-MoA6, 7
Crommie, M.F.: 2D+EM+MS+NS-FrM3, 56
Cui, Y.: EM-TuP31, 26
Culbertson, J.: 2D+AS+EM+NS+SS-MoA3, 7
Cullen, P.J.: SE+EM+EN+PS+TF-MoM6, 5

Culver, J.: EN+EM+NS-TuA10, 19; EN+EM+NS-TuA9, 18

Cun, H.Y.: 2D+AS+EM+NS+SS-MoA1, 7

— D —

Darakchieva, V.: EL+AS+EM+MC+SS-ThA9, 50

Datta, S.: EM2-WeM5, 30

Davis, A.: SS+EM-FrM9, 64

Davis, R.C.: EM+EN+TF-WeA9, 36; TF+EM+EN-WeA11, 40

de Marneffe, J.-F.: EM-TuM6, 12

de Martino, A.: EL+AS+BI+EM+SS-FrM3, 57

Dean, C.R.: 2D+EM+MI+MN+NS+SS+TF-ThA4, 48

DeCervo, J.N.: EM-TuP18, 24

Decoster, S.: EM-TuM6, 12

Demirkan, K.: EN+AS+EM+SE-WeM2, 31

Demkov, A.A.: EM+MI+NS-MoM11, 3; EM+MI+NS-MoM3, 2; EM1-ThA10, 52; EM2-WeM10, 30

Deng, W.: SP+2D+AS+EM+MC+NS+SS-ThM11, 47

Dietz, N.: EM+EN-FrM11, 60; EM-TuP15, 24; EM-TuP17, 24

Dijon, J.: 2D+EM+MI+MN+NS+SS+TF-ThA10, 49

Dil, J.H.: 2D+EM+MI+MN+NS+SS+TF-ThA6, 48

Diwan, A.: TF+EM+EN-WeA11, 40; TF+EM+EN-WeA7, 40

Djara, V.: EM+2D-TuA8, 17

Dominguez, J.: EM1-ThA6, 51

Dong, H.: EM+2D-TuA7, 16

Dorgan, V.E.: EM1-WeM12, 29

Dorman, J.: EM2-ThA8, 53; EN+EM+MN+NS+TR-MoA10, 11

Dougherty, D.B.: MI+EM-MoM10, 4

Dowben, P.A.: 2D+EM+MI+MN+NS+SS+TF-ThA8, 48; EM+MI+NS-MoM10, 3

Droopad, R.: EM1-ThA9, 52; EM-WeA12, 37

Druce, J.: EN+AS+EM+SE-WeM2, 31

Du, D.: EM-MoA3, 8

Du, H.: EL+AS+BI+EM+SS-FrM5, 58

Du, S.X.: 2D+AS+EM+NS+SS-MoA10, 8

Du, W.: EM+EN+TF-WeA1, 35

Dubourdieu, C.: EM+MI+NS-MoM8, 3

Duerloo, K.-A.N.: 2D+AS+EM+MI+MN+NS+TF-WeA12, 35

Duerr, H.: MI+EM-MoM11, 4

Durand, C.P.: SP+2D+AS+EM+MC+NS+SS-ThM10, 47; SP+2D+AS+EM+MC+NS+SS-ThM11, 47

Durbin, S.: EN+AS+EM+SE-WeM11, 33

Durcan, C.: SP+AS+BI+EM+NS+SE+SS-FrM5, 62

Dwyer, K.J.: EM1-ThA3, 51

Dziaugys, A.: 2D+EM+MI+MN+NS+SS+TF-ThA9, 49

— E —

Ebnonnasir, A.: 2D+EM+NS+PS+SS+TF-MoM10, 2

Eddy, C.R.: EM1-ThM12, 44; EM1-WeM10, 29

Eddy, Jr., C.R.: EM1-WeM5, 29

Edelstein, D.C.: EM-TuM1, 12

Edmonds, M.: EM1-ThA9, 52; EM-WeA12, 37

Eichfeld, S.M.: 2D+EM+NS+SS+TF-WeM6, 27

Einstein, T.L.: 2D+AS+EM+MI+MN+NS+TF-WeA8, 34

Eizenberg, M.: EM1-ThA11, 53

Ekerdt, J.G.: EM+MI+NS-MoM11, 3; EM1-ThA10, 52

Elisabeth, S.: TF+AS+EM-TuA3, 20

Eliseev, E.: 2D+EM+MI+MN+NS+SS+TF-ThA9, 49

Emmelkamp, J.: TF+AS+EM-TuA2, 19

Empante, T.: 2D+EM+NS+SS+TF-WeM10, 28

Engelhard, M.H.: EM-MoA3, 8

English, C.D.: EM1-WeM12, 29

Ercius, P.: EN+AS+EM+SE-WeM2, 31

Exarhos, S.: EM-MoA4, 8

— F —

Fan, R.: EM+EN+TF-WeA9, 36

Feenstra, R.M.: 2D+EM+NS+PS+SS+TF-MoM6, 1; SP+2D+AS+EM+MC+NS+SS-ThM6, 46

Feldberg, N.: EN+AS+EM+SE-WeM11, 33

Feng, P.X.-L.: 2D+EM+MS+NS-FrM5, 56

Ferguson, I.T.: EM+EN-FrM11, 60; EM-TuP15, 24; EM-TuP17, 24

Fête, A.: MI+EM-MoM3, 3

Filippov, A.: SS+EM-FrM4, 63

Finckenor, M.: TF+EM+EN-WeA1, 39

First, P.N.: SP+2D+AS+EM+MC+NS+SS-ThM3, 46

Fischetti, M.V.: EM-WeA7, 37

Fisher, B.L.: 2D+EM+NS+SS+TF-WeM3, 27

Fleurial, J.P.: EN+AS+EM+SE-TuM13, 14

Flores-Gracia, F.J.: EM-TuP30, 26

Foos, E.E.: EM-MoA10, 9; EM-TuP20, 25

Fortunato, E.: EM+NS+TF-FrM8, 61

Fowlkes, J.: SP+2D+AS+EM+MC+NS+SS-ThM10, 47

Frank, M.M.: EM+MI+NS-MoM8, 3

Fredrickson, K.D.: EM+MI+NS-MoM3, 2

Freitas, Jr., J.A.: EM1-ThM12, 44

Freund, H.-J.: 2D+EM+NS+SS+TF-WeM12, 28

Frey Meyer, N.J.: EM-MoA11, 9

Friedman, A.: 2D+AS+EM+NS+SS-MoA3, 7

Frisch, J.: MI+EM-MoM11, 4

Fu, C.: SS+EM-FrM1, 62

Fujii, H.: EN+EM+MN+NS+TR-MoA11, 11

Fukuyama, A.: EN+EM+MN+NS+TR-MoA11, 11

— G —

Gall, D.: EM-TuM12, 13

Gallagher, M.C.: SS+EM-FrM1, 62

Gamage, S.: EM+EN-FrM11, 60

Gangarapu, S.: SS+EM-FrM4, 63

Gao, H.-J.: 2D+AS+EM+NS+SS-MoA10, 8

Gao, Y.: 2D+EM+MI+MN+NS+SS+TF-ThA4, 48

Garcia-Cauel, E.: EL+AS+BI+EM+SS-FrM3, 57

Gariglio, S.: MI+EM-MoM3, 3

Gartstein, Y.: EN+EM+MN+NS+TR-MoA3, 10

Gaskill, D.K.: EM1-WeM10, 29; EM1-WeM5, 29

Gates, R.: TF+EM+EN-WeA11, 40

Gautier, B.: EM+MI+NS-MoM8, 3

Gellman, A.J.: TF+AS+EM-TuA11, 20

Gerasopoulos, K.D.: EN+EM+NS-TuA10, 19

Ghimire, K.: EL+AS+EM+EN+SS-ThM11, 43

Ghodssi, R.: EN+EM+NS-TuA10, 19;

EN+EM+NS-TuA9, 18

Ghosh, S.: EM1-ThA4, 51; EM1-ThA8, 52; EM1-ThM5, 44; EM-TuP5, 22; TF+AS+EM-TuA12, 21

Giangregorio, M.: EL+AS+EM+EN+SS-ThM6, 43

Gillette, E.: EN+EM+NS-TuA3, 17

Glaser, C.: EM-TuP16, 24

Glenn, S.: EL+AS+BI+EM+SS-FrM5, 58

Gnerlich, M.: EN+EM+NS-TuA10, 19;

EN+EM+NS-TuA9, 18

Gompf, B.: EL+AS+EM+MC+SS-ThA1, 49

Gonzales, J.M.: 2D+AS+EM+MI+MN+NS+TF-WeA11, 34; 2D+EM+NS+SS+TF-WeM5, 27

Goodyear, A.: EM-TuM6, 12

Goswami, R.: EM1-ThM12, 44

Götzen, J.: 2D+EM+NS+SS+TF-WeM4, 27

Gouillet, A.: TF+AS+EM-TuA3, 20

Gowthaman, P.: EM+EN+TF-WeA2, 35

Granier, A.: TF+AS+EM-TuA3, 20

Grant, J.T.: TF+EM+EN-WeA10, 40

Greber, T.: 2D+AS+EM+NS+SS-MoA1, 7; 2D+EM+NS+PS+SS+TF-MoM8, 2

Grierson, D.S.: SP+AS+BI+EM+NS+SE+SS-FrM2, 61

Gu, G.: SP+2D+AS+EM+MC+NS+SS-ThM11, 47; SP+2D+AS+EM+MC+NS+SS-ThM6, 46

Guan, D.: EM-TuM12, 13

Guglietta, G.W.: EN+AS+EM-WeA3, 38

Guillet, J.-F.: 2D+EM+MI+MN+NS+SS+TF-ThA10, 49

Guisinger, N.P.: 2D+AS+EM+NS+SS-MoA7, 7; 2D+EM+NS+SS+TF-WeM3, 27

Gundlach, D.J.: EN+AS+EM-WeA11, 38; SS+EM-FrM2, 62

Gunlycke, D.: 2D+EM+MI+MN+NS+SS+TF-ThA3, 48

Guo, H.: SP+2D+AS+EM+MC+NS+SS-ThM5, 46

Guo, X.: EM-TuP11, 23

Gupta, S.: TF+AS+EM-TuA1, 19

Gurary, A.: EM+EN-FrM8, 59

— H —

Ha, J.: SP+AS+BI+EM+NS+SE+SS-FrM6, 62;

SP+AS+EM+NS+SS-ThP3, 55

Hacker, C.A.: EN+AS+EM-WeA11, 38; SS+EM-FrM2, 62

Hage, D.: EL+AS+BI+EM+SS-FrM8, 58

Haider, A.: EM+EN-FrM4, 59; TF+EM+EN-WeA2, 39

Haight, R.: EN+AS+EM+SE-WeM4, 32

Haile, S.M.: EN+AS+EM+SE-TuM1, 13

Hamasaki, M.: EM-TuP7, 22

Han, S.E.: EM1-ThM5, 44; EM1-ThM6, 44; EM-TuP5, 22

Han, S.M.: EM1-ThA4, 51; EM1-ThA8, 52; EM1-ThM5, 44; EM-TuP5, 22; TF+AS+EM-TuA12, 21

Hanbicki, A.T.: 2D+EM+NS+PS+SS+TF-MoM4, 1

Haneef, H.: EL+AS+EM+EN+SS-ThM11, 43

Haney, P.: EN+AS+EM+SE-WeM12, 33

Hanley, L.: EM-MoA9, 9; EM-TuP31, 26

Hanrath, T.: EM-MoA8, 9

Haque, M.A.: 2D+EM+NS+PS+SS+TF-MoM5, 1

Harrison, J.A.: SP+AS+BI+EM+NS+SE+SS-FrM2, 61

Hart, C.: EM+MI+NS-MoM4, 2;

SE+EM+EN+PS+TF-MoM2, 4

He, G.: 2D+EM+NS+PS+SS+TF-MoM6, 1;

SP+2D+AS+EM+MC+NS+SS-ThM6, 46

He, Q.: 2D+EM+MI+MN+NS+SS+TF-ThA9, 49

He, X.: EN+AS+EM+SE-WeM2, 31

He, Y.: TF+EM+EN-WeA8, 40; TF+EM+EN-WeA9, 40

Hearn, G.: EL+AS+EM+MC+SS-ThA10, 51;

EL+AS+EM+MC+SS-ThA7, 50

Hellman, A.: EN+AS+EM+SE-TuM5, 14

Hemmi, A.: 2D+AS+EM+NS+SS-MoA1, 7;

2D+EM+NS+PS+SS+TF-MoM8, 2

Hemminger, J.C.: EN+AS+EM+SE-WeM5, 32

Herath, N.: EN+EM+MN+NS+TR-MoA9, 10

Herman, G.S.: EM+NS+TF-FrM3, 60

Hersam, M.C.: 2D+AS+EM+NS+SS-MoA7, 7;

2D+EM+NS+SS+TF-WeM3, 27

Herzinger, C.M.: EL+AS+EM+MC+SS-ThA9, 50

Heyde, M.: 2D+EM+NS+SS+TF-WeM12, 28

Heylen, N.: EM-TuM6, 12

Heyne, M.H.: EM-TuM6, 12

Hight Walker, A.R.:

2D+AS+EM+MI+MN+NS+TF-WeA7, 34

Hight-Walker, A.R.:

2D+AS+EM+MI+MN+NS+TF-WeA4, 34

Hingerl, K.: EL+AS+BI+EM+SS-FrM6, 58;

EL+AS+EM+EN+SS-ThM12, 43

Hinkle, C.L.: EM-WeA4, 37

Hinton, K.: EM+EN+TF-WeA9, 36

Hipps, K.W.: SP+2D+AS+EM+MC+NS+SS-ThM1, 46

Hiramatsu, M.: 2D+EM+MS+NS-FrM10, 57

Hite, J.K.: EM1-ThM12, 44

Hoard, B.R.: EM1-ThM5, 44

Hofer, W.: 2D+AS+EM+NS+SS-MoA10, 8

Hoffman, A.: EM-TuP15, 24

Hofmann, T.: EL+AS+BI+EM+SS-FrM8, 58;

EL+AS+EM+MC+SS-ThA4, 50;

EL+AS+EM+MC+SS-ThA6, 50;

EL+AS+EM+MC+SS-ThA9, 50

Holcomb, M.B.: MI+EM-MoM2, 3

Holleitner, A.W.: EL+AS+EM+MC+SS-ThA10, 51

- Holmes, R.J.: EN+AS+EM+WeA9, **38**
Hone, J.C.: 2D+EM+MI+MN+NS+SS+TF-ThA4, 48
Hori, M.: 2D+EM+MS+NS-FrM10, 57
Horn, M.W.: EN+AS+EM+SE+WeM6, 32
Hose, S.: EM2-WeM2, 30
Hossain, K.: EM+EN-FrM10, 60
Hossain, L.: 2D+EM+NS+SS+TF-WeM6, 27
Hossain, M.: EM-TuM3, 12
Howansky, A.: EN+EM+NS-TuA4, 18
Hsiao, C.N.: SP+AS+EM+NS+SS-ThP5, 55
Hsieh, C.: EM+EN-FrM5, 59
Hsu, K.W.: EM-WeA11, 37
Hsu, W.-C.: EM1-ThM3, 44
Hu, C.: EM1-ThA10, 52
Hu, J.J.: 2D+EM+NS+PS+SS+TF-MoM5, 1; SE+EM+EN+PS+TF-MoM8, 5
Huang, C.Y.: EM-WeA12, 37
Huang, C.-Y.: MI+EM-MoM2, 3
Huang, E.: 2D+EM+MS+NS-FrM3, 56
Huang, J.S.: EL+AS+EM+EN+SS-ThM10, 43
Hunter, K.: EN+AS+EM+SE-WeM3, 31
Hurlley, P.K.: EM+2D-TuA8, 17
Hussain, B.: EM-TuP17, 24
Hytech, M.: EM+MI+NS-MoM8, 3
- **I** —
Iannuzzi, M.: 2D+AS+EM+NS+SS-MoA1, 7
Idrobo, J.-C.: SP+2D+AS+EM+MC+NS+SS-ThM11, 47
Ielmini, D.: EM2-ThM3, 45
Ikari, T.: EN+EM+MN+NS+TR-MoA11, 11
Imai, S.: 2D+EM+MS+NS-FrM10, 57
Ingram, W.: TF+EM+EN-WeA8, 40; TF+EM+EN-WeA9, 40
Ishihara, T.: EN+AS+EM+SE-WeM2, 31
Ishikawa, K.: 2D+EM+MS+NS-FrM10, 57
Islam, M.F.: EM+NS+TF-FrM11, 61
Islam, S.: EM1-WeM12, 29
Iwasawa, H.: 2D+EM+MI+MN+NS+SS+TF-ThA8, 48
- **J** —
Jacobs, T.D.B.: SP+AS+BI+EM+NS+SE+SS-FrM2, 61
Jain, R.: SS+EM-FrM8, 64
Jamieson, S.: TF+EM+EN-WeA11, 40
Jang, H.-J.: EN+AS+EM-WeA11, 38; SS+EM-FrM2, 62
Järrendahl, K.: EL+AS+BI+EM+SS-FrM3, 57
Jennings, J.: EN+EM+NS-TuA11, 19
Jeon, M.H.: 2D+AS+EM+NS+SS-MoA8, 8
Jespersion, M.L.: 2D+EM+NS+PS+SS+TF-MoM5, 1
Jiao, C.Q.: EM-TuP18, 24
Johnson, G.: EM-MoA3, 8
Johnson, M.B.: EM+EN-FrM10, 60; EM-TuP1, 22
Jones, J.G.: TF+EM+EN-WeA10, 40
Jonker, B.T.: 2D+EM+NS+PS+SS+TF-MoM4, 1
Jordan-Sweet, J.: EM+MI+NS-MoM8, 3
Jourdan, N.J.: EM-TuM5, 12
Ju, H.X.: EN+AS+EM-WeA12, 39
Ju, L.: 2D+EM+MS+NS-FrM3, 56
Junda, M.M.: EL+AS+EM+EN+SS-ThM5, 42
Jung, S.: 2D+EM+MI+MN+NS+SS+TF-ThA4, 48
Junkermier, C.: 2D+AS+EM+NS+SS-MoA3, 7
Jurcescu, O.D.: EN+AS+EM-WeA11, 38; SS+EM-FrM2, 62
- **K** —
Kahn, A.L.: EM2-ThA10, 53
Kahn, S.: 2D+EM+MS+NS-FrM3, 56
Kaiser, D.: EM1-ThA4, 51; EM1-ThA8, 52
Kajihara, S.: EM-TuP7, 22
Kale, M.J.: EN+AS+EM+SE-TuM3, 13
Kalinin, S.V.: 2D+EM+MI+MN+NS+SS+TF-ThA9, 49
Kaminski, P.M.: EN+AS+EM+SE-WeM13, 33
Kane, M.H.: EM+EN-FrM10, 60; EM-TuP1, 22
Karabacak, T.: TF+EM+EN-WeA1, 39; TF+EM+EN-WeA2, 39
Katsumata, H.: EM-TuP7, 22; EM-TuP9, 23
Kattareeya, T.: EM-TuP8, 23
Katz, H.: EM+NS+TF-FrM6, 61
Kaufman-Osborn, T.: EM+2D-TuA4, 16; EM1-ThA9, 52; EN+AS+EM+SE-WeM4, 32
Kawaguchi, S.: EM-TuP9, 23
Kaykhaei, M.: TF+EM+EN-WeA7, 40
Keating, P.L.: SP+AS+BI+EM+NS+SE+SS-FrM2, 61
Kelly, M.: 2D+EM+NS+SS+TF-WeM11, 28
Kennedy, R.J.: EN+AS+EM+SE-WeM11, 33
Kent, T.: EM1-ThA9, 52; EM-WeA12, 37
Kessels, W.M.M.: 2D+EM+MS+NS-FrM6, 56
Ketchum, D.: EN+EM+NS-TuA9, 18
Ketkar, M.: EN+AS+EM+SE-WeM3, 31
Kiang, Y.W.: EM+EN-FrM5, 59
Kilner, J.: EN+AS+EM+SE-WeM2, 31
Kim, C.: EM-MoA11, 9
Kim, H.: 2D+EM+MI+MN+NS+SS+TF-ThA10, 49
Kim, H.J.K.: EM-TuP25, 25
Kim, J.Y.: EM+2D-TuA7, 16; EM-WeA4, 37
Kim, K.N.: 2D+AS+EM+NS+SS-MoA8, 8
Kim, K.S.: 2D+AS+EM+NS+SS-MoA4, 7; 2D+AS+EM+NS+SS-MoA8, 8
Kim, M.: EM-WeA4, 37; EM-WeA9, 37
Kim, P.: 2D+EM+MI+MN+NS+SS+TF-ThA4, 48
Kim, S.: SP+AS+EM+NS+SS-ThP3, 55
Kim, Y.: SP+AS+EM+NS+SS-ThP3, 55
Kimoto, T.: EM1-WeM3, 28
Kippelen, B.J.: EM2-ThA6, 53
Kiraly, B.T.: 2D+AS+EM+NS+SS-MoA7, 7; 2D+EM+NS+SS+TF-WeM3, 27
Kirillov, O.A.: EM2-WeM13, 31; SS+EM-FrM2, 62
Kirillova, O.A.: EN+AS+EM-WeA11, 38
Kis, A.: 2D+AS+EM+MI+MN+NS+TF-WeA4, 34
Klar, T.: EM2-WeM13, 31
Klee, V.: 2D+EM+NS+SS+TF-WeM10, 28
Klein, P.B.: EM1-WeM5, 29
Klimov, N.N.: 2D+EM+MS+NS-FrM4, 56
Kline, R.J.: EN+AS+EM-WeA11, 38
Knoll, A.J.: SE+EM+EN+PS+TF-MoM2, 4
Kocabas, C.: 2D+EM+MI+MN+NS+SS+TF-ThA11, 49
Kodambaka, S.: 2D+EM+NS+PS+SS+TF-MoM10, 2
Koirala, P.: EL+AS+EM+EN+SS-ThM4, 42; EN+AS+EM+SE-WeM12, 33
Kolagani, R.: EM+MI+NS-MoM4, 2
Kolasinski, K.W.: SS+EM-FrM6, 63
Komesu, T.: 2D+EM+MI+MN+NS+SS+TF-ThA8, 48
Komuro, A.: SE+EM+EN+PS+TF-MoM3, 5
Kondo, H.: 2D+EM+MS+NS-FrM10, 57
Kotulak, N.A.: SS+EM-FrM3, 63
Kozen, A.C.: EM+EN+TF-WeA10, 36; EN+EM+NS-TuA7, 18; EN+EM+NS-TuA8, 18
Kraya, L.Y.: SP+2D+AS+EM+MC+NS+SS-ThM2, 46
Kraya, R.: SP+2D+AS+EM+MC+NS+SS-ThM2, 46
Krishtab, M.: EM-TuM6, 12
Kropman, D.: EM-TuP22, 25
Kühne, P.: EL+AS+EM+MC+SS-ThA9, 50
Kujofsa, T.: TF+AS+EM-TuA7, 20
Kuk, Y.: SP+AS+BI+EM+NS+SE+SS-FrM6, 62; SP+AS+EM+NS+SS-ThP3, 55
Kukreja, R.: MI+EM-MoM11, 4
Kummel, A.C.: EM+2D-TuA4, 16; EM1-ThA9, 52; EM-WeA12, 37; EM-WeA3, 36; EN+AS+EM+SE-WeM4, 32
Kuo, Y.: EM+2D-TuA12, 17; EM1-ThM13, 45
Kusunoki, A.: EM-TuP9, 23
Kwak, I.J.: EM1-ThA9, 52
- **L** —
Laas, T.: EM-TuP22, 25
LaBella, V.P.: SP+AS+BI+EM+NS+SE+SS-FrM5, 62
Laha, A.: EM1-ThA11, 53
Lai, R.Y.: EL+AS+EM+MC+SS-ThA6, 50
Lal, R.: EM1-WeM1, 28
Lalor, J.: SE+EM+EN+PS+TF-MoM6, 5
Larsen, G.K.: TF+EM+EN-WeA8, 40; TF+EM+EN-WeA9, 40
Larson, P.: EM-TuP1, 22
Laskin, J.: EM-MoA3, 8
Lau, C.N.: 2D+EM+MS+NS-FrM1, 56
Lauer, I.: EM+MI+NS-MoM8, 3
Laughlin, K.: TF+EM+EN-WeA11, 40
Lauter, V.: EN+EM+MN+NS+TR-MoA9, 10
Law, M.: EN+AS+EM+SE-WeM5, 32
Le Lay, G.: 2D+EM+NS+SS+TF-WeM1, 27
Le, D.: EM1-WeM10, 29
Le, D.T.: 2D+AS+EM+MI+MN+NS+TF-WeA3, 34; 2D+EM+MI+MN+NS+SS+TF-ThA8, 48
Le, S.: 2D+EM+MS+NS-FrM4, 56
Lee, B.G.: EM1-ThM10, 44
Lee, H.: EN+AS+EM+SE-WeM6, 32
Lee, J.U.: 2D+EM+MS+NS-FrM4, 56
Lee, K.-M.: EM1-WeM10, 29
Lee, S.: EM-WeA12, 37
Lee, S.B.: EM+EN+TF-WeA10, 36; EN+EM+NS-TuA3, 17; EN+EM+NS-TuA7, 18; EN+EM+NS-TuA8, 18
Lee, Y.B.: EM-TuM3, 12
Lefever, J.A.: SP+AS+BI+EM+NS+SE+SS-FrM2, 61
Levi, D.: EL+AS+BI+EM+SS-FrM5, 58
Lewis, J.S.: EN+AS+EM+SE-TuM12, 14
Li, A.P.: SP+2D+AS+EM+MC+NS+SS-ThM10, 47; SP+2D+AS+EM+MC+NS+SS-ThM11, 47; SP+2D+AS+EM+MC+NS+SS-ThM6, 46
Li, D.: MI+EM-MoM3, 3; TF+AS+EM-TuA3, 20
Li, J.: 2D+EM+NS+PS+SS+TF-MoM6, 1; EL+AS+BI+EM+SS-FrM5, 58; EL+AS+EM+EN+SS-ThM3, 42; EL+AS+EM+EN+SS-ThM4, 42
Li, J.J.: EN+AS+EM+SE-WeM10, 32
Li, Y.: 2D+AS+EM+MI+MN+NS+TF-WeA12, 35
Li, Y.S.: EM+NS+TF-FrM5, 60
Li, Z.: EM1-WeM12, 29; SP+AS+EM+NS+SS-ThP8, 55
Lian, G.: EM-WeA9, 37
Liao, C.H.: EM+EN-FrM5, 59
Lichtenstein, L.: 2D+EM+NS+SS+TF-WeM12, 28
Lilly, M.P.: EM1-ThA6, 51
Lin, C.-C.: EM1-ThM13, 45
Lin, C.F.: EM+EN+TF-WeA10, 36
Lin, J.: EM+2D-TuA8, 17
Lin, Y.: EM-MoA3, 8
Lin, Y.C.: 2D+EM+NS+SS+TF-WeM6, 27
Linford, M.R.: TF+EM+EN-WeA11, 40; TF+EM+EN-WeA7, 40
Linhart, W.M.: EN+AS+EM+SE-WeM11, 33
Liu, C.: EN+EM+NS-TuA7, 18
Liu, D.-J.: EN+EM+NS-TuA1, 17
Liu, H.: EM-TuM3, 12
Liu, J.: SP+AS+BI+EM+NS+SE+SS-FrM2, 61
Liu, L.: SP+2D+AS+EM+MC+NS+SS-ThM11, 47
Liu, M.: EM2-ThM12, 45; MI+EM-MoM5, 4
Liu, Q.: EM2-ThM12, 45
Liu, R.: SS+EM-FrM1, 62
Liu, S.Y.: EL+AS+EM+MC+SS-ThA3, 50
Liu, W.: MI+EM-MoM3, 3
Liu, X.: EM+NS+TF-FrM11, 61
Liu, Y.: EM+NS+TF-FrM6, 61; EN+AS+EM+SE-WeM5, 32; TF+EM+EN-WeA11, 40
Liu, Z.: EN+AS+EM+SE-WeM5, 32
Long, J.W.: EM+EN+TF-WeA11, 36
Long, S.B.: EM2-ThM12, 45
Lopez, T.: EN+AS+EM+SE-TuM13, 14
Lordi, V.: EN+AS+EM+SE-WeM2, 31
Losurdo, M.: EL+AS+EM+EN+SS-ThM6, 43
Lou, J.: 2D+EM+NS+PS+SS+TF-MoM1, 1; SP+2D+AS+EM+MC+NS+SS-ThM10, 47

Lownsbury, J.M.: EM2-ThA9, **53**
 Lu, I.: 2D+EM+NS+SS+TF-WeM10, **28**
 Lu, N.: EM-WeA4, **37**; EM-WeA9, **37**
 Luan, P.: SE+EM+EN+PS+TF-MoM2, **4**
 Lukaszew, R.A.: TF+AS+EM-TuA9, **20**
 Luna-López, J.A.: EM-TuP28, **25**
 Lunt, B.: TF+EM+EN-WeA11, **40**
 Lv, H.B.: EM2-ThM12, **45**
 Lynn, K.G.: EN+EM+NS-TuA11, **19**
 — **M** —
 Ma, Q.: 2D+EM+MI+MN+NS+SS+TF-ThA8, **48**
 Maboudian, R.: EM+EN+TF-WeA8, **35**
 Mackus, A.J.M.: 2D+EM+MS+NS-FrM6, **56**
 Madaan, N.: TF+EM+EN-WeA11, **40**
 Magnusson, R.: EL+AS+BI+EM+SS-FrM3, **57**
 Mahadik, N.A.: EM1-WeM5, **29**
 Majeski, M.: EM-MoA9, **9**; EM-TuP31, **26**
 Maksymowych, P.: 2D+EM+MI+MN+NS+SS+TF-ThA9, **49**
 Malko, A.: EN+EM+MN+NS+TR-MoA3, **10**
 Mancheno, P.: EM-TuP2, **22**
 Mancheno-Posso, P.L.: SS+EM-FrM8, **64**
 Mangolini, L.: EM-MoA4, **8**; EN+AS+EM+SE-TuM13, **14**
 Mann, J.: 2D+EM+NS+SS+TF-WeM10, **28**;
 EL+AS+BI+EM+SS-FrM5, **58**
 Mannheim, A.: TF+AS+EM-TuA2, **19**
 Mannix, A.J.: 2D+AS+EM+NS+SS-MoA7, **7**;
 2D+EM+NS+SS+TF-WeM3, **27**
 Mansfield, L.: EL+AS+BI+EM+SS-FrM5, **58**
 Mariano, W.C.: EM-TuP3, **22**
 Mariolle, D.: 2D+EM+MI+MN+NS+SS+TF-ThA10, **49**
 Martin, L.W.: EM+MI+NS-MoM5, **2**
 Martinez, E.: SS+EM-FrM9, **64**
 Martins, B.: SP+2D+AS+EM+MC+NS+SS-ThM5, **46**
 Martins, R.: EM+NS+TF-FrM8, **61**
 Mastro, M.A.: EM1-ThM12, **44**
 Masuda, S.: EM-TuP12, **23**; EM-TuP13, **24**
 Matsui, F.: 2D+EM+NS+PS+SS+TF-MoM8, **2**
 Matsumuro, A.: SP+AS+EM+NS+SS-ThP2, **55**
 Matsunaga, K.: EM-TuM6, **12**
 Mayer, T.S.: EM-WeA1, **36**
 Mazet, L.: EM+MI+NS-MoM8, **3**
 McCann, P.J.: EM+EN-FrM10, **60**; EM-TuP1, **22**
 McCartney, M.R.: EM+MI+NS-MoM3, **2**
 McCarty, K.F.: 2D+EM+NS+PS+SS+TF-MoM10, **2**;
 SP+2D+AS+EM+MC+NS+SS-ThM11, **47**
 McConney, M.E.: 2D+EM+NS+PS+SS+TF-MoM5, **1**
 McCreary, K.M.: 2D+EM+NS+PS+SS+TF-MoM4, **1**
 McDaniel, M.D.: EM+MI+NS-MoM11, **3**; EM1-ThA10, **52**
 McDonnell, S.: 2D+EM+NS+SS+TF-WeM6, **27**;
 EM+2D-TuA3, **16**; EM-WeA4, **37**; EM-WeA9, **37**
 McGlone, J.: EM2-WeM13, **31**
 McIntyre, P.C.: EM-WeA12, **37**
 McNamara, J.D.: EM+EN-FrM3, **59**
 Mergos, I.A.: EL+AS+BI+EM+SS-FrM4, **58**
 Merrett, J.N.: EM-TuP18, **24**
 Meyer, J.R.: EM1-ThM12, **44**
 Meysing, D.: EN+AS+EM+SE-WeM10, **32**
 Mihara, S.: EM-TuP13, **24**
 Miller, B.: EL+AS+EM+MC+SS-ThA10, **51**
 Miller, J.: TF+AS+EM-TuA11, **20**
 Miller, M.A.: SE+EM+EN+PS+TF-MoM5, **5**
 Milosavljevic, V.: SE+EM+EN+PS+TF-MoM6, **5**
 Minnal, C.: EN+EM+NS-TuA11, **19**
 Misra, S.: EM1-ThA6, **51**; EM1-ThA7, **52**
 Mitzi, D.B.: EN+AS+EM+SE-WeM4, **32**
 Mok, H.S.: 2D+EM+NS+PS+SS+TF-MoM10, **2**
 Monaghan, S.: EM+2D-TuA8, **17**
 Monfil-Leyva, K.: EM-TuP28, **25**; EM-TuP30, **26**
 Moon, D.W.: EL+AS+BI+EM+SS-FrM1, **57**
 Moon, J.-S.: EM1-WeM10, **29**

Morales-Cifuentes, J.R.:
 2D+AS+EM+MI+MN+NS+TF-WeA8, **34**
 Morales-Sánchez, A.: EM-TuP30, **26**
 Morel, N.: SS+EM-FrM9, **64**
 Moreno-Moreno, M.: EM-TuP30, **26**
 Moret, M.P.: SS+EM-FrM9, **64**
 Morozovska, A.: 2D+EM+MI+MN+NS+SS+TF-ThA9, **49**
 Mowll, T.R.: 2D+EM+NS+PS+SS+TF-MoM3, **1**
 Mueller, T.: EN+AS+EM+SE-TuM6, **14**
 Mulders, J.J.L.: 2D+EM+MS+NS-FrM6, **56**
 Muñoz-Zurita, A.L.: EM-TuP28, **25**; EM-TuP30, **26**
 Murata, Y.: 2D+EM+NS+PS+SS+TF-MoM10, **2**
 Muratore, C.: 2D+EM+NS+PS+SS+TF-MoM5, **1**;
 SE+EM+EN+PS+TF-MoM8, **5**
 Murphy, N.R.: TF+EM+EN-WeA10, **40**
 Muscat, A.J.: EM-TuP2, **22**; SS+EM-FrM8, **64**
 Myers-Ward, R.L.: EM1-WeM10, **29**; EM1-WeM5, **29**
 — **N** —
 Nabatame, T.: EM+NS+TF-FrM10, **61**; EM-TuP8, **23**
 Nafus, K.: EM-TuM6, **12**
 Naghibi, S.: 2D+EM+NS+SS+TF-WeM10, **28**
 Najmaei, S.: SP+2D+AS+EM+MC+NS+SS-ThM10, **47**
 Nakajima, Y.: SP+AS+BI+EM+NS+SE+SS-FrM6, **62**
 Nakano, Y.: EN+EM+MN+NS+TR-MoA11, **11**
 Narayanan, V.: EM+MI+NS-MoM8, **3**
 Narimannezhad, A.: EN+EM+NS-TuA11, **19**
 Nasr, J.R.: EN+AS+EM+SE-WeM6, **32**
 Natterer, F.D.: 2D+EM+MI+MN+NS+SS+TF-ThA4, **48**
 Nayyar, N.: 2D+AS+EM+MI+MN+NS+TF-WeA3, **34**
 Negara, M.A.: EM+2D-TuA8, **17**
 Nelson, E.S.: EM+EN+TF-WeA11, **36**
 Nesterenko, P.: TF+EM+EN-WeA7, **40**
 Newell, D.B.: 2D+EM+MS+NS-FrM4, **56**
 Ngo, T.Q.: EM+MI+NS-MoM11, **3**; EM1-ThA10, **52**
 Nguyen, A.: 2D+EM+NS+SS+TF-WeM10, **28**
 Nguyen, H.: EN+EM+MN+NS+TR-MoA3, **10**
 Nguyen, N.V.: EM2-WeM13, **31**
 Nie, S.: 2D+EM+NS+PS+SS+TF-MoM10, **2**
 Nishi, Y.: EM-TuP11, **23**; EM-WeA11, **37**
 Nishioka, K.: EN+EM+MN+NS+TR-MoA11, **11**
 Noebels, M.: EM2-ThA8, **53**;
 EN+EM+MN+NS+TR-MoA10, **11**
 Noked, M.: EM+EN+TF-WeA10, **36**;
 EN+EM+NS-TuA7, **18**; EN+EM+NS-TuA8, **18**
 Nolde, J.: SS+EM-FrM5, **63**
 Norman, A.: EL+AS+BI+EM+SS-FrM5, **58**
 Nosiglia, C.: 2D+EM+MS+NS-FrM3, **56**
 Nyakiti, L.O.: EM1-WeM10, **29**

— **O** —
 O'Connor, E.: EM+2D-TuA8, **17**
 Oehrlein, G.S.: SE+EM+EN+PS+TF-MoM2, **4**
 Ohi, A.: EM+NS+TF-FrM10, **61**
 Ohishi, T.: EM-TuP8, **23**
 Ohldag, H.: MI+EM-MoM11, **4**
 Ohno, R.: SE+EM+EN+PS+TF-MoM3, **5**
 Ohno, T.R.: EN+AS+EM+SE-WeM10, **32**
 Ohsumimoto, S.: SP+AS+EM+NS+SS-ThP2, **55**
 Oishi, T.: EM+NS+TF-FrM10, **61**
 Ojeda-Durán, E.: EM-TuP30, **26**
 Okada, T.: 2D+AS+EM+NS+SS-MoA9, **8**
 Okyay, A.K.: EM+EN-FrM4, **59**; TF+EM+EN-WeA2, **39**
 Oleynik, I.I.: 2D+AS+EM+MI+MN+NS+TF-WeA11, **34**;
 2D+EM+NS+SS+TF-WeM5, **27**
 Ong, E.W.: 2D+EM+NS+PS+SS+TF-MoM3, **1**
 Oplá, R.L.: SS+EM-FrM3, **63**
 Ossikovski, R.: EL+AS+BI+EM+SS-FrM3, **57**
 Osten, H.J.: EM1-ThA11, **53**

Osterwalder, J.: 2D+AS+EM+NS+SS-MoA1, **7**;
 2D+EM+NS+PS+SS+TF-MoM8, **2**
 Oviedo, J.: EM-WeA9, **37**
 Ozgit-Akgun, C.: EM+EN-FrM4, **59**
 — **P** —
 Paglione, J.: SP+AS+BI+EM+NS+SE+SS-FrM6, **62**
 Pala, I.R.: EM+EN+TF-WeA11, **36**
 Palazzo, J.: EM-TuM3, **12**
 Parikh, P.: EM1-WeM1, **28**
 Park, J.: SP+2D+AS+EM+MC+NS+SS-ThM11, **47**;
 SP+2D+AS+EM+MC+NS+SS-ThM6, **46**
 Park, J.H.: EM1-ThA9, **52**
 Park, S.W.: EM+2D-TuA4, **16**; EM1-ThA9, **52**;
 EN+AS+EM+SE-WeM4, **32**
 Parker, J.F.: EM+EN+TF-WeA11, **36**
 Parzinger, E.: EL+AS+EM+MC+SS-ThA10, **51**
 Paudel, T.: EM+MI+NS-MoM10, **3**
 Paul, B.: TF+EM+EN-WeA7, **40**
 Payne, M.: TF+AS+EM-TuA11, **20**
 Pearse, A.J.: EM+EN+TF-WeA10, **36**;
 EN+EM+NS-TuA3, **17**; EN+EM+NS-TuA7, **18**;
 EN+EM+NS-TuA8, **18**
 Pearson, A.: TF+EM+EN-WeA11, **40**
 Peev, D.: EL+AS+BI+EM+SS-FrM8, **58**
 Peña, V.: EM-TuP26, **25**
 Peng, W.: EN+EM+MN+NS+TR-MoA3, **10**
 Peng, X.: EM-WeA4, **37**; EM-WeA9, **37**
 Perepichka, D.F.: SS+EM-FrM1, **62**
 Perriot, R.: 2D+AS+EM+MI+MN+NS+TF-WeA11, **34**
 Pfadler, T.: EM2-ThA8, **53**;
 EN+EM+MN+NS+TR-MoA10, **11**
 Pfaunmiller, E.: EL+AS+BI+EM+SS-FrM8, **58**
 Pfnür, H.: SP+2D+AS+EM+MC+NS+SS-ThM12, **47**
 Phumisithikul, K.L.: EM+EN-FrM3, **59**
 Phuong, P.V.: 2D+AS+EM+NS+SS-MoA8, **8**
 Piasecki, A.: 2D+EM+NS+SS+TF-WeM6, **27**
 Piper, L.F.J.: EN+AS+EM+SE-WeM11, **33**
 Placencia, D.: EM-MoA10, **9**; EM-TuP20, **25**
 Plass, K.E.: EM-MoA11, **9**
 Podraza, N.J.: EL+AS+EM+EN+SS-ThM1, **42**;
 EL+AS+EM+EN+SS-ThM11, **43**;
 EL+AS+EM+EN+SS-ThM4, **42**;
 EL+AS+EM+EN+SS-ThM5, **42**
 Poenitzsch, V.Z.: SE+EM+EN+PS+TF-MoM5, **5**
 Polat, E.O.: 2D+EM+MI+MN+NS+SS+TF-ThA11, **49**
 Pomeroy, J.: EM1-ThA3, **51**
 Ponath, P.: EM+MI+NS-MoM3, **2**
 Pookpanratana, S.J.: EN+AS+EM-WeA11, **38**;
 SS+EM-FrM2, **62**
 Pop, E.: EM1-WeM12, **29**
 Porter, L.M.: EM+NS+TF-FrM11, **61**
 Posadas, A.B.: EM+MI+NS-MoM11, **3**;
 EM+MI+NS-MoM3, **2**; EM1-ThA10, **52**
 Povey, I.M.: EM+2D-TuA8, **17**
 Pradhan, A.K.: EM-TuP24, **25**
 Pradhan, P.: EL+AS+BI+EM+SS-FrM5, **58**
 Pradhan, S.: EM-TuP24, **25**
 Preciado, E.: 2D+EM+NS+SS+TF-WeM10, **28**
 Price, D.: EM2-WeM2, **30**
 Pritchett, B.N.: EM+EN-FrM10, **60**
 Pujari, S.: SS+EM-FrM4, **63**
 Putnik, M.: EN+EM+MN+NS+TR-MoA10, **11**
 — **Q** —
 Qin, X.: EM+2D-TuA7, **16**
 — **R** —
 Rahman, T.S.: 2D+AS+EM+MI+MN+NS+TF-WeA3, **34**;
 2D+EM+MI+MN+NS+SS+TF-ThA8, **48**
 Raitzes, Y.: SE+EM+EN+PS+TF-MoM2, **4**
 Raman, K.V.: MI+EM-MoM8, **4**
 Ramana, C.V.: EN+AS+EM-WeA4, **38**
 Ramanathan, K.: EL+AS+BI+EM+SS-FrM5, **58**
 Ramanathan, S.: EM2-WeM3, **30**
 Ramaswamy, N.: EM2-ThM10, **45**

- Rangan, S.: EN+EM+NS-TuA4, 18
Ravikumar, S.: EM+EN+TF-WeA2, 35
Reed, E.J.: 2D+AS+EM+MI+MN+NS+TF-WeA12, 35
Reese, M.O.: EN+AS+EM+SE-WeM10, 32
Reeves, R.J.: EN+AS+EM+SE-WeM11, 33
Reichmanis, E.: EN+AS+EM-WeA1, 38
Reinecke, T.: 2D+AS+EM+NS+SS-MoA3, 7
Ren, H.: EM-WeA11, 37
Renault, O.J.: 2D+EM+MI+MN+NS+SS+TF-ThA10, 49
Repins, I.: EL+AS+EM+EN+SS-ThM3, 42
Reshchikov, M.A.: EM+EN-FrM3, 59
Reutt-Robey, J.: 2D+AS+EM+MI+MN+NS+TF-WeA8, 34
Rice, C.: EL+AS+BI+EM+SS-FrM8, 58
Richter, C.A.: 2D+EM+MS+NS-FrM4, 56; EN+AS+EM-WeA11, 38; SS+EM-FrM2, 62
Robinson, J.: 2D+AS+EM+NS+SS-MoA3, 7; 2D+EM+NS+PS+SS+TF-MoM4, 1
Robinson, J.A.: 2D+EM+NS+SS+TF-WeM11, 28; 2D+EM+NS+SS+TF-WeM6, 27
Robinson, Z.R.: 2D+EM+NS+PS+SS+TF-MoM3, 1; EM1-WeM5, 29
Rockett, A.: EN+AS+EM+SE-WeM2, 31
Rodrigues, J.N.: 2D+EM+MI+MN+NS+SS+TF-ThA4, 48
Röling, C.: EL+AS+EM+MC+SS-ThA10, 51; EL+AS+EM+MC+SS-ThA7, 50
Rolison, D.R.: EM+EN+TF-WeA11, 36
Romero, D.: 2D+AS+EM+MI+MN+NS+TF-WeA7, 34
Roth, S.: 2D+EM+NS+PS+SS+TF-MoM8, 2
Rouchon, D.: 2D+EM+MI+MN+NS+SS+TF-ThA10, 49
Rowe, J.E.: MI+EM-MoM10, 4
Roy Choudhury, K.: EN+AS+EM-WeA3, 38
Rubloff, G.W.: EM+EN+TF-WeA10, 36; EN+EM+NS-TuA3, 17; EN+EM+NS-TuA7, 18; EN+EM+NS-TuA8, 18
Rudolph, M.: EM1-ThA6, 51; EM1-ThA7, 52
Rullan, J.: EM-TuM3, 12
Rupich, S.: EN+EM+MN+NS+TR-MoA3, 10
Rutigliani, V.: EM-TuM6, 12
Ryan, K.E.: SP+AS+BI+EM+NS+SE+SS-FrM2, 61
- S —
Saint-Girons, G.: EM+MI+NS-MoM8, 3
Samaraweera, R.L.: EM-TuP15, 24; EM-TuP17, 24
Sampat, S.: EN+EM+MN+NS+TR-MoA3, 10
Sampath, W.: EN+AS+EM+SE-WeM13, 33
Samukawa, S.: 2D+AS+EM+NS+SS-MoA9, 8
Sanchez, E.: SP+AS+EM+NS+SS-ThP8, 55
Sardashti, K.: EM-WeA12, 37; EN+AS+EM+SE-WeM4, 32
Saroja, M.: EM+EN+TF-WeA2, 35
Sato, H.: EM-TuP12, 23; EM-TuP13, 24
Savage, T.: EM-TuM6, 12
Scanlon, D.O.: EN+AS+EM+SE-WeM11, 33
Schaefer, D.: EM+MI+NS-MoM4, 2
Schamm-Chardon, S.: EM+MI+NS-MoM8, 3
Schell, M.: EM-TuP16, 24
Scheu, C.: EN+EM+MN+NS+TR-MoA10, 11
Schlaf, R.: 2D+EM+NS+SS+TF-WeM5, 27
Schmidt, D.: EL+AS+EM+MC+SS-ThA4, 50
Schmidt-Mende, L.: EM2-ThA8, 53; EN+EM+MN+NS+TR-MoA10, 11
Schmitz, A.: EM1-WeM10, 29
Schreiber, N.J.: SS+EM-FrM3, 63
Schroeder, M.A.: EM+EN+TF-WeA10, 36; EN+EM+NS-TuA7, 18; EN+EM+NS-TuA8, 18
Schubert, E.: EL+AS+EM+MC+SS-ThA4, 50; EL+AS+EM+MC+SS-ThA6, 50
Schubert, M.: EL+AS+BI+EM+SS-FrM8, 58; EL+AS+EM+MC+SS-ThA4, 50; EL+AS+EM+MC+SS-ThA6, 50; EL+AS+EM+MC+SS-ThA9, 50
- Schuller, J.: 2D+AS+EM+MI+MN+NS+TF-WeA9, 34
Schwarm, S.: TF+AS+EM-TuA1, 19
Schwarz, U.D.: 2D+EM+NS+SS+TF-WeM4, 27
Schwier, E.F.: 2D+EM+MI+MN+NS+SS+TF-ThA8, 48
Segalman, R.: EN+AS+EM+SE-TuM10, 14
Seidlitz, D.: EM-TuP15, 24; EM-TuP17, 24
Sekine, M.: 2D+EM+MS+NS-FrM10, 57
Sekora, D.: EL+AS+BI+EM+SS-FrM8, 58; EL+AS+EM+MC+SS-ThA6, 50
Senabulya, N.: EN+AS+EM+SE-WeM11, 33
Senevirathna, M.K.I.: EM+EN-FrM11, 60; EM-TuP17, 24
Senevirathne, I.: EM-TuP16, 24
Seo, H.-C.: EM1-WeM10, 29
Shamberger, P.J.: 2D+EM+NS+PS+SS+TF-MoM5, 1
Shankar, S.: EM+EN+TF-WeA2, 35
Sharma, P.: EM+MI+NS-MoM4, 2
Sheehan, B.: EM+2D-TuA8, 17
Sheehan, P.E.: 2D+AS+EM+NS+SS-MoA3, 7
Shekhter, P.: EM1-ThA11, 53
Shepard, K.: 2D+EM+MI+MN+NS+SS+TF-ThA4, 48
Shiao, M.H.: SP+AS+EM+NS+SS-ThP5, 55
Shimada, M.: 2D+EM+MI+MN+NS+SS+TF-ThA8, 48
Shohet, J.L.: EM-TuP11, 23; EM-WeA11, 37
Shu, J.: EM-TuM3, 12
Shudo, K.: EM-TuP12, 23; EM-TuP13, 24
Shutthanandan, V.: TF+EM+EN-WeA11, 40
Siegel, D.A.: SP+2D+AS+EM+MC+NS+SS-ThM11, 47
Simonato, J.-P.: 2D+EM+MI+MN+NS+SS+TF-ThA10, 49
Simons, D.: EM1-ThA3, 51
Simpson, J.R.: 2D+AS+EM+MI+MN+NS+TF-WeA4, 34; 2D+AS+EM+MI+MN+NS+TF-WeA7, 34
Singh, B.: TF+EM+EN-WeA7, 40
Sinno, T.R.: EM1-ThA4, 51; EM1-ThA8, 52
Smeu, M.: SP+2D+AS+EM+MC+NS+SS-ThM5, 46
Smith, D.J.: EM+MI+NS-MoM3, 2
Smith, R.: 2D+EM+NS+PS+SS+TF-MoM5, 1
Solares, S.D.: SP+AS+BI+EM+NS+SE+SS-FrM8, 62
Solokha, V.: EL+AS+EM+EN+SS-ThM12, 43
Son, K.A.: EM1-WeM10, 29
Song, Y.J.: SP+AS+EM+NS+SS-ThP3, 55
Sonnenfeld, A.: 2D+EM+NS+SS+TF-WeM4, 27
Stahlbush, R.E.: EM1-WeM5, 29
Stampe, P.A.: EN+AS+EM+SE-WeM11, 33
Stemmer, S.: EM+MI+NS-MoM1, 2
Stevenson, R.: 2D+EM+NS+PS+SS+TF-MoM5, 1
Stoehr, J.: MI+EM-MoM11, 4
Stradins, P.: EM1-ThM10, 44
Stroscio, J.A.: 2D+EM+MI+MN+NS+SS+TF-ThA4, 48; SP+AS+BI+EM+NS+SE+SS-FrM6, 62; SP+AS+EM+NS+SS-ThP3, 55
Stumpf, C.: EM+MI+NS-MoM4, 2
Su, C.Y.: EM+EN-FrM5, 59
Su, J.Y.: SP+AS+EM+NS+SS-ThP5, 55
Subramania, G.: EM1-ThA6, 51
Sugiyama, M.: EN+EM+MN+NS+TR-MoA11, 11
Sun, L.: TF+EM+EN-WeA10, 40
Sun, Z.: EM-TuM3, 12
Sundar, U.: EM+EN+TF-WeA1, 35
Suzer, S.: 2D+EM+MI+MN+NS+SS+TF-ThA11, 49
Suzuki, A.: EM-TuP12, 23
Suzuki, H.: EN+EM+MN+NS+TR-MoA11, 11
Syed, M.: EM-TuP16, 24
Syers, P.S.: SP+AS+BI+EM+NS+SE+SS-FrM6, 62
- T —
Takahashi, K.: SE+EM+EN+PS+TF-MoM3, 5
Talledo, A.F.: EM-TuP26, 25
- Tan, X.: EL+AS+EM+EN+SS-ThM4, 42
Tanen, N.J.: EN+AS+EM+SE-WeM6, 32
Tang, G.: SE+EM+EN+PS+TF-MoM3, 5
Tang, K.: EM-WeA12, 37
Taniguchi, T.: 2D+EM+MI+MN+NS+SS+TF-ThA4, 48; 2D+EM+MS+NS-FrM3, 56
Taylor, D.: EN+EM+MN+NS+TR-MoA3, 10
Teckcan, B.: TF+EM+EN-WeA2, 39
Teeter, G.: EL+AS+BI+EM+SS-FrM5, 58
Tellez, H.: EN+AS+EM+SE-WeM2, 31
Ten Eyck, G.: EM1-ThA6, 51
Thamaraiselvan, P.: EM+EN+TF-WeA2, 35
Thiesen, P.H.: EL+AS+EM+MC+SS-ThA10, 51; EL+AS+EM+MC+SS-ThA7, 50
Thissen, N.F.W.: 2D+EM+MS+NS-FrM6, 56
Thompson, C.V.: EM-TuM10, 13; EM-TuM4, 12
Thon, S.M.: EN+EM+MN+NS+TR-MoA1, 10
Thorpe, R.: EN+EM+NS-TuA4, 18
Timm, R.: EM+2D-TuA1, 16
Tischler, J.G.: EM-MoA10, 9; EM-TuP20, 25
Tiwald, T.: EL+AS+EM+EN+SS-ThM10, 43
Tokei, Z.: EM-TuM6, 12
Tolstaya, E.I.: EN+EM+NS-TuA9, 18
Tra, V.: MI+EM-MoM2, 3
Trappen, R.: MI+EM-MoM2, 3
Triscone, J.-M.: MI+EM-MoM3, 3
Trouiller, C.: SS+EM-FrM9, 64
Tsai, C.H.: EM+NS+TF-FrM5, 60
Tsai, H.-Z.: 2D+EM+MS+NS-FrM3, 56
Tsukagoshi, K.: EM-TuP8, 23
Tsybal, E.Y.: EM+MI+NS-MoM10, 3
Tu, C.G.: EM+EN-FrM5, 59
Turkowski, V.: 2D+AS+EM+MI+MN+NS+TF-WeA3, 34
Turner, K.T.: SP+AS+BI+EM+NS+SE+SS-FrM2, 61
Tyagi, P.: 2D+EM+NS+PS+SS+TF-MoM3, 1
Tyani, E.: EM-TuP24, 25
Tyurnina, A.: 2D+EM+MI+MN+NS+SS+TF-ThA10, 49
- U —
Urena, R.E.: EN+AS+EM+SE-WeM6, 32
- V —
Vandenbergh, W.G.: EM-WeA7, 37
VanDerslice, J.: EL+AS+EM+EN+SS-ThM10, 43
Vanfleet, R.R.: EM+EN+TF-WeA9, 36
Vargas, M.: EN+AS+EM-WeA4, 38
Varshney, V.: SE+EM+EN+PS+TF-MoM8, 5
Veal, T.D.: EN+AS+EM+SE-WeM11, 33
Velasco Jr., J.: 2D+EM+MS+NS-FrM3, 56
Venkatachalam, M.: EM+EN+TF-WeA2, 35
Ventrice, Jr., C.A.: 2D+EM+NS+PS+SS+TF-MoM3, 1
Vervuurt, R.H.J.: 2D+EM+MS+NS-FrM6, 56
Verweij, H.: EL+AS+BI+EM+SS-FrM4, 58
Vescovo, E.: MI+EM-MoM10, 4
Vishwanath, S.: EM-WeA9, 37
Voevodin, A.A.: 2D+EM+NS+PS+SS+TF-MoM5, 1; SE+EM+EN+PS+TF-MoM8, 5
Von Son Palacio, G.: 2D+EM+NS+SS+TF-WeM10, 28
Vurgaftman, I.: EM1-ThM12, 44
Vysochanskii, Y.: 2D+EM+MI+MN+NS+SS+TF-ThA9, 49
- W —
Wager, J.: EM2-WeM13, 31
Waite, A.: 2D+EM+NS+PS+SS+TF-MoM5, 1
Wallace, R.M.: 2D+EM+NS+SS+TF-WeM6, 27; EM+2D-TuA3, 16; EM+2D-TuA7, 16; EM-WeA4, 37; EM-WeA9, 37
Walls, J.M.: EN+AS+EM+SE-WeM13, 33
Wang, B.: 2D+EM+NS+PS+SS+TF-MoM5, 1
Wang, F.: 2D+EM+MS+NS-FrM3, 56
Wang, H.: TF+EM+EN-WeA11, 40
Wang, J.: EM-WeA9, 37
Wang, K.: SP+AS+BI+EM+NS+SE+SS-FrM6, 62
Wang, L.: 2D+EM+MI+MN+NS+SS+TF-ThA4, 48

- Wang, W.: EN+AS+EM+SE-WeM4, 32
Wang, X.: SP+AS+BI+EM+NS+SE+SS-FrM6, 62
Wang, Y.: 2D+AS+EM+MI+MN+NS+TF-WeA8, 34
Wang, Z.: 2D+EM+MS+NS-FrM5, 56
Wang, Z.L.: EN+EM+MN+NS+TR-MoA6, 10
Watanabe, K.: 2D+EM+MS+NS-FrM3, 56
Warecki, Z.: EM+MI+NS-MoM4, 2
Watanabe, K.: 2D+EM+MI+MN+NS+SS+TF-ThA4, 48
Watson, M.: 2D+AS+EM+MI+MN+NS+TF-WeA4, 34; 2D+AS+EM+MI+MN+NS+TF-WeA7, 34
Weber, J.W.: 2D+EM+MS+NS-FrM6, 56
Weber, M.H.: EN+EM+NS-TuA11, 19
Wei, L.: EM2-WeM13, 31
Wei, R.: SE+EM+EN+PS+TF-MoM5, 5
Weickert, J.: EM2-ThA8, 53; EN+EM+MN+NS+TR-MoA10, 11
Wen, L.G.: EM-TuM6, 12
Wetherington, M.: 2D+EM+NS+SS+TF-WeM11, 28
Wheeler, V.D.: EM1-WeM10, 29; EM1-WeM5, 29
White, C.T.: 2D+EM+MI+MN+NS+SS+TF-ThA3, 48
Whitham, K.: EM-MoA8, 9
Widom, M.: 2D+EM+NS+PS+SS+TF-MoM6, 1
Wiggins, B.C.: SP+2D+AS+EM+MC+NS+SS-ThM1, 46
Wilson, C.J.: EM-TuM6, 12
Winkler, K.: EM+2D-TuA3, 16
Wisdo, C.J.: EM-MoA11, 9
Wisnet, A.: EN+EM+MN+NS+TR-MoA10, 11
Wolden, C.A.: EN+AS+EM+SE-WeM10, 32
Wolkow, R.: SP+2D+AS+EM+MC+NS+SS-ThM5, 46
Wu, R.Q.: EN+AS+EM+SE-WeM5, 32
Wurstbauer, U.: EL+AS+EM+MC+SS-ThA10, 51
Wyrick, J.E.: 2D+EM+MI+MN+NS+SS+TF-ThA4, 48
— **X** —
Xiao, Z.: EL+AS+EM+EN+SS-ThM10, 43
Xin, H.: EN+AS+EM+SE-TuM3, 13
Xing, H.: 2D+AS+EM+MI+MN+NS+TF-WeA4, 34; EM-WeA9, 37
Xu, X.D.: 2D+EM+MI+MN+NS+SS+TF-ThA1, 48
Xu, X.S.: EM+MI+NS-MoM10, 3
— **Y** —
Yamada, H.: EM+NS+TF-FrM10, 61
Yamamoto, I.: EM-TuP8, 23
Yan, J.: 2D+EM+MS+NS-FrM4, 56; EN+AS+EM+SE-TuM3, 13
Yan, R.: 2D+AS+EM+MI+MN+NS+TF-WeA4, 34
Yang, B.: EM1-WeM10, 29
Yang, C.-C.: EM+EN-FrM5, 59
Yang, J.J.: EM2-ThM1, 45
Yang, K.: 2D+EM+NS+SS+TF-WeM10, 28
Yang, R.: 2D+EM+MS+NS-FrM5, 56
Yang, W.: 2D+EM+MS+NS-FrM3, 56
Yang, Y.: EN+AS+EM+SE-WeM11, 33
Yao, Y.F.: EM+EN-FrM5, 59
Yarlequé, M.: EM-TuP26, 25
Yeom, G.: 2D+AS+EM+NS+SS-MoA4, 7; 2D+AS+EM+NS+SS-MoA8, 8
Yerci, S.: EM1-ThM3, 44
Yitamben, E.: EM1-ThA7, 52
Yong, G.: EM+MI+NS-MoM4, 2
Yoon, H.: EN+AS+EM+SE-WeM12, 33
Yoon, W.: EM-TuP20, 25
Yoon, Y.: EN+AS+EM+SE-WeM12, 33
Yoshida, S.: EM-TuP9, 23
Young, A.F.: 2D+EM+MI+MN+NS+SS+TF-ThA4, 48
Yu, E.T.: EM1-ThA10, 52
Yu, H.Z.: EM-TuM4, 12
Yue, R.: EM-WeA4, 37
— **Z** —
Zalalutdinov, M.: 2D+AS+EM+NS+SS-MoA3, 7
Zettl, A.: 2D+EM+MS+NS-FrM3, 56
Zhang, C.W.: EL+AS+EM+MC+SS-ThA3, 50
Zhang, D.: SP+AS+BI+EM+NS+SE+SS-FrM6, 62; SP+AS+EM+NS+SS-ThP3, 55
Zhang, G.: 2D+EM+MS+NS-FrM3, 56
Zhang, L.: EM-TuM6, 12
Zhang, L.Z.: 2D+AS+EM+NS+SS-MoA10, 8
Zhang, S.: EM+2D-TuA12, 17
Zhang, X.: EM1-ThM13, 45; SP+2D+AS+EM+MC+NS+SS-ThM6, 46
Zhang, Y.: 2D+EM+MS+NS-FrM3, 56
Zhang, Y.N.: EN+AS+EM+SE-WeM5, 32
Zhao, L.: EM-WeA11, 37
Zhao, Y.: 2D+EM+MI+MN+NS+SS+TF-ThA4, 48
Zhao, Y.P.: TF+EM+EN-WeA8, 40; TF+EM+EN-WeA9, 40
Zheng, P.: EM-TuM12, 13
Zhernokletov, D.M.: EM2-WeM1, 30
Zhitenev, N.B.: 2D+EM+MI+MN+NS+SS+TF-ThA4, 48; EN+AS+EM+SE-WeM12, 33
Zhou, J.: MI+EM-MoM2, 3
Zhou, M.: EM-TuP5, 22
Zhou, T.: EM-TuM12, 13
Zhu, J.F.: EN+AS+EM-WeA12, 39
Zhu, X.: 2D+EM+NS+SS+TF-WeM4, 27
Zide, J.M.O.: EM-MoA6, 9
Zuilhof, H.: SS+EM-FrM4, 63